

STRUCTURAL, MAGNETIC AND THERMAL PROPERTIES OF DOPED ORTHOFERRITE MATERIALS

Ph.D. THESIS

by

ANKITA SINGH



**DEPARTMENT OF PHYSICS
INDIAN INSTITUTE OF TECHNOLOGY ROORKEE
ROORKEE - 247667 (INDIA)
SEPTEMBER, 2019**



STRUCTURAL, MAGNETIC AND THERMAL PROPERTIES OF DOPED ORTHOFERRITE MATERIALS

A THESIS

*Submitted in partial fulfillment of the
requirements for the award of the degree*

of

DOCTOR OF PHILOSOPHY

in

PHYSICS

by

ANKITA SINGH



**DEPARTMENT OF PHYSICS
INDIAN INSTITUTE OF TECHNOLOGY ROORKEE
ROORKEE - 247667 (INDIA)
SEPTEMBER, 2019**





**©INDIAN INSTITUTE OF TECHNOLOGY ROORKEE, ROORKEE-2019
ALL RIGHTS RESERVED**





INDIAN INSTITUTE OF TECHNOLOGY ROORKEE

STUDENT'S DECLARATION

I hereby certify that the work presented in the thesis entitled "STRUCTURAL, MAGNETIC AND THERMAL PROPERTIES OF DOPED ORTHOFERRITE MATERIALS" is my own work carried out during a period from December, 2014 to September, 2019 under the supervision of Dr. Vivek Kumar Malik, Assistant Professor, Department of Physics, Indian Institute of Technology Roorkee, Roorkee.

The matter presented in the thesis has not been submitted for the award of any other degree of this or any other Institute.


Dated: 11/12/19


(ANKITA SINGH)


SUPERVISOR'S DECLARATION


This is to certify that the above mentioned work is carried out under my supervision.

Dated: 12/12/19


(VIVEK KUMAR MALIK)


The Ph.D. Viva-Voce Examination of Ms. ANKITA SINGH, Research Scholar, has been held on December 11, 2019.


Chairman, SRC


Signature of External Examiner

This is to certify that the student has made all the corrections in the thesis.


Signature of Supervisor


Head of the Department

Dated: December 11, 2019



ABSTRACT

Among transition metal oxides, Orthoferrites ($R\text{FeO}_3$), where R = rare earth element, are widely studied because of their unique magnetic properties. The magnetic ground state of Orthoferrites is primarily determined by the Fe^{3+} - Fe^{3+} exchange interaction at ambient temperatures which is antiferromagnetic G - type ordering having easy axis along the x - direction. In most of the Orthoferrites at high temperature, the magnetic ordering is canted antiferromagnetic with a weak ferromagnetic component. This canting is present due to weaker and antisymmetric superexchange interaction known as Dzyaloshinsky – Moriya interaction. A relatively weaker Fe^{3+} - R^{3+} exchange interaction is also active in Orthoferrites. Due to antisymmetric and anisotropic-symmetric part of Fe^{3+} - R^{3+} exchange interaction, Fe spins undergo spin reorientation with the easy axis changing from x -direction to y -/ z -direction. R^{3+} - R^{3+} exchange interaction in Orthoferrites is the weakest as compared to Fe^{3+} - Fe^{3+} and Fe^{3+} - R^{3+} interactions. This interaction occurs at very low temperature (below 10 K) and decides the possible magnetic ordering of rare earth ions.

In the present work, mainly the Orthoferrite (NdFeO_3) has been studied by varying the transition metal site properties in one case and the rare earth site properties in the other case. The main objective of this thesis is to study the structural, magnetic and thermal properties of polycrystalline Orthoferrite. In the first part of the thesis, 50% doping of Mn is done on the Fe site to study the change in structural and magnetic properties of the compound with the doping. In the second part of the thesis, doping was done on the rare earth site, i.e. 50% Dy was doped on the Nd site to study the change in magnetic property and structure of Fe^{3+} and rare-earth ($\text{Dy}^{3+}/\text{Nd}^{3+}$) spins. Spin reorientation of Fe^{3+} ions in both compounds is studied in detail. Study of magnetocaloric effect is also performed on both the compounds in this thesis. Further, structural and magnetic properties of $\text{NdFe}_{0.5}\text{Mn}_{0.5}\text{O}_3$ thin film on SrTiO_3 are studied.

The chapter-wise overview of the present thesis work has been discussed below:

Chapter 1 gives the general introduction of transition metal oxides and Orthoferrites with a brief description of the origin of magnetism in these compounds. Further, spin reorientation which is observed in all the Orthoferrites with magnetic rare earth ion is discussed in detail. The factors affecting the direction and transition temperature of spin reorientation along with the type of

magnetic structure is discussed. In this thesis magnetocaloric effect has been studied in Orthoferrite compounds. Thus the magnetocaloric effect is explained in detail. The previous studies on Mn doped Orthoferrites materials have been discussed. A literature survey has been done on the substitution of Mn on Fe site for different rare earth material as well as for doping on rare earth site. Finally, the scope of the thesis is outlined in the last section.

Chapter 2 describes the details of experimental techniques, which have been used throughout the work in the present thesis for the synthesis and characterization of perovskite structure based orthoferrites in polycrystalline as well as thin film forms. The polycrystalline compound has been prepared by using conventional solid-state reaction route. The synthesis of thin films has been carried out by pulsed laser deposition technique. The structural properties of the samples were studied using X-Ray diffraction (XRD) and Neutron diffraction. Magnetic properties of all the samples were studied using Superconducting Quantum Interference Device (SQUID). Heat capacity measurements were carried out using specific heat option of Physical Property Measurement System (PPMS).

In chapter 3, structural and magnetic properties of $\text{NdFe}_{0.5}\text{Mn}_{0.5}\text{O}_3$ (NFMO) has been investigated in detail. The synthesis of the sample was done by conventional solid-state reaction method. Rietveld refinement of powder X-Ray diffraction data suggest that NFMO possesses an orthorhombic structure with space group $Pbnm$. Due to the presence of 50% Mn on Fe site, Jahn – Teller distortion is present in the MO_6 ($M = \text{Fe}, \text{Mn}$) octahedra. The M - T curves of NFMO exhibit paramagnetic to antiferromagnetic transition at 250 K which is intermediate to the T_N of NdFeO_3 and NdMnO_3 . Additionally, another magnetic transition is observed at 36 K which denotes the spin reorientation of $\text{Fe}^{3+}/\text{Mn}^{3+}$ spins. The spin reorientation is also confirmed by M - H curves measured at different temperatures. According to Mössbauer spectroscopy, Fe^{3+} spins show paramagnetic behavior at 300 K. At lower temperatures (5 - 100K) Mössbauer spectra is fitted using two sextets which confirms the magnetic ordering of Fe^{3+} spins. The data analysis of Mössbauer spectra also indicates the spin reorientation of Fe^{3+} spins in lower temperature range.

Chapter 4 deals with the powder neutron diffraction studies of polycrystalline NFMO sample in the temperature range 1.5 – 400 K. Initially, 3- dimensional short-range ordering is discussed that is present over the whole temperature range 400 – 1.5 K and suppressed by the long-range ordering with the decreasing temperature. There is a presence of broad magnetic Bragg peak at

300 K. This peak represents the mixture of $\Gamma_4 (G_x, A_y, F_z)$ and $\Gamma_1 (A_x, G_y, C_z)$ magnetic structures, not like other orthoferrites which have Γ_4 magnetic structure at 300 K. The possible reason for the presence of Γ_1 magnetic structure is the presence of Mn^{3+} ions which have large single ion anisotropy. Below T_N , the contribution from Γ_4 magnetic structure starts decreasing gradually with an increase in the contribution of Γ_1 structure. At 150 K, contribution of Γ_4 vanishes completely, leaving pure Γ_1 magnetic structure till 90 K. The magnetic structure undergoes another spin reorientation transition between temperature 75 and 25 K where the magnetic structure exists as a sum of two irreducible representations ($\Gamma_1 + \Gamma_2$). In this chapter, two-fold spin reorientation is discussed which is seen rarely in orthoferrites. At 1.5 K, antiferromagnetic structure belongs entirely to $\Gamma_2 (G_z)$ with small ferromagnetic canting (f_x) due to Nd. To further investigate rare earth ordering at low temperature, specific heat of NFMO have been measured and analyzed where $Nd^{3+} - Fe^{3+}/Mn^{3+}$ exchange interactions dominates over $Nd^{3+} - Nd^{3+}$ interactions, as evident from the presence of Schottky anomaly.

Chapter 5 describes the synthesis and characterization of $Nd_{0.5}Dy_{0.5}FeO_3$ (NDFO). Rietveld refinement of XRD data suggests that NDFO is orthorhombic in structure with $Pbnm$ space-group. In the case of magnetic structure, the magnetic structure of Fe^{3+} belongs to $\Gamma_4 (G_x, F_z)$ at room temperature. The magnetization data indicate the occurrence of spin reorientation below 60 K. The neutron diffraction studies confirmed the spin reorientation where the magnetic structure of Fe^{3+} changes gradually from Γ_4 to Γ_2 between 60 and 20 K while maintaining G type configuration. Between 20 and 10 K, the Fe^{3+} magnetic structure is represented by Γ_2 with Fe^{3+} magnetic moments arranged in G_z type configuration with a small ferromagnetic moment along a direction. Interestingly, Γ_4 magnetic structure of Fe^{3+} re-emerges below 10 K which also coincides with the development of rare earth (Nd^{3+}/Dy^{3+}) magnetic ordering having C_y configuration with magnetic moment of $1.8 \mu_B$. The absence of any signature of second order phase transition in the specific heat confirms the role of $R(Nd^{3+}/Dy^{3+}) - Fe^{3+}$ exchange interaction in the observed rare – earth ordering unlike $DyFeO_3$ where Dy^{3+} ordering takes place independently to the magnetic ordering of Fe^{3+} magnetic structure.

In chapter 6, magnetocaloric effect has been studied in detail for $Nd_{0.5}Dy_{0.5}FeO_3$ and $NdFe_{0.5}Mn_{0.5}O_3$. An enhancement in the magnetization led to a large change in magnetic entropy ($10.4 Jkg^{-1}K^{-1}$) at 4K in NDFO. The observed entropy change is remarkable considering the smaller

value of Nd^{3+} moment as compared to that of Dy^{3+} . Change in magnetic entropy of NFMO is $2.98 \text{ Jkg}^{-1}\text{K}^{-1}$ at 4.75 K which is smaller as compared to NDFO. On comparison with other Nd based transition metal oxide, NFMO has higher value making it suitable for application due to the relatively high abundance of Nd in nature.

From application point of view, the presence of such a high value of change in magnetic entropy, as well as relative cooling power of NDFO and NFMO, makes both the compound good alternative for magnetic refrigeration at lower temperature which will also prove to be environment friendly.

In chapter 7, the growth and characterization of $\text{NdFe}_{0.5}\text{Mn}_{0.5}\text{O}_3$ thin films have been discussed in detail which is deposited using pulsed laser deposition technique on STO substrate. The thin film deposition was optimized by varying various deposition parameters. X-ray diffraction confirms the out-of-plane growth of the films i.e. they are (00 l) oriented. Magnetic property of NFMO thin film on STO substrate has also been studied. In the magnetic studies, magnetic ordering with the low temperature spin reorientation transition has been observed in the thin film.

Chapter 8 summarizes the work done in the present thesis and presents a brief conclusion with some future scope of the research findings.

Keywords: Antiferromagnet, spin reorientation, entropy change, heat capacity, thin films

ACKNOWLEDGEMENT

At the completion of my PhD, I would like to express my honest gratefulness to all the people who made significant contribution and motivated me in this journey on the professional as well as personal front. The completion of this thesis has took enormous support and encouragement of numerous people including my supervisor, family, colleagues, friends and my second home my institute. At this stage I would like to express my thanks to all those who contributed in many ways to this study and made it an unforgettable experience for me. It would have been impossible for me to reach at this important stage of my career without their immense support and encouragement.

On the first note, I would like to express my heartfelt thanks to my supervisor Dr. Vivek Kumar Malik for giving me the opportunity to pursue my PhD under his supervision. I heartily thank him for giving me adequate room in my work so I could flourish. I am indebted to him for his valuable advice, support and endless patience he showed in my work. He also helped me a lot in improving my writing. I thank him for allowing me to lay my hands on all the equipment which widened my exposure and enhanced my versatility. I am really thankful to him for explaining me major to minute details of different techniques/experiment/methodology with utmost patience, which I will carry with me for lifetime. I thank him from the core of my heart for keeping me motivated in my work during my entire PhD duration.

I would like to extend my regards and gratitude to Prof. Ramesh Chandra, Professor, Institute Instrumentation Center, for allowing me to carry out my entire PhD work in his lab, “Nano Science Lab”. I thank him for accepting me in his group like his own student. He has always given me positive and friendly environment which really helped me in carrying out the research in my own way. His inspiring guidance, constant encouragement, moral support and keen interest in minute details of my work really helped me in carrying out my work in most efficient manner. I thank him for making me learn new instruments during their installations and inspiring me to work out of my own limits.

I am thankful to Prof. K. L. Yadav, Head, Department of Physics for his keen interest in my research work. I am also thankful to Prof. Tashi Nautiyal, Department of Physics, for her invaluable suggestions during the presentation of my initial PhD days. She taught and encouraged me to learn and understand even the smallest and basic concept of physics. I will keep her lessons with me as it improved my presentation a lot. My gratitude and sincere thanks to Prof. Davinder

Kaur, chairman DRC, Department of Physics, whose encouragement and timely suggestions helped me a lot. I am thankful to my SRC members, Prof. G. D. Varma, Chairman SRC, Department of Physics, Dr. Tulika Maitra, Internal expert, Department of Physics, Dr. T. K. Mandal, External expert, Department of Chemistry for their invaluable direction, encouragement and support, and above all the noblest treatment extended by them during the course of my studies at IIT Roorkee.

I am thankful to Dr. Yusuf, Head, SSPD Division, BARC, Mumbai and Dr. Anil Jain, BARC Mumbai for allowing me to visit BARC for experiment as well as discussion purpose. My special thanks to Dr. Anil Jain for teaching me the basic concepts of neutron diffraction and also helping me in carrying out the refinements which seemed very difficult to me at initial stage of my work. I thank him for squeezing out his valuable time in BARC as well as Roorkee whenever I had any doubt during my data analysis. My regard for Dr. Sujeet Chaudhary to carry out magnetization measurement in his lab at Department of Physics, IIT Delhi. I am grateful to Dr. Venugopal Reddy, UGC-DAE, Indore, for carrying out Mössbauer spectroscopy in his lab. I thank Sher Singh Meena, BARC, Mumbai for explaining me the experiment as well as data analysis of Mössbauer spectroscopy.

I thank Dr. Ruchika Yadav, Dr. Vivian Nassif for carrying out the powder neutron diffraction experiment at ILL, Grenoble. I thank Dr. Francoise Damay for carrying out the powder neutron diffraction experiment at LLB, Saclay. I am obliged to Dr. P.D. Babu and Dr. Naveen for carrying out the specific heat experiments in their respective labs at UGC Center, BARC, Mumbai and University of Vienna, Vienna, Austria respectively.

I am thankful to the clerical staff at the office of Department of Physics as well as IIC. I am thankful to Mrs. Arti Sharma and Mr. Akhilesh for providing the help on a single call at Department of Physics. At IIC, I am really thankful to Mr. Anil and Mr. Upendra for their help. My special thanks to Mr. Yashpal, Mr. Charan Singh and Mr. Kamal Singh Gotiyan for their help to sort out any technical problem at IIC. I am thankful to Mr. Kapil and Mr. Vikas at Department of Physics for their help in carrying out all my presentations in a befitting manner.

I am extremely grateful to Dr. Padmanabhan Balasubramanian for encouraging me throughout my work. He was always available for me to clear my doubts or problems that I encountered during my PhD journey. His gracious support and valuable suggestions on innumerable occasions have

expedited my research work and is nonpareil. He always gave new directions in the analysis of my results. I am thankful to my senior, Dr. Samta Chauhan for her guidance and constant support specially during the initial days of my PhD. She has helped me tremendously in learning the techniques and methodology of the work that I have performed. I am extremely thankful to Dr. Amit Kumar Singh for always being there for me and extending me his full support during my PhD. He is the perfect blend of a friend and a professional senior. I express my sincere thanks to all my seniors Dr. Paritosh, Dr. Archana, Dr. Monu, Dr. Ashwani, Dr. Jyoti, Dr. Arvind, Satyendra, Gaurav for supporting me during this whole period. I extend my sincere thanks to my colleagues Neetika, Anas, Jignesh, Shubham, Alisha, Reenu, Rinku, Parvesh, Sarita, Anita, Dharmendra, Ravikant, Brijmohan, and Pranjala for sharing and supporting me during my research work. I am thankful to Mrs. Meena Kothiyari for make me feel like home during the days when I used to feel very low at times.

I am lucky enough to have friends who stood by me through all ups and downs that I endured during my PhD journey. I thank my dearest childhood friend Akanksha for being at beck and call, whether to seek help or to share my moments of happiness and sorrow. I am also thankful to Komal, Sayantika, Priyamvada, Vandana, Rohit and Prabhat with whom I shared the memories of my graduation. I specially thank Prabhat for coming to Roorkee to join PhD and helping me during last days of my PhD. After spending the whole day in Lab while doing experiments, lengthy calculations one gets exhausted so did I use to, the moments of fun joy and happiness came as solace for me that I had in the company of fun loving and caring friends like Dr. Paritosh, Dr. Rashmi, Dr. Amit and Prapti who not only supported me but also helped me in settling down in IIT's life. I missed the company of these guys during last one year of my PhD. I thank Sarita for planning impromptu road trips that we took many times during the PhD journey which were most thrilling and exciting. I am thankful to Ravikant and Kirti for tolerating my mood swings specially during odd hours. I specially thank Kirti for listening my talks whole night many a times. I like to thank my best friend Chandan for his moral support, continuous encouragement and understanding in all the possible ways. I have learnt a lot from his attitude towards life, by miniaturizing the problems and being solution centric, concentrating rather than worrying about it. In brief to be conscious and alive.

I am also grateful to the Ministry of Human Resources and Development, Government of India, New Delhi for sponsoring my doctoral research work.

I shall be forever indebted to my family for their immense support and faith in me. I fell short of words in expressing my sincere gratitude to my parents Smt. Suman Pundir and Sh. Charan Singh Pundir for their love, blessings, supports and sacrifice to bring me up for achieving what I am today. I owe a deep sense of gratitude to my brother Mr. Ashish Pundir and my sister-in-law or say sister-in-love Mrs. Renu Pundir for their incessant emotional and mental support in this journey of PhD. They always kept me motivated to achieve my goals with constant advices and directions.

Last but not the least; I am thankful to the almighty who gave me the strength and health for completing my work.

(Ankita Singh)



CONTENTS

ABSTRACT	i
ACKNOWLEDGEMENT	v
LIST OF FIGURES	xiii
LIST OF TABLES	xix
ABBREVIATIONS	xxi
RESEARCH PUBLICATIONS	xxiii
Chapter 1.....	01
Introduction.....	01
1.1 Transition metal oxides	01
1.2 Rare earth orthoferrite.....	06
1.2.1 Magnetic properties.....	07
1.2.2 Magnetic phase transitions.....	10
1.2.2.1 Spin reorientation in orthoferrites	11
1.2.3 Heat Capacity.....	13
1.3 Magnetocaloric Effect.....	14
1.4 Literature survey.....	18
1.4.1 Doping of Mn on Fe site in rare earth orthoferrite.....	18
1.4.2 Doping on rare earth site in rare earth orthoferrite.....	24
1.4.3 Magnetocaloric effect in orthoferrites.....	26
1.5 Motivation for the present work.....	27
1.6 Objective of the Present Work.....	29
1.7 Organization of Thesis.....	30

Chapter 2	32
Experimental Techniques	32
2.1 Synthesis Techniques	32
2.1.1 Synthesis of Polycrystalline powder	32
2.1.2 Synthesis of Thin Film	35
2.1.2.1 Pulsed Laser Deposition	37
2.2 Characterization Techniques	40
2.2.1 X-Ray Diffraction	40
2.2.2 Reciprocal Space Map	46
2.2.3 Neutron Diffraction.....	49
2.2.3.1 Neutron Scattering.....	50
2.2.3.2 Elastic nuclear scattering.....	52
2.2.3.3 Magnetic structure determination from neutron scattering.....	53
2.2.3.4 Elastic neutron powder diffractometer.....	56
2.2.4 Rietveld analysis.....	58
2.2.5 Superconducting Quantum Interference Device Magnetometer	60
2.2.6 Specific Heat.....	65
Chapter 3	67
Synthesis and characterization of NdFe_{0.5}Mn_{0.5}O₃	67
3.1 Introduction	67
3.2 Experimental details	69
3.3 Results and discussion	71
3.3.1 Structural characterization	71

3.3.2 Magnetic properties	76
3.3.3 Mössbauer Spectroscopy.....	79
3.4 Conclusion	83
Chapter 4	85
Magnetic structure and specific heat of $\text{NdFe}_{0.5}\text{Mn}_{0.5}\text{O}_3$	85
4.1 Introduction	85
4.2 Experimental details	86
4.3 Results and discussion	87
4.3.1 Neutron diffraction measurements.....	87
4.3.1.1 Short range diffused scattering.....	90
4.3.1.2 High temperature neutron diffraction measurements.....	96
4.3.1.3. Low temperature neutron diffraction measurements.....	98
4.3.1.4 Neutron depolarization	102
4.3.1.5 Phenomenological explanation of spin reorientation at low temperature.....	103
4.3.2 Specific heat measurement.....	105
4.4 Conclusion	108
Chapter 5	110
Magnetic and thermal properties of $\text{Nd}_{0.5}\text{Dy}_{0.5}\text{FeO}_3$.....	110
5.1 Introduction	110
5.2 Experimental method	112
5.3 Results and discussion	113
5.3.1 Structural Characterization.....	113
5.3.2 Magnetic Properties.....	115

5.3.3 Dielectric Properties.....	118
5.3.4 Neutron Diffraction.....	119
5.3.5 Specific heat	125
5.4 Conclusion	126
Chapter 6	127
Magnetocaloric studies in Nd_{0.5}Dy_{0.5}FeO₃ and NdFe_{0.5}Mn_{0.5}O₃.....	127
6.1 Introduction	127
6.2 Experimental Technique.....	129
6.3 Results and discussion	130
6.3.1 Nd _{0.5} Dy _{0.5} FeO ₃ (NDFO).....	130
6.3.2 NdFe _{0.5} Mn _{0.5} O ₃ (NFMO).....	136
6.4 Conclusion	141
Chapter 7.....	142
Growth and characterization of orthoferrite epitaxial thin film.....	142
7.1 Introduction.....	142
7.2 Experimental details.....	144
7.3 Results and Discussion.....	146
7.4 Conclusion.....	152
Chapter 8	153
Conclusion and future scope.....	153
8.1 General Conclusions	153
8.2 Future Scope.....	156
Bibliography.....	159

LIST OF FIGURES

Figure 1.1 Block Diagram showing different properties of transition metal oxides	1
Figure 1.2 Crystal structure of the simple cubic perovskite ABO_3 . The A ions are shown as blue spheres on the corners of the cube, B ions are shown as green sphere at the center, the corners of the octahedral have oxygen ions denoted by red color.....	2
Figure 1.3 Different types of magnetic structure.....	7
Figure 1.3 Allowed spin configurations in the rare earth orthoferrites.....	8
Figure 1.5 Schematic diagram showing the two process isothermal magnetization (top panels) and adiabatic demagnetization (bottom panels) to understand the phenomenon of magnetocaloric effect	14
Figure 1.6 Schematic description of magnetic refrigeration cycle, which transports heat from heat load to surroundings	16
Figure 1.7 Left: Q_2 – distorted MnO_6 octahedron. Right: Three-dimensional network of cooperatively Jahn – Teller distorted MnO_6 – octahedral, which is connected to an antiferro-orbital ordering (adapted from ref. [74])	18
Figure 2.1 Flow chart of solid state reaction method.....	33
Figure 2.2 Schematic diagram of Pulsed Laser Deposition technique (adapted from ref. [151])....	38
Figure 2.3 Schematic diagram for diffraction of X-Ray from a crystalline structure.....	39
Figure 2.4 Coherent scattering of X-rays by a single electron (adapted from ref. [154])	41
Figure 2.5 Schematic diagram of beam path in Bruker D8 powder X-Ray diffractometer in Bragg-Brentano geometry (adapted from ref [155])	43
Figure 2.6 $\theta/2\theta$ measurement in Rigaku X-Ray diffractometer (adapted from ref. [156])	44
Figure 2.7 2θ scan with fixed ω measurement in Rigaku X-Ray diffractometer (adapted from ref. [156])	45
Figure 2.8 Schematic of the angles involved in X-Ray diffraction of a sample.....	46
Figure 2.9 Reciprocal space mapping measurement.....	47
Figure 2.10 Reciprocal space maps of hetero epitaxial thin films in different states. (a) Relaxed (b) Strained (c) Misoriented (adapted from ref. [156])	48

Figure 2.11 Geometry for scattering experiment (adapted from ref. [162])	50
Figure 2.12 Instrument layout of a typical modern neutron powder diffractometer D2B at ILL (adapted from ref. [165])	55
Figure 2.13 Layout of the cold neutron two axis diffractometer G4.1 at LLB (adapted from ref. [166])	56
Figure 2.14 Layout of the powder diffractometer II (PD-II) at Dhruva reactor at BARC ((adapted from ref. [167])......	57
Figure 2.15 Schematic of the MPMS magnetometer.....	61
Figure 2.16 Schematic for the detection coils wound in a second-order gradiometer configuration.....	63
Figure 2.17 Schematic of thermal connections to sample and sample platform in PPMS.....	65
Figure 3.1 Observed X-ray diffraction pattern of NFMO at room temperature, refined using orthorhombic <i>Pbnm</i> space group.....	70
Figure 3.2. Observed and refined neutron diffraction patterns of NFMO at room temperature confirm formation of the orthorhombic structure with <i>Pbnm</i> space group. The measurement was performed at PD-II using a neutron wavelength of 1.2443 Å.....	70
Figure 3.3 Crystal structure of NdFe _{0.5} Mn _{0.5} O ₃ showing the atomic positions of Nd, Fe, Mn and O.....	71
Figure 3.4 Variation of lattice parameter with temperature obtained from powder neutron diffraction in the range 1.5-400K.....	74
Figure 3.5 ZFC-FC plots of NFMO from 2 to 350K showing Néel temperature (T_N) at 250 K and weak ferromagnetism below 70 K.....	75
Figure 3.6 Real part of ac susceptibility for different frequencies.....	76
Figure 3.7 <i>M-H</i> plots of NFMO at (a) 5, (b) 10, (c) 25, (d) 45, (e) 70, (f) 100, (g) 200, (h) 300K.....	77
Figure 3.8 Variation of retentivity with temperature in NFMO.....	78
Figure 3.9 Mossbauer spectrum of NFMO sample recorded at 300 K showing the paramagnetic behaviour of Fe ³⁺ ions. Inset shows the spectrum recorded at higher velocity (± 11.5 mm/s)	79
Figure 3.10 Mossbauer spectra of NFMO sample recorded at 5 K, 40 K, and 100 K.....	80

Figure 3.11 Variation in (a) Hyperfine magnetic field (H_f), (b) Quadrupole splitting (Δ), (c) Isomer shift (δ), (d) Outer line width (Γ), (e) Relative area of sextets (R_A) and (f) Average outer line width ($\langle \Gamma \rangle$) with decreasing the temperature.....	82
Figure 4.1 Evolution of magnetic peak in neutron diffraction data as a function of temperature. These temperature dependent measurements were performed at PD-I ($\lambda = 1.094 \text{ \AA}$)	87
Figure 4.2. Neutron powder diffraction data from NFMO with a neutron wavelength of 2.414 \AA showing onset of short-ranged ordering centered around 1.4 \AA^{-1} . The box at 1.7 \AA^{-1} is from the (111) nuclear Bragg peak.....	89
Figure 4.3. Neutron powder diffraction data from NFMO with a neutron wavelength of 2.52 \AA at D1B ILL from $T = 300 \text{ K}$ to 15 K showing the prominent diffused scattering peak at 1.4 \AA^{-1} , on which the magnetic Bragg peak is superposed.....	90
Figure 4.4 The diffused only magnetic peak obtained by removing the long ranged magnetic Bragg peaks.....	91
Figure 4.5 Neutron powder diffraction data of NFMO from (a) $T = 300 \text{ K}$ to (d) 15 K . The magnetic Bragg peaks are fitted to sum of two Gaussian functions, while diffused scattering is fitted to Lorentzian function peaks.....	92
Figure 4.6 Temperature variation of intensity of the (011), (101) magnetic Bragg peaks, and the diffused peak.....	93
Figure 4.7 The temperature variation of FWHM and correlation length ξ	94
Figure 4.8. Experimental and refined powder neutron diffraction pattern for various temperature in the spin reorientation region measured at G4.1.....	95
Figure 4.9 Temperature dependence of three components of ordered Fe^{3+} magnetic moment obtained from Rietveld refinement of powder neutron diffraction.....	97
Figure 4.10 Experimental and refined neutron diffraction patterns of NFMO for various temperatures from 1.5 to 90 K measured at D1B (CRG). Inset shows the changed in the magnetic Bragg peak as a function of temperature. Inset in (e) weak magnetic signal at 38° due to Nd magnetism (f_x).....	99
Figure 4.11 Magnetic structure of NFMO represented by (a) $\Gamma_4 + \Gamma_1$ phase ordering at $\geq 200 \text{ K}$, (b) Γ_1 phase ordering $70\text{-}150 \text{ K}$, (c) Γ_2 phase ordering at 1.5 K with Nd^{3+} ferromagnetic ordering.....	100
Figure 4.12 Temperature variation of flipping ratio (R) under an applied magnetic guide field of 50 Oe for NFMO. Polarized neutron spectrometer was used for measurement.....	103
Figure 4.13 Specific heat of $\text{NdFe}_{0.5}\text{Mn}_{0.5}\text{O}_3$ and LaGaO_3	104

Figure 4.14 Magnetic contribution of specific heat of NFMO in the PM-AFM transition region.	105
Figure 4.15 Specific heat of NFMO under zero magnetic field and applied field of 3 T and 5 T which shows the presence of Schottky anomaly at lower temperature region.	106
Figure 5.1 Observed X-ray diffraction pattern of NDFO at room temperature, refined using orthorhombic <i>Pbnm</i> space group.	112
Figure 5.2 Temperature variation of lattice parameters and unit cell volume of NDFO.	113
Figure 5.3 ZFC-FC plots of NDFO at 100 Oe and 200 Oe. In the inset transition due to spin reorientation is shown at $T_{SR1} = 60$ K and $T_{SR2} = 30$ K.	116
Figure 5.4 ZFC-FC plots of NDFO at 1000 Oe and 5000 Oe.	116
Figure 5.5 M- H plots of NDFO at 5 K, 30 K, 60 K, 300 K, inset shows the M-H at 5 K in the field range ± 400 Oe.	117
Figure 5.6 Temperature dependence of real part of dielectric constant (ϵ) and dielectric loss ($\tan(\delta)$) for a) 5 KHz and b) 50 KHz at various magnetic fields.	118
Figure 5.7 Powder neutron diffraction at 300 K with Γ_4 magnetic representation showing magnetic peak at 32° .	119
Figure 5.8 Evolution of magnetic peak in neutron diffraction data as a function of temperature.	120
Figure 5.9 Temperature variation of Magnetic moment of Fe^{3+} and Nd^{3+}/Dy^{3+} spins from 1.5 K to 300 K for the various representations.	121
Figure 5.10 Variation of magnetic structure of NDFO from temperature 300 K to 1.5 K showing the gradual spin reorientation over the whole range.	122
Figure 5.11 The specific heat of NDFO for various fields plotted along with the fitting results. The inset contains specific heat in full temperature range.	124
Figure 6.1 Field cooled curve of NDFO under 100 Oe and 1000 Oe applied field.	130
Figure 6.2 (a) <i>M-H</i> isotherm for NDFO at different temperatures. Inset shows the hysteresis with coercivity in <i>M-H</i> loop at 5 K. (b) 300, 60 and 30 K <i>M-H</i> isotherms data at low magnetic field values to show hysteresis with coercivity clearly.	131
Figure 6.3 Field dependence of NDFO magnetization at different temperatures, measured to determine the adiabatic change in magnetic entropy.	132
Figure 6.4 Calculated ΔS_M values for NDFO from experimental magnetization data are shown in the form of points for different values of ΔH .	133

Figure 6.5 Field cooled magnetization data for NFMO under an applied field 100 Oe and 1000 Oe showing the drastic difference in magnetization at lower temperature.....	135
Figure 6.6 <i>M-H</i> isotherm of NFMO at different temperature showing clearly the hysteresis loop with coercivity at 5, 25 and 75 K while at 300 K paramagnetic behavior is shown. Inset shows the <i>M-H</i> isotherm at 5K under an applied field (± 5 T)	136
Figure 6.7 Field dependence of NFMO magnetization at different temperatures, measured to determine the adiabatic change in magnetic entropy.....	137
Figure 6.8 Calculated ΔS_M values for NFMO from experimental magnetization data are shown in the form of points for different values of ΔH	138
Figure 6.9 Variation of change in magnetic entropy under an applied magnetic field at spin reorientation region getting suppressed under a higher applied magnetic field.....	139
Figure 7.1 (a) $\theta/2\theta$ scan of NFMO thin film on STO substrate in the range 10° - 80° , (b) Narrow $\theta/2\theta$ scan of NFMO thin film on STO substrate in the range 46° - 47.8° to observe NFMO peak more clearly.....	144
Figure 7.2 X-Ray Diffraction Rocking curve for the (a) NFMO (004) peak and (b) STO (002) peak.....	145
Figure 7.3 Logarithmic intensity mapping along symmetric (002) peak in reciprocal space for NFMO thin film on STO substrate.....	146
Figure 7.4 Pole figure measurement on the logarithmic scale at (022) peak and black color circled data points indicate the (022) peak planes. Picture showing the angles related to pole figure is adapted from ref [249].....	147
Figure 7.5 ϕ scan of in-plane (022) peak of NFMO thin film on STO substrate.....	148
Figure 7.6 Atomic arrangement of (a) STO (100) with (b) NFMO (022) thin film. Ti and Sr atoms are shown with yellow and mauve color respectively in (a). Fe and Mn atoms occupy the same position in (b) shown with pink and blue color respectively, while Nd atom is shown by purple color.....	148
Figure 7.7 (a) XPS spectra for Mn2p and (b) XPS spectra for Fe2p in NFMO thin film.....	149
Figure 7.8 AC susceptibility of NFMO thin film on STO substrate in presence of zero DC field.....	150
Figure 7.9 <i>M-H</i> isotherm of NFMO thin film on STO substrate at 5 K.....	151




LIST OF TABLES

Table 1.1 Atomic position in cubic perovskites	3
Table 1.2 The Neel temperatures for different rare earth ions at R site in orthoferrites.....	6
Table 1.3 Irreducible representation of magnetic configuration corresponding to $R\text{FeO}_3$	8
Table 3.1 Structural parameters of $\text{NdFe}_{0.5}\text{Mn}_{0.5}\text{O}_3$ in comparison to NdMnO_3 and NdFeO_3	72
Table 3.2 Mössbauer parameters calculated from Mössbauer spectra recorded at low temperatures.....	81
Table 4.1 Magnetic structural details and transition temperatures of $\text{NdFe}_{0.5}\text{Mn}_{0.5}\text{O}_3$ from present studies and comparison with literature for end compounds NdFeO_3 , NdMnO_3 and related compounds. We list the three magnetic moment components along with rare earth moment M_R and the corresponding representations for various temperatures.....	101
Table 5.1 Structural parameters of $\text{Nd}_{0.5}\text{Dy}_{0.5}\text{FeO}_3$ obtained from neutron diffraction using Rietveld refinement for 300 K and 1.5 K.....	114
Table 6.1 Change in magnetic entropy for different rare earth orthoferrites.....	128
Table 6.2 Magnetic entropy change value for NDFO and NFMO for different applied field at 4 K and 6.5 K respectively.....	140



ABBREVIATIONS



AFM	Antiferromagnetic
BARC	Bhabha Atomic Research Center
CEF	Crystalline Electric Field
CVD	Chemical Vapor Deposition
DM	Dzyaloshinskii-Moriya
FC	Field Cooled
FM	Ferromagnetic
FWHM	Full Width Half Maxima
ILL	Institute Laue-Langevin
J-T	Jahn Teller
LAO	LaAlO ₃
LLB	Laboratoire Léon Brillouin
LRO	Long Ranged Ordering
MBE	Molecular Beam Epitaxy
MCE	Magnetocaloric effect
ME	Magneto-electric
M-H	Magnetization vs Magnetic Field
MOCVD	Metal-Organic Chemical Vapor Deposition
MPMS	Magnetic Property Measurement System
MR	Magnetic Refrigeration
NDFO	Nd _{0.5} Dy _{0.5} FeO ₃
NFMO	NdFe _{0.5} Mn _{0.5} O ₃
NPD	Neutron Powder Diffraction
PACVD	Plasma Enhanced Chemical Vapor

	Deposition
PLD	Pulse Laser Deposition
PM	Paramagnetic
PMFO	$\text{PrMn}_{1-x}\text{Fe}_x\text{O}_3$
PNS	Polarized Neutron Spectrometer
PPMS	Physical Property Measurement System
PSD	Position Sensitive Detector
PVA	Polyvinyl Alcohol
PVD	Physical Vapor Deposition
QD	Quantum Design
RE	Rare Earth
RSM	Reciprocal Space Map
SFMO	$\text{SmFe}_{1-x}\text{Mn}_x\text{O}_3$
SQUID	Superconducting Quantum Interference Device
SRO	Short Ranged Ordering
SRT	Spin reorientation Transition
STO	SrTiO_3
TMOs	Transition metal oxides
UV	Ultraviolet
VSM	Vibrating Sample Magnetometer
WFM	Weak ferromagnetic
XRR	X-ray reflectivity
XPS	X-ray photoelectron spectroscopy
XRD	X-Ray Diffraction
ZFC	Zero Field Cooled

Research Publications

Peer-Reviewed Journals

Publications related to the Thesis

- Spin reorientation in $\text{NdFe}_{0.5}\text{Mn}_{0.5}\text{O}_3$: Neutron scattering and Ab-initio study. **Ankita Singh**, A.Jain, Avijeet Ray, Padmanabhan B., Ruchika Yadav, Vivian Nassif, Sajid Husain, S.M. Yusuf, T. Maitra and V. K. Malik. *Phys. Rev. B* 96, 144420, 2017.
- An experimental and theoretical study of magnetocaloric effect in $\text{Nd}_{0.5}\text{Dy}_{0.5}\text{FeO}_3$. **Ankita Singh**, Sarita Rajput, Padmanabhan B., Kedarsh Kaushik, M. Anas, Ruchika Yadav, T. Maitra and V. K. Malik. *J. Phys. Cond. Mat.* 31, 355802, 2019.
- Successive spin reorientation and rare earth ordering in $\text{Nd}_{0.5}\text{Dy}_{0.5}\text{FeO}_3$: Experimental and Ab-initio investigations. **Ankita Singh**, Sarita Rajput, Padmanabhan B., M. Anas, Françoise Damay, C. M. N. Kumar, Gaku Eguchi, T. Maitra and V. K. Malik. Manuscript in [arXiv:1904.05837](https://arxiv.org/abs/1904.05837).
- Study of short range correlations and two-fold spin reorientation in $\text{NdFe}_{0.5}\text{Mn}_{0.5}\text{O}_3$: Ankita Singh, Padmanabhan B., Ruchika Yadav, Vivian Nassif, and V. K. Malik. Manuscript Submitted.
- Magnetocaloric and heat capacity studies on $\text{NdFe}_{0.5}\text{Mn}_{0.5}\text{O}_3$: Ankita Singh, Padmanabhan B., Mohd. Anas, P. D. Babu, C. M. N. Kumar, Wojciech Tabis and V. K. Malik. Manuscript Submitted.

Other Publications

- Structural transformation, Griffiths phase and metal-insulator transition in polycrystalline $\text{Nd}_{2-x}\text{Sr}_x\text{NiMnO}_6$ ($x = 0, 0.2, 0.4, 0.5$ and 1) compound. Amit Kumar Singh, Padmanabhan B. **Ankita Singh**, M.K. Gupta, Ramesh Chandra. *J. Phys. Cond. Mat.* 30, 355401, 2018.

- Electronic structure of $\text{Pr}_2\text{NiMnO}_6$ from X-Ray photoemission, absorption and density functional theory. Padmanabhan B., Shalik Ram Joshi, Ruchika Yadav, Frank M. F. deGroot, Amit Kumar Singh, Avijeet Ray, Mukul Gupta, **Ankita Singh**, Suja Elizabeth, Shikha Varma, T. Maitra and V. K. Malik. *J. Phys. Cond. Mat.* 30, 435603, 2018.

Oral/Poster Papers Presented in Conferences

- Presented poster on “**Effect of Sintering temperatures on structural and magnetic properties of $\text{Nd}_2\text{FeMnO}_6$** ” at **International Conference on Condensed Matter & Applied Physics**, Bikaner in October 2015.
- Oral presentation on “**Magnetic Properties of Fe doped Manganite $\text{NdMn}_{0.5}\text{Fe}_{0.5}\text{O}_3$** ” at **International Conference on Materials and Technology** at University of Delhi in March 2016.
- Presented a poster on “**Spin reorientation in polycrystalline $\text{NdFe}_{0.5}\text{Mn}_{0.5}\text{O}_3$ studied by neutron diffraction**” at **Conference on Neutron Scattering** at BARC Mumbai in November 2016.
- Presented poster on “**Effect of oxygen stoichiometry on the structural and magnetic properties of epitaxial $\text{Nd}_2\text{NiMnO}_6$ thin films**” at **International conference on Thin Films** at NPL, Delhi in November 2017.
- Presented a poster at **Recent Advances in Strongly Correlated Electronic Materials** at IIT Roorkee in February 2017.
- Presented poster on “**Study of Magnetocaloric effect in $\text{Nd}_{0.5}\text{Dy}_{0.5}\text{FeO}_3$** ” at **SSP-DAE Symposium at BARC**, Mumbai in December 2017.
- Presented poster presentation on “**Presence of unusual spin reorientation of $\text{Fe}^{3+}/\text{Mn}^{3+}$ spins in $\text{NdFe}_{0.5}\text{Mn}_{0.5}\text{O}_3$** ” at **2019 Joint InterMag-MMM Conference**, Washington, U.S.A. in January 2019.
- Presented poster on “**Presence of short range ordering in $\text{NdFe}_{0.5}\text{Mn}_{0.5}\text{O}_3$** ” at **2nd Annual Meeting on Physics of Strongly Correlated Electron Systems** at IIT Delhi in March 2019.





Chapter 1

Introduction

1.1 Transition metal oxides

Transition metal oxides (TMOs) have attracted large attention due to their wide range of applications in the bulk form as well as thin films[1][2]. Back in 12th century, iron ore mineral was used in the form of magnetic compass needle which is usually referred as first technological application of TMOs [3]. Since then, research on the magnetic properties of TMOs has been growing by leaps and bounds further making it more and more application oriented in the form of storage and memory devices, magnetic fluids, spintronics etc. The mixed valence state of transition metal ions is one of the key factor responsible for interesting electro-magnetic properties of TMOs [4][5]. TMOs show very rich phase diagram consisting of various electronic, ionic and magnetic properties e.g. ferromagnetic-insulating, antiferromagnetic-insulating or ferromagnetic-metallic, antiferromagnetic-metallic, high-

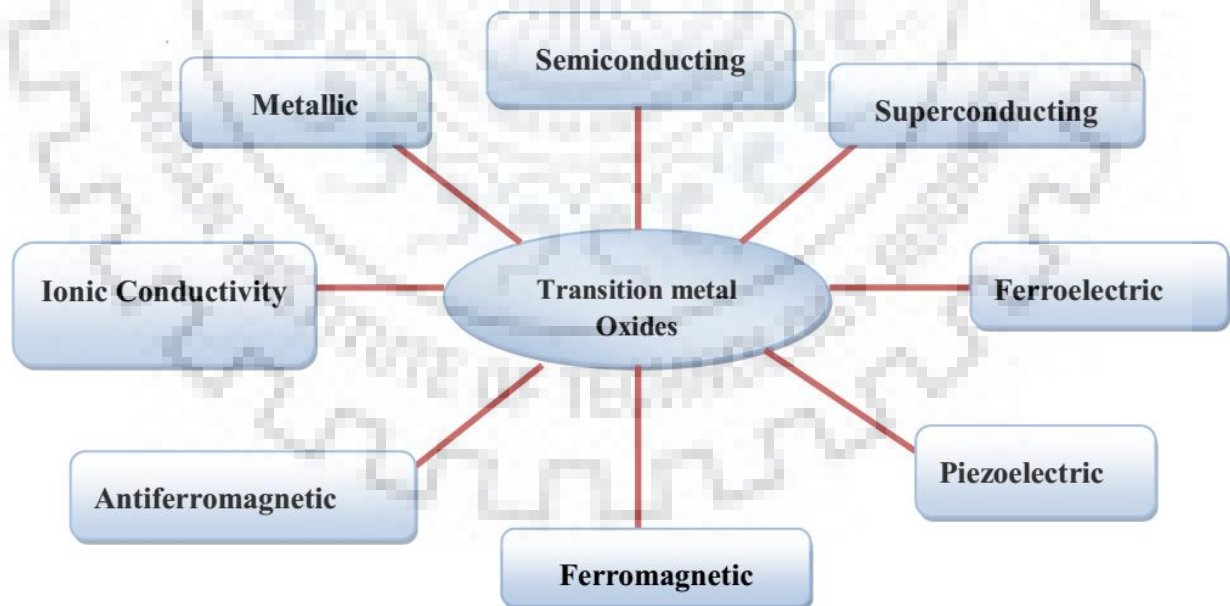


Figure 1.1 Block diagram showing different properties of transition metal oxides

temperature superconductivity, metal-to-insulator transition etc. [6][7][8]. Different properties of TMOs are shown in Figure 1.1.

Properties of most of the TMOs can be explained by Ligand field theory which is based on molecular orbital theory. This theory describes that the electronic structure of any complex compounds has central atom surrounded by electron-rich atoms known as ligands[4][7]. s and p electrons are known for strong interaction with neighboring atoms and are explained by the collective-electron model. Whereas outer f electrons are tightly bound to nuclei and screened from neighboring atoms, therefore best described by localized electron model. TMOs have d electrons with intermediate character that are not screened by the outer electrons and have better interaction with neighboring atoms. Therefore, d electrons have localized as well as itinerant nature in TMOs [9][10].

Most of the structural properties of TMO are based on MO_6 (M = transition metal) octahedra. Many different type of structures can be formed by the octahedra either by sharing

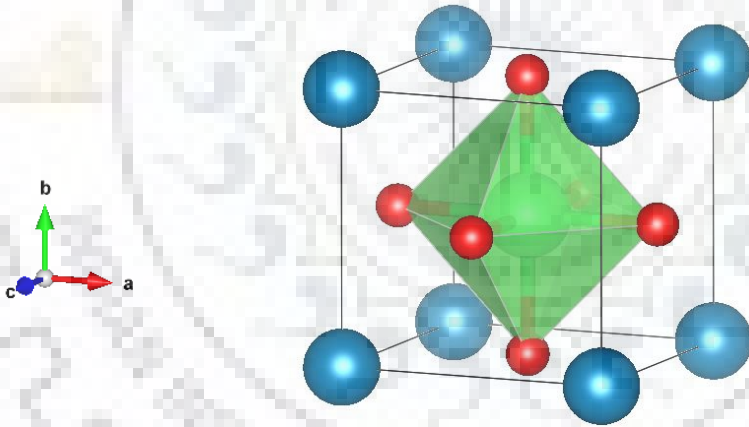


Figure 1.2 Crystal structure of the simple cubic perovskite ABO_3 . The A ions are shown as blue spheres at the corners of the cube, B ions are shown as green sphere at the center, the corners of the octahedral have oxygen ions denoted by red color

edges or corners. In some special cases, both edges and corners are shared. TMOs mainly have three types of structure which have their own set of material properties. These structures are spinel, perovskite and rutile structures. In the last few decades, TMOs with perovskite structure are intensely studied owing to their rich variety of magnetic, electrical and optical properties[11][12].

The perovskite structure has ABO_3 stoichiometry, where A and B are cations and O is anion, respectively. ABO_3 consists of B ions at the center of oxygen octahedra in a corner sharing arrangement. The A ions reside at the center of the remaining space and normally have less direct effect on the properties of the perovskite than the BO_6 octahedra. Another arrangement of perovskite is shown in Figure 1.2. Owing to their structure, strongly correlated electronic properties, perovskite oxides show features such as multiferroicity, piezoelectricity, ferroelectricity, etc[13].

Ideal crystal structure of perovskite is cubic with the space group $Pm\bar{3}m$ with the atomic position mentioned in Table 1.1[14]. Each cation and anion radii in cubic structure is related according to the relation

$$R_A + R_O = \sqrt{2}(R_B + R_O) \quad (1.1)$$

Table 1.1 Atomic positions in cubic perovskites

Site	Location	Co-ordinates
A cation	(2a)	(0, 0, 0)
B cation	(2a)	(1/2, 1/2, 1/2)
O anion	(6b)	(1/2, 1/2, 0) (1/2, 0, 1/2) (0, 1/2, 1/2)

In perovskite oxides, BO_6 octahedra is coordinated by 6 oxygen ions, giving rise to a 180° $B-O-B$ bond angle. Distortion from the ideal cubic structure is largely related to a mismatch between $A-O$ and $B-O$ bond lengths. If the A cation is replaced by a smaller one, BO_6 octahedra would rotate about cubic crystallographic axis to release the structural stress. The cooperative rotation of the BO_6 octahedra consequently leads to a decrease in the $B-O-B$ bond angle and a reduction in the coordination number of A cation. Such distortions, controlled by different A cation for the same B cation, play crucial roles in observed metal-to-insulator transition, magnetoresistance, magnetic transitions etc.

These distortions can be related to anionic and cationic radii. Deviation from the cubic symmetry, leading to orthorhombic or tetragonal polymorphs, can be rationalized using the tolerance factor. For this distortion, a constant t is included in the equation 1.1 which results into

$$R_A + R_O = t\sqrt{2}(R_B + R_O) \quad (1.2)$$

Where R_A , R_B , and R_O are the respective radii of A cation, B cation and O anion in the appropriate coordinate and t is also known as Goldschmidt tolerance factor which is defined to quantify the distortion of perovskite structure from an ideal cubic structure. The distortion in the crystal structure appears due to the different sizes of both ' A ' cation and ' B ' cation. When the radius of ' A ' cation is smaller in comparison to ' B ', the structure becomes more distorted leading to either tetragonal or orthorhombic distortion, i.e. $GdFeO_3$ type distortion, where the individual BO_6 corner shared octahedra are rotated and tilted[15][16]. It is well known that the degree of distortion increases as tolerance factor decreases.

The ideal cubic structure is formed for $t=1$, when the A cation matches in size with the O^{2-} ions to form cubic close-packed layers, and the B cation matches the size of the interstitial sites formed by the oxygen to give an array of corner – shared BO_6 octahedra. The reduction in symmetry is driven by the necessity to accommodate the anion coordinate number around the cations. One or more of the following processes usually happen in absence of an ideal cubic structure:

1. Tilting of the anion octahedral
2. Displacement of the cations
3. Distortion of the octahedral

Distortion factor causes the compression or tension of cation – anion bond. These stresses lower the symmetry of space group from cubic ($Pm\bar{3}m$) to distorted structure by rotating the octahedra. If the rotation of the octahedral is about a cubic $[001]$ axis then it results into distorted structure as tetragonal but space group depends on the direction, i.e. if the rotation is out of phase then space group is $I4/mcm$, but if rotation is in-phase then space group is $P4/mbm$. If the rotation of octahedral is about $[110]$ axis, then it results into orthorhombic structure with space group $Pbnm$ or $Pnma$. If the rotation of octahedral is about $[111]$ axis, then the structure come out to be rhombohedral with space group $R\bar{3}c$ (out of phase rotation) or $Im\bar{3}$ (in phase rotation) [17].

On the basis of presence of different B and A cations, several routes could be taken from lower to higher structure symmetry. For example, the well- established criteria are explained well by Aleksandrov and Barnighausen in the case of manganites [18]. According to

Aleksandrov criterion, the reduction in symmetry (cubic to orthorhombic) takes place through five intermediate space groups. On the other hand, Barnighausen showed a path of continuous phase transitions from $Pm\bar{3}m$ to $Pnma$ through a sequence of space groups subgroup steps. For instance, in the case of $La_{1-x}Sr_xMnO_3$ from $x = 0$ to 0.15 the structure remains orthorhombic. At $x = 0.15$, the system becomes rhombohedral which persists till $x = 0.6$ [19]. In perovskites, another structural change is observed as a function of the size of the R - ion (Lanthanide). As the size of the R - ion decreases, the structure transforms from perovskites type to hexagonal. For example, Y, Lu, Sc, and Yb form hexagonal structure. Interestingly, the orthorhombic and hexagonal structures can be realized for Y, Lu, Ho, and Dy by careful selection of growth conditions[20].

In 1950, Jonker and Van Santen, while studying manganites ($A_{1-x}B_xMnO_3$: A = trivalent cation, B = divalent cation), first reported the oxide perovskites with near room temperature ferromagnetism[21]. The existence of mixed valence states of Mn in these compounds allow transfer of electrons between oxygen orbitals, which was invoked to further explain the paramagnetic-to-ferromagnetism transition through a double exchange mechanism[22][23]. In case of several manganites, metal-to-insulator transition is also observed in proximity of the magnetic transition. Additionally, application of magnetic field leads to a significant reduction in resistance of these materials at the transition temperature. This negative magnetoresistance has paved the way to the current research on colossal magneto-resistive materials, which could be applicable in magnetic storage devices[24]. Further, the discovery of high temperature superconductivity in ceramic copper oxides by Muller and Bednorz accelerated the research in the field of doped perovskites[25].

Perovskite based materials are generally named on the basis of transition metal ions at B site e.g. Cobalites, Manganites, Orthoferrites, Orthochromites, Cuprates, etc. In general, most of these materials possess the orthorhombic structure but the magnetic behavior of these materials is different depending on the difference in the electronic shell structure of the transition metal and rare earth ions. Among these materials, rare earth orthoferrites found special status due to unique magnetic and electrical properties[26][27][28][29].

1.2 Rare earth orthoferrite

Rare earth orthoferrites with general formula $R\text{FeO}_3$ (where R is a rare earth ion) belong to a widely studied family of transition metal oxides with an orthorhombic perovskite structure. These materials have attracted large interest since the 1950's due to their novel magnetic and magneto-optic properties. The remarkable properties of these materials were realized when Forestier and Guiot-Guillain published the very first article about the magnetic properties of rare earth orthoferrites [30]. The presence of weak ferromagnetic moment in these compounds along with the long range antiferromagnetic ordering and other magnetic phase transitions sparked the interest of scientific community and inspires new investigations till present date. In addition to purely academic research, studies on possible device applications of orthoferrites have also been undertaken by many groups since 1960's and 1970's. The magnetic domain behavior in these materials led to a large number of investigations focusing on potential applications as memory or logic devices[30][31]. Although, orthoferrites have been overtaken by ferromagnetic garnets for magnetic bubble devices, interest in orthoferrites resurged in the 1990's, particularly from the view point of their domain wall dynamics. The velocity of the domain wall motion (at upto 20 km/s) is reported to be the highest amongst the magnetically ordered media[32]. Recent investigations by Didosyan *et. al.* have reported that orthoferrites show promise for use in various innovative micro technological devices such as magnetic sensors, magneto-optical currents sensors, light spot position measurers, magneto-optical rotational speed sensors and fast latching optical switches[33][34].

Table 1.2 The Néel temperatures for different rare earth ions at R site in orthoferrites [39]

Rare earth ion on R site	La	Pr	Nd	Sm	Eu	Gd	Tb	Dy	Y	Ho	Er	Tm	Yb	Lu
$T_N(\text{K})$ of $R\text{FeO}_3$	740	707	687	674	662	657	647	645	640	639	636	632	627	623

In rare earth orthoferrites, due to the presence of two magnetic subsystems (one on the rare earth ions and another on the iron ions) and their interactions such as $\text{Fe}^{3+}\text{-Fe}^{3+}$, $R^{3+}\text{-Fe}^{3+}$ and $R^{3+}\text{-R}^{3+}$ give rise to interesting magnetic properties. It would be interesting to study these competing interactions along with the controlling external perturbations such as temperature,

electric and magnetic fields, pressure etc. [35][36][37][38]. At ambient temperatures, the magnetic properties of $R\text{FeO}_3$ systems depend primarily on the Fe^{3+} - Fe^{3+} interaction which leads to antiferromagnetic type ordering with Néel temperatures ranging from 623 K (Lu) to 740 K (La) as shown in Table 1.2[39]. Most members of the rare earth orthoferrite family are classified as canted antiferromagnets (AFM). For example, Magnetic moment of Fe^{3+} in ErFeO_3 and YFeO_3 align at an angle to the c -axis in such a way that the perpendicular components of magnetization cancel out, whereas the parallel components of c -axis give rise to spontaneous weak magnetization [40][41].

1.2.1 Magnetic Properties

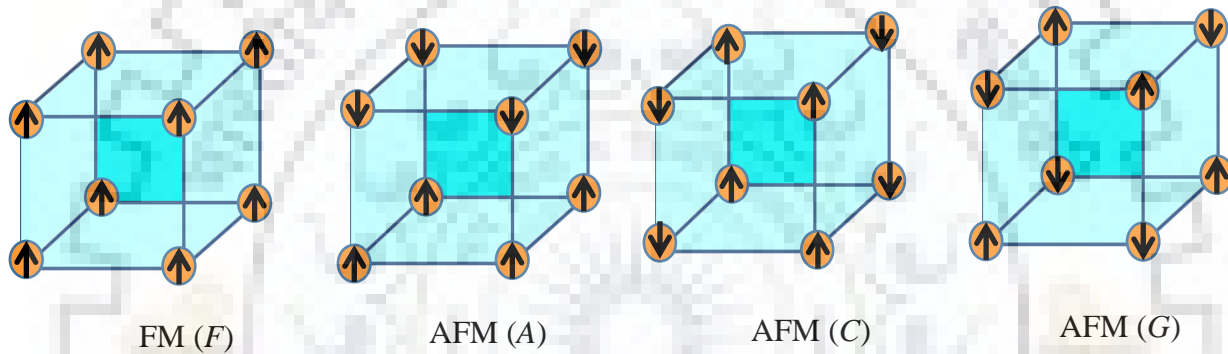


Figure 1.3 Different types of magnetic structure

Schematics of different magnetic structures are shown in Figure 1.3. *F* shows the ferromagnetic ordering where all the spins are aligned parallel to one another. AFM shows the anti-parallel alignment of spins. AFM ordering is categorized into three types depending upon intra-planer ordering whereas inter-planer ordering is always antiferromagnetic

In *A*-type ordering, ferromagnetism occurs within (001) plane.

In *C*-type ordering, ferromagnetism ordering occurs within (110) plane.

In *G*-type ordering, ferromagnetic ordering occurs within (111) plane while nearest neighbor is aligned in anti-parallel alignment.

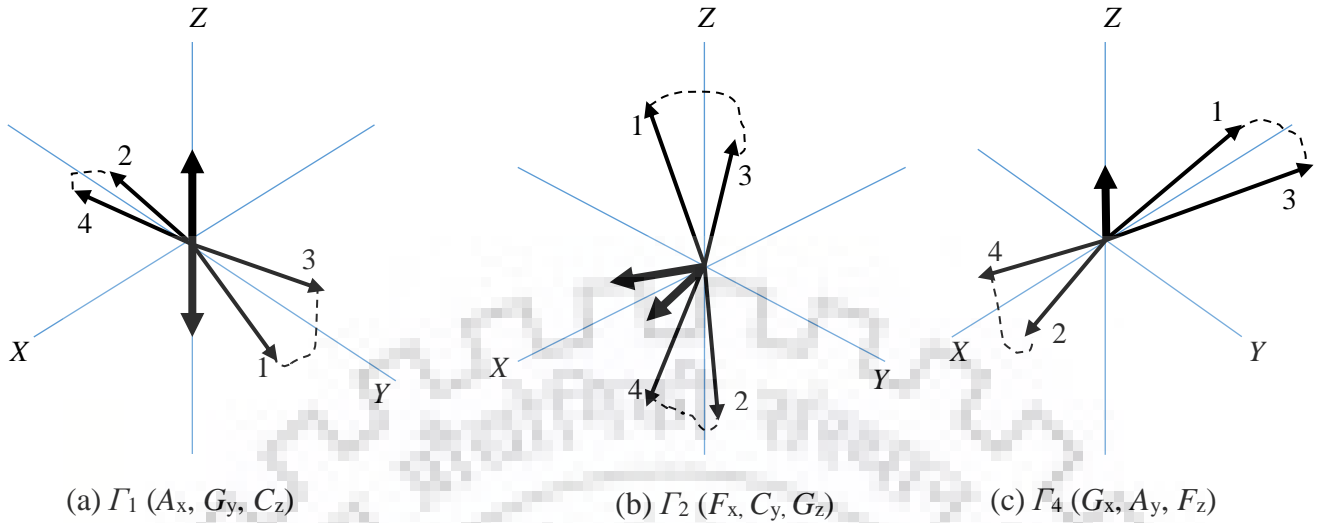


Figure 1.4 Allowed spin configurations in the rare earth orthoferrites

Orthoferrites have very unusual magnetic properties. The possible reason behind this is the presence of two types of magnetic ions in the material. Another reason is the multitude of magnetic interactions that follows from the interactions of two magnetic ions. From literature, the strongest interaction known is the isotropic superexchange interaction between neighboring Fe^{3+} ions. This interaction tends to align Fe^{3+} magnetic moments into an antiferromagnetic ordering. But, due to spin orbit coupling, there also exists a weaker, antisymmetric

Table 1.3 Irreducible representation of magnetic configuration corresponding to RFeO_3 [45]

Γ	I	$\bar{2}_x$	$\bar{2}_y$	Components of the Basis Vectors					
				Fe^{3+} ions			R^{3+} ions		
Γ_1	1	1	1	A_x	G_y	C_z	0	0	c_z
Γ_2	1	1	-1	F_x	C_y	G_z	f_x	c_y	0
Γ_3	1	-1	1	C_x	F_y	A_z	c_x	f_y	0
Γ_4	1	-1	-1	G_x	A_y	F_z	0	0	f_z
Γ_5	-1	1	1	-	-	-	g_x	a_y	0
Γ_6	-1	1	-1	-	-	-	0	0	a_z
Γ_7	-1	-1	1	-	-	-	0	0	g_z
Γ_8	-1	-1	-1	-	-	-	a_x	g_y	0

superexchange interaction known as Dzyaloshinsky – Moriya interaction[42][43]. This interaction favors orthogonal alignment of the spins and also manifests itself a small canting

of approximately 0.5° of the sublattices towards each other[44]. This results into several configurations of four Fe^{3+} sublattices which have magnetization pointing in different directions. Few of these configurations also allow the possibility of weak ferromagnetism in orthoferrites.

In each unit cell, there are four magnetic sublattices which correspond to Fe^{3+} ions ($M_i = 1,2,3,4$) and four magnetic sublattices for R^{3+} ions ($M_j = 5,6,7,8$). Combinations of these eight magnetic sublattices characterize the magnetic structure. These combinations are mentioned as below equations where F , G , A and C type denotes the different magnetic ordering of Fe^{3+} ions while f , g , a and c denotes the different magnetic ordering of rare earth ions (R^{3+}).

$$F = M_1 + M_2 + M_3 + M_4, \quad (1.3)$$

$$f = M_5 + M_6 + M_7 + M_8 \quad (1.7)$$

$$G = M_1 - M_2 + M_3 - M_4, \quad (1.4)$$

$$g = M_5 - M_6 + M_7 - M_8 \quad (1.8)$$

$$A = M_1 - M_2 - M_3 + M_4, \quad (1.5)$$

$$a = M_5 - M_6 - M_7 + M_8 \quad (1.9)$$

$$C = M_1 + M_2 - M_3 - M_4, \quad (1.6)$$

$$c = M_5 + M_6 - M_7 - M_8 \quad (1.10)$$

In table 1.3 all the possible combinations for spin configuration are shown for Fe^{3+} ions as well as for R^{3+} ions. Γ denotes the possible magnetic phase while I , $\overline{2}_x$, and $\overline{2}_y$ denotes possible magnetic symmetry corresponding to $D_{2h}^{16} - Pbnm$ spacegroup [45].

Due to symmetry considerations and the antiferromagnetic nature of the coupling between the ions, only three magnetic configurations are allowed for the Fe^{3+} sublattices: the Γ_1 , Γ_2 and Γ_4 configurations [45].

In the Γ_1 configurations, (Figure 1.4 (a)) there is no net magnetization \mathbf{m} and the antiferromagnetic vector \mathbf{l} points along the b axis. Therefore, the resulted magnetic structure is G -type antiferromagnetic where Fe^{3+} spins are primarily aligned along y axis. Such antiferromagnetic structure is represented by G_y . In addition to G_y , A_x and C_z type antiferromagnetic orderings also exist in Γ_1 configurations. As shown in Figure 1.4 (a), such additional ordering exists due to hidden canting of Fe^{3+} spins.

As shown in Figure 1.4 (b), the Γ_2 configuration is characterized by \mathbf{m} and \mathbf{l} pointing along a axis and c axis, respectively. As net magnetization is not zero in this case and it is pointing in the x direction. Thus, this magnetic configuration shows weak ferromagnetic canting along x direction (F_x), along with another C -type ordering along y direction (C_y) due to canting of magnetic moments. The major ordering of this configuration is G -type along z axis (G_z).

If Γ_2 configuration is rotated, such that \mathbf{m} points along the c axis and \mathbf{l} along a axis, one obtains the Γ_4 configuration. Therefore, in this configuration weak ferromagnetic ordering due to canting exists along z direction (F_z), canting is also present where small components of magnetic moments point along y direction having A type arrangement (A_y). The main antiferromagnetic ordering in this configuration (Γ_2) is G -type where magnetic moments are primarily aligned along x axis. Such arrangement of spins is represented by G_x .

Just below the Néel temperature, the magnetic ordering of Fe^{3+} spins in all the orthoferrites adopt the Γ_4 configuration. However, the magnetic ordering of orthoferrites changes in to Γ_1 or the Γ_2 configuration at low temperatures.

The superexchange interactions involving the rare earth ions (Fe^{3+} - R^{3+}) are much weaker. However, their effect often become noticeable in magnetic properties at temperatures below 140 K. As a result, interesting variations for various rare earth orthoferrites arise due to difference in strength of Fe^{3+} - R^{3+} interactions. The strongest influence on rare earth magnetization, if present, is due to the superexchange interaction with the Fe^{3+} neighbors. The resulting alignment of the rare earth spin has a paramagnetic nature. The net rare earth magnetization can point either in the direction of the iron magnetization or opposite to that, depending on the type of rare earth and the temperature. At very low temperatures, below 10 K, ordering of the rare earth sublattices has been reported in some orthoferrites[35]. It is a result of the superexchange interaction between the neighboring rare earth ions. The ordering of the rare earth ions can have far reaching consequences for the magnetic structure of the material, such as the appearance of multiferroicity[46] and a doubling of the unit cell[47].

1.2.2 Magnetic phase transitions

The rare earth orthoferrites undergo different magnetic phase transitions, due to change in temperature and/or magnetic field. In all the phase transitions, specific magnetic interaction

plays a crucial role. Phase transitions can be divided into three categories: firstly, all rare earth orthoferrites are paramagnetic in nature at higher temperature. With the lowering of temperature, there is transition into antiferromagnetic phase with weak ferromagnetic component at a particular Néel temperature. It marks the onset of magnetic ordering in the system. This temperature is determined by $\text{Fe}^{3+} - \text{Fe}^{3+}$ exchange interactions and therefore it is more or less same in all the orthoferrites (around 700 K). Due to strong super-exchange interaction between $\text{Fe}^{3+} - \text{Fe}^{3+}$ leads to G -type antiferromagnetic structure of Fe^{3+} ions [48]. Generally, Néel temperature of orthoferrites is between 620 – 740 K. In orthoferrites, two more magnetic interactions exist due to $\text{Fe}^{3+} - R^{3+}$ and $R^{3+} - R^{3+}$ exchange interactions. Isotropic exchange between Fe^{3+} and R^{3+} is 90° super-exchange interaction but it is weak as compared to $\text{Fe}^{3+} - \text{Fe}^{3+}$ exchange interaction[49]. Due to this anisotropic-symmetric and antisymmetric exchange interaction, spin reorientation of Fe^{3+} ions occurs where direction of easy axis i.e. direction in which spins are aligned changes gradually or abruptly from one direction to other depending upon the rare earth ion. These phase transitions, which can be first as well as second order, are driven by $\text{Fe}^{3+} - R^{3+}$ interactions [48]. Last and the weakest exchange interaction occurs between R^{3+} and R^{3+} ion at very low temperature which is 90° superexchange interaction.

1.2.2.1 Spin reorientation in orthoferrites

Among different types of transitions between magnetic configuration observed in orthoferrites, the most common is spin reorientation transition (SRT) between Γ_4 and Γ_2 configuration via the intermediate phase Γ_{24} . This phase transition can be triggered by variation of temperature in the orthoferrites with different rare earth elements Nd, Sm, Tb, Er, Tm, and Yb [49][50]. In the intermediate phase the spins rotate gradually from one easy axis to another keeping the G - type antiferromagnetic ordering. The phase transitions at $\Gamma_2 - \Gamma_{24}$ and $\Gamma_4 - \Gamma_{24}$ boundaries are of second order nature. Orthoferrite with Dy ion i.e. DyFeO_3 , prefer the Γ_1 configuration at low temperatures. At the Morin transition ($T_M = 36$ K) in DyFeO_3 , an abrupt transition takes place between the Γ_4 and Γ_1 configurations[35][51][52]. This is first order phase transition. In the same material, a transition between Γ_1 and Γ_2 via Γ_{12} (two second order phase transitions) can be triggered by the applications of a magnetic field along a axis at low temperatures[51]. With the application of magnetic field in DyFeO_3 , the reorientation occurs

as $\Gamma_4 \rightarrow \Gamma_{24} \rightarrow \Gamma_{12} \rightarrow \Gamma_2$ [53]. In this case, the phase transition between the Γ_{12} and Γ_{24} configurations is of first order and coexist near the Morin point with the Morin transition $T_M = 51.6$ K. Similar kind of transition is observed in HoFeO_3 , where abrupt reorientation of spin from Γ_4 to Γ_1 configuration occurs at 55 K. This phase transition is also of the first order nature. Below 35 K, another gradual reorientation ($\Gamma_1 \rightarrow \Gamma_2$) occurs with intermediate Γ_{12} phase. This transition is observed in HoFeO_3 without the presence of an applied magnetic field[54][55][56].

The spin reorientation transitions discussed above can be described phenomenologically by Landau theory. Horner and Varma pioneered this approach in 1968 for the Γ_2 to Γ_4 spin reorientation transition [57]. In Landau theory, the free energy of the spin system can be expanded in terms of the order parameter which, in this case, is the angle θ between the easy axis of the magnetization and a axis:

$$F(\theta) = F_0 + K_2 \sin^2 \theta + K_4 \sin^4 \theta \quad (1.11)$$

Here F_0 is the isotropic free energy, K_2 is the second order anisotropy constant, and K_4 is the fourth order anisotropy constant. Provided that the free energy function $F(\theta)$ is analytic, one finds the following global minimum:

$$\theta = \begin{cases} 0 & \text{if } K_2 \leq -2K_4 \\ \arcsin \sqrt{\frac{-K_2}{2K_4}} & \text{if } -2K_4 \leq K_2 \leq 0 \\ \frac{\pi}{2} & \text{if } K_2 \geq 0 \end{cases} \quad (1.12)$$

As the equations display, the actual angle for which the free energy is minimal depends on the values of the anisotropy constants. Under the conditions described in equation 1.12, Horner and Varma explained the spin reorientation transition. If K_4 is positive, the spin system undergoes two second order phase transitions. Starting from T_1 , the spin system starts to rotate continuously with changing temperature and reaches at an angle of 90° with the earlier direction at T_2 . If K_4 is negative, then spins change direction abruptly which is first order transition. Remarkably, this simple approach describes both the abrupt and continuous spin reorientation transitions encountered in orthoferrites very well. The more complicated spin reorientation transitions which include first as well as second order phase transitions can be described with a similar strategy[53].

The phenomenological Landau approach showed the presence of a strong enough temperature dependence of the second order anisotropy constant. The right sign for the fourth order anisotropy constant are sufficient to describe the simpler spin reorientation transitions. Further understanding can now be gained by looking at the microscopic mechanisms that determine these anisotropy constants. In general, magnetic anisotropy can arise from three sources: The Fe^{3+} single ion anisotropy, the rare earth single ion anisotropy and the antisymmetric exchange interaction. Yamaguchi has shown that for most rare earth orthoferrites, the Fe^{3+} single ion anisotropy and the $\text{Fe}^{3+} - \text{R}^{3+}$ antisymmetric super-exchange interaction play a major role in spin reorientation transition[48].

1.2.3 Heat Capacity

Heat capacity measurement provide information about the lattice, electronic and magnetic properties of the materials. Heat capacity measurements below Debye temperature, directly probe the electronic and magnetic energy levels of material[58]. The heat capacity of a substance is governed by the manner in which the internal energy is distributed among its constituents. In a solid, the main contribution to specific heat arises from lattice mode of thermal excitation and internal vibrations of molecules. There is appreciable contribution from free electrons to the specific heat ($\propto T$) in metals. The behavior of specific heat of magnetic materials is a matter of wide-spread interest. The heat capacity at low temperature can be shared among spin-wave excitations ($T^{3/2}$), hyper-fine excitations due to nuclear magnetic moments (T^{-2}) or Schottky effect due to two level spin systems[59]. The Schottky effect, which occurs due to crystal field splitting of unfilled rare earth ion is observed in orthoferrites and manganites having R ion other than La. Thus, the study of Schottky effect sheds light into the crystal field levels and its surrounding interaction. The magnetic contribution can be extracted from the specific heat measurements close to the transition temperature. In general, the FM-PM (Paramagnetic) transition is a second order transition which is observed usually as λ -shaped anomaly in specific heat. Manganites show large change in specific heat due to order-disorder transition [60]. In charge ordered manganites, a large peak is observed corresponding to first order transition [61].

In compounds with magnetic rare earth, the low temperature specific heat is dominated by single ion excitations of rare earth. The overall crystal-filed splitting of the lowest J multiplet

is about 100 meV for Pr or Nd. The crystal field levels are further split by the exchange field acting at the rare-earth site [59][62].

1.3 Magnetocaloric Effect

Magnetocaloric effect (MCE) is defined as the cooling or heating of any magnetic material under the application of externally applied magnetic field[63]. Now a days, MCE has been used as an alternative for refrigeration in the wide range of temperature that extends from room

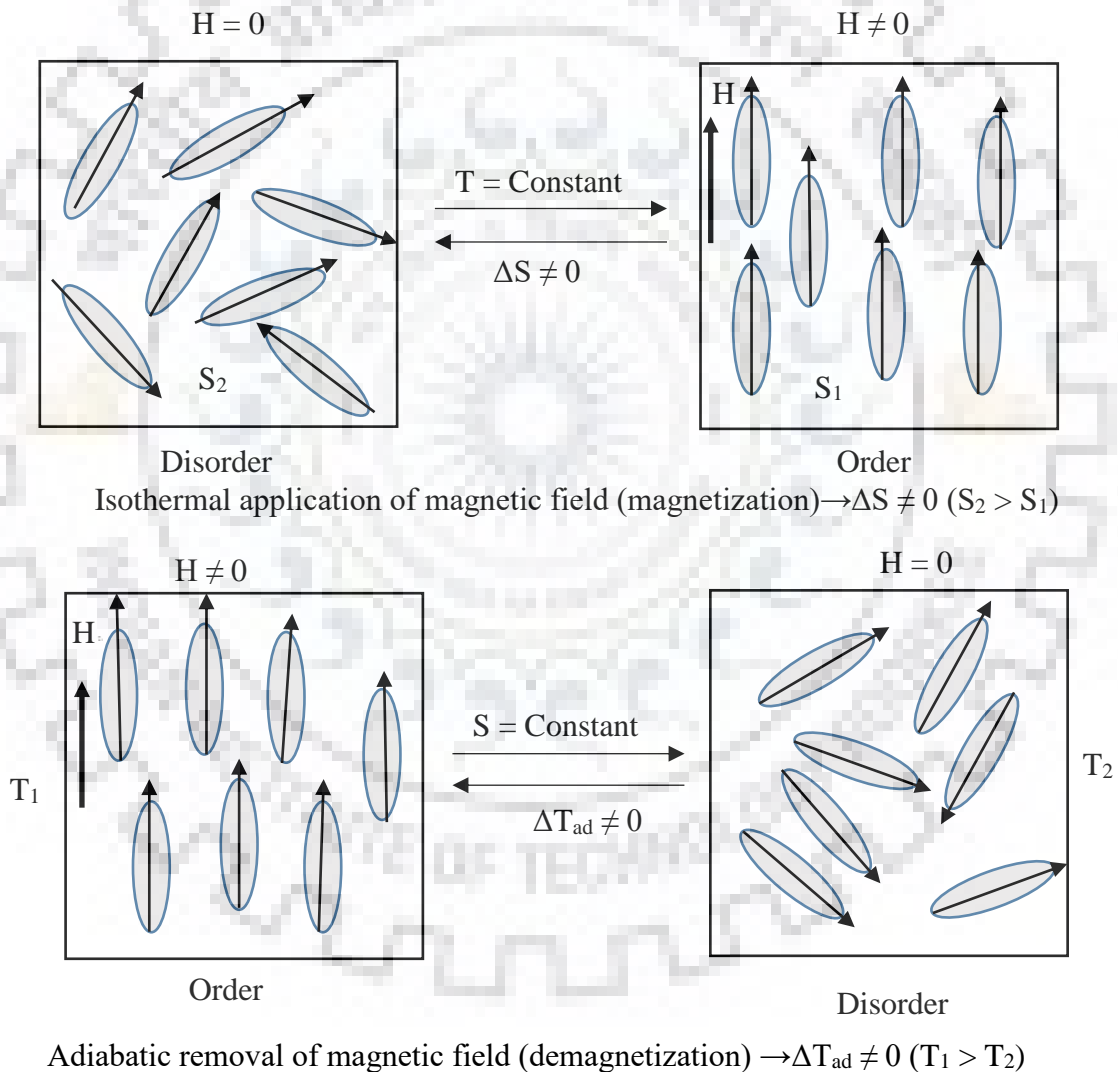


Figure 1.5 Schematic diagram showing the two isothermal magnetization (top panels) and adiabatic demagnetization (bottom panels) to understand the phenomenon of magnetocaloric effect

temperature to lower temperature (2-5 K) as this technology is very much energy efficient as well as environment friendly in comparison to vapor-cycle refrigeration technology[64].

Basis of MCE is thermodynamics where the magnetic variables such as magnetization and magnetic field are related to entropy and temperature. Though, MCE is observed in all the magnetic materials but the magnitude varies for different material and this defines the property of materials for the application of magnetic refrigeration. The entropy value for any magnetic compound depends on applied magnetic field H and temperature T . Thus total entropy is defined as[65]

$$S(T, H) = S_m(T, H) + S_{lat}(T) + S_{el}(T) \quad (1.13)$$

MCE comprises of two basic processes through which we can understand the thermodynamics of MCE:

- 1) When total entropy is constant i.e. magnetic field is applied adiabatically in a reversible process which results in the decrease of magnetic entropy with a relative increase in lattice entropy and electronic entropy keeping the total entropy remains constant resulting as

$$S(T_0, H_0) = S(T_1, H_1) \quad (1.14)$$

This results in the increment of temperature. Thus it can be defined as isentropic difference between corresponding $S(T, H)$ function and MCE can be calculated as

$$\Delta T_{ad} = T_1 - T_0 \quad (1.15)$$

- 2) In the case of isothermal process where temperature remains constant, a decrease in total entropy is observed when externally magnetic field is applied and this occurs because of the decrease in magnetic entropy that is defined as

$$\Delta S_m = S(T_0, H_0) - S(T_0, H_1) \quad (1.16)$$

Both ΔT_{ad} and ΔS_m are the characteristic values of MCE which are the function of initial temperature T_0 and change in applied magnetic field i.e. $\Delta H = H_1 - H_0$ [66][67].

It can be concluded that if with the increase in applied field, an increase in magnetic ordering is observed, then $\Delta T_{ad}(T, \Delta H)$ will be positive while $\Delta S_m(T, \Delta H)$ will be negative and vice versa. This phenomenon is shown in Figure 1.5.

Thermodynamic relation between applied field H , magnetization M , and temperature T with the MCE values is explained by using Maxwell's equation

$$\left(\frac{\partial S(T,H)}{\partial H}\right)_T = \left(\frac{\partial M(T,H)}{\partial T}\right)_H \quad (1.17)$$

On integrating equation (1.17) for isobaric as well as isothermal processes, we obtain[68]

$$\Delta S_m(T, \Delta H) = \int_{H_1}^{H_2} \left(\frac{\partial M(T,H)}{\partial T}\right)_H dH \quad (1.18)$$

Thus it can be concluded about change in magnetic entropy from equation 1.18. that $\Delta S_m(T, \Delta H)$ should be negative for positive change in field i.e. $\Delta H > 0$ as magnetization at constant field usually decreases with an increase in the temperature for ferromagnets, canted antiferromagnets.

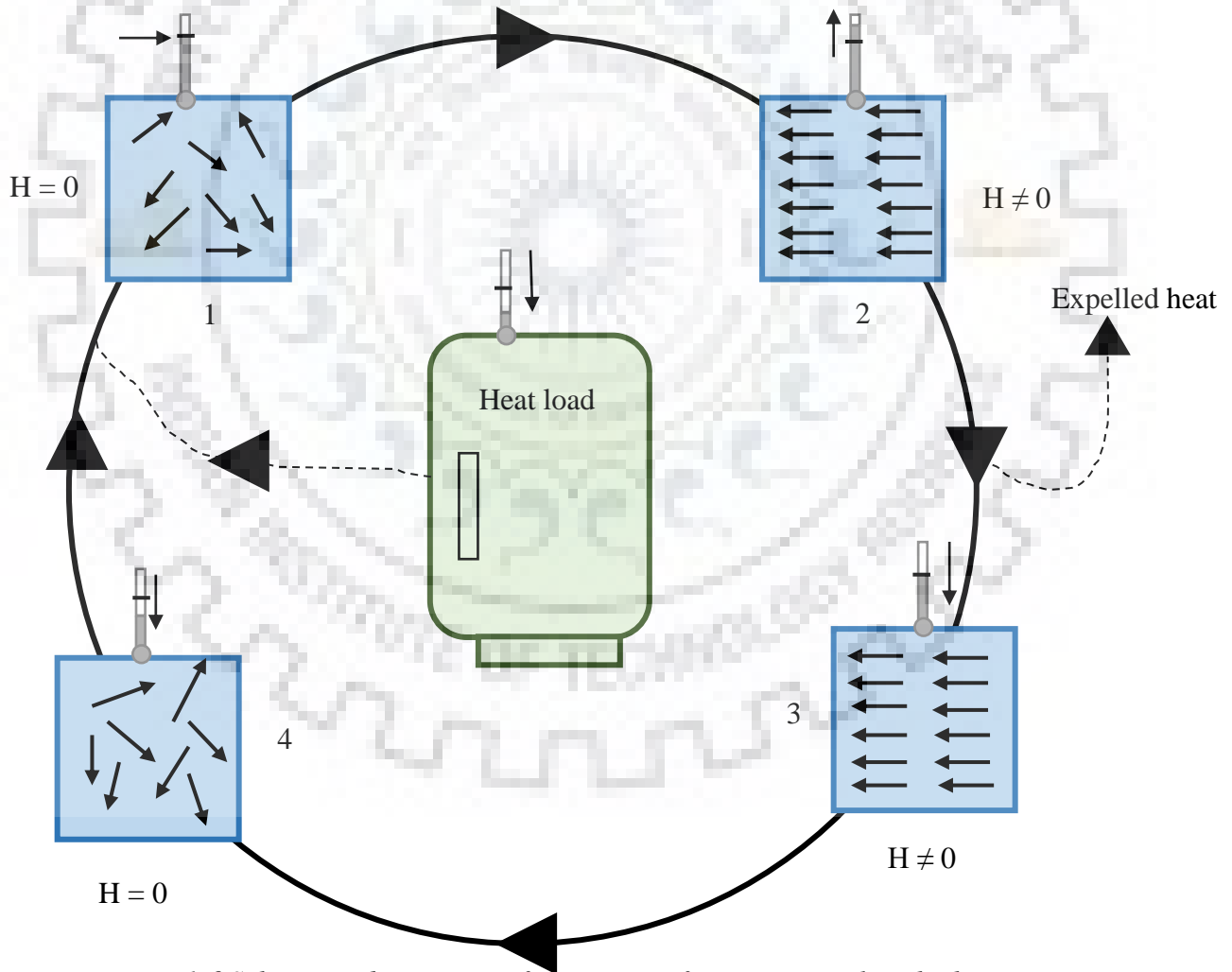


Figure 1.6 Schematic description of magnetic refrigeration cycle, which transports heat from heat load to surroundings.

Now a days MCE has become the topic of more interest because it can be used as an alternative for refrigeration which proved to be environment friendly as compare to other techniques using ozone depleting chemicals, hazardous chemical or greenhouse gases[69][70]. Thus materials which can be used as an efficient material for the application of magnetic refrigerant should have certain properties such as:

- i) Around the working temperature, there should be the presence of first order field induced transition, so that it can utilize the entropy change which is associated with it.
- ii) It should have high refrigerant capacity that is calculated as

$$q = \int_{T_{cold}}^{T_{hot}} \Delta S(T)_{\Delta H} dT \quad \text{or} \quad q = \Delta S * \delta T_{FWHM} \quad (1.19)$$

Also known as relative cooling power, q measures the amount of heat which is transferred between heat load and sink in an ideal refrigerator [64][71].

Representation of magnetic refrigeration cycle is shown in Figure 1.6 where heat transformation from system to surroundings is shown. In this Figure, magnetic material in the presence and absence of magnetic field is shown. Initially magnetic moments are in disordered state under the absence of applied field which are aligned by applying the magnetic field. The alignment results in heating of the magnetic material. This heat is further removed by transferring the excess heat to the surroundings by heat-transfer medium. Then, field is removed after thermally delinking the material from surrounding, which resulted in randomizing the magnetic moments. Due to random magnetic moments temperature decreases leading to cooling of magnetic material below the surrounding temperature. Finally, heat is taken from the system to be cooled which again can be extracted using heat-transfer medium[72].

For any practical application, ΔS_m should be sufficiently high and therefore, rare earth elements and their alloys such as Gd, $Gd_5Si_2Ge_2$, RAI_2 etc have been explored for MCE. For low temperature application such as liquefaction of hydrogen or cryogenic technology in space science, several TMOs are studied for low temperature MCE. Due to the peculiar magnetic properties of orthoferrites at low temperature, large entropy change is also observed in comparison to other TMOs. In addition to this, spin reorientation in orthoferrites is useful in the field of magnetic refrigeration due to rotating magnetization vector.

1.4 Literature Survey

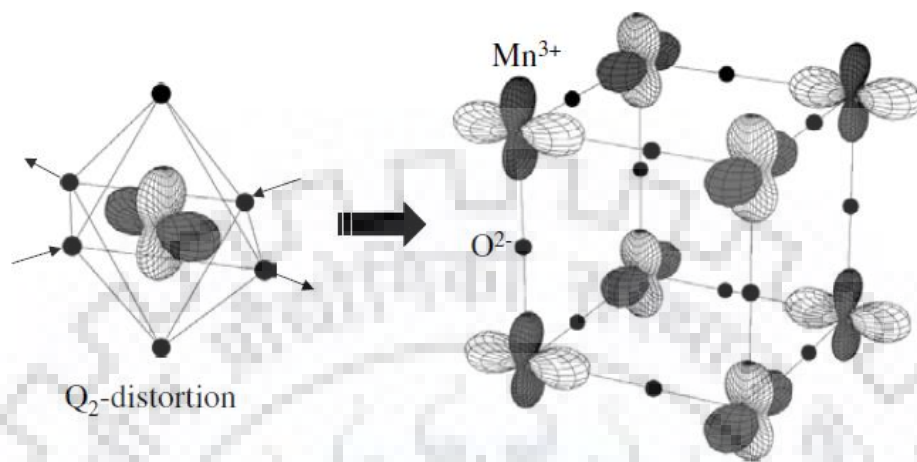


Figure 1.7 Left: Q_2 – distorted MnO_6 octahedron. Right: Three-dimensional network of cooperatively Jahn – Teller distorted MnO_6 – octahedral, which is connected to an antiferro-orbital ordering [74]

During past few years, a lot of research has been done on polycrystalline orthoferrite by doping on transition metal site as well as rare earth site.

1.4.1 Doping of Mn on Fe site in rare earth orthoferrite

The crystal structure of $RFe_{1-x}Mn_xO_3$ is orthorhombic with $Pbnm$ space group. The R site is surrounded by eight corner sharing MnO_6 or FeO_6 octahedra which build up a three dimensional network. However, due to a misfit of the mean (Nd or Dy in our case) and Mn/Fe site radii, this ideal structure is not observed in nature. The octahedra in $RMnO_3$ are not only tilted but also Jahn-Teller distorted: referring to formal valences. $RMnO_3$ contains only Mn^{3+} ion with a $3d^4$ configuration which is Jahn-teller active. As the MnO_6 octahedra are connected to each other, therefore, it is clear that cooperative distortions can occur. The cooperative ordering of Q_2 -distorted octahedral is exhibited in Figure 1.7[73][74][75]. As the long axis of a distorted octahedron points to the short axes of its neighbors, this antiferro-distortive ordering reduces the elastic energy of the crystal. In other words, elastic interactions significantly contribute to the stabilization of the cooperative Jahn-Teller distorted phase of $RMnO_3$.

The cooperative Jahn-Teller distortions, which determines the magnetic superexchange interactions between neighboring manganese sites, correspond to an orbital ordering. The

dependence of the superexchange interactions on the orbital occupation is summarized by the so-called Goodenough-Kanamori-Anderson (GKA) rules[74][76]. In the specific case, illustrated in Figure 1.7, two GKA rules are relevant: firstly, the 180° - superexchange between two half-filled orbitals along the c -direction is antiferromagnetic. Second, the 180° - superexchange between an empty and a half occupied orbital gives rise to a ferromagnetic nearest neighbor interaction within the ab plane. It follows that the orbital order is connected to the A-type antiferromagnetic ordering, consisting of ferromagnetic ab planes which are antiferromagnetically aligned along the c axis as shown in Figure 1.7. For LaMnO_3 which is A type antiferromagnetic below $T_N \approx 140$ K have almost constant order parameter of orbital ordering below T_N which decreases with an increase in temperature. This phenomenon is observed from the temperature dependence of the order parameter of orbital ordering using resonant scattering. The constant nature of orbital ordering below T_N is due to coupling of spin and orbital degree of freedom. Though this orbital ordering start to decrease with an increase in temperature and persists till $T_{JT} \approx 780$ K, above which it rapidly goes to zero showing the orthorhombic to orthorhombic structural transition [77].

In the recent years, lot of studies have been done for different rare earth orthoferrites and manganites where Mn(Fe) was doped on the Fe(Mn) site to change the structural and magnetic properties. Tong *et al.* [78] studied LaMnO_3 , which is antiferromagnetic in nature, by doping Fe on Mn site resulting into $\text{LaMn}_{1-x}\text{Fe}_x\text{O}_3$ ($0.0 \leq x \leq 0.4$). Structurally, it remained rhombohedral for ($0.0 \leq x \leq 0.3$) but on further increasing the doping of Fe to $x=0.4$, its structure changes to orthorhombic which is actually the structure for most of the orthoferrites [78]. In terms of magnetic properties, there is transition from paramagnetic to ferromagnetic phase at T_N which decreases from 210 K to 125 K with the increase in Fe doping. The PM-FM transition is observed in $\text{LaMnO}_3(x=0)$ due to the presence of double exchange in $\text{La}_{1-y}\text{Mn}_y\text{O}_{3+\delta}$ which creates Mn^{4+} ions due to oxygen excess. With the increase in Fe doping, the DE exchange between Mn^{4+} - O - Mn^{3+} decreases, resulting in the decrease of transition temperature. Some cluster formation of spin glass state has also been observed in this study. Due to decrease in PM-FM transition temperature with the increase in Fe doping, further study has been carried out by Lima *et al.* where they have studied $\text{LaMn}_{1-x}\text{Fe}_x\text{O}_3$ covering the whole doping range ($0.0 \leq x \leq 1.0$)[79]. In this case, it has been found out that the structure of the compound is orthorhombic with $Pnma$ space group in contradiction to the study by Tong *et*

al.[78] . In this compound, due to the presence of excess oxygen, cationic vacancies were created on the La and Mn site resulting in the presence of 18% Mn^{4+} ions. Structurally, this compound exists as O' type orthorhombic structure (O') where Jahn-Teller distortion is suppressed favoring an isotropic superexchange ferromagnetic interaction. Thus, Magnetically, an evolution of FM magnetic phase is observed at $x = 0.0$ due to ferromagnetic double exchange ($Mn^{3+} - O - Mn^{4+}$) and super exchange couplings ($Mn^{3+} - O - Mn^{3+}$)[79]. With an increase in Fe^{3+} doping, decrease in FM and an increase in AFM coupling is observed. There is development of canted antiferromagnetic behavior in $LaFeO_3$ with Néel Temperature of 790 K. Thus an evolution from ferromagnetic phase to antiferromagnetic ordering is observed for $LaMn_{1-x}Fe_xO_3$ in the full range with an increase in Fe doping.

Doping of Fe on Mn site has also been done by Mihalik *et. al.* in $PrMn_{1-x}Fe_xO_3$ ($0.0 \leq x \leq 1.0$) (PMFO)[80]. As both $PrMnO_3$ and $PrFeO_3$ are orthorhombic, therefore, PMFO is also orthorhombic with *Pbnm* space group. Magnetically, PM – AFM transition temperature decreases from 95.9 K to 39 K for $x= 0.0 - 0.3$ and again it starts increasing from 42.9 K to 738 K for $x = 0.35 - 1.00$ [80]. The main reason behind this change in paramagnetic to magnetic ordering transition temperature is the presence of Fe ions and change in the Mn – O – Mn and Mn – O – Fe exchange interactions. For small doping of Fe, Fe^{3+} ions do not order separately and thus T_N decreases till $x < 0.3$. Thus when Fe concentration is very small, only A type antiferromagnetic ordering of Mn is present. When Fe concentration increases, it leads to superexchange interaction resulting in higher temperature transition for long range G type antiferromagnetic ordering [80].

Another study has been done by Silva-Santana *et. al.* [81] where they have studied magnetic properties of $SmFe_{0.5}Mn_{0.5}O_3$. In the ZFC-FC measurement, two transitions were observed: one at 234 K which is due to AFM – WFM (Weak Ferromagnetic) ordering as substitution of Mn^{3+} weakens the $Fe^{3+}-Fe^{3+}$ interaction leading to decrease in the T_N which is 670 K and spin reorientation of AFM – WFM below 480 K for $SmFeO_3$. Another transition is observed at 18 K due to Sm – Fe/Mn interactions. Similar kind of study has also been done by Bouziane *et. al.* on $SmFe_{1-x}Mn_xO_3$ ($x = 0.1, 0.2, 0.3$) (SFMO) [82] but with the contradiction that here spin reorientation occur for WFM - AFM ordering. Further, it has been found out that PM – WFM transition temperature decreases with the increase in the Mn doping. In the

case of SFMO, transition temperature from WFM to AFM decreases to 176 K for $x=0.3$ while for $x=0.1$ and 0.2 , AFM is not established completely indicating a competition between WFM and AFM orderings. As we know from orthoferrites that $\text{Fe}^{3+} - \text{Fe}^{3+}$ interaction is antiferromagnetic while $\text{Mn}^{3+} - \text{Mn}^{4+}$ interaction is ferromagnetic as observed in the case of $\text{La}_{1-x}\text{M}_x\text{MnO}_3$ ($M = \text{Ca}$ or Sr) [21], then the third interaction $\text{Fe}^{3+} - \text{Mn}^{3+}$ seems to be antiferromagnetic as this ordering increases with the Mn content. Another possible reason of ferromagnetic coupling is the presence of Fe^{2+} (orbitally frustrated Jahn-Teller ions) ions which will yield Mn^{4+} ions and may further lead to multiple and complex interactions resulting into weak ferromagnetic configurations. Thus, with the increase in Mn content PM-WFM transition temperature as well as spin reorientation temperature from WFM-AFM decreases [82].

Nair *et. al.* [83] and Fang *et. al.* [84] studied the magnetic structure and magnetic phase transition of $\text{TbFe}_{0.5}\text{Mn}_{0.5}\text{O}_3$ and $\text{TbFe}_{1-x}\text{Mn}_x\text{O}_3$ ($0.0 \leq x \leq 1.0$) respectively in the form of single crystal. Phase transition, $\Gamma_4 \rightarrow \Gamma_1$ (for $x < 0.6$) exist near room temperature while at low temperature again re-entrant transition $\Gamma_1 \rightarrow \Gamma_4$ (studied only for $x = 0.25$) occurs in the single crystals of $\text{TbFe}_{1-x}\text{Mn}_x\text{O}_3$ series [84]. Similar kind of observation has also been made by Nair *et. al.* [83] in case of $\text{TbFe}_{0.5}\text{Mn}_{0.5}\text{O}_3$ where Γ_4 exits at 295 K while between 250 K and 26 K a mixed phase of $\Gamma_4 + \Gamma_1$ exists below which Γ_4 becomes stable again around 2 K. At 2 K, Tb also begins to order ferromagnetically along c axis[83]. Whereas in the case of TbFeO_3 , spin reorientation occurs $\Gamma_4 \rightarrow \Gamma_2$ in contrast to the Mn doped TbFeO_3 having Γ_1 as low temperature (after spin reorientation) ground state [83], [84]. In comparison to $\text{TbFe}_{1-x}\text{Mn}_x\text{O}_3$, two types of ordering for Tb are observed in TbFeO_3 below 10 K: $f_x c_y$ and $a_x g_y$. Thus with the doping of Mn on Fe site, spin reorientation of transition metal ions as well as rare earth ions get effected in the case of TbFeO_3 .

Another interesting rare earth compound (YMn/FeO_3) was studied in past few years where manganite and orthoferrite have different crystal structure. YMnO_3 has hexagonal structure with $P6_3cm$ space group while YFeO_3 can be formed in orthorhombic structure as well as hexagonal structure but orthorhombic structure is more stable[85], [86]. Mandal *et. al.* have studied spin reorientation of $\text{YFe}_{1-x}\text{Mn}_x\text{O}_3$ ($0.0 \leq x \leq 0.45$) using powder neutron diffraction[41]. Structure remains orthorhombic with $Pnma$ space group as per the parent

compound YFeO_3 . As probed with neutron diffraction, the magnetic structure changes from Γ_4 to Γ_1 at 2 K abruptly similar to the case of DyFeO_3 but at very low temperature. Neetika *et. al.* studied $\text{YMn}_{1-x}\text{Fe}_x\text{O}_3$ ($x \leq 0.5$). The study concluded that the structure of the compound is hexagonal with $P6_3cm$ space group for $x < 0.2$ and orthorhombic with $Pnma$ space group for higher doping of Fe ion[87]. For YMnO_3 , magnetic structure at 6 K is majorly Γ_3 with 26% mixing of Γ_4 . With the increase of Fe doping there is significant increase in Γ_4 . For hexagonal structure there is the mixture of $\Gamma_3 + \Gamma_4$ but as doping of Fe^{3+} ion increases it leads the structure to orthorhombic, therefore magnetic structure was also described by Γ_1 structure at lower temperature which is also being found by Mandal *et. al.*[41].

In the present thesis work, study has been performed on doped compound of two parent transition metal oxides with completely different magnetic properties and magnetic structure i.e. NdFeO_3 and NdMnO_3 .

NdFeO_3 is one of the well-studied family members of orthoferrite materials, which exhibits antiferromagnetic ordering and temperature dependent spin reorientation [45][88]–[100]. It crystallizes in orthorhombic crystal structure of the space group $Pbnm$ and comprises of distorted corner shared FeO_6 octahedra. NdFeO_3 is a canted G -type antiferromagnet with a high Néel temperature (T_N) of 690K[100]. The magnetic structure is represented as G_xF_z belonging to irreducible representation Γ_4 , in which the spins form a G -type antiferromagnetic order along a direction (G_x), with a small ferromagnetic component along c direction due to canting (F_z). As the temperature is lowered, Fe spins rotate continuously in ac plane in the temperature range 200 to 105 K resulting in a change in the magnetic configuration from G_xF_z of Γ_4 to F_xG_z of Γ_2 representation with G -type ordering along the c direction (G_z) and a weak ferromagnetic ordering in the a direction (F_x)[95]. Though the whole process of spin reorientation is quiet complex, a noticeable ordering of Nd moments as C -type antiferromagnetic emerges at 1.5K [97]–[99]. The weak ferromagnetic moments, F_x of Fe and f_x of Nd, in NdFeO_3 single crystals are antiparallel and the overall spontaneous magnetization is compensated at $T = 8\text{K}$ [90].

Another RE transition metal oxide which has drawn considerable attention for its intriguing properties is NdMnO_3 . NdMnO_3 is A -type antiferromagnet with relatively low T_N of 75 K[101]. Although NdMnO_3 and NdFeO_3 are isostructural and antiferromagnetic, the underlying

mechanism responsible for their complex magnetic properties is quite different. In NdMnO₃, the Mn ion has 3+ oxidation state with 3d⁴ electronic configuration, which splits under crystal field into low lying triply degenerate t_{2g} states and doubly degenerate e_g states at higher energies[102][103]. The doubly degenerate e_g is split into e_g^1 and e_g^2 states due to the Jahn-Teller (J-T) distortion, which is also manifested as structural distortion. This results in tilting of octahedral by ~45° in a zigzag manner and also compression of the in-plane Mn-O bonds and elongation of the apical Mn-O bond. As a consequence of crystal field splitting and cooperative J-T effect, the highest occupied e_g orbital orders as $d_{3x^2-r^2}$ and $d_{3y^2-r^2}$ alternately at adjacent Mn sites in the ab plane[104]. Such a staggered in-plane orbital ordering leads to a ferromagnetic alignment of spins in ab plane and antiferromagnetic alignment along the c direction resulting in A-type antiferromagnetic structure below T_N (~75K)[101]. As the temperature is further reduced, the Nd sublattice orders ferromagnetically along the a direction below 20K[106][107]. The ordered Nd moment induces a Mn spin reorientation and a negative magnetization in NdMnO₃ [106].

In view of the very different magnetic properties shown by NdFeO₃ and NdMnO₃, it would be extremely interesting to look at an intermediate system where we substitute half of the Fe ions with Mn. Chakraborty *et. al.* studied that in NdFe_{1-x}Mn_xO₃ (0.0 ≤ x ≤ 1.0) an increase in Jahn-Teller distortion increases with the x doping and it changes from dynamic to static distortion[107]. Structurally, lattice parameter a and c decrease with an increase in x content while b lattice parameter remains unchanged till x=0.5 and starts decreasing till x=0.7 and further it started increasing with x doping beyond x=0.7. Mihalik *et. al.* studied by doping Fe on Mn site i.e. NdMn_{1-x}Fe_xO₃ (0.0 ≤ x ≤ 0.3) in one case and doping of Mn on Fe site NdFe_{1-x}Mn_xO₃ (0.0 ≤ x ≤ 1.0) in other case [108][109]. In the prior study, it was shown that the Néel temperature decreases with the increase in Fe substitution from 85.5 K to 36 K while in the latter case Néel temperature also decreases from 691 K to 356 K from x=0 to x=0.4. Another phenomenon that is observed in these compounds by Mihalik *et. al.* is the presence of second transition at lower temperature which remains around 11 K for the whole range and it has been related with the shift in ac susceptibility data for different frequency but still microscopic origin for this transition is not made clear[109]. Though in latter study, Mihalik *et. al.* shows the presence of spin reorientation in this compound using magnetization data and concluded that

T_{SR} increases with an increase in Mn doping but detailed study using neutron powder diffraction has not been performed[108]. Troyanchuk *et. al.* [110] studied 50% substitution of Mn at Fe site i.e. $NdFe_{0.5}Mn_{0.5}O_3$, using neutron diffraction at 4.3 K. Magnetic structure was found to be G -type at 4.3 K. However, the authors did not provide any information about the direction of magnetic moments and spin reorientation.

In this thesis, detailed work has been performed on 50% doping of Fe ion on Mn site i.e. $NdFe_{0.5}Mn_{0.5}O_3$. In this situation, one would expect a very complex interplay of spin, lattice and orbital degrees of freedom between the Mn and Fe sublattices and hence a new set of enriching physical properties. Substitution of Mn^{3+} ions at the Fe site not only makes it J-T active, it also tunes the super-exchange interaction, influences the magnetic magnetic symmetry, and spin reorientation through the Mn-Fe, Nd-Mn, and Nd-Fe interactions[109]–[111]. The electron-phonon coupling will also change due to modified J-T interaction upon substitution.

1.4.2 Doping on rare earth site in rare earth orthoferrite

Magnetic properties of the orthoferrites can also be altered by doping on the rare earth site. Most of the magnetic properties such as rare earth ordering at lower temperature, change in magnetic entropy, magnetic structure at lower temperature depend either on the rare earth ion or interaction between rare earth and transition metal ions. Therefore, the presence of different rare earth ion on same site has different magnetic structure, ordering temperature and Néel temperature for the orthoferrite.

One of the such work was reported back in 1967 when Sherwood *et. al.* did the doping in $SmFeO_3$ on Sm site with Gd in one case and Er in the other case resulting into $Gd_xSm_{1-x}FeO_3$ and $Er_xSm_{1-x}FeO_3$ respectively[112]. $SmFeO_3$ is well known for the very high spin reorientation temperature around 480 K [113]. With the doping of Er or Gd on the Sm site, its spin reorientation temperature decreases, more effectively when doped with 60% of Er, as compared to Gd doping. Further, other rare earth elements were also being doped on the Sm site in $SmFeO_3$. Zhao *et. al.* studied $Sm_{0.5}Tb_{0.5}FeO_3$ in the form of single crystal [114]. Spin reorientation transition is observed in the temperature range 150-250 K from Γ_2 to Γ_4 with the increase in temperature. Xu *et. al.* doped Sm on Dy site in $DyFeO_3$, $Sm_xDy_{1-x}FeO_3$ ($x = 0 - 1$)

in the form of single crystal. Lattice parameter b remains unchanged while a and c lattice parameter increases with the increasing x content of Sm which is in accordance with the change in rare-earth ionic radii as Sm ion is larger in size in comparison with Dy ion [115][116]. For $x = 0.7$, spin reorientation transition occurs near room temperature. From magnetization data of single crystal along three axes, it has been confirmed that the magnetic structure changes from Γ_2 to Γ_4 as temperature changes from 300 K to 330 K [115].

Belov *et. al.* studied 50 % doping of Dy on Ho site in single crystals of $\text{Ho}_{0.5}\text{Dy}_{0.5}\text{FeO}_3$ [117]. In this compound, two spin reorientation transitions related to Fe^{3+} spins are observed i.e. from WFM to AFM and further back to WFM but along different direction. Generally, in orthoferrites Γ_4 to Γ_2 was observed with an exception of DyFeO_3 , where abrupt Γ_4 to Γ_1 was observed[52][118]. But, in this case, the combination of both transitions i.e. $\Gamma_4(G_x, F_z) \rightarrow \Gamma_1(G_y) \rightarrow \Gamma_2(G_z, F_x)$ was observed. Both the transitions occur at 47 K and 25 K respectively and known as Morin transitions. Wang *et. al.* doped HoFeO_3 by 50% Pr on Ho site, $\text{Ho}_{0.5}\text{Pr}_{0.5}\text{FeO}_3$, in the form of the single crystal[119]. Similar to most of the orthoferrites, Γ_4 phase exist below Néel temperature, till 90 K. Between 90 – 75 K, gradual spin reorientation occurs from Γ_4 to Γ_2 configuration, which exists till 3 K. Another mixed rare earth material $\text{Dy}_{0.5}\text{Pr}_{0.5}\text{FeO}_3$ was studied in single crystal form by Hailong *et. al.* [120] where two-fold abrupt spin reorientation, $\Gamma_4(G_x, F_z) \rightarrow \Gamma_1(G_y) \rightarrow \Gamma_2(G_z, F_x)$, has been observed near spin reorientation temperatures $T_{\text{SR1}} = 77$ K and $T_{\text{SR2}} = 45$ K. In this compound, in the presence of 20 KOe magnetic field, two incomplete spin reorientations were observed at 45 K and 28 K as $\Gamma_4 \rightarrow \Gamma_{41} \rightarrow \Gamma_{42}$ respectively. When higher field of 40 KOe is applied, then, $\Gamma_4 \rightarrow \Gamma_{41}$ is suppressed and magnetic configuration Γ_1 changes again in to Γ_4 below T_{SR2} after coexisting in $\Gamma_4 + \Gamma_1(\Gamma_{41})$ configuration within 77-45 K range . With the application of higher applied magnetic field, phase transition starting at H_{crL} changes to another stable magnetic configuration at higher field H_{crH} . Therefore, field induced spin reorientation $\Gamma_1 \rightarrow \Gamma_4$ occurs.

Among all the orthoferrites, DyFeO_3 is the only rare earth orthoferrite which shows the Morin transition where Fe^{3+} ions change the spin direction abruptly from x – axis to y – axis at 35 K i.e. an abrupt change in magnetic structure is observed as $\Gamma_4 \rightarrow \Gamma_1$ [121] where as in all the other orthoferrites including NdFeO_3 , Fe^{3+} spin undergoes gradual rotation from x – axis to z – axis which follows magnetic structure as $\Gamma_4 \rightarrow \Gamma_2$ over a range of temperature. In DyFeO_3 ,

Dy^{3+} ordering occurs at higher temperature (4 K) as G – type antiferromagnet. While in NdFeO_3 , Nd^{3+} orders as C –type antiferromagnet with a weak ferromagnetic ordering at 1.5 K [100].

Thus in the second part of thesis, the impact of 50% doping of Dy ion on Nd site has been studied. This mixed rare earth doping ($\text{Nd}_{0.5}\text{Dy}_{0.5}\text{FeO}_3$) has never been carried out for any transition metal oxide. Moreover, it would be very interesting to study the crystal structure as well as the magnetic structure of the compound in detail. At lower temperature, the rare-earth ordering has been studied in this compound. Also the magnetocaloric effect in $\text{Nd}_{0.5}\text{Dy}_{0.5}\text{FeO}_3$ has also been studied.

1.4.3 Magnetocaloric effect in orthoferrites

Among orthoferrites, GdFeO_3 shows very high magnetic entropy change $52.5 \text{ Jkg}^{-1}\text{K}^{-1}$ at low temperature under an applied field of 9 T as per study done by Das *et. al.* [122]. The magnetocaloric effect in orthoferrites occurs due to magneto-crystalline anisotropy of rare earth ions. Another reason for the presence of such a high value of entropy change in GdFeO_3 is the high moment of Gd^{3+} ions and weaker crystal field effect. Thus, this compound could be potential material for magnetic refrigeration. Cao *et. al.* studied TbFeO_3 in the form of single crystal which shows giant magnetic entropy change ($19.55 \text{ Jkg}^{-1}\text{K}^{-1}$) at 9 K ($T_N^{\text{Tb}} \sim 8.5 \text{ K}$) under an applied field of 9 T due to ferromagnetic ordering of Tb^{3+} ions which is dominant under higher applied magnetic field. In this compound, when the applied magnetic field is low i.e. below 5 T, maximum entropy change occurs around 5 K. This is due to metamagnetic phase transition which is dominant in the temperature range 2 – 4.5 K under low applied magnetic field[123]. Jiao *et. al.* studied anisotropic MCE in DyFeO_3 in the form of single crystal[124]. In this case, due to strong magneto-crystalline anisotropy between b and c axes, giant rotating magnetic entropy change $16.62 \text{ Jkg}^{-1}\text{K}^{-1}$ is observed at low applied field as 2 T which is maximum in comparison to other orthoferrites at 5 K and 2 T. Shao *et. al.* studied the magnetocaloric effect in the single crystal of HoFeO_3 [125]. At 4.5 K, maximum change in entropy is observed to be $19.2 \text{ Jkg}^{-1}\text{K}^{-1}$ under an applied field of 7 T. The maximum change in entropy is observed around the antiferromagnetic ordering temperature of Ho^{3+} . In this compound another increase in entropy change is obtained at 9.5 K with the value $-\Delta S_M = 15.8 \text{ Jkg}^{-1}\text{K}^{-1}$, when applied field is larger than H_r^{Fe} (reorientation field of Fe^{3+}). Another trough is

also present in this compound at 6.5 K in the magnetic entropy change indicating the compensation behavior of antiferromagnetic coupling of Ho and Fe spins [125].

Another study has been done by Silva-Santana *et. al.* [81] on $\text{SmFe}_{0.5}\text{Mn}_{0.5}\text{O}_3$ where they have studied MCE in the compound. Two transitions are observed in MCE calculations, one at 18 K where $-\Delta S_M = 5.6 \text{ Jkg}^{-1}\text{K}^{-1}$ while inverse magnetocaloric is observed at 234 K. The peak at 234 K is smaller peak, due to AFM-WFM transition and it leads to inverse magnetocaloric effect followed by a depression at 222 K. At 18 K, maximum change in magnetic entropy is observed due to the change in magnetic configuration. Mandal *et. al.* [41] studied the positive as well as negative change in entropy at 300 K and 327 K respectively under an applied field of 7 T in $\text{YFe}_{1-x}\text{Mn}_x\text{O}_3$ ($0 \leq x \leq 0.45$). The maximum change in entropy is observed for $x = 0.15$, though the obtained value is less i.e. around $4 \text{ Jkg}^{-1}\text{K}^{-1}$, as compared to Gd based compound[41]. The presence of dual behavior of MCE in $\text{YFe}_{1-x}\text{Mn}_x\text{O}_3$ enables the material to be used as refrigerant during magnetization and demagnetization process[41].

So the study of MCE in rare earth orthoferrites has paved the way for new opportunities in the field of magnetic refrigeration. It helps in getting the deeper insight of understanding MCE in antiferromagnetic material at low temperatures under the influence of applied magnetic field.

1.5 Motivation for the present work

As seen from the previous reports on orthoferrites, 50% doping on Fe^{3+} site with another transition metal ion (Co, Mo, W, etc.) resulted into double perovskite where cationic ordering at *B* site leads to charge transfer among two different transition metal ions[126]–[128]. *B* site ordering is mainly determined by the charge difference and ionic radii difference between two *B* cations [129]. With the increase in valence state difference between two *B* site cation, ordered arrangement is favored. In the case of Fe^{3+} and Mn^{3+} ions, there is atomic number/charge difference of one. It would be interesting to investigate the structural, magnetic, and electronic properties of the manganese doped Orthoferrite in detail. Though, from literature, it has been studied that for a charge difference greater than 2, rock salt arrangement is preferred while for a charge difference less than 2, random arrangement is preferred [129], this would be the expected case for Fe/Mn doped compound.

Orthoferrite and manganite have very different magnetic structure. Orthoferrites with Néel temperature around 600 K have antiferromagnetic ordering with *G*-type magnetic structure [100] whereas Manganites have very low Néel temperature i.e. around 80 K with *A*-type antiferromagnetic ordering [130].

In the case of orthoferrite, due to the isotropic exchange interaction between Fe^{3+} and R^{3+} , weak ferromagnetic canting of Fe^{3+} makes the R^{3+} spins polarized. Further, antisymmetric exchange interaction between the two ions i.e. Fe^{3+} and R^{3+} , becomes perpendicular to each other. Thus, the effective field, produced by the antisymmetric exchange interaction, rotates the weak ferromagnetic moment and spin reorientation takes place [48]. Though Fe^{3+} and Mn^{3+} have charge difference of only 1 but single ion anisotropy of Mn^{3+} is large as compared to Fe^{3+} which influences the magnetic structure strongly. Thus, with the presence of large anisotropy, it would be interesting to study the magnetic structure and spin reorientation of doped orthoferrites.

In this thesis, the doping on rare earth site is also investigated with emphasis on quenched disorder that arises from ionic radii mismatch between Nd and Dy in orthoferrite. There is qualitative difference in spin reorientation of Fe^{3+} spins in the case of NdFeO_3 and DyFeO_3 . In the case of NdFeO_3 , Fe^{3+} spins undergo gradual spin reorientation from Γ_4 (G_x) to Γ_2 (G_z) in the temperature range 100 – 150 K [100]. While, in the case of DyFeO_3 , Fe^{3+} spins undergo abrupt spin reorientation from Γ_4 (G_x) to Γ_1 (G_y) at 50 K [51]. It would be interesting to study the effect of 50% Dy doping on Nd site in NdFeO_3 . Dy^{3+} ions have large anisotropy and therefore ordering of Dy^{3+} spins is independent of Fe^{3+} magnetic structure. Magnetic anisotropy of Dy^{3+} is very large in comparison to Fe^{3+} - Dy^{3+} magnetic interaction. Thus, Ising like spins of Dy^{3+} are confined to its anisotropic axis and therefore order antiferromagnetically as *G*-type along *x* axis. On the other hand, magnetic anisotropy of Nd^{3+} spins is not large enough, therefore, Nd^{3+} spins order as *C*-type antiferromagnet which is dictated by Fe^{3+} magnetic structure through Nd^{3+} - Fe^{3+} exchange interaction along with competing Nd^{3+} - Nd^{3+} interaction. It would be very interesting to study the effect of 50% Dy doping in NdFeO_3 on the spin reorientation of Fe^{3+} ions as well as on the rare earth (Nd/Dy) ordering. Detailed investigation of the magnetic structure is performed on NDFO.

Further, magnetocaloric effect (MCE) has been studied in detail for both the compounds, i.e., NFMO and NDFO. Order/disorder of rare-earth in presence/absence of magnetic field plays an important criterion in the observation of significant MCE. In the above section literature survey for magnetocaloric effect in rare earth orthoferrites has been done in detail. It has been discussed that rare earth orthoferrites involving rare-earth elements with large magnetic moment and low abundance i.e. Tb, Tm, Dy, Er etc. shows significant change in entropy [131][132]. Compounds, having rare-earth elements with relatively high abundance like La and Nd, show a small change in entropy and hence MCE in such compounds is not significant. Economic considerations require development of materials having high abundance rare-earth elements like La, Nd for cryogenic applications. In both the above mentioned compounds (NFMO & NDFO) change in entropy has been studied in the lower temperature region which can be exploited further in specialized application and niche markets.

In the latter part of the thesis, thin film of NFMO has been deposited using pulsed laser deposition. The motivation to deposit the thin film comes from the non-equilibrium nature of growth mechanism in case of pulsed laser deposition. Non-equilibrium nature of growth mechanism may lead to cationic ($\text{Fe}^{3+}/\text{Mn}^{3+}$) ordering which is not possible in bulk form. It would also be interesting to investigate the change in the magnetic anisotropy of the material due to variation of shape anisotropy and strain of the film which is influenced by the substrate. Further, magnetic structure and spin reorientation of NFMO thin films shall be studied to observe the effect of dimensionality and strain.

1.6 Objective of the Present Work

After going through the physics involved in rich magnetic and thermal properties of rare earth orthoferrites and after having a literature survey related to the research for rare earth orthoferrites, the present thesis is aimed to achieve following objectives:

1. To synthesize the $\text{NdFe}_{0.5}\text{Mn}_{0.5}\text{O}_3$ polycrystalline and study the structural and magnetic properties using X-ray diffraction, Mössbauer spectroscopy and SQUID magnetometer. Presence of 50% Mn ion on Fe site induces the octahedral distortion in MO_6 octahedra and also alter the magnetic properties by decreasing the Néel temperature.

2. To study the magnetic structure of $\text{NdFe}_{0.5}\text{Mn}_{0.5}\text{O}_3$ in detail using powder neutron diffraction in the lower temperature region to determine the ordering temperature of rare earth ion along with the spin reorientation of Fe^{3+} ion. Along with this, magnetic structure is also studied in detail above room temperature as there is presence of short range ordering of Fe^{3+} ions.
3. To synthesize the $\text{Nd}_{0.5}\text{Dy}_{0.5}\text{FeO}_3$ polycrystalline and study its crystal structure and magnetic structure in detail. Presence of two rare earths with completely different properties have significant effect on the magnetic properties and its structure along with the ordering temperature.
4. To study the magnetocaloric effect in $\text{Nd}_{0.5}\text{Dy}_{0.5}\text{FeO}_3$ and $\text{NdFe}_{0.5}\text{Mn}_{0.5}\text{O}_3$ and their comparison to show the effect of rare earth ordering on change in magnetic entropy.
5. To synthesize the epitaxial thin films of $\text{NdFe}_{0.5}\text{Mn}_{0.5}\text{O}_3$ on STO substrate using Pulsed laser deposition technique and study their structural, electronic and magnetic properties.

1.7 Organization of Thesis

The present thesis has been organized in the following chapters:

Chapter 1: Introduction

Chapter 2: Experimental Techniques describes all the experimental techniques which have been used in the present work for synthesis and characterization of compounds studied in the thesis.

Chapter 3: Synthesis and characterization of $\text{NdFe}_{0.5}\text{Mn}_{0.5}\text{O}_3$ discusses the synthesis of polycrystalline compound and study its structural and magnetic properties. The effect of 50 % doping of Mn on Fe site is discussed in terms of magnetic properties and Mössbauer spectroscopy.

Chapter 4: Magnetic structure and specific heat of $\text{NdFe}_{0.5}\text{Mn}_{0.5}\text{O}_3$ discusses the magnetic structure over the range of temperature 1.5 – 400 K using powder neutron diffraction. Diffused scattering which is present at temperature well above Néel temperature

and extend till lowermost temperature is discussed. Further rare earth ordering at lower temperature is also discussed using powder neutron diffraction and specific heat studies.

Chapter 5: Magnetic and thermal properties of $\text{Nd}_{0.5}\text{Dy}_{0.5}\text{FeO}_3$ discusses effect of 50% doping of Dy on Nd site on its structural and magnetic properties. Further magnetic structure of the compound is also discussed using powder neutron diffraction.

Chapter 6: Magnetocaloric studies in $\text{Nd}_{0.5}\text{Dy}_{0.5}\text{FeO}_3$ and $\text{NdFe}_{0.5}\text{Mn}_{0.5}\text{O}_3$ discusses the change in magnetic entropy of both the compounds with the change in applied magnetic

Chapter 7: Growth and characterization of epitaxial thin film of orthoferrite describes the synthesis of epitaxial thin film of $\text{NdFe}_{0.5}\text{Mn}_{0.5}\text{O}_3$ on STO substrate using pulsed laser deposition technique. The structural, electronic and magnetic properties have been studied in detail.

Chapter 8: Conclusion and Future scope concluded the present work and contains the findings from the present research work as well as the scope of future work.

Experimental Techniques

In the present chapter, synthesis and characterization techniques, used throughout in the present thesis, has been discussed. First, the growth techniques for the synthesis of polycrystalline particles are described. Afterwards, the synthesis of thin films has been discussed. Finally, the characterization techniques used at different stages of the thesis are elaborated.

2.1 Synthesis Techniques

2.1.1 Synthesis of Polycrystalline powder

Polycrystalline $\text{NdFe}_{0.5}\text{Mn}_{0.5}\text{O}_3$ (NFMO) and $\text{Nd}_{0.5}\text{Dy}_{0.5}\text{FeO}_3$ (NDFO) have been prepared by conventional solid state reaction method. It is the most commonly used and easiest method for the polycrystalline powder synthesis[133][134]. In the present work, all the chemicals were purchased from Sigma Aldrich with purity not less than 99.99%. Since the impurities can greatly affect the properties of the final products, so it is desirable to use powders of finest purity. The powders of Nd_2O_3 , Fe_2O_3 , MnO_2 and Dy_2O_3 used in the present work. The as received powders were first heated at 500°C for 5 hours to remove any moisture present in the powders. Figure 2.1 shows the block diagram of the steps which are involved in the solid state reaction method.

The solid state reaction method involves the following major steps:

1. Grinding
2. Calcination
3. High temperature Sintering
4. Pelletization (If required)

For the preparation of polycrystalline powder, only first two steps were followed. However, all the steps were followed for the preparation of targets to be used for the synthesis of thin films. The details for each step are discussed as follows:

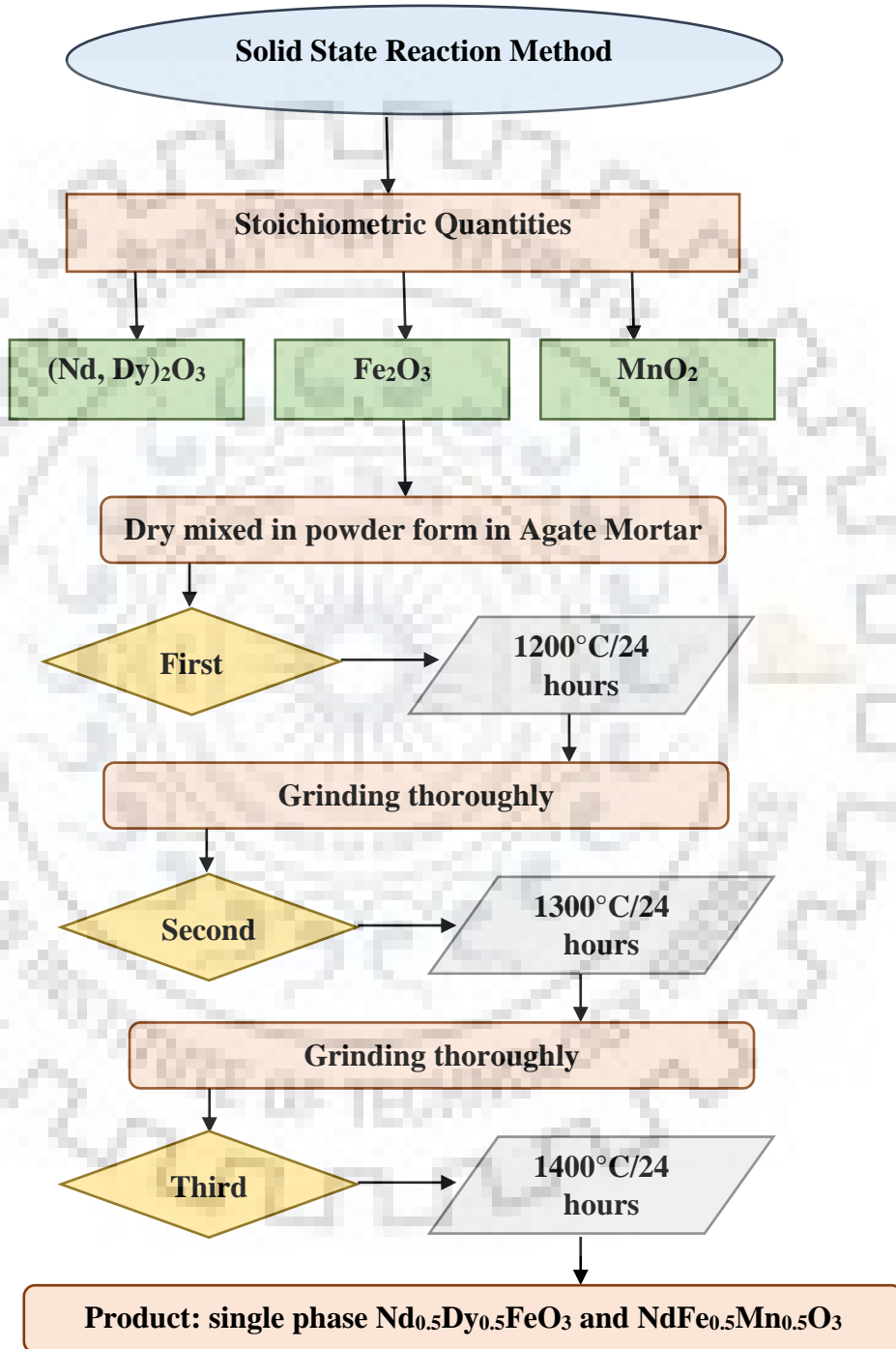


Figure 2.1 Flow chart of solid state reaction method

1. *Grinding*: In the first step, all the powders were mixed in a proper stoichiometric ratio, following the well balanced chemical reaction involved, to get the final compound. The mixing or grinding was done in an agate pestle mortar for around 12-13 hours to obtain finely sized reactants in the homogeneous powder mixture.
2. *Calcination*: After grinding, the calcination of the powders was done by heating them at high enough temperature to remove other unwanted volatile substances like carbon and nitrogen if present. The temperature for calcination was kept less than the melting point of the mixed constituents. Calcination is done at high temperature to enable the proper reaction mechanism to obtain the desired phase without any impurity. High temperature in solid state reaction is the driving force for the diffusion and movement of atoms or ions in the lattice to reach the desired reaction site which results in the proper phase of final product[135]. For the two compounds, the calcination was performed in ambient atmosphere at 1200° C for 24 hours.
3. *High temperature sintering*: In the final step, the calcined powders were sintered at high temperature (1300°C) for 24 hours in the ambient atmosphere after grinding for 2-3 hours. Further, in the last step, after sintering again powder was ground for 3-4 hours and then final sintering was done at 1400 ° C for 24 hours.

“Most of the measurements such as X-ray diffraction, Magnetization and powder neutron diffraction were carried out on the powder form of the compounds”.

In Figure 2.1, flow chart described the synthesis of NFMO and NDFO in powder form. Once the phase has been obtained in the powder form then it has been further used for the palletization process.

4. *Pelletization*: After high temperature sintering, the powders were again ground in an agate pestle mortar for nearly 4-5 hours to get a well-mixed final product. Before making the pellets of the prepared powder, a small amount (around 5% of the weight of the total powder) of polyvinyl alcohol (PVA) was mixed in around 20-30ml of distilled water to make the binder. The binder was mixed with powder which was then again ground for 7-8 hours to get fine powder. This fine powder was then pressed into pellets of diameter 5 mm for specific heat measurements and 16 mm for thin film deposition. The thickness of the film is approximately 1-2 mm,

using a hydraulic pellet press under a pressure of 20 tons for 15 seconds. During sintering at 1400 ° C for 24 hours in ambient atmosphere, controlled heating and cooling was done to ensure the diffusion of atoms across the boundaries of adjacent particles, which then coalesce together to produce a solid dense piece of material.

2.1.2 Synthesis of Thin Film

In the simplest words, a thin film can be defined as a layer of a material with thickness in the range of nanometers to micrometer. The ever increasing demand of miniaturization in electronic devices, with advances in the thin film synthesis techniques, has accelerated the investigation of thin films of different materials[126][136][137][138]. The applications of thin films are countless as they are now involved in almost every aspect of the physical world[139][140][141][142][143][144]. From the household mirror to a computer memory or a solar cell, thin films are widely used for their multiple advantages in different ways.

In general, the growth of a thin film on a substrate depends strongly on the surface energy of the depositing material and the substrate[145]. Nucleation and agglomeration processes for the depositing material depends upon the type and temperature of the substrate. Nucleation of islands on the surface of a substrate occurs when an atom or ion imparts a part or whole of its kinetic energy to the substrate, thus causing it to get adsorbed onto the surface of the substrate. These adsorbed atoms or adatoms are bound to the substrate either via Van der Waals or via covalent forces[145]. If the residual kinetic energy of these adatoms is enough to overcome the binding forces, then, they can diffuse onto the surface or might get desorbed from the surface back into the gas phase. The diffused atoms will keep moving around the surface until they lose some energy or come across a region where the binding forces are strong enough to reach minimum energy position. The diffused atoms may be mobile on time scales of microseconds to several seconds depending upon their surface energy. The common regions where these diffused adatoms will become bound are mainly the surface defects such as grain boundary dislocations, step edges or surface impurities. The bound adatoms then themselves become the points for binding other diffusing adatoms for nucleation of islands. Each nucleation site will become an island and each island will then become a crystallite. The density of grain boundaries is determined by the size of the metal crystallites, which is initially determined by the distance between nucleation sites.

Typically, two types of deposition processes, physical process and chemical process are used for the deposition of crystalline thin films and both types of processes involve three main steps:

- Production of appropriate atomic, molecular or ionic species.
- Transport of these species to the substrate through a medium.
- Condensing on the substrate, either directly or via a chemical and/or electrochemical reaction, to form a solid deposit.

The physical process is composed of the physical vapor deposition (PVD) processes like thermal evaporation, electron beam evaporation, sputtering, molecular beam epitaxy (MBE), pulse laser deposition (PLD) and the chemical process is composed of chemical vapor deposition (CVD) methods like metal-organic chemical vapor deposition (MOCVD), plasma enhanced chemical vapor deposition (PACVD) and the chemical solvent deposition process like spray pyrolysis, sol-gel. Various CVD and PVD processes, used for synthesis of crystalline thin films, have their own specific advantages and disadvantages.

The selection of a deposition process for thin films usually depends upon the specific characteristics of a film required for a study or application of interest. The basic requirements of good quality thin films are:

- i) Good uniformity of the films throughout exposed area,
- ii) Required stoichiometry and crystalline phase
- iii) The films with good physical and chemical properties such as low stress, good adhesion to the substrates, high density, low films defect, controlled grain size and its distribution, boundary property and orientation.
- iv) Equipment initial cost and running cost.

To get highly uniform, nanocrystalline thin films with a moderate size distribution, physical vapor deposition processes such as thermal evaporation, laser ablation, e-beam evaporation and magnetron sputtering are found to be very effective for depositing thin films with aforementioned microstructural characteristics.

In the present work, only pulsed laser deposition was employed. As PLD provide a stoichiometric transfer of material from the target to the substrate in crystalline form. Thus

PLD ensures very effective stoichiometric control with oxide targets. PLD has been used in the present work for depositing thin films[146]. The thin films of a particular compound are usually deposited from the polycrystalline target of the same compound. The purity of films is controlled by purity of the target, base vacuum and purity of the used gas. The following section describes the pulsed laser deposition technique used in the present work for the deposition.

2.1.2.1 Pulsed Laser Deposition

Pulsed Laser Deposition (PLD) is a versatile technique for the preparation of thin films by ablation of one or more targets illuminated using a focused pulse of laser beam. The main characteristics of using this technique is the proper stoichiometry transfer between the target and the deposited thin film, high deposition rate (~ 0.1 nm per pulse) and the occurrence of droplets on the surface of substrate[147][148][149][150]. This technique has been intensively used for the deposition of oxides, nitrides, carbides, metallic, and polymer thin films. In the present work, NFMO and NDFO thin films were deposited by PLD technique using KrF excimer laser source (Compex Pro 201, Lambda Physik) with pulse duration $\tau = 25$ ns and wavelength $\lambda = 248$ nm. The schematic of the experimental set-up used for the deposition of thin films is shown in Figure 2.2 [151].

The deposition chamber is evacuated using a turbo molecular pump which is backed by a rotary pump. The laser pulse strikes the stoichiometric target of desired composition at an angle of 45° . The frequency of the laser pulse can be varied from 1Hz to 10Hz. The total out coming energy of the laser beam can be controlled with the mask located at the output window of the laser source. The fluence of the laser beam at the target can be adjusted either by varying size of laser spot or by varying the laser energy. The fluence used in the present work lies in the range $1.5-2.5 \text{ J/cm}^2$. The target is mounted on a rotating carousel which can accommodate four number of targets. The target is rotated around its own axis (using a dc motor) as well as given an angular motion (using a stepper motor) for uniform ablation of the target. Threshold power density is required to produce the plume which depends on the target material and morphology. The power density required for the deposition using ultraviolet (UV) excimer laser is of the order $10-500 \text{ MWcm}^{-2}$.

Ablation from the target using laser depends mainly on the optical penetration depth and thermal conductivity of the target and the rate of incoming photons. In this process, deposition takes place via electronic process. The target should be insulating/semiconducting for efficient transfer of energy to the target from laser pulse. Vaporization of the absorption depth starts within the first 100 ps of a 25 ns pulse. After this, the target material under the plasma will be screened from the remainder of the laser pulse which will be absorbed by the plasma, as it becomes more directional [148][146]. The congruent ablation in PLD process leads to simultaneous ejection of the components of target material as the laser energy is absorbed in a small volume ($\sim 10^{-13} \text{ m}^3$) for a small duration of time (25ns). This ensures the stoichiometric transfer of target material onto the surface of the substrate. With the expansion of the plasma, the electron density tends to decrease and the plasma becomes transparent to the laser beam.

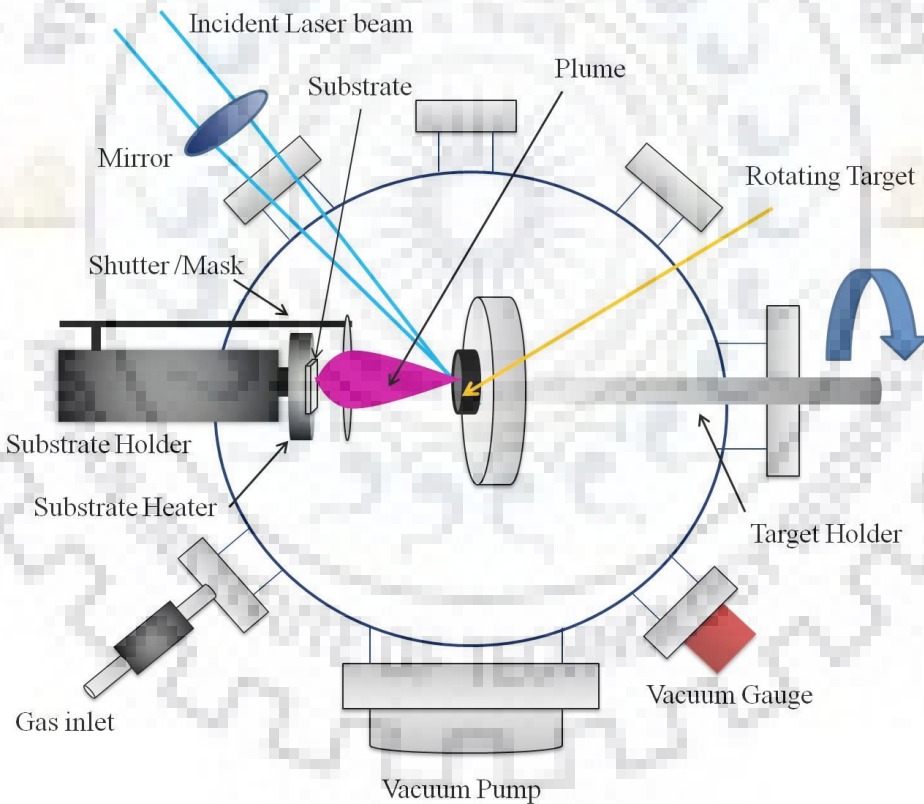


Figure 2.2 Schematic diagram of Pulsed Laser Deposition technique [151]

The ejection of the target material is followed by the formation of plasma or plume which expands very fast in a perpendicular direction to the plane of the target. The ablated plume of

the material is characterized by a cone-shaped distribution having $\cos^n\theta$ dependence ($9 < n < 12$) and θ is measured with respect to the normal at the target surface[147]. During the deposition, the O_2 pressure is maintained in the chamber using an automated mass flow controller and a manual butterfly valve situated in the chamber. The O_2 pressure controls the expansion of the plume making it broader and thermalize the plume. Also, the O_2 pressure plays an important role in the growth of oxide thin films as it helps in controlling the oxygen stoichiometry.

The ejected target material gets deposited on the substrate which is placed on a substrate holder cum heater with a silver paste. The substrate holder is placed opposite to the target and the distance between both can be adjusted between 3 cm to 6 cm. The temperature of the substrate holder or heater is usually varied in the range 600- 900°C. The temperature of the heater is monitored by a thermocouple situated beneath the heater surface and is controlled by using an automated PID controller. The temperature of the substrate regulates the mobility of the incoming particles on the surface of the substrate.

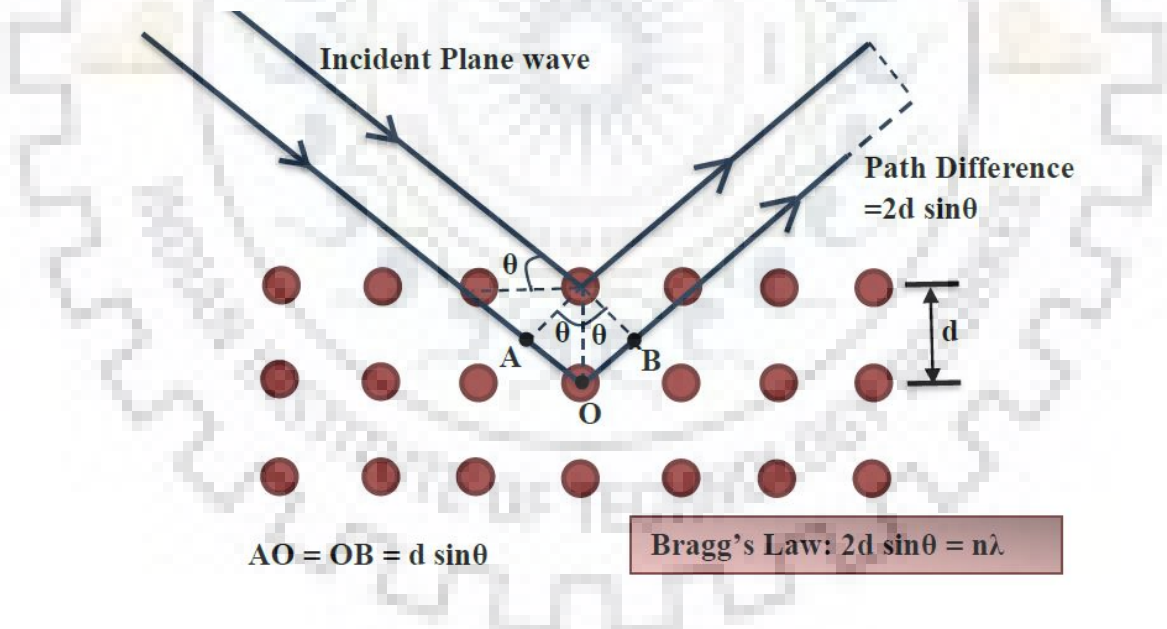


Figure 2.3 Schematic diagram for diffraction of X-Ray from a crystalline structure

Initially, pre ablation of the target is performed to remove the surface contamination by putting the shutter in front of the substrate. The number of pulses is the deciding factor for the thickness of the film. The nominal rates of growth for NFMO thin film was $\sim 0.10-0.20 \text{ \AA/}$

pulse. After the completion of the pulse sequence, the laser power was switched off and the deposited thin films were annealed under O₂ pressure of 500 Torr controlled by the manual butterfly valve. After doing the annealing for an hour, the cooling was done at a rate of 5°C/min. The sample was then removed from the chamber after it attains the room temperature.

2.2 Characterization Techniques

2.2.1 X- Ray Diffraction

X-ray diffraction (XRD) is considered as the most widely used non-destructive technique for the identification of crystal structure, phase, orientation, lattice parameters and stress in a crystalline material[154]. X-rays are electromagnetic radiations with their wavelength ranging from 0.01 nm to 10 nm. X-ray diffraction results from the interference of diffracted beams of a monochromatic X-Ray source incident on a crystalline structure.

The process of diffraction can also be understood in the simple manner by the Bragg's law which is:

$$2d_{hkl}\sin\theta = n\lambda \quad (2.1)$$

Where d_{hkl} is the spacing between the adjacent atomic planes with Miller indices (hkl) , θ is the angle between the planes and λ is the wavelength of the incoming X-Ray and n is an integer number as shown in Figure 2.3. Now, since the maximum value of $\sin\theta$ could be 1. So, we can write $\frac{n\lambda}{2d} < 1$, and therefore $n\lambda$ should be less than $2d_{hkl}$. The smallest possible value of n is 1, so $\lambda < 2d$. Since, for most sets of crystal planes d_{hkl} is of the order of or less than 3Å, therefore, the λ of the incoming radiations should be less than 6 Å. X-rays whose wavelength is of the order of few Å, are suitable for resolving the spacing between the atomic planes in common oxides or metals which is also of the order of few Å[154]. The crystallographic information of a material can be obtained by evaluating the d_{hkl} values and indexing the reflections obtained from the diffraction pattern. The characteristic diffraction of a given substance can always be obtained whether the substance is present in pure state or as one constituent in a mixture of several substances. This fact is the basis of the diffraction method of chemical analysis. X-ray diffraction pattern is characterized by a set of line positions

(2θ) and a set of relative intensities (I). The angular position (2θ) of lines depends on the wavelength (λ) of the incident ray and spacing (d) of the lattice planes[154].

X-rays are scattered by electrons. The intensity of the scattered beam from an electron is given by:

$$I = I_o \left(\frac{\mu_o}{4\pi}\right)^2 \left(\frac{e^4}{m^2 r^2}\right) \sin^2 \alpha = I_o \frac{K}{r^2} \sin^2 \alpha \quad (2.2)$$

Where I_o is the intensity of the incident beam, K is constant, known as square of scattering length and α is the angle between the observer and direction of acceleration of electron, r is the distance of the observer from the electron in meters [154].

As shown in Figure 2.4, An unpolarized X-ray beam travelling in x direction encounters an electron at O , so the scattered intensity at P (at distance r from electron) will be the sum of two components, i.e. in the y direction and in the z direction. As in the y direction $\alpha = \pi/2$, therefore,

$$I_{Py} = I_{Oy} \frac{K}{r^2} \quad (2.3)$$

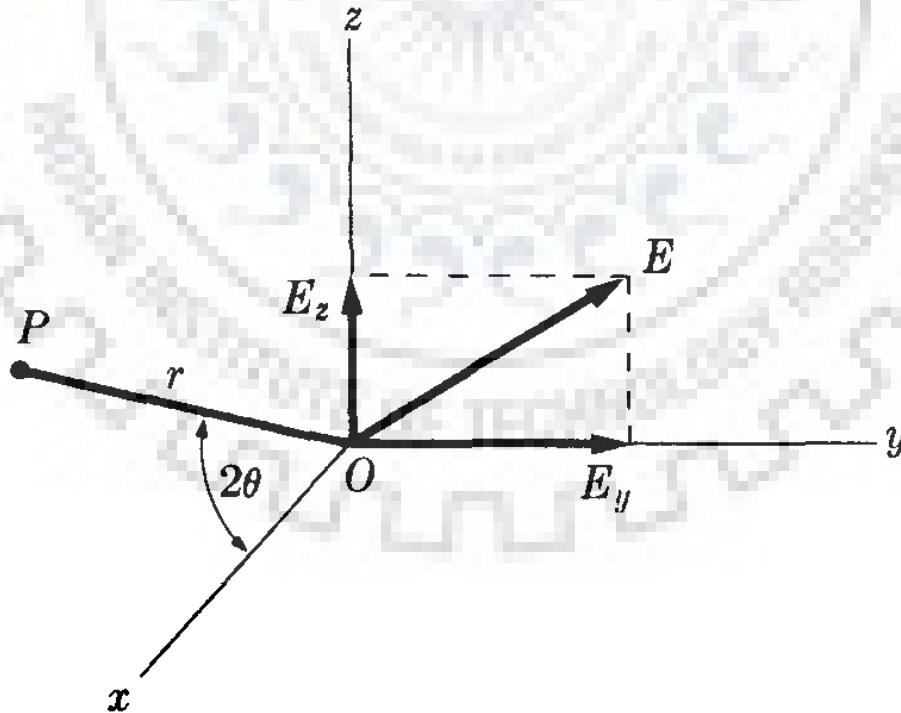


Figure 2.4 Coherent scattering of X-rays by a single electron [154]

In the z direction, $\alpha = \frac{\pi}{2} - 2\theta$, therefore,

$$I_{Pz} = I_{Oz} \frac{K}{r^2} \cos^2 \theta \quad (2.4)$$

Since incident intensity is I_0 , therefore incident intensity in the two directions is:

$$I_{Oy} = I_{Oz} = \frac{1}{2} I_0 \quad (2.5)$$

The total scattered intensity at P is:

$$I_P = I_{Py} + I_{Pz} \quad (2.6)$$

$$I_P = I_0 \frac{K}{r^2} \left(\frac{1 + \cos^2 2\theta}{2} \right) \quad (2.7)$$

The term $(1 + \cos^2 2\theta)/2$ is the polarization factor only valid when the incident beam is unpolarized.

In the powder diffractometer, relative integrated intensity, from a polycrystalline material is given by:

$$I = F_{hkl}^2 p \left(\frac{1 + \cos^2 2\theta}{\sin^2 \theta \cos \theta} \right) \quad (2.8)$$

Another factor that is important in the powder diffraction is, $F_{hkl} = \sum_{i=1}^n f_i \exp[2\pi i(hx_i + ky_i + lz_i)]$, defined as the structure factor for the lattice plane (hkl) (in case of cubic crystal) where f_i is the scattering factor for the i^{th} atom. Structure factor is independent of the shape and size of the unit cell. It explains the atomic arrangement within the unit cell [154].

Whenever reflection occurs from the plane of the same family then multiplicity factor is important to consider as it is defined as the number of different planes which have the same spacing and is given by p .

The factor $1/(\sin^2\theta\cos\theta)$ is known as *Lorentz factor* which depends on three factors: (i) Geometrical factor, (ii) Orientation factor, and (iii) Diffraction geometry factor.

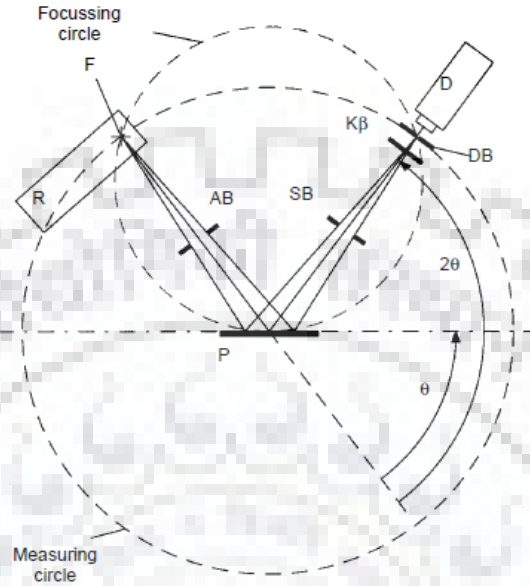


Figure 2.5 Schematic diagram of beam path in Bruker D8 powder X-Ray diffractometer in Bragg-Brentano geometry [155]

According to Geometrical factor, a non-zero diffracted intensity can be produced by the crystal, for angles slightly different from the Bragg angle. In this case, $I \propto 1/\sin 2\theta$.

According to Orientation factor, the number of crystals oriented near Bragg angle is not constant at all angle. In this case, $I \propto \cos\theta$.

According to diffraction geometry factor, the detector will see a greater proportion of a diffraction cone when reflections are at lower 2θ . Intensity per unit length $\propto 1/\sin 2\theta$.

On combining the three factors in Lorentz factor, $I \propto \left(\frac{1}{\sin 2\theta}\right) \cdot (\cos\theta) \cdot \left(\frac{1}{\sin 2\theta}\right)$.

Furthermore, thermal agitations were neglected while deducing equation (2.8). But in reality the atoms vibrate about their mean positions with an amplitude which increases with temperature. Because of thermal agitation, the intensity of the selective reflections gets reduced. Therefore, the scattered as given by equation (2.8) is multiplied by a coefficient e^{-2D} which is less than unity; known as *Debye or temperature factor*. The D value depends on

thermal vibrations as well as scattering angle 2θ , given by $D = (\sin\theta/\lambda)^2$. Even for larger values of θ this effect can be important which includes room temperature too[154].

For powder X-ray diffraction technique, sample is always taken in the form of powder or pellet which consists of very fine grain of single crystals that are also known as crystallites. By the word “powder”, we mean that the crystallites are oriented randomly in the sample. In the present work, Bruker D8 Advance X-ray diffractometer was used to investigate the crystal structure, phase, lattice parameters and bond lengths of the powder compound. In the powder diffractometer, radiation emitting from the X-ray tube is diffracted from the sample and further recorded by the detector. Bruker D8 Advance X-ray diffractometer follows Bragg-Brentano geometry as shown in Figure 2.5. The diffraction angle (2θ) is thus always equal to twice the glancing angle (θ) [155]. In Figure 2.5, D is the detector, DB is the detector slit, F is the focus, $K\beta$ is the $K\beta$ filter, P is the sample, R is the X-ray tube, AB is the aperture slit and SB is the scattering slit. The Bragg-Brentano geometry is used for focusing. Focus and detector slit is present on the focusing as well measuring circle while sample is present only on the focusing circle. Aperture slit is used between the tube and sample to delimits the irradiated sample area while the scattered slit is used to suppress the undesired scattered radiation.

In the present thesis, Rigaku Smartlab X-ray Diffractometer was used to investigate the crystal structure, phase, lattice parameters, orientation and any parasitic impurity phase present in the synthesized thin film of NFMO. For all the samples, the measurements were done mostly in θ - 2θ scan as shown in Figure 2.6. In θ - 2θ scan, the tube and detector moves simultaneously

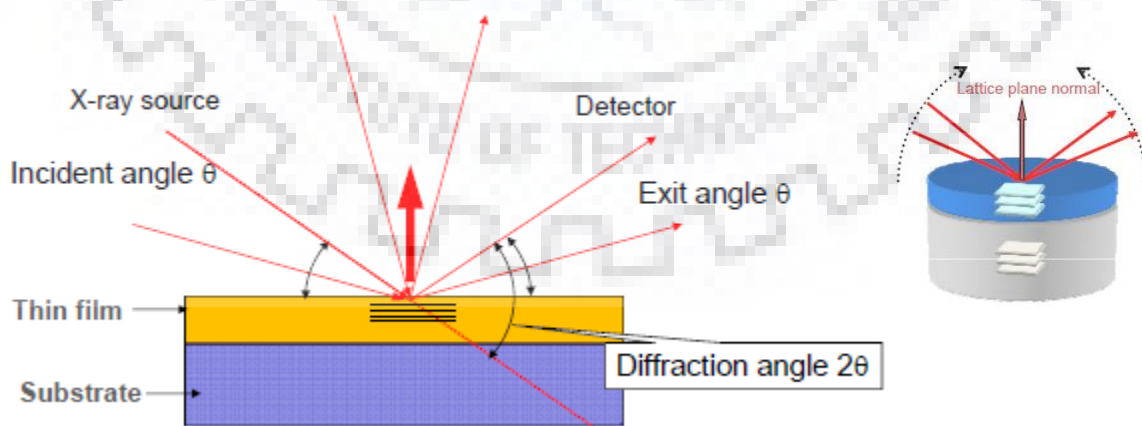


Figure 2.6 $\theta/2\theta$ measurement in Rigaku X-Ray diffractometer [156]

to cover the whole 2θ range (say $5 - 90^\circ$). Thus angle ω , between the tube and the surface of the sample, and θ between the detector and the sample surface always remain same during the scan. All the lattice planes parallel to the sample surface are measured in this arrangement. In this case, penetration depth increases with the increase in the incident angle. Another diffraction measurement is performed by scanning 2θ angle and incident angle is kept fixed at some angle, 0.5° in our case as shown in Figure 2.7. In this case, incident angle is not half of the 2θ angle of detector. Therefore, when the scattering angle changes in this case, diffraction pattern corresponding to different orientation of crystal is obtained [156]. Figure 2.8 shows the sketch of all the angles involved in the thin film X-ray diffraction experiment. Here, χ represents tilt of the sample, ϕ corresponds to the in plane rotation and ω is the angle between the plane of the sample and the X-ray tube. For all the samples, $CuK_{\alpha 1}$ radiations source with $\lambda = 1.54\text{\AA}$ has been used. The operating voltage and current for the X-ray tube are maintained at 45 kV and 200 mA, respectively. The peaks obtained in the diffraction pattern can then be indexed to identify the phase formation and to estimate the lattice parameters and particle size from peak's angle and their FWHM.

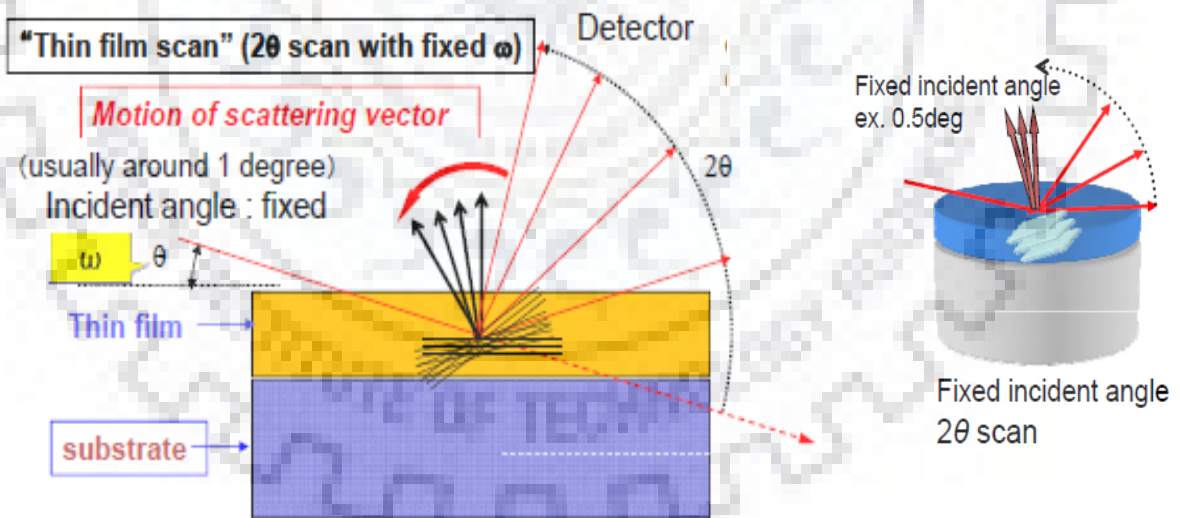


Figure 2.7 2θ scan with fixed ω measurement in Rigaku X-Ray diffractometer [156]

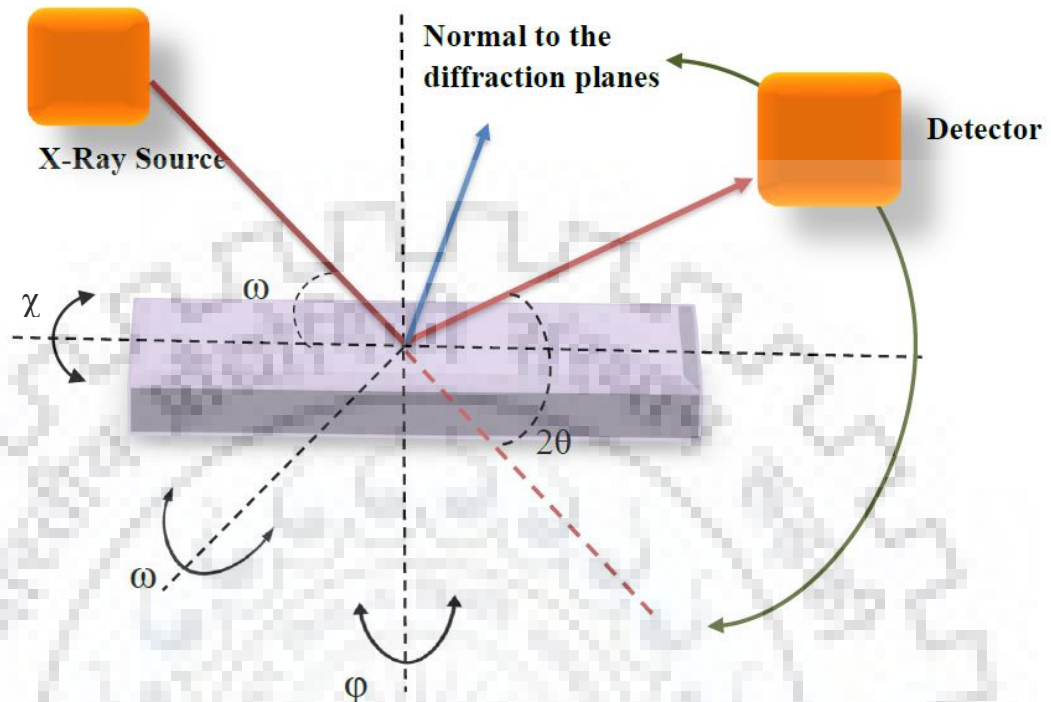


Figure 2.8 Schematic of the angles involved in X-Ray diffraction of a sample

2.2.2 Reciprocal Space Map

The reciprocal space map (RSM) measurement records diffraction intensity distributions by scanning both the diffraction angle and sample rotation axes, and plots the result in the reciprocal space. The reciprocal lattice map can provide detailed information on the crystal structure, crystal orientation relationships, crystallinity and favored orientation of the sample investigated. The central co-ordinates, shapes and positional relationships of the reciprocal lattice points appearing in a two dimensional data plotted in the reciprocal space provide a wide range of information on crystal structure. So, this method obtains two dimensional distribution maps with the scanning scattering vector K as shown in Figure 2.9. The distributions of the directions and intensities of reciprocal points at right angle to the specimens' surface are observed using the in-plane measurements method instead of using the out of plane measurement. To combine these two methods, distributions of reciprocal points can be observed three dimensionally and the orientation relationships between a thin film and

its substrate. Lattice constants and the condition of strain can be analyzed from the information of the positional relationships and the shape of reciprocal points.

It is very useful to express the positions and shapes of reciprocal lattice points using the Cartesian coordinate system (i.e. Q_x, Q_z) instead of 2θ and ω for calculating the d – spacings. This conversion can be done following the simple formula shown in equations 2.13 and 2.14.

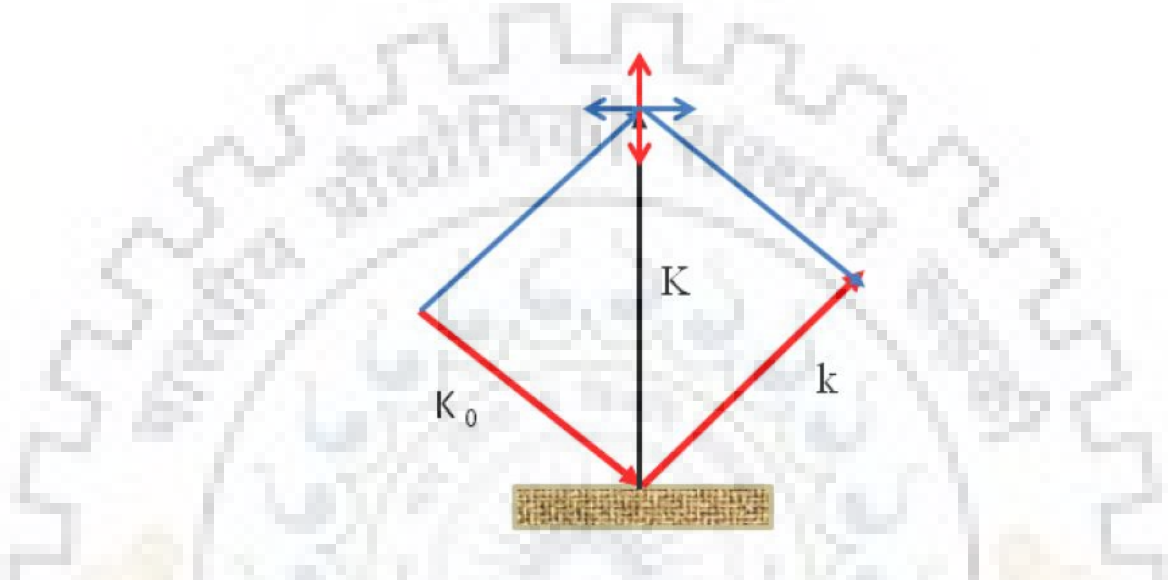


Figure 2.9 Reciprocal space mapping measurement

$$Q_x = 2\pi \frac{2}{\lambda} \sin \frac{2\theta}{2} \sin \left(\frac{2\theta}{2} - \omega \right) = 2\pi \frac{1}{\lambda} \{ \cos \omega - \cos(2\theta - \omega) \} \quad (2.13)$$

$$Q_z = 2\pi \frac{2}{\lambda} \sin \frac{2\theta}{2} \cos \left(\frac{2\theta}{2} - \omega \right) = 2\pi \frac{1}{\lambda} \{ \sin \omega - \sin(2\theta - \omega) \} \quad (2.14)$$

Both Q_x and Q_z are the inverse of lattice spacings and are also expressed as $Q_{||}$ and Q_{\perp} because of the position relationships of the sample surface normal. For example, Q_z is parallel to $[00l]$ direction of the sample and Q_x is parallel to $[hk0]$. In this instance, d_{hk0} and d_{00l} are calculated from the central co-ordinates of reciprocal lattice point distribution (Q_x, Q_z) and from that the lattice constants can be calculated.

The relative sites of the reciprocal lattice points of an epitaxial film and substrate change reliant on the lattice match as well as the lattice relaxation. Figure 2.10 schematically describes the reciprocal space plots for relaxed, strained and misoriented films.

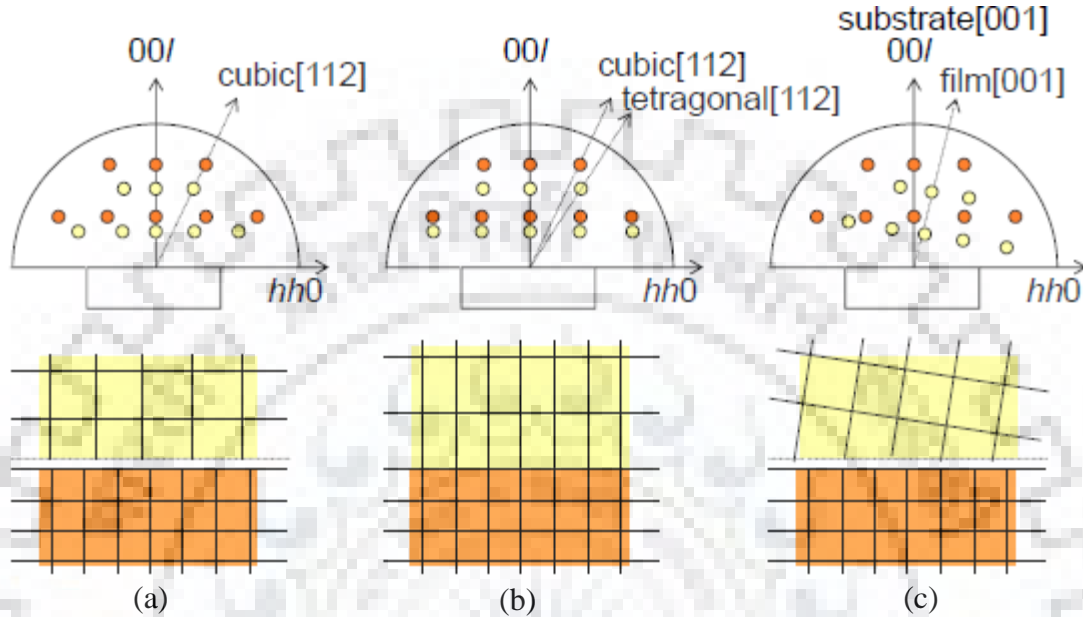


Figure 2.10 Reciprocal space maps of hetero epitaxial thin films in different states. (a) Relaxed (b) Strained (c) Misoriented [156].

The term lattice relaxation refers to the state of an epitaxial film in which the lattice parameters of the film relax to the values in bulk form. As shown in Figure 2.10(a), the reciprocal lattice point of the relaxed film with the indices (hkl) is positioned on the line joining the reciprocal lattice point (hkl) of the substrate and the origin of the reciprocal lattice along the line of the $2\theta/\omega$ scan for both symmetric and asymmetric diffractions.

If the film is strained at the interface between the epitaxial film and the substrate in such a way that the in-plane lattice constants of the epitaxial film and substrate match, the reciprocal lattice point of the film with the indices (hkl) is positioned directly below the reciprocal lattice (hkl) of the substrate for both symmetric and asymmetric diffractions (see Figure 2.10 (b)). In the case for asymmetric diffraction, the reciprocal lattice points of the substrate and the films are not positioned on the same line of a $2\theta/\omega$ scan.

If crystal orientation direction of thin film is tilted in relation with the substrate, the reciprocal lattice of thin film is also tilted as shown in Figure 2.10(c). In this case, reciprocal lattice points of film and substrate can never be on the same straight line.

2.2.3 Neutron Diffraction

Neutron diffraction has many advantages over X-ray diffraction [157][158]. X-rays primarily interact with electrons while neutrons interact with nucleus. Neutrons are sub atomic particles with no charge and have mass (m) equal to 1.0087 atomic mass units (1.675×10^{-27} Kg), spin $\frac{1}{2}$ and a magnetic moment (μ_n) of -1.9132 nuclear magnetons[159]. These properties of neutron give rise to two principle mode of interaction which are different from those of X-rays.

Nuclear interaction of neutrons with matter are short ranged and possible reason behind this is that neutrons do not have any charge. Neutrons penetrate deep into the condensed matter due to small interaction probability. Further, interactions between the neutrons and atomic nuclei involve complex nuclear interactions providing information of structure, complementary to X-ray which probe the electronic cloud surrounding the nucleus. Therefore, atom's ability to scatter neutrons do not follow any general trend in periodic table. But in the case of X-rays, X-ray atomic scattering factor increases with atomic number. In neutron scattering, isotopic substitution can be explored using neutron diffraction as isotopes of the same element have different scattering lengths [160].

Another interaction is the magnetic dipole interaction that occurs between nuclear magnetic moment of neutron and the magnetic moment associated with unpaired electron spins in magnetic samples. As a result, spin-down and spin-up electron 'look' different to neutrons. New peaks appear in the neutron diffraction pattern whenever a new magnetic order evolves in sample. The direction and strength of magnetic moments is determined by the position and amplitude of the magnetic Bragg peak. Hence, the arrangement of atomic magnetic moment in magnetically ordered system can be determined by neutron scattering. This is the most direct available method to determine the details of the magnetic structure[161].

Thermal neutrons are required for condensed matter research. These are produced from more energetic neutrons that are slowed down by inelastic collisions in moderating material having light atoms. Most of the slow neutrons have kinetic energies of the order $K_B T$, are produced through inelastic collision. T is the moderator temperature, whose value is about

300K for thermal neutrons, and K_B is the Boltzmann's constant. If the wave nature of the neutron is considered, then it is described by a wavelength λ given by:

$$\lambda = \frac{h}{\sqrt{2mk_B T}} \quad (2.13)$$

Where h is Planck's constant and m is the mass of the neutron. In equation (2.13), we find that a neutron with an energy of ~ 25 meV has a wavelength of $\lambda \sim 1.8$ Å, which is comparable distance with the mean atomic separation in solid or dense liquid[160]. Therefore, to resolve the atomic structure as well as the magnetic structure of materials with sub-nanometer periodicity, *thermal neutrons* are preferred.

2.2.3.1 Neutron Scattering

The neutron scattering intensity obtained from magnetic materials is a superposition of magnetic and nuclear scattering. In neutron scattering, neutrons are scattered into a given solid angle element $d\Omega_f$, with a final energy between E_f and $E_f + dE_f$, in the direction of the wave vector \mathbf{k}_f as shown in Figure 2.11 with a rate given by the product of $\Phi(k_i)$ and the double differential cross section, $d^2\sigma/d\Omega_f dE_f$. The rate at which the neutrons are scattered is given by $\Phi(k_i)\sigma$, where σ is the scattering cross section[161]. The double differential scattering cross section is expressed as a sum of coherent and incoherent parts:

$$\frac{d^2\sigma}{d\Omega_f dE_f} = \left. \frac{d^2\sigma}{d\Omega_f dE_f} \right|_{coh} + \left. \frac{d^2\sigma}{d\Omega_f dE_f} \right|_{inc} \quad (2.14)$$

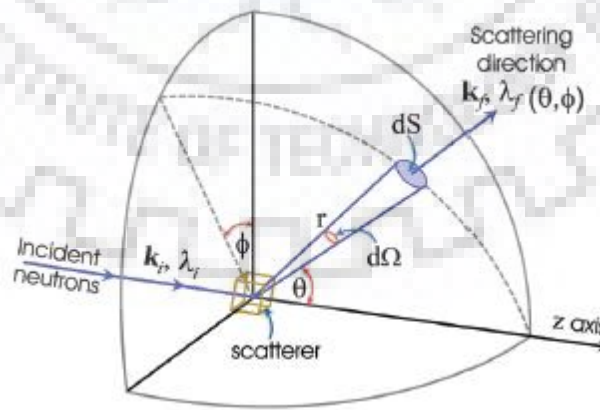


Figure 2.11 Geometry for scattering experiment [162]

The information about the cooperative effects among different atoms is provided by the coherent part, such as inelastic scattering by phonons or magnons or elastic Bragg scattering. The incoherent part provides information about individual particle motion and is proportional to the time correlation of an atom with itself, such as diffusion.

Van Hove assumed scattering from a sample that has only one type of atom and one isotope having scattering length b , and showed that:

$$\frac{d^2\sigma}{d\Omega_f dE_f} = N \frac{k_f}{k_i} b^2 S(\mathbf{Q}, \omega) \quad (2.15)$$

Where,

$$S(\mathbf{Q}, \omega) = \frac{1}{2\pi\hbar N} \sum_{u'} \int_{-\infty}^{\infty} dt \langle e^{-i\mathbf{Q}\cdot\mathbf{r}_{l'}(0)} e^{i\mathbf{Q}\cdot\mathbf{r}_{l'}(t)} \rangle e^{-i\omega t} \quad (2.16)$$

the angle brackets $\langle \dots \rangle$, show the average over initial states, N is the number of nuclei, t is time. The scattering function depends upon the energy and momentum transferred from neutron to sample, and not on absolute values of \mathbf{k}_i and \mathbf{k}_f . It contains information on both the positions and motions of the atoms in the sample. Most of the neutron scattering experiments measure $S(\mathbf{Q}, \omega)$ and thereby determine the microscopic properties of the system under investigation. $\mathbf{Q} = \mathbf{k}_f - \mathbf{k}_i$, \mathbf{Q} is the scattering vector and \mathbf{k}_i & \mathbf{k}_f are initial and final direction of wave vector respectively. \mathbf{r}_l , the coordinates of the scattering centers [160][162].

If v is the velocity of incoming neutron, in case of elastic scattering, then no. of neutron passing through area ds per second is

$$vdS|\psi_{sc}|^2 = vdS \frac{b^2}{r^2} = vb^2 d\Omega \quad (2.17)$$

Where ψ_{sc} is the wave function of scattering wave at point r in Figure 2.11, given by $\psi_{sc} = -\frac{b}{r} \exp(ikr)$

Flux of incident neutron is given by

$$\Phi = v|\psi_{inc}|^2 = v \quad (2.18)$$

Where ψ_{inc} is the incident neutron wave function given by $\psi_{inc} = \exp(ikz)$.

Therefore, cross-section is given by

$$\frac{d\sigma}{d\Omega} = \frac{vb^2 d\Omega}{\Omega d\Omega} = b^2 \quad (2.19)$$

The total scattering cross-section is given by

$$\sigma_{tot} = 4\pi b^2 \quad (2.20)$$

Scattering length depends on the spin state of nucleus. Therefore, for nucleus with spin I , spin of nucleus neutron system would be either $I+1/2$ or $I-1/2$, thus, resulting the value of scattering length as b^+ or b^- respectively.

On considering the coherent scattering of atoms in a monoatomic sample which contains isotopic nuclei with different scattering length. If the i^{th} distinct nuclear spin state or isotope has scattering length b_i , then average scattering length is

$$\bar{b} = \frac{1}{N} \sum_{i=1}^N b_i \quad (2.21)$$

Therefore, the average coherent cross section per atom is

$$\sigma_{coh} = 4\pi(\bar{b})^2 \quad (2.22)$$

2.2.3.2 Elastic nuclear scattering

For elastic coherent nuclear scattering, the time average of the density operator is considered which is given by (2.23) for infinite Bravais lattice:

$$S(\mathbf{Q}, \omega) = \delta(\hbar\omega) \frac{(2\pi)^3}{v_0} \sum_{\mathbf{G}} \delta(\mathbf{Q} - \mathbf{G}) \quad (2.23)$$

Where v_0 is the unit cell volume and the vector \mathbf{G} are reciprocal –lattice vectors. The coherent, elastic cross section is then

$$\left. \frac{d\sigma}{d\Omega} \right|_{coh}^{el} = N \frac{(2\pi)^3}{v_0} (\bar{b})^2 \sum_{\mathbf{G}} \delta(\mathbf{Q} - \mathbf{G}) \quad (2.24)$$

Equation (2.24) shows the scattering from a perfectly rigid lattice. Now, if a lattice that has more than one atom per unit cell is considered [163]. Then, in the atom, if the j^{th} atom occupies the position \mathbf{d}_j within the unit cell, then equation (2.24) is generalized to

$$\left. \frac{d\sigma}{d\Omega} \right|_{coh}^{el} = N \frac{(2\pi)^3}{v_0} (\bar{b})^2 \sum_G \delta(\mathbf{Q} - \mathbf{G}) |F_N(\mathbf{G})|^2 \quad (2.25)$$

Where,

$$F_N(\mathbf{G}) = \sum_j \bar{b}_j e^{i\mathbf{G} \cdot \mathbf{d}_j} e^{-W_j} \quad (2.26)$$

The static nuclear structure factor $F_N(\mathbf{G}) = F_N(hkl)$ and it contains information on the atomic positions \mathbf{d}_j within a unit cell and the mean square displacements $\langle u_{jx}^2 \rangle$. In crystallography, for a large number of reflections, structure factors are measured and then fitted to a model for the atomic parameters to get the results. From a scan through a Bragg peak, the square of the nuclear structure factor can be obtained. W is Debye-Waller factor, obtained by averaging phase factor $\exp(-i\mathbf{Q} \cdot \mathbf{r})$, resulting an extra factor in equation 2.25 equal to $\exp(-2W)$.

In the case of polycrystalline sample (which have randomly oriented grains), there is no orientation of the sample. A Bragg peak is measured either by rotating the detector or from a fixed array of detectors that cover large 2θ range. Therefore, the formula for integrate intensity becomes

$$I = A \frac{m_{hkl} \lambda^3 |F_N|^2}{v_0^2 \sin\theta \sin 2\theta} \quad (2.27)$$

Where m_{hkl} is the multiplicity of the reflection (hkl) [160]. The multiplicity is the number of equivalent permutations of the indices hkl . For example, the multiplicity of (100) reflections from a cubic crystal is 6. As in the cubic crystal, (100) , $(\bar{1}00)$, (010) , $(0\bar{1}0)$, (001) and $(00\bar{1})$ are equivalent reflections and all deflect along same 2θ direction which adds up 6 times to the intensity of (100) .

2.2.3.3 Magnetic structure determination from neutron scattering

In an atom, neutrons scatter from the magnetization density which comes from the contribution due to orbital angular momentum and spin angular momentum. Magnetic scattering can be obtained by considering neutron spin state. It depends on the initial and final neutron spin states \mathbf{S}_i and \mathbf{S}_f , corresponding to initial and final wave vector with $\mathbf{S} = \sigma/2$. If we have spin-only moment, then

$$M(\mathbf{Q})/\mu_B = g\mathbf{S}f(\mathbf{Q}) \quad (2.28)$$

With $g=2$. Let $\phi(r)$ is the radial wave function which corresponds to the unpaired spin, then

$$f(\mathbf{Q}) = \int_0^\infty dr r^2 j_0(\mathbf{Q}_r) |\phi(r)|^2 \equiv \langle j_0 \rangle \quad (2.29)$$

Where $j_0(\mathbf{Q}_r)$ is a spherical Bessel function of order 0 with ignoring aspherical effects. If the orbital moment can also be included in equation (2.28) in a simple form, with the condition that \mathbf{Q} is much smaller than the inverse of the mean radius of wave function for the unpaired electrons [164]. Then equation (2.28) becomes

$$M(\mathbf{Q})/\mu_B = 2\langle j_0 \rangle \mathbf{S} + (\langle j_0 \rangle + \langle j_2 \rangle) \mathbf{L} \quad (2.30)$$

Where \mathbf{L} is the angular moment vector.

For some transition-metal ions which exhibit small orbital moments, the Landé splitting factor g differs slightly from its spin-only value of 2. In such a case the form factor as in equation (2.29) is given by

$$f(\mathbf{Q}) = \langle j_0 \rangle + \left(\frac{g-2}{2}\right) \langle j_2 \rangle \quad (2.31)$$

In the case of rare-earth ions, the orbital moment is generally unquenched. Therefore, we can consider angular moment \mathbf{J} resulting from \mathbf{S} and \mathbf{L} . Within the given states of \mathbf{J} , we have

$$2\mathbf{S} = g_s \mathbf{J} \quad (2.32)$$

$$\mathbf{L} = g_L \mathbf{J} \quad (2.33)$$

$$\mathbf{L} + 2\mathbf{S} = g\mathbf{J} \quad (2.34)$$

Where

$$g_s = \frac{J(J+1) - L(L+1) + S(S+1)}{2J(J+1)} \quad (2.35)$$

$$g_L = \frac{J(J+1) + L(L+1) - S(S+1)}{2J(J+1)} \quad (2.36)$$

And $g = g_s + g_L$. Thus in the scattering formula as given in equation (2.31) we can replace $g\mathbf{S}$ with $g\mathbf{J}$ and the form factor is given by

$$f(\mathbf{Q}) = \langle j_0 \rangle + \frac{g_L}{g} \langle j_2 \rangle \quad (2.37)$$

The coherent elastic differential cross section for magnetic scattering from a magnetically ordered crystal is therefore modified from equation (2.24) and is further given as [164]

$$\left. \frac{d\sigma}{d\Omega_f} \right|_{coh}^{el} = N_M \frac{(2\pi)^3}{v_M} \sum_{\mathbf{G}_M} \delta(\mathbf{Q} - \mathbf{G}_M) |F_M(\mathbf{G}_M)|^2 \quad (2.38)$$

Where F_M , the static magnetic structure factor is given by

$$F_M(\mathbf{G}_M) = \sum_j p_j \mathbf{S}_\perp e^{i\mathbf{G}_M \cdot \mathbf{d}_j} e^{W_j} \quad (2.39)$$

The subscript M indicate that N_M and v_M refer to the number of the magnetic unit cell and the volume of such cells in the sample respectively; the sum in equation (2.39) is over all the sites within the magnetic unit cell. The magnetic unit cell is typically larger than the chemical unit cell except the case of ferromagnetic ordering. This leads to a new reciprocal –lattice vector

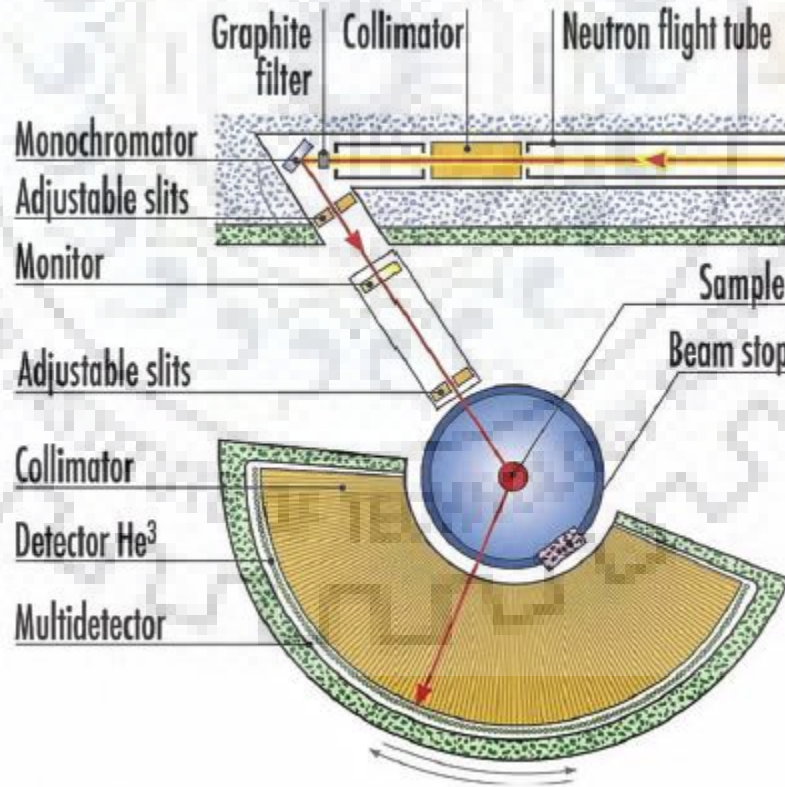


Figure 2.12 Instrument layout of a typical modern neutron powder diffractometer D2B at ILL [165]

\mathbf{G}_M . The relation between the integrated intensity of a magnetic Bragg peak and $|\mathbf{F}_M(hkl)|$ is same as that for nuclear scattering i.e. by substituting $|\mathbf{F}_M|$ for F_N in equation (2.27). The quantity \mathbf{S}_\perp is the magnetic interaction vector given by,

$$\begin{aligned}\mathbf{S}_\perp &= \hat{\mathbf{Q}} \times (\mathbf{S} \times \hat{\mathbf{Q}}) \\ &= \mathbf{S} - \hat{\mathbf{Q}}(\hat{\mathbf{Q}} \cdot \mathbf{S})\end{aligned}\quad (2.40)$$

Where $\hat{\mathbf{Q}}$ is unit vector along \mathbf{Q} . Only the component of \mathbf{S} perpendicular to \mathbf{Q} contributes to the scattering amplitude[160].

2.2.3.4 Elastic neutron powder diffractometer

All the neutron powder diffraction (NPD) measurements presented in this thesis were carried out with the high resolution neutron powder diffractometer D2B located at Institute Laue-Langevin (ILL), Grenoble and G4.1 located at Laboratoire Léon Brillouin (LLB), Saclay and Powder diffractometer – I & Powder diffractometer-II at BARC Mumbai.

The diffractometer D2B as shown in Figure 2.12 is equipped with monochromator consisting of 28 Ge [551] crystals of $1 \times 5 \times 1 \text{ cm}^3$. The orientation (551) was used to obtain neutrons of wavelength 1.464 \AA and the take-off angle for the monochromator is very high i.e.

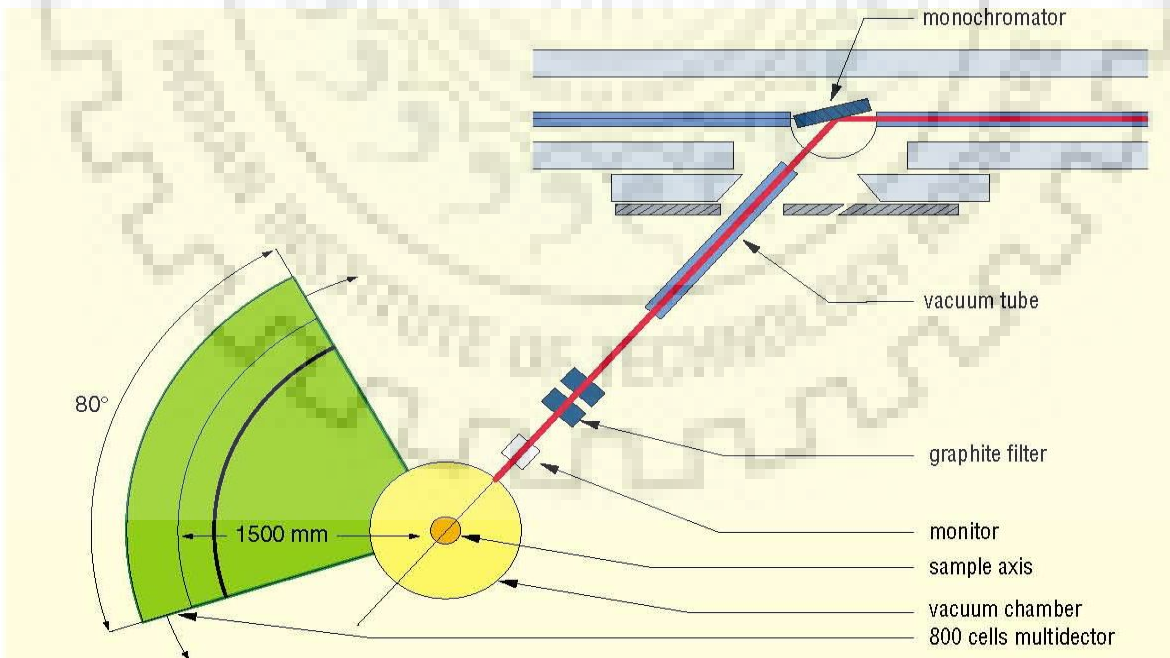


Figure 2.13 Layout of the cold neutron two axis diffractometer G4.1 at LLB [166]

135°. The detector array consists of 128 ^3He position sensitive detectors which are spaced equally at 1.25° intervals with fixed collimators of 20' horizontal divergence located in front of each detector. As each detector covers 1.25° the data collection is performed via step wise positioning of the detector array to obtain a diffraction pattern of desired step-width $\Delta(2\theta)$. For example, a typical step-width of $\Delta(2\theta) = 0.05^\circ$ requires the number of steps $N=1.25^\circ/\Delta(2\theta) = 25$. Finally, one dimensional diffraction patterns suitable for Rietveld-refinement programs, which was treated later by using program *FullProf* to determine the nuclear and magnetic structures of the sample under study[165].

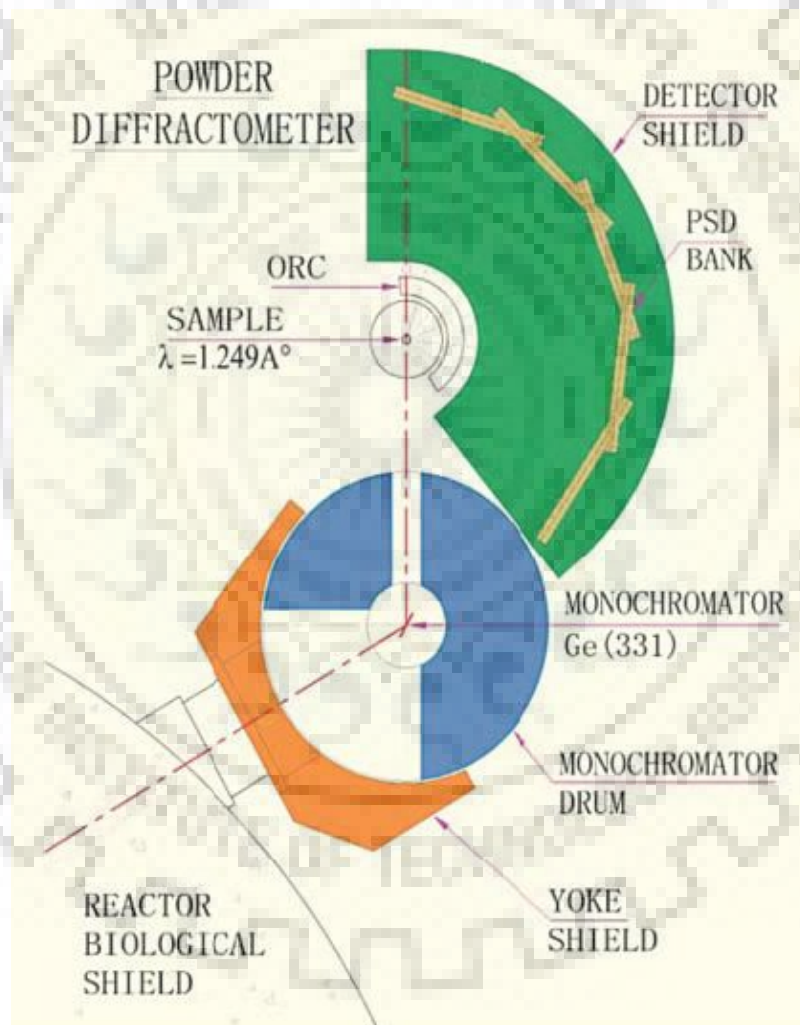


Figure 2.14 Layout of the powder diffractometer II (PD-II) at Dhruva reactor at BARC [167]

The two axis diffractometer G4.1 shown in Figure 2.12 is equipped with pyrolytic graphite (002) monochromator which is vertical focusing. There are 800 multi-detector present which cover the angular range of 80° with step size of 0.1°. in this diffractometer most commonly used wavelength is 2.43Å [166].

Powder diffractometer-II at Dhruva reactor shown in Figure 2.13 is multiple position sensitive detector (PSD) having 5 PSDs covering Q -range upto 9.4 Å and scattering angle range 4° to 140°. Wavelength used in this detector is 1.249 Å and monochromator is Ge (331) [167].

2.2.4 Rietveld analysis

The Rietveld analysis[168], [169] is a refinement method to study the nuclear and magnetic structures of powder diffraction pattern. In this analysis, lattice parameters and atomic positions of atoms in unit cell is determined using the information of the crystal symmetry. Further, from magnetic point of view, magnetic representation for magnetic ion is determined using propagation vectors which leads to the simulation and fitting of the complete diffraction pattern. There are nine parameters for the experimental equipment: the wavelength, the scale factor, the zero point for 2θ and six parameters for a polynomial background, only if we choose this option or else we can manually choose the background points and refine them.

For the typical $RFe_{1-x}Mn_xO_3$ (ABO_3) type perovskite structure, most of the parameters have to be refined. The gradient for the weighted sum of squared difference between the calculated intensities and the measured intensities, R_p , can be determined relative to these parameters. The gradient is then used to change the parameters and this is repeated until a minimum in the R_p function is reached. The definition of R_p and the profile factors have taken from FULLPROF manual.

Intensity profile factor R_p is defined as

$$R_p = 100 \frac{\sum_{i=1,n} |y_i - y_{c,i}|}{\sum_{i=1,n} y_i} \quad (2.41)$$

Where y_i is the observed intensity at angular step i , $y_{c,i}$ is the corresponding calculated intensity. To control the quality of the refinement, several agreement factors were calculated. The weighted profile factor R_{wp} is the square root of the quantity minimized and is given by

$$R_{wp} = 100 \left[\frac{\sum_{i=1,n} w_i |y_i - y_{c,i}|^2}{\sum_{i=1,n} w_i y_i^2} \right]^{1/2} \quad (2.42)$$

This parameter reflects the progress of the refinement in the most meaningful manner.

And the expectation profile factor,

$$R_{exp} = 100 \left[\frac{n-p}{\sum_i w_i y_i^2} \right]^{1/2} \quad (2.43)$$

The Bragg R - factor,

$$R_B = 100 \frac{\sum_h |I_{obs,h} - I_{cal,h}|}{\sum_h |I_{obs,h}|} \quad (2.44)$$

And crystallographic R_F – factor

$$R_F = 100 \frac{\sum_h |F_{obs,h} - F_{cal,h}|}{\sum_h |F_{obs,h}|} \quad (2.45)$$

The goodness of fit,

$$\chi^2 = \left[\frac{R_{wp}}{R_{exp}} \right]^2 \quad (2.46)$$

Here, I_{obs} and I_{cal} are the observed and calculated integrated intensities for the different Bragg peaks j and $(n - p)$ is the number of degrees of freedom. n is the number of points in the pattern observed and p is the number of refined parameters, $w_i = \frac{1}{\sigma_i^2}$, where σ_i^2 is the variance of the “observation” of y_i . $F_{obs,h}$ and $F_{cal,h}$ are observed and calculated structure factor.

The refinement of the XRD and neutron data of the samples in the present work are carried out using the FULLPROF program. The order of the refining the parameters was: the scale factor, the zero point for 2θ , background points, the cell parameters, three of the peak shape parameters, the isotropic displacement parameters, the occupation numbers, the fourth peak shape parameter, the anisotropic displacement parameters and the background parameters. A few different routes to convergence were tried to confirm the optimal result. The R factors are good indicator if a route is not converging to a reliable result. In present work, anisotropic displacement parameters at the Fe/Mn-O sites led to better refinements.

2.2.5 Superconducting Quantum Interference Device Magnetometer

A superconducting quantum interference device (SQUID) magnetometer is based on the principle of Josephson effect proposed by the great scientist B. D. Josephson in 1962 [170][171][172]. He observed that a superconducting current could flow when two superconductors (e.g Niobium) are separated by a very small insulating gap (e.g. aluminum oxide) named as Josephson junction. When the junction is cooled down to a very low temperature (less than 4.2K), the superconductor current would flow with zero volts across the junction. The magnitude of this current (I_C) flowing through the Josephson junction is a periodic function of the magnetic flux present in the vicinity of the junction. The relation between the current I_C as a function of flux is given by the equation:

$$I_C(\phi) \propto I_C(0) \left| \cos \frac{\pi\phi}{\phi_0} \right| \quad (2.47)$$

Here ϕ_0 is one flux quantum ($2 \times 10^{-15} \text{ Tm}^2$). The maximum value of the current therefore occurs for $\phi = n\phi_0$ ($n = 0, \pm 1, \pm 2, \dots$), while minimum value occurs for $\phi = \left(n + \frac{1}{2}\right) \phi_0$. The phenomenon is called as DC Josephson effect which forms the basis for the working of a SQUID magnetometer.

In MPMS magnetometer rf-biased SQUID has been used that has a maximum slewing rate of 250 flux quanta/sec and therefore it is capable to detecting changes of order 10^{-4} of flux quantum. The sensitivity of SQUID magnetometer can be measured by considering N no. of aligned spins.

$$N = \frac{l}{\mu_0 \mu_B} \cdot (\phi_0/2) \quad (2.48)$$

Where l is the length of sample, thus giving 2×10^{11} detectable spins for a sample of length 2 mm, corresponding to magnetic moment of $2 \times 10^{-9} \text{ emu}$ [173]. In rf SQUID, only one Josephson junction is utilized which is coupled with a flux into a SQUID loop. This coupling occurs via an input coil which connects SQUID to experiment and “rf” coil, which is a part of high Q resonant circuit, to read the current changes in SQUID loop [170].

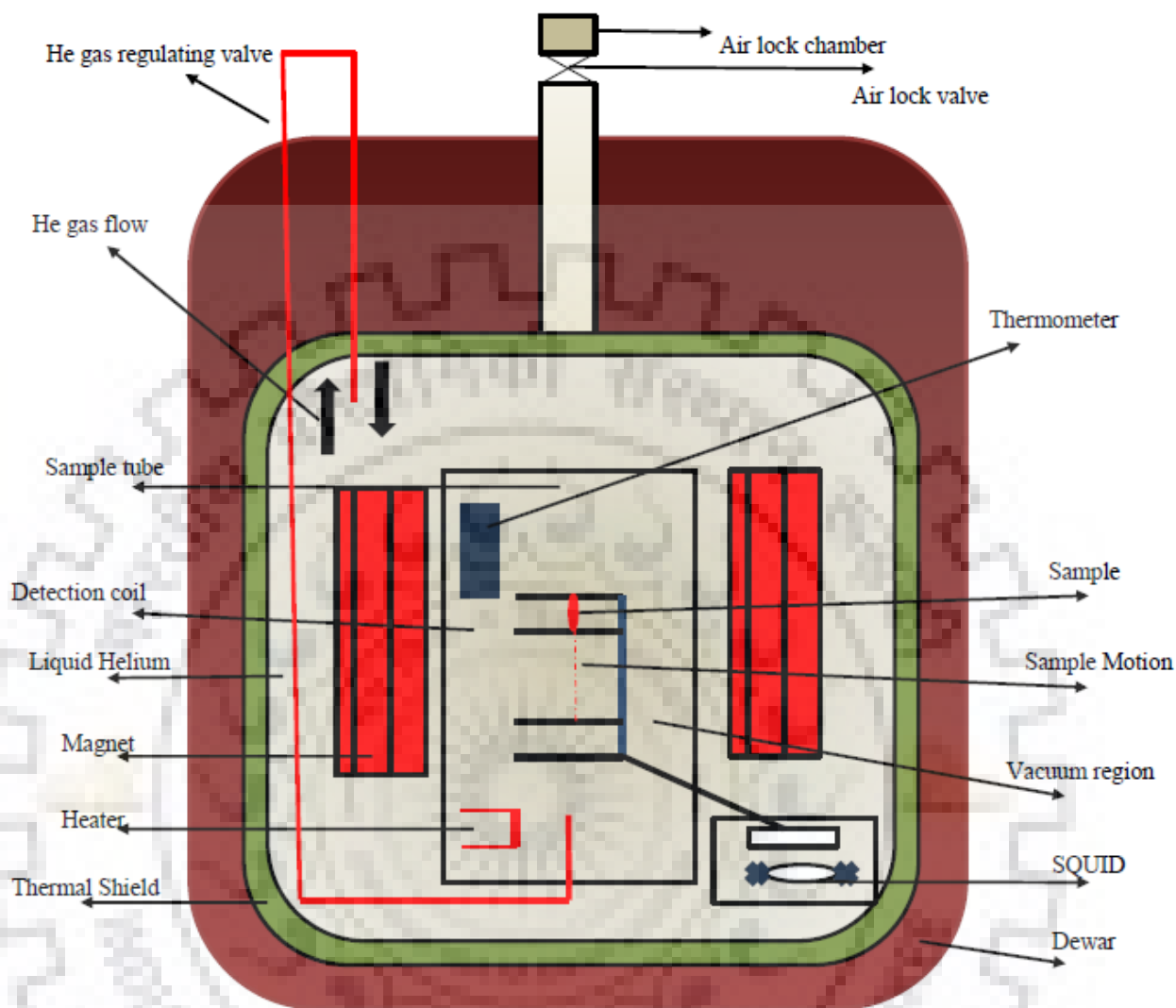


Figure 2.15 Schematic of the MPMS magnetometer

In the present study, magnetic properties of all the samples (nanoparticles and thin films) were measured using SQUID magnetometer (MPMS XL Evercool, Quantum Design). The major components of the measurement system are as following:

1. *Temperature Control System*: The temperature is controlled precisely by the controlled flow of heat into the sample space and active control of gas flow to provide cooling power. The system can be used to operate in a temperature range of 2 K to 400 K.
2. *Magnetic Control System*: A power supply is used to provide current to set magnetic field in the superconducting magnet. The magnetic field can be set from -7 Tesla to +7 Tesla.

3. *Superconducting SQUID amplifier system*: the rf SQUID detector system is the heart of this measurement system. It provides reset circuitry, auto-ranging capability, EMI protection and a highly balanced second-derivative detection coil array.
4. *Sample handling system*: It is very important to step in and scan the sample inside the detection coils without transmitting any mechanical vibrations. This system allows for varied scan lengths and options for acquiring the data for a particular measurement.
5. *Computer operating system*: the operating features of MPMS are very user friendly and the measurements are performed by making sequence of commands depending on the type of measurement required.

The schematic for the magnetometer used in the present work is shown in Figure 2.15[170]. The MPMS system consists of a superconducting magnet to generate magnetic fields, a superconducting detection coil which inductively couples with the sample, a rf SQUID amplifier connected to the detection coil and superconducting magnetic shield surrounding the SQUID. A SQUID is the most sensitive device to measure the magnetic field, however, it doesn't directly measure the magnetic field from the sample. The sample is moved through a pair of superconducting detection coil which are connected to the SQUID sensor using superconducting wires. These wires allow the current from the detection coils to be inductively coupled to the SQUID sensor. The electronic circuitry used in the SQUID produces an output voltage proportional to the current flowing in the input coil of SQUID. The SQUID therefore works as current-to-voltage converter, situated approximately 11 cm below the magnet, inside a superconducting shield[170]. The measurement is performed by moving the sample between the detection coils situated outside the sample chamber and at the center of the magnet. The movement of the sample between the detection coils induces a magnetic moment in the sample, the change in its magnetic moment produces an electric current in the detection coils. Since the detection coils, the connecting wires and the input coils of the SQUID sensor makes a close superconducting loop, any change of the magnetic flux in the detection coils produces a proportional current in the detection circuit. The variation of the current in the detection coils is then converted to a voltage signal by the SQUID and this output voltage of SQUID is proportional to the magnetic moment of the sample. In a well calibrated system, these voltage variations in the SQUID detector gives highly accurate values of the sample's magnetic moment.

Superconducting detection coil: The detection coil is second order gradiometer made by winding a single superconducting wire into a set of three coils configuration as shown in Figure 2.16. In this configuration, the upper and lower coils are single turns of the wire which are wound clockwise while the middle coil comprises of two turns wound anticlockwise[170]. The coils are placed inside the superconducting magnet and outside the sample chamber. This configuration minimizes the noise in the detection circuit which is caused by the fluctuations in the large magnetic field created by the superconducting magnet. In an ideal case, when the background magnetic field is changing uniformly, the change in the magnetic flux of the

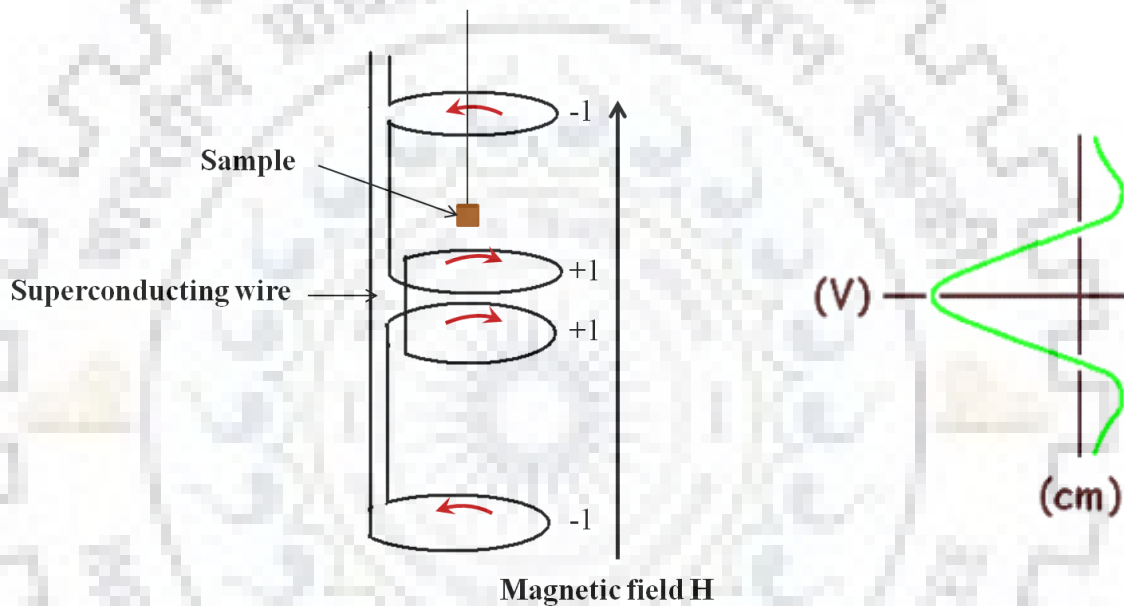


Figure 2.16 Schematic for the detection coils wound in a second-order gradiometer configuration middle two-turn counter-wound coil is exactly cancelled by the change in the magnetic flux of the upper and lower single turn coils. However, the magnetic moment of the sample can still be measured because the two-turn counter-wound coil measured the local changes in the magnetic flux density produced by the dipole field of the sample.

Superconducting magnet: The superconducting magnet is wound in the form of a solenoid and forms a closed loop. The magnet can be charged up to a specific current operating in a persistent mode during a measurement without using any external power supply or current. To change the current flowing into the magnet, the superconducting loop must be opened up electrically; this is done by wrapping a small segment (switch) of the magnet's superconducting wire with a heater. The small segment of the wire can then be set into a normal

(non-superconducting) state by heating, thus making the loop electrically open. By attaching a power supply to the heater, the current in the magnet can now be changed to the desired value thus changing the magnetic field of the magnet. The heater can be now switched off by disconnecting the power supply. The current set in the superconducting wire thus continues to flow, as the wire attains its superconducting state again, sustaining the desired value of the magnetic field. The condition of magnet state is called persistent mode[170].

Sample space: The sample space is made up of a tube with inner diameter of 9 mm, maintained at low pressure by static helium gas. This is an airlock valve at the top of the sample space that can be evacuated and purged using the clean helium gas. An airlock valve situated in between the airlock and the sample space, when opened, makes the airlock and sample space a continuous part. A high thermal uniformity is provided by lining the lower portion of the sample space (about 30 cm) with copper. Two thermometers are used to provide and control the sample temperature[170].

Procedure for measurement: The samples were mounted in a straw and then attached to a sample rod which is around 1 m in length. The sample rod is then inserted into the sample chamber through a double seal, which allows the sample rod to be actuated with a stepper motor controlled drive mechanism. This drive enables the sample to be passed through the detection coils in discrete steps. The change in the sample's position causes a corresponding change in the magnetic flux through the detection coils, thus changing the magnitude of current in the superconducting circuit. The sample is stopped at discrete steps through the detection coils and at each step several reading of the SQUID voltage were recorded and averaged to minimize the signal-to-noise ratio. The dimension of the sample matters a lot for getting good data. Too large length of the sample as compared to the scan length will not bring any observable change in the SQUID voltage. The sensitivity of MPMS XL is around 10^{-8} emu to 2 emu with standard configuration which can be extended to 300 emu with extended range option.

2.2.6 Specific Heat

The specific heat measurements are carried out by Physical Property Measurement System (PPMS). This *Quantum Design* Heat Capacity option measures the heat capacity at constant pressure[58].

$$C_P = \left(\frac{dQ}{dT}\right)_P \quad (2.49)$$

During a measurement, a known amount of heat is applied at constant power for a fixed time, and then this heating period is followed by a cooling period of the same duration. A heater and thermometer are attached to the bottom side of the sample platform as shown in Figure 2.17. Small wires provide the electrical connection to the heater and thermometer. They also provide the thermal connection and structural support for the platform. The sample is mounted on the platform by using a thin layer of grease (Apiezon N or H Grease), which provides the required thermal contact to the platform. The turbo pump or cryopump provides sufficient high-vacuum, so that the thermal conductance between the sample platform and the thermal bath (puck) is totally dominated by the conductance of the wires. This gives a

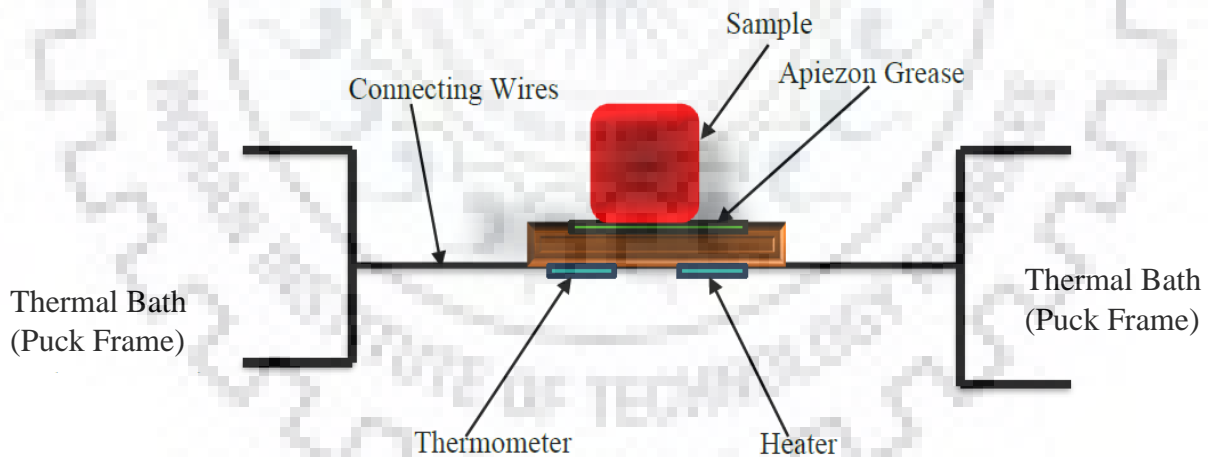


Figure 2.17 Schematic of thermal connections to sample and sample platform in PPMS

reproducible heat link to the bath with a corresponding time-constant large enough to allow both the platform and sample to achieve sufficient thermal equilibrium during the measurement.

The basic puck configuration can accommodate samples weighing approximately 1 to 200mg. Given the thermal characteristics of the calorimeter, this range of masses produces, for most solids varying relaxation time-constants that may be a fraction of second at 1.9K or many minutes at 300K. A single heat capacity measurement can require nearly 10 time-constants for the settling time that occurs between measurements.

To measure the heat capacity in the sample, different measurement techniques are optimized according to sample size as well as accuracy. In the quantum design heat capacity option, relaxation technique is used. In this technique, after each measurement cycle (heating period followed by cooling period), the entire temperature response of the sample platform is fitted to a model which accounts for both thermal relaxation of sample platform to the bath temperature and relaxation between sample platform and sample[58].

The wires that connect the sample platform with the puck frame create well-controlled thermal links to thermal bath. To avoid any other thermal links with residual gases, high vacuum must be created within the probe. For this purpose, a charcoal holder is used to decrease the pressure at the bottom of probe below 10 K temperature. With the activation of H-Vacuum option, the base pressure is approximately 0.01 mTorr at the top of probe.

Synthesis and characterization of $\text{NdFe}_{0.5}\text{Mn}_{0.5}\text{O}_3$

3.1 Introduction

Ferromagnetic materials have been utilized extensively for practical applications starting from 200 BC as compass till recently as information storage and read/write devices[170][171]. Such versatile applications of ferromagnetic materials have been feasible by virtue of easy manipulation of magnetization utilizing moderate magnetic fields. On the other hand, antiferromagnetic ordering is difficult to control through an external magnetic field and found limited applications as a pinning layer for adjacent ferromagnetic layer in read heads of storage devices[176]. Rapid generation of digital data requires enhancement of the data storage density and speed of the data transfer. The latter is specifically limited by the time scale of magnetization manipulation (~ 10 ns) due to slow decay and rise time of magnetic fields in present data storage devices. Novel methods to manipulate magnetic order using ultrashort (\sim picoseconds) pulses of coherent electromagnetic radiation have unwrapped the possibilities for development of faster storage devices having manipulation time at (sub)picosecond scale [177].

Rare-earth orthoferrites $R\text{FeO}_3$ are potential candidates for multiferroic materials with large magneto-electric (ME) coupling[178] and have demonstrated ultrafast optical control of spins[177]. Lot of research has been done on magneto coupling to explore the mutual control of electric and magnetic degrees of freedom[124][175]. Rare-earth (RE) orthoferrites, from a family of strongly correlated materials, exhibit two orders of magnitude faster spin dynamics in comparison to conventional ferromagnetic material[176][177]. Structurally, most $R\text{FeO}_3$ crystallize in distorted orthorhombic perovskite structure in the space group $Pbnm$ [44].

Most of the RE orthoferrites ($R\text{FeO}_3$) are G -type canted antiferromagnets with a weak ferromagnetic component due to Dzyaloshinskii-Moriya (DM) interaction and show temperature-induced spin reorientation from one magnetic symmetry to another. Exchange

interactions between $\text{Fe}^{3+}\text{-Fe}^{3+}$, $R^{3+}\text{-Fe}^{3+}$, and $R^{3+}\text{-}R^{3+}$ play an important role to determine the complex magnetic properties (e.g., magnetic structure and spin reorientation) of $R\text{FeO}_3$. Isotropic $\text{Fe}^{3+}\text{-Fe}^{3+}$ exchange interaction dictates the magnetic structure of Fe^{3+} spins below ordering temperature (T_N). With a large T_N anywhere between 650 and 750 K, the Fe^{3+} magnetic moments order in the Γ_4 (G_x, F_z) structure. Exchange field due to Fe^{3+} moment on R sublattice polarizes the R^{3+} spins. Further, comparatively weaker anisotropic exchange interaction between R^{3+} and Fe^{3+} generate effective fields on Fe^{3+} spins, which in turn start to rotate and try to align perpendicular to R^{3+} spins. This transition might be continuous/abrupt depending upon the RE element[48]. For most R , this is of the form $\Gamma_4 \rightarrow \Gamma_2$ (F_x, G_z), with exception of $R = \text{Dy}$ in which spins undergo a $\Gamma_4 \rightarrow \Gamma_1$ (G_y) transition [51]. The $\Gamma_4 \rightarrow \Gamma_2$ transitions are gradual, covering a wide temperature range of nearly 50 K. In NdFeO_3 , which can be considered as canonical orthoferrite, shows a gradual spin reorientation in the range 150-100 K. The reason behind the reorientation is attributed to magnetic presence of $\text{Nd}^{3+}\text{-Fe}^{3+}$ isotropic and anisotropic exchange interactions which compete with the Fe-Fe interaction over the entire temperature range [101][178]. Therefore, orthoferrites have been investigated in detail for ultrafast manipulation of spins which is induced thermally through spin reorientation transitions which arises due to $R^{3+}\text{-Fe}^{3+}$ interactions[181].

Studies have shown that substitution at the Fe-site with another transition metal, the fundamental ordering remains G -type for a large value of dopant. However, the substitution results in a series of newer properties. For example, Ni doped LaFeO_3 [183] or Ni doped PrFeO_3 [184] shows semiconducting ferromagnetic behavior while Ni doped NdFeO_3 show mixture of ferromagnetic and antiferromagnetic behavior[185]. In the case of $\text{NdCr}_{1-x}\text{Fe}_x\text{O}_3$, where Fe is doped on the Cr site, magnetic reversal is observed where FC magnetization crossover ZFC magnetization passing through magnetic compensation ($M=0$) point. The possible for this magnetic reversibility is due to competition between weak ferromagnetic component of canted Cr^{3+} ions and paramagnetic moments of Nd^{3+} and Fe^{3+} ions under the influence of negative internal magnetic field due to AFM ordering of Cr^{3+} ions. [186]. A well-studied system is $\text{NdFe}_{1-x}\text{Mn}_x\text{O}_3$. Substitution of Mn drastically reduces the Néel temperature [15]. Due to static long ranged Jahn Teller distortion in the parent manganite NdMnO_3 [17], there occurs local dynamic Jahn-Teller effects due to unequal Mn-O bond lengths coexisting with nearly equal Fe-O bond lengths[130]. In NdMnO_3 , Mn^{3+} spins order as A -type below 80

K [104] but even with a very small doping of Fe on Mn site i.e.in $\text{NdFe}_{1-x}\text{Mn}_x\text{O}_3$ ($x=0.8$), the magnetic ordering is found to be *G*-type. [188]

In the present work, we have studied the effect of 50% Mn substitution at Fe sites on the magnetic structure and spin reorientation of $\text{NdFe}_{0.5}\text{Mn}_{0.5}\text{O}_3$ (NFMO). We have used various experimental techniques, viz. X-Ray diffraction, magnetization, neutron diffraction, Mössbauer Spectroscopy to establish the complex magnetic structure of NFMO.

3.2 Experimental details

The polycrystalline NFMO has been synthesized by conventional solid state reaction method using stoichiometric proportions of highly pure (99.999%) Nd_2O_3 , Fe_2O_3 and MnO_2 powders as starting materials. The powders were taken according to the following chemical reactions:



Mixture of raw powders was ground for 10-12 hours in an agate pestle mortar and then calcined for 24 hours at 1100°C and further sintered at 1200°C, 1300°C and 1400°C for 24 hours with intermediate grinding. The structural phase of the sample was identified using a Bruker D8 two-circle X-ray diffractometer at $\text{CuK}\alpha$ wavelength. Average magnetization measurements were performed using a vibrating sample magnetometer (VSM) module of the Quantum Design make Physical Property Measurement System (QD-PPMS) Evercool – II. Further magnetic measurements were repeated using Quantum Interference Device (SQUID) of Quantum Design Magnetic Property Measurement System (MPMS) to confirm the results obtained from VSM. Zero-field cooled (ZFC) and field cooled (FC) measurements from 350 K to 4 K in 0.01T magnetic field were carried out to identify the different magnetic transitions and their respective temperatures. Field variations of magnetization was carried out at various temperatures between 300 K and 5 K. Neutron diffraction studied in absence of magnetic field were carried out at various temperatures in the range 1.5-400 K to identify the crystal as well as magnetic structures and their variations as a function of temperature. The diffraction data were analyzed using FULLPROF [169] suite of programs employing the Rietveld method. Magnetic ordering of Fe^{3+} present in sample is studied using the ^{57}Fe Mössbauer spectroscopy technique

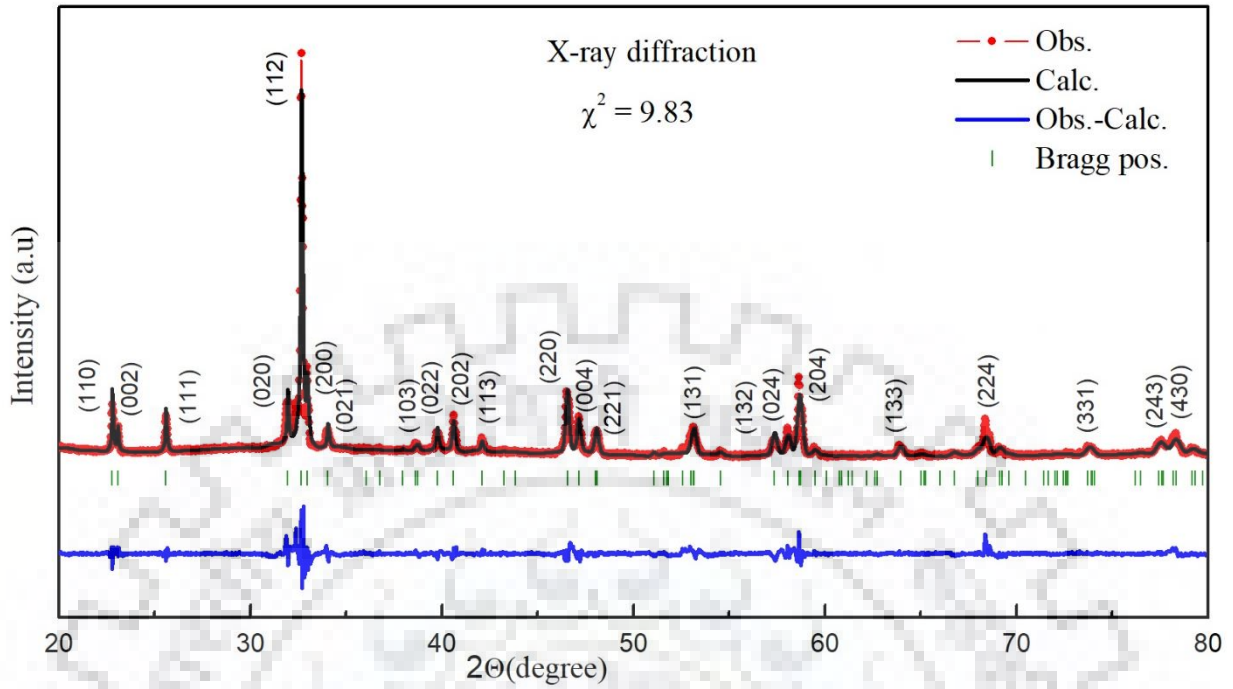


Figure 3.1 Observed X-ray diffraction pattern of NFMO at room temperature, refined using orthorhombic $Pbnm$ space group

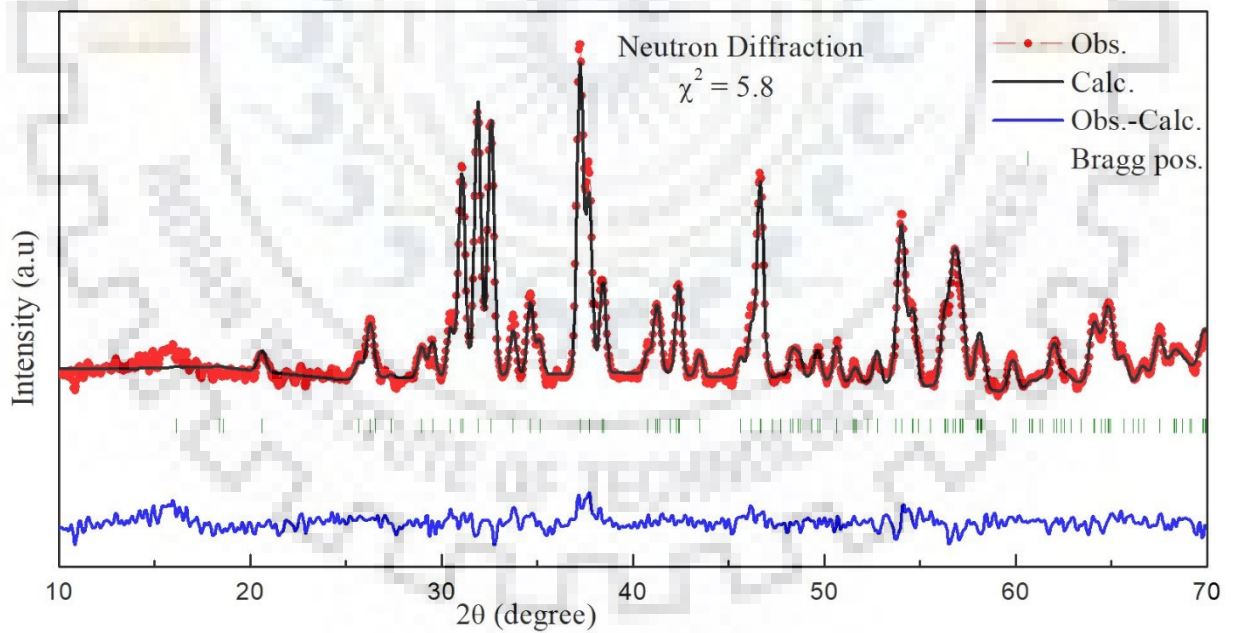


Figure 3.2. Observed and refined neutron diffraction patterns of NFMO at room temperature confirm formation of the orthorhombic structure with $Pbnm$ space group. The measurement was performed at PD-II using a neutron wavelength of 1.2443 \AA

3.3 Results and Discussion

3.3.1 Structural Characterization

Figure 3.1 shows the room-temperature X-ray diffraction pattern of the NFMO powder sample. Orthorhombic structure of the sample, as reported for the end members NdFeO_3 [100] and NdMnO_3 , [185][186] has been considered for refinement shown in Figure 3.1. The preliminary analysis of the X-ray diffraction data confirms the phase formation and purity of the NFMO sample. The mixed doped NFMO compound can be considered as double perovskite $\text{Nd}_2\text{FeMnO}_6$ with *B*-site ordering of Mn and Fe ions. *B*-site ordering of the compound should mark the unique positions for transition metal ions which results in monoclinic structure. Random occupation of *B*-site by transition metal ions leads to the orthorhombic crystal structure. The diffraction pattern was refined to orthorhombic (*Pbnm*) as well as monoclinic (*P2₁/n*) space groups with comparable χ^2 values. Hence it is not possible to confirm the crystal structure using X-ray diffraction alone. However, our attempts to find traces of weak (021) Bragg peak, which should occur only in monoclinic structure, did not succeed

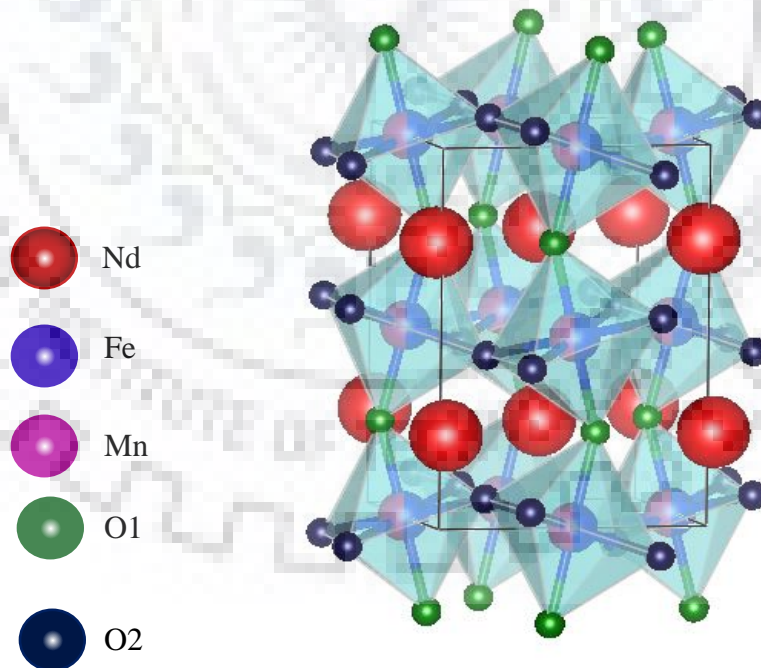


Figure 3.3 Crystal structure of $\text{NdFe}_{0.5}\text{Mn}_{0.5}\text{O}_3$ showing the atomic positions of Nd, Fe, Mn and O

because of similar scattering factors of Mn and Fe. Besides the observed magnetic behavior is

entirely different from that expected from a double perovskite compound which predominately show ferromagnetism, e.g. in R_2MnBO_6 ($R=$ La, Nd and $B=$ Ni, Co)[191]–[193]. This information indicates the possible phase formation of NFMO with the orthorhombic symmetry as shown in Figure 3.3. However, the structure could be confirmed using neutron diffraction measurements. Unlike X-ray diffraction, the scattering lengths of Mn (-3.73×10^{-15}) and Fe (9.94×10^{-15}) are different in case of neutron diffraction. This distinction helps to identify the B -site order/disorder. Figure 3.2 shows measured and refined neutron diffraction patterns of NFMO for 300K at PD-II using neutron wavelength of 1.2443 Å. The diffraction pattern was fitted to orthorhombic structure as shown in Figure 3.2, which shows good agreement with the experimental pattern. However, the monoclinic structure gives a much poorer quality of fitting. Thus it can be concluded that NFMO crystallizes in the orthorhombic space group and the Mn/Fe atoms are arranged in a random manner at the $4b$ Wyckoff positions.

Table 3.1 Structural parameters of $NdFe_{0.5}Mn_{0.5}O_3$ in comparison to $NdMnO_3$ and $NdFeO_3$

Compound	$NdFe_{0.5}Mn_{0.5}O_3$			$NdMnO_3$	$NdFeO_3$
	300 K	90 K	1.5 K	295 K	295 K
a (Å)	5.4341(5)	5.4199(2)	5.4195(2)	5.4170	5.4510
b (Å)	5.5972(6)	5.6062(3)	5.6061(3)	5.8317	5.5880
c (Å)	7.7041(9)	7.6795(4)	7.6778(2)	7.5546	7.7616
$Mn(Fe)-O(1)(m)$ (Å)	1.9897(8)	1.9843(9)	1.9834(9)	1.951	2.0012
$Mn(Fe)-O(2)(l)$ (Å)	2.0543(19)	2.0576(23)	2.0555(24)	2.218	2.0226
$Mn(Fe)-O(2)(s)$ (Å)	1.9659(20)	1.9648(22)	1.9670(26)	1.905	2.0072
$Mn(Fe)-Mn(Fe)(p)$ (Å)	3.8519(15)	3.8990(5)	3.8394(9)	3.9342	3.8810
$Mn(Fe)-Mn(Fe)(o)$ (Å)	3.9016(10)	3.8990(5)	3.8990(5)	3.7945	3.9031
	Present Study			[190]	[100]

In this section, we compare the structural parameters of NFMO (obtained from the present study) with those reported in literature for $NdFeO_3$ [100] and $NdMnO_3$ [190]. In table 3.1, the lattice constants along with $M-O$ ($M =$ Fe, Mn) bond lengths of $NdFe_{0.5}Mn_{0.5}O_3$ have been shown for 300, 90, and 1.5 K. We observe that the lattice parameters (a and c) of $NdFeO_3$ are larger than those of NFMO while b of $NdMnO_3$ is larger than that of NFMO. Thus the lattice

parameters of NFMFO are intermediate, though we find that the values of b and c are closer to that of NdFeO_3 ($\Delta a = -0.38\%$, $\Delta b = +0.17\%$, $\Delta c = -0.75\%$), while a is closer to that of parent manganite NdMnO_3 ($\Delta a = +0.24\%$, $\Delta b = -4\%$, $\Delta c = +1.93\%$). We note the large changes in b and c lattice parameters in comparison to NdMnO_3 . These values are also in good agreement with recent work done by Chakraborty *et. al.* on a series of $\text{NdFe}_{1-x}\text{Mn}_x\text{O}_3$ samples. In case of $\text{RMn}_x\text{Fe}_{1-x}\text{O}_3$ ($R = \text{RE element}$), it has been observed that the long-range cooperative (static) J-T distortion is effective for higher values of x (>0.8) and the structure is classified as O'-orthorhombic with $c/\sqrt{2} < a < b$ in this regime. Static J-T distortion disappears for $x \leq 0.8$ and structure changes into O-orthorhombic with $a < c/\sqrt{2} < b$. A weaker orbital ordering associated with dynamical J-T effect at Mn sites may still be present in the system down to $x \approx 0.5$ [107][188][189]. This inequality $a < c/\sqrt{2} < b$ is also observed in the case of NFMFO with a small difference between a and $c/\sqrt{2}$.

Three different M -O bond lengths have been listed in Table 3.1 Long (l) and short (s) bond lengths correspond to the M -O(2) bond in the ab plane. Medium (m) bond length corresponds to the out of plane M -O(1) apical bond which is almost parallel to the c axis. In NdFeO_3 , l , m and s are almost equal implying that the distortion of the octahedral is minimal. While in NdMnO_3 , the bond lengths are highly unequal due to the J-T distortion associated with orbital ordering in the ab plane. In NFMFO, it is expected that the Mn-O and Fe-O bond lengths should be unequal. However, only average bond lengths for the three M -O bonds are obtained experimentally. Comparing the M -O bond lengths of NFMFO with NdFeO_3 , a slight decrease in s and an increment in l , m is observed. Though the changes are minimal, it indicates the possibility of J-T distortion in the ab plane. The in-plane and out-of-plane distortions are characterized by the J-T parameters $Q_2 = 2(l - s)/\sqrt{2}$ and $Q_3 = 2(2m - l - s)/\sqrt{6}$ respectively[190]. Here, Q_2 is associated with in-plane J-T distortion, while Q_3 is an indicator of the out-of-plane tetragonal distortion. Values of Q_2 and Q_3 are nearly zero in case of NdFeO_3 . For NFMFO, we find that at 300K, $Q_2 = 0.125$ and $Q_3 = -0.0331$, as obtained using bond lengths from Table 3.1. In this case (NFMFO), both the distortion parameters are nonzero, but are much smaller compared to NdMnO_3 ($Q_2 = 0.4426$ and $Q_3 = -0.1797$). Thus the in-plane J-T distortion appears stronger than the out-of-plane tetragonal distortion. An additional parameter often used to quantify the distortion of the octahedral is Δ_d defined as $\Delta_d =$

$(1/6) \sum_{n=1,6} [(d_n - \langle d \rangle) / \langle d \rangle]^2$ [190], where d_n 's are the individual M -O bond lengths. In case of NFMO, we observe that the level of octahedral distortion ($10^4 \Delta_d = 3.47$) is smaller by an order of magnitude in comparison to NdMnO_3 ($10^4 \Delta_d = 46.4$), but higher than NdFeO_3 ($10^4 \Delta_d = 0.2$). Due to the presence of long-range static J-T effect and orbital ordering, such high level of octahedral distortions is seen to exist in NdMnO_3 [107].

In case of NFMO, the temperature variations of lattice parameters as shown in Figure 3.4, the lattice parameters were obtained from powder neutron diffraction patterns between 400 and 1.5 K. Starting from 400 K, a and c decreases with the decrease in temperature, similar to both the parent compounds[101][105]. However, the parameter b shows anomalous behavior. After an initial decrease from 400 K, near 350 K it shows continuous increase till 200 K, with a peak near 250 K, coinciding with the Néel temperature, will be discussed in detail in next section.

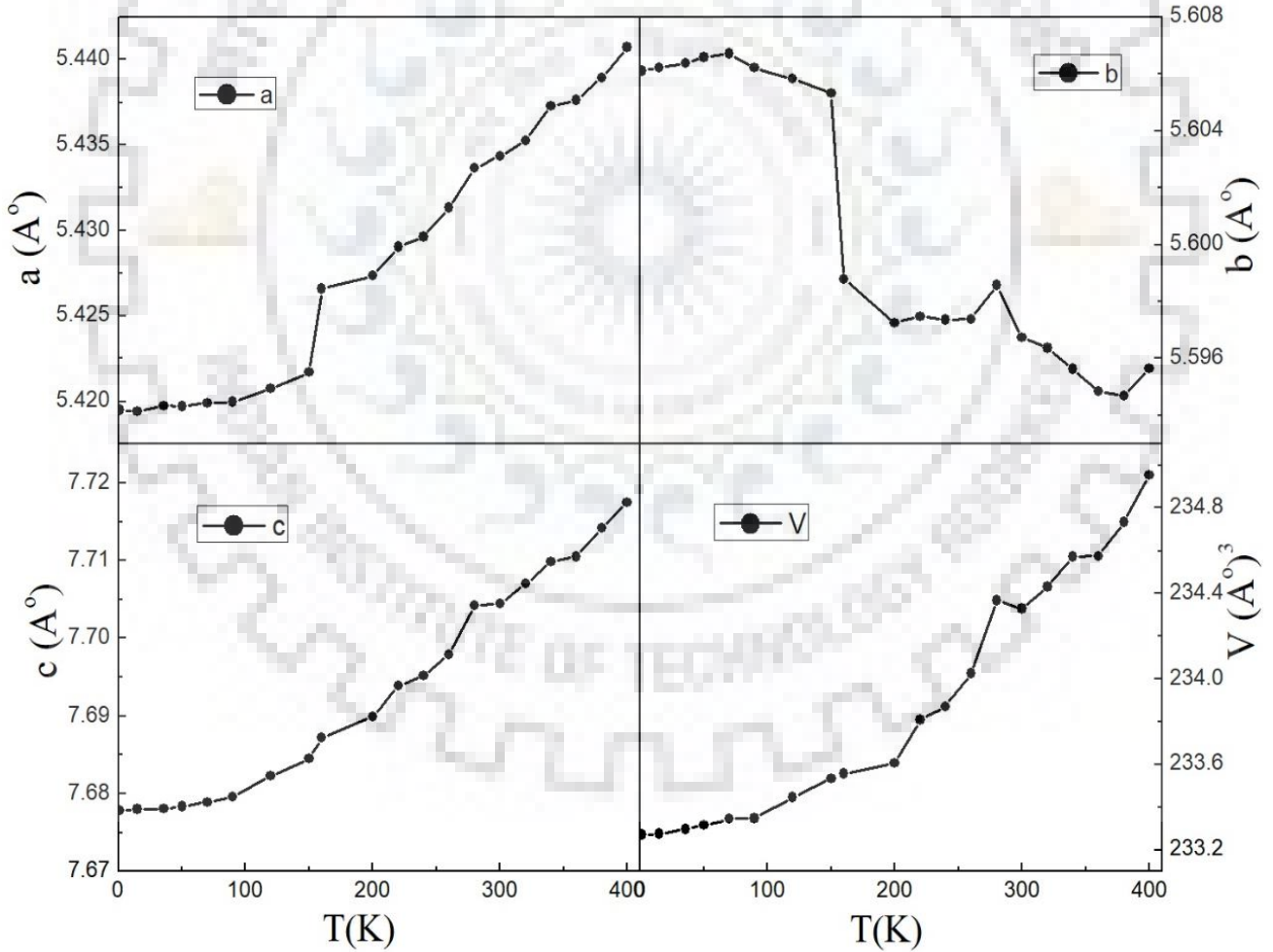


Figure 3.4 Variation of lattice parameter with temperature obtained from powder neutron diffraction in the range 1.5-400K

Such a trend is not observed in both the parent compounds. In NdFeO_3 , b decreases sharply from 300 till 150 K [100] while in NdMnO_3 b almost remains constant till a sudden drop near Néel temperature [104]. A similar rise in lattice parameter c (in $Pnma$ setting) of $\text{NdFe}_{0.2}\text{Mn}_{0.8}\text{O}_3$ is observed near 100 K, which is slightly above its Néel temperature [188].

The opposite trends in temperature variation of b as compared to a and c can be attributed to changes in local J-T effects. Below 200 K, a and c decrease continuously with decrease in temperature except for a discontinuity in a near 150 K in case of a lattice parameter. In this region (around 150 K), b shows a sharp increase and finally below 100 K, the variation in b is less significant. A similar trend is shown in NdFeO_3 also, which shows a minimum in b near 150 K. Below 150 K, b starts to rise in gradual manner[100]. This is in contrast to the sudden increase of b in our system. A similar jump in lattice parameter is also seen in case of NdMnO_3 , which however shows a sharp decrease with temperature below the jump [104]. This has been

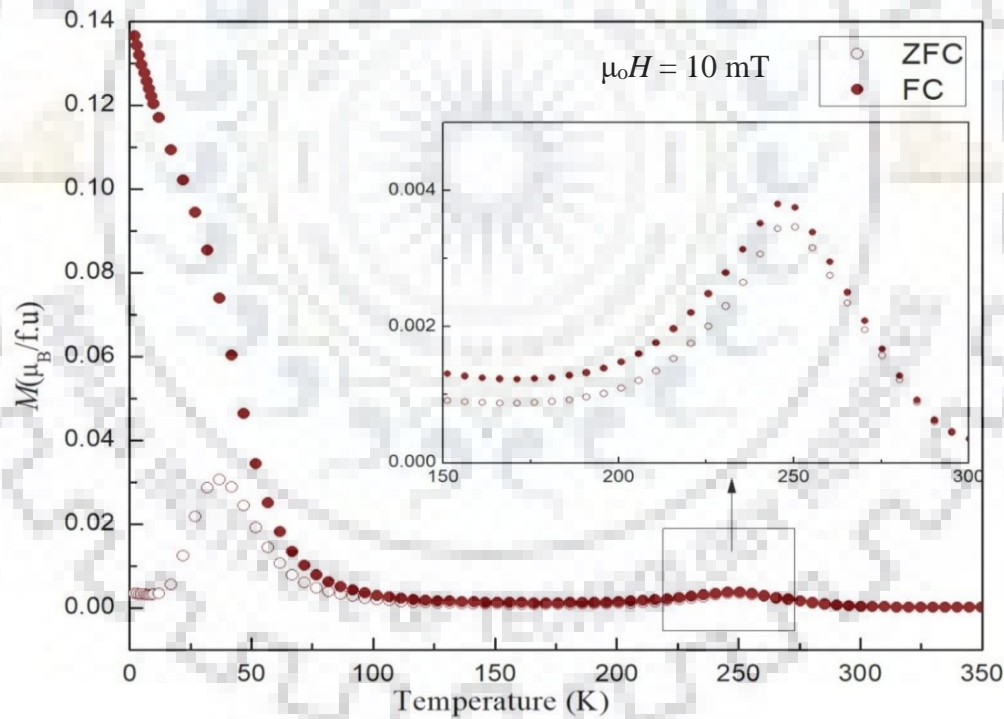


Figure 3.5 ZFC-FC plots of NFMO from 2 to 350K showing Néel temperature (T_N) at 250 K and weak ferromagnetism below 70 K

attributed to magneto-elastic effect by Chatterji *et.al.*[104] where strain is observed along b parameter which leads to its decrement.

For NFMO, the increase in b can also be linked with the variation of the $M-O(2)(l)$ bond lengths with temperature and possible increase in J-T distortion at Mn sites. Similarly, the medium bond length (m) shows a systematic decrease with temperature as shown in Table 3.1. However, l shows an overall increase with decreasing temperature, though it shows a higher value for 90K compared to 1.5K, indicating a possible reduction in J-T distortion below 90K. Presence of a dynamical J-T effect associated with a weak and short-range orbital ordering in NFMO could be inferred from the above mentioned facts about lattice constants, bond lengths, J-T parameter and temperature dependent data.

3.3.2 Magnetic Properties

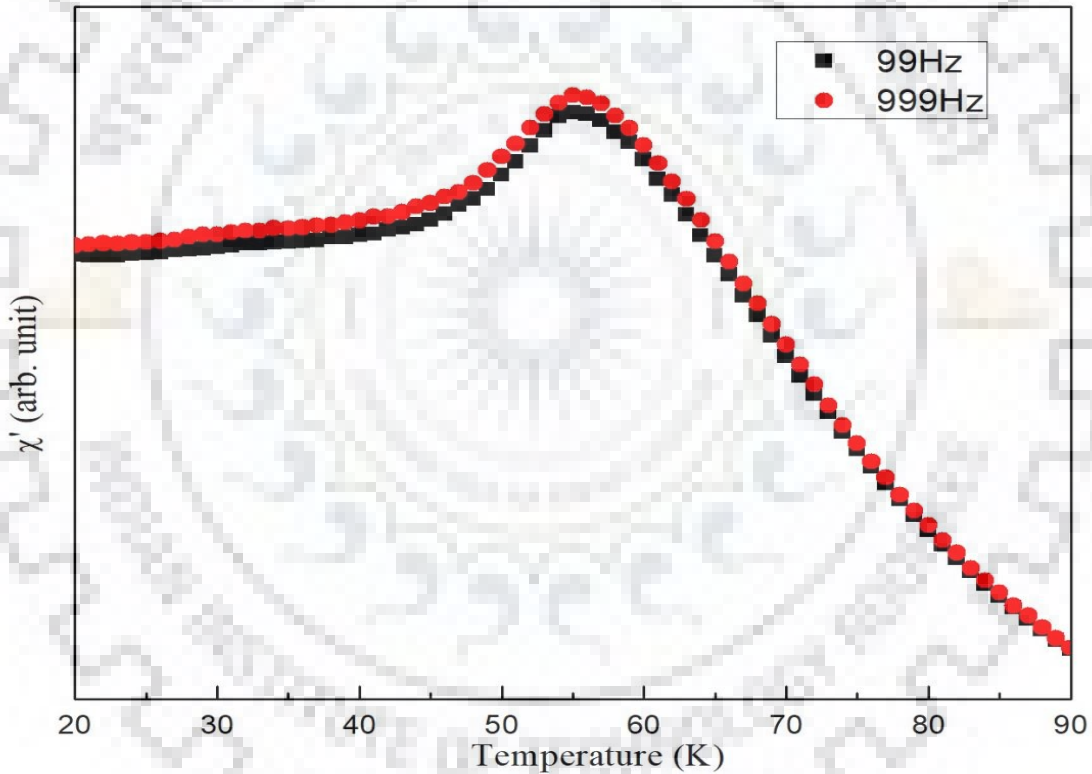


Figure 3.6 Real part of ac susceptibility for different frequencies

As shown in Figure 3.5, ZFC and FC magnetization measurements were performed from 2 to 350 K in the magnetic field of 10mT. Temperature dependent ZFC and FC show a characteristic cusp (inset of Figure 3.5) at 250 K denoting a long range antiferromagnetic ordering of the M (Mn/Fe) spins. The parent compound $NdFeO_3$ undergoes from paramagnetic state to G -type antiferromagnetic state at 690 K [100]. As recently reported by Chakraborty *et. al.*

al. [107] T_N is seen to decrease systematically with increase of Mn substitution in $\text{NdFe}_{1-x}\text{Mn}_x\text{O}_3$. Since the value of T_N is 622 K for $x = 0.1$, 529 K for $x = 0.2$, 449 K for $x = 0.3$ and 356 K for $x = 0.4$ in $\text{NdFe}_{1-x}\text{Mn}_x\text{O}_3$ [108]; therefore, the observed value of T_N (250 K) for NFMO is consistent with previous reports. ZFC and FC magnetization exhibit an increase below 70 K, and large bifurcation below 37 K, whereas FC magnetization keeps increasing with a slight change in slope at 37 K. Such magnetization is observed typically for spin glass

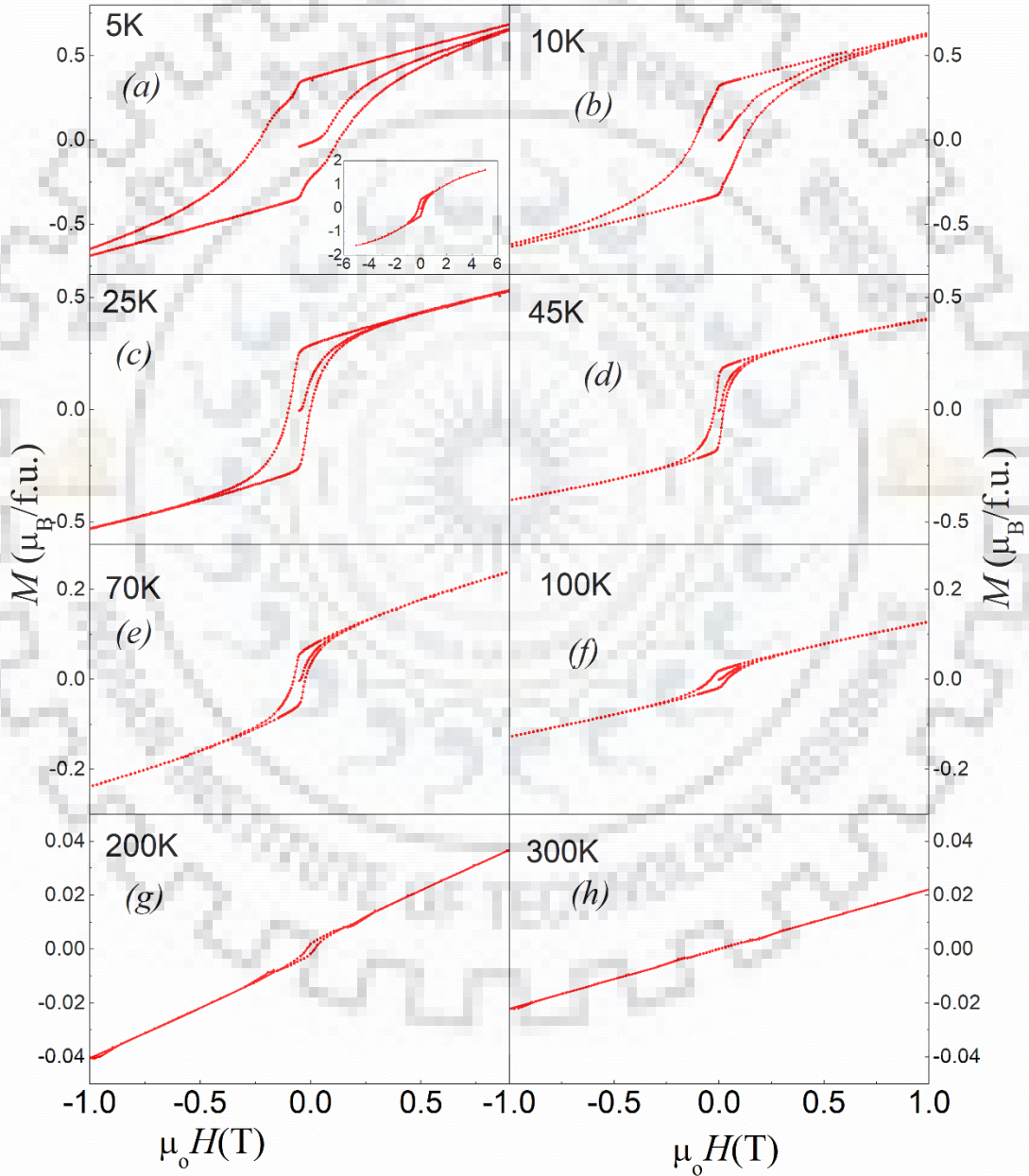


Figure 3.7 M - H plots of NFMO at (a) 5, (b) 10, (c) 25, (d) 45, (e) 70, (f) 100, (g) 200, (h) 300K

systems, weak ferromagnetic systems and systems with short-range magnetic correlations[196]. FC magnetization does not follow the mean-field magnetization for a ferromagnet with long-range ordering. Troyanchuk *et. al.* [110] attributed the low-temperature magnetic behavior in NFMO entirely to a spin glass state. However, frequency-dependent ac-susceptibility measurements ruled out the presence of a spin glass state in the present study as shown in Figure 3.6. Further, magnetization (M) versus magnetic field (H) loops were measured at various temperatures to understand the low-temperature magnetic behavior (below 70 K) of NFMO.

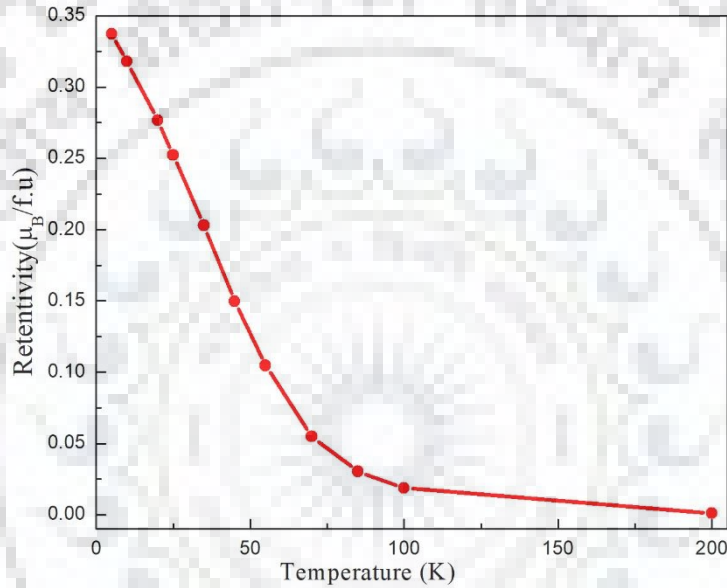


Figure 3.8 Variation of retentivity with temperature in NFMO

The magnetization isotherms (M - H loops) of NFMO at various temperatures from 5 till 300K have been shown in Figure 3.7. At 300K, the magnetization isotherms show linear behavior with negligible hysteresis as expected from a majority of paramagnetic phase. At 200 and 100 K, the M - H loops are quite similar having a deviation from the linear behavior with a small coercivity, retentivity and unsaturated magnetization. Such magnetization data (linear M - H loops) indicate the presence of antiferromagnetic order without canting. The nature of M - H loops below 70 K changes considerably (both qualitatively and quantitatively) with an increase in coercivity and retentivity. Another qualitative change in the M - H loop occurs below 25 K with a large coercivity value. The shape of the M - H loops obtained at 10 and 5 K is significantly different from the loops measured at 25, 45 and 70 K. The M - H loops below 100 K indicate development of a ferromagnetic component. However, the magnetization does not

undergo saturation even at 5 K in a field of 5 T as seen in inset of Figure 3.7(a), indicative of a ferromagnetic component superimposed over an antiferromagnetic phase. We present the variation of retentivity versus temperature in Figure 3.8. The remanent magnetization is seen to increase below 100 K suggesting development of a small ferromagnetic component.

As the spin-reorientation effects are characteristic features of the orthoferrite compounds in which the spins rotate from one crystallographic direction to another in a continuous manner, indicative of a second order phase transition [83][197], such scenario can also provide a possible explanation to the magnetization data of the NFMO presented above. However, it is very difficult to conclude about the type of magnetic structure and nature of spin reorientation based on the average magnetization data alone. It is expected that a magnetic transition occurs most probably from one type of antiferromagnetic order to another type having a weak ferromagnetism below 100 K.

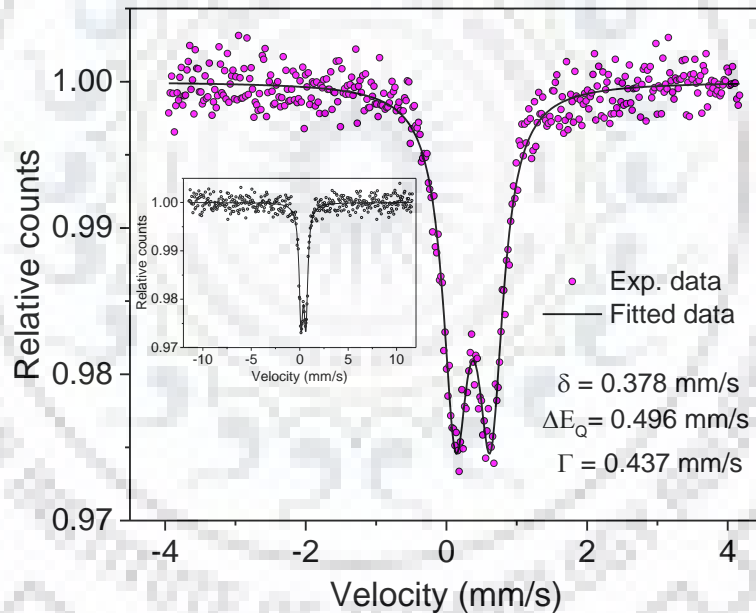


Figure 3.9 Mössbauer spectrum of NFMO sample recorded at 300 K showing the paramagnetic behavior of Fe^{3+} ion. Inset shows the spectrum recorded at higher velocity (± 11.5 mm/s)

3.3.3 Mössbauer Spectroscopy

In this section Mössbauer spectroscopy is discussed. Room temperature Mössbauer spectrum of NFMO is recorded using a Mössbauer spectrometer operated in constant acceleration

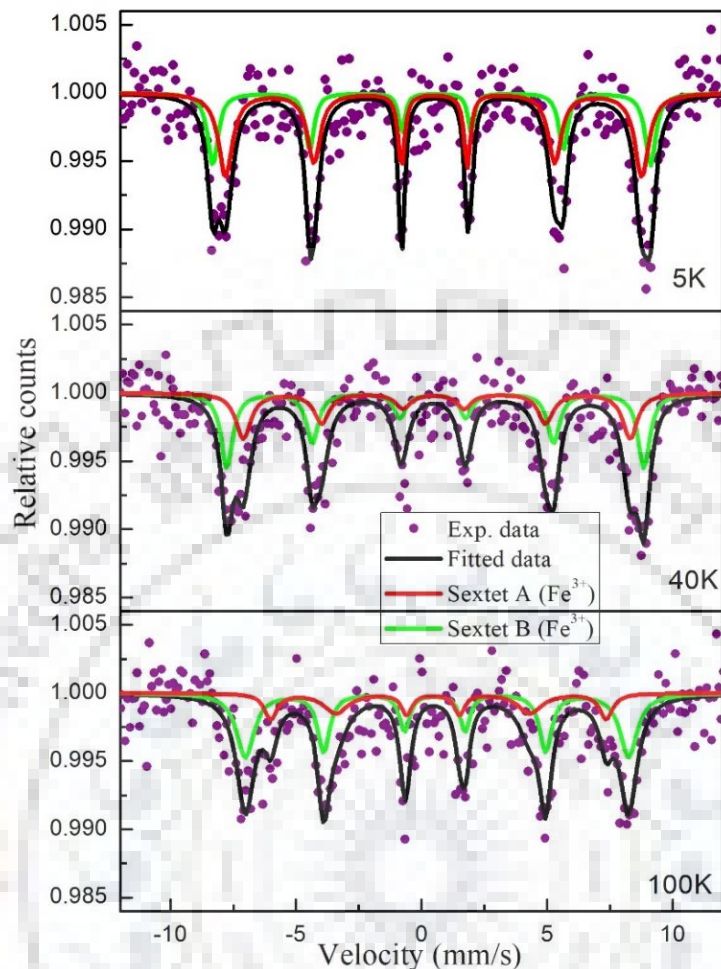


Figure 3.10 Mössbauer spectra of NFM0 sample recorded at 5 K, 40 K, and 100 K

mode (triangular wave) in transmission geometry at BARC Mumbai. Mössbauer spectra at 5 K, 40 K and 100 K are recorded using an another spectrometer in transmission geometry at UGC-DAE Indore. The source employed was Co-57 in Rh matrix of strength 50 mCi. The calibration of the velocity scale is done by using an enriched α - Fe metal foil. The line width (inner) of calibration spectra is $\approx 0.25 \text{ mm s}^{-1}$.

Room temperature Mössbauer spectrum is fitted with a symmetric doublet as shown in Figure 3.9. The values of isomer shift (δ), quadrupole splitting (ΔE_Q), and line width (Γ) are found to be 0.378 mm/s, 496 mm/s, and 437 mm/s respectively. These values are confirmed that the Fe ions are in Fe^{3+} high spin states at octahedral site (FeO_6). The inset shows the Mössbauer spectrum of the NFM0 sample with a higher velocity of $\pm 11.5 \text{ mm/s}$ in order to

check any possibility of an ordered magnetic phase (sextet) which confirms that there is no magnetic sextet (hyperfine

Table 3.2 Mössbauer parameters calculated from Mössbauer spectra recorded at low temperatures

Temp. (K)	Fe site	R_A (%)	Hyperfine field H_f (Tesla) ± 0.2	Quadrupole splitting, (Δ) mm/s ± 0.02	Isomer shift, (δ) mm/s ± 0.04	Outer line width, (Γ) mm/s ± 0.02	Fitting quality (χ²)
100 K	Sextet A	68.2	47.3	0.089	0.455	0.845	1.05548
	Sextet B	31.8	41.4	0.219	0.451	0.620	
40 K	Sextet A	51.4	51.4	0.104	0.498	0.577	1.18535
	Sextet B	48.6	48.6	0.121	0.537	0.719	
5 K	Sextet A	36.9	54.1	-0.187	0.489	0.497	1.00411
	Sextet B	63.1	51.4	-0.023	0.451	0.683	

splitting pattern) present in the sample. This confirms that a magnetic ordering does not exist in NFMO at 300 K.

Figure 3.10 shows the Mössbauer spectra at three different temperatures in the spin reorientation region as predicted from magnetization data that the Fe³⁺/Mn³⁺ spins undergo gradual spin reorientation in the temperature range 70 K – 20 K. It is well known that the orthoferrite show simple Zeeman split sextets below T_N and doublet (two line) above T_N in Mössbauer spectra which also indicate the presence of crystallographic site of Fe ions. The Mössbauer spectra at temperatures 5 K, 40 K and 100 K are fitted with two sextets (six line Zeeman splitting patterns) as shown in Figure 3.10. Mössbauer parameters which are calculated from the Mössbauer spectra recorded at lower temperatures are shown in Table 3.2. The variation of different Mössbauer parameters with decreasing temperatures are shown in Figure 3.11 (a-f).

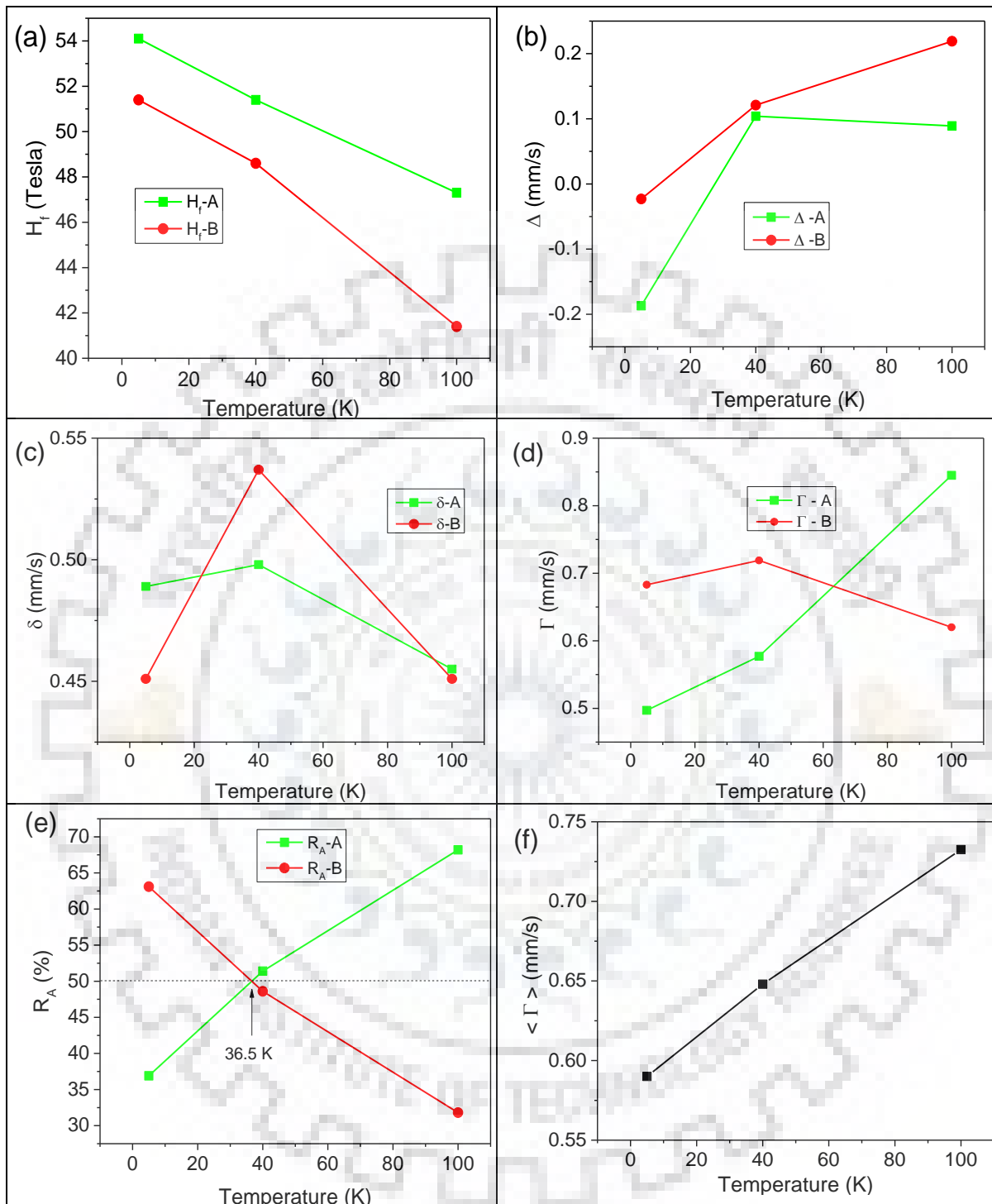


Figure 3.11 Variation in (a) Hyperfine magnetic field (H_f), (b) Quadrupole splitting (Δ), (c) Isomer shift (δ), (d) Outer line width (Γ), (e) Relative area of sextets (R_A) and (f) Average outer line width ($\langle \Gamma \rangle$) with decreasing the temperature

The values of isomer shift for both sextets are found between 0.451 – 0.53 mm/s, which further confirms the presence of Fe ions in +3 high spin states at octahedral site. The value of isomer shift (δ) for both the sextets increases at 40 K and further decreases at 5 K (Figure 3.11 (c)). Isomer shift occurs due to electron charge density due to the presence of *s*-electron within it and is very important in determining the valence states and electron shielding. As during spin reorientation Fe^{3+} ions are in gradual motion which leads to the increment in δ parameter in that region.

The two sextets belong to two different spin directions corresponding to Fe^{3+} spins creating different hyperfine magnetic fields present in the sample at the same site. The relative areas of these two sextets (Fe^{3+} spins) are temperature dependent as shown in Figure 3.11 (e). The values of Δ and average outer line width ($\langle \Gamma \rangle$) are found to decrease (Fig. 3.11 (b, f)) whereas the hyperfine magnetic fields (H_f) values are found to increase (Fig. 3.11 (a)) with decreasing the temperature which confirm the magnetic symmetry (spins aligning in particular direction) in the sample. The relative area of sextet - A found to decrease whereas for sextet - B it is increasing with the decrease in temperature. This is due to the Fe^{3+} spins undergoing gradual spin reorientation which is studied in detail in the next chapter from powder neutron diffraction studies. At temperature ~ 36.5 K, the relative area of both the sextets are nearly equal.

3.4 Conclusion

In summary, NFMO polycrystalline samples have been prepared and investigated in detail in order to understand its structural and magnetic properties. The sample crystallizes in the space group *Pbnm* with both Fe and Mn occupying the same crystallographic position and thus being randomly distributed in the crystal. Presence of local J-T distortion at substituted Mn sites was evident from the change in measured lattice parameters, and Mn(Fe)-O bond lengths. In addition the values of various other distortion parameters are also observed to be higher in comparison to their corresponding values for orthoferrite NdFeO_3 , though these values are an order of magnitude smaller than those of NdMnO_3 . At 150 K sharp jump is seen in *b* which can be attributed to magneto – elastic effects. The magnetic properties of NFMO are similar to NdFeO_3 although with many interesting differences. The antiferromagnetic transition occurs at relatively low temperature at 250 K in comparison to NdFeO_3 where $T_N \sim 690$ K indicating a reduction in the strength of the exchange interaction due to Mn. From Mössbauer

spectroscopy, it has been concluded that at lower temperature there is antiferromagnetic ordering of Fe^{3+} ions but at room temperature it shows the paramagnetic behavior as observed from magnetic measurements also. Mössbauer study indicates a temperature dependent spin reorientation of Fe^{3+} spins which is discussed in detail in the next chapter.



Magnetic structure and specific heat of $\text{NdFe}_{0.5}\text{Mn}_{0.5}\text{O}_3$

4.1 Introduction

This chapter is based on the neutron diffraction studies on $\text{NdFe}_{0.5}\text{Mn}_{0.5}\text{O}_3$, which has a T_N nearly 250K. Due to atomic no. difference of only 1 between Mn and Fe, the compound prefers to stay in disordered $\text{NdFe}_{0.5}\text{Mn}_{0.5}\text{O}_3$ state, rather than the ordered $\text{Nd}_2\text{FeMnO}_6$. The random distribution of Fe/Mn ions drastically modifies the various exchange interactions and anisotropy behavior which results in an unexpectedly interesting properties even though the magnetism is more closely linked to the orthoferrites. As shown in Figure 3.2, the magnetic broad hump in the powder neutron diffraction data at 300 K indicated the presence of short range magnetic ordering above T_N . The indication of short range ordering at higher temperature is also revealed from Curie-Weiss fitting, discussed in the previous chapter. As shown in Figure 3.5, another transition is also observed at lower temperature in the magnetization data of NFMO, which is due to the possible spin reorientation of $\text{Fe}^{3+}/\text{Mn}^{3+}$ spins. In the same temperature range, change in coercivity is also observed in $M-H$ curves.

Presence of short range ordering and spin reorientation in NFMO motivated to perform powder neutron diffraction in the lower temperature region (1.5 – 90 K) as well as in the higher temperature region (120 – 400 K) to investigate the behavior of spin reorientation of $\text{Fe}^{3+}/\text{Mn}^{3+}$ spins in detail. The observed broad hump at 300 K remains in the form of diffuse scattering near magnetic Bragg peaks below T_N . Thus, the development of short range ordering in NFMO has been investigated in detail. In addition, specific heat studies have also been performed to find any signature of spin reorientation or additional phase transition associated with the ordering of rare-earth ions.

4.2 Experimental details

As explained in chapter 3, polycrystalline NFMO has been synthesized by solid state reaction method. Neutron diffraction study in absence of magnetic field was carried out at various temperatures in the range 1.5-400 K to identify the crystal as well as magnetic structures and their variations as a function of temperature. Neutron diffraction measurements were carried out using powder diffractometers PD-I ($\lambda = 1.094 \text{ \AA}$) and PD-II ($\lambda = 1.2443 \text{ \AA}$) at the Dhruva Reactor, Trombay, Mumbai, India. High resolution neutron diffraction measurements were performed at D1B (CRG)- high resolution two-axis neutron powder diffractometer ($\lambda = 2.524 \text{ \AA}$), Institut Laue-Langevin, Grenoble, France and some high temperature neutron diffraction measurements were performed at G4.1, cold neutron two axis diffractometer ($\lambda = 2.426 \text{ \AA}$), Laboratoire Léon Brillouin, Saclay, France. Magnetic structure was determined using the irreducible representation from BASIREPS, and refined using FULLPROF. One dimensional neutron depolarization measurements were carried out using the polarized neutron spectrometer (PNS) at the Dhruva reactor in 4 – 300 K temperature range and 50 Oe magnetic guide field to identify the presence of weak ferromagnetism. For the neutron depolarization measurements, polarized neutrons ($\lambda = 1.205 \text{ \AA}$) were produced and analyzed by using Cu_2MnAl (111) and $\text{Co}_{0.92}\text{Fe}_{0.08}$ (200) single crystals, respectively. The two different states (up and down) of the incident neutron beam polarization were achieved by a π flipper just before the sample. The polarization of the neutron beam was determined by measuring the intensities of neutrons in non-spin flip and spin flip channels with the flipper off and on (flipping ratio, R) respectively. Specific Heat measurement was carried out using physical property measurement system in the temperature range 2 – 30 K in the presence of different applied field at UGC-DAE Center, BARC, Mumbai to study the schottky anomaly due to the degeneracy of $4f$ electrons of rare earth ions.

4.3 Results and Discussion

4.3.1 Neutron diffraction measurements

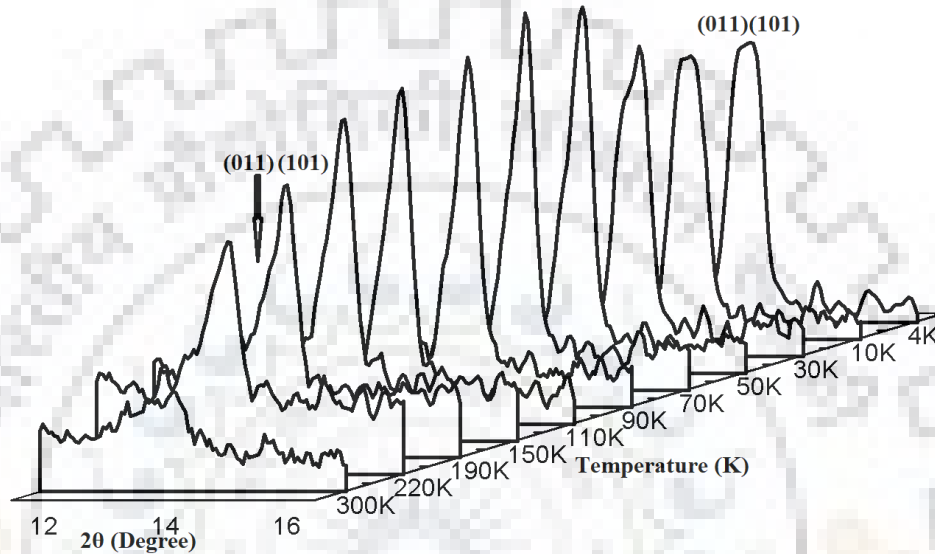


Figure 4.1 Evolution of magnetic peak in neutron diffraction data as a function of temperature. These temperature dependent measurements were performed at PD-I ($\lambda = 1.094 \text{ \AA}$)

In this section, a systematic evolution of the NFMFO magnetic structure based on neutron diffraction data has been discussed. In Figure 3.2, we have already seen the neutron diffraction pattern at 300 K, with a broad hump corresponding to short range magnetic ordering centered at $2\theta = 16^\circ$ ($\lambda = 1.2443 \text{ \AA}$), which indicates presence of the magnetic correlations even above T_N as suggested by the limitation of Curie-Weiss fitting to explain the magnetization data in Chapter 3 (3.3.2).

As shown in Figure 4.1, the temperature dependent neutron diffraction measurements were performed at PD-I ($\lambda = 1.094 \text{ \AA}$) in the temperature range 4 – 300 K. As temperature is lowered below 250 K, a clear magnetic Bragg peak is observed at $\sim 14.2^\circ$, which is convolution of (011) and (101) peaks. The nuclear Bragg reflections due to the two peaks are forbidden in the $Pbnm$ space group. However, their magnetic reflections have non-zero structure factors. This further confirms 250 K as the value of T_N , which is also suggested by magnetization

measurements in previous chapter. Intensity of the magnetic peak increases and (011) peak occurs at lower angle in the form of shoulder hump on the total magnetic Bragg peak down to 70 K. The intensity ratio of two peaks [$I(011)/I(101)$] is approximately 1/3 at 70 K suggesting a *G*-type antiferromagnetic structure with spins aligned along *y* direction. The spectral weight of the (101) peak shifts to the (011) peak below 70 K and the ratio of both peaks becomes equal close to 4 K, which represents a *G*-type antiferromagnetic structure with spins aligned along *z* direction[93]. Such temperature induced changes in the magnetic peak clearly stipulate a spin reorientation below 70 K. However, it is not possible to completely resolve both the peaks at the incident neutron wavelength of 1.094 Å due to the resolution limit of the instrument PD-I.

The systematic evolution of the $I(011)/I(101)$ is better understood with neutron diffraction experiments performed at D1B (CRG), ILL using a wavelength of 2.524 Å between 1.5 and 90 K. Above this temperature, neutron diffraction experiment is performed at G4.1, LLB in the temperature range 120 – 400 K using a wavelength of 2.426 Å. At such higher wavelength, the magnetic Bragg peaks (011) and (101) are well resolved. Further detailed analysis has been performed on low temperature neutron diffraction data (from D1B) as well as on high temperature neutron diffraction data (from G4.1) to quantify the magnetic structure and temperature induced spin reorientation in two temperature range in NFMO.

The ordering vector in NFMO is $k = (0,0,0)$, which is same for two end compounds, indicating that the magnetic and structural unit cells are identical. Comparison of the diffraction pattern with the two end compounds suggests that the antiferromagnetic ordering is identical with *G*-type NdFeO_3 rather than the *A*-type NdMnO_3 . For experimentally determined magnetic ordering vector $k = (0,0,0)$, there exists eight irreducible representations, Γ_1 to Γ_8 . Four (Γ_5 to Γ_8) out of these eight representations correspond to zero coefficients for the Fe site. Thus we consider four irreducible representations Γ_1 to Γ_4 which corresponds to the Shubnikov magnetic spacegroups, $\Gamma_1 (Pbnm)$, $\Gamma_2 (Pbn'm')$, $\Gamma_3 (Pb'nm')$ and $\Gamma_4 (Pb'n'm)$. Using Bertraut's notation, these four magnetic space groups can be written in a simplified manner as $A_x G_y C_z$, $F_x A_y G_z$, $C_x F_y A_z$, and $G_x C_y F_z$, respectively corresponding to magnetic ordering of the Cartesian components of M^{3+} spins in the unit cell. *A*- and *C*-type antiferromagnetic ordering is due to hidden canting of the spins, while F_x is due to overt canting of spins corresponding to ferromagnetic component. *A*- and *C*-type antiferromagnetic orderings are not observed

experimentally in present study probably due to small magnitude of the overt and hidden angles and have not been discussed further. Corresponding to Γ_1 , Γ_2 , Γ_3 , and Γ_4 representations, Nd spin can order as C_x , $F_x C_y$, $C_x F_y$ and F_z respectively[83].

To obtain the detailed spin configuration in a unit cell, refinement of the magnetic structure has been performed for the data collected from D1B (CRG) and G4.1 in three steps:

- I. **Short range diffused scattering:** First of all, short range diffused scattering has been studied in detail. The short range diffused scattering starting from 400 K and extended till 1.5K has been discussed.
- II. **High temperature (120 – 400 K) neutron diffraction measurements:** Further, refinement has been performed for the data collected from G4.1 in the higher temperature region 120 – 400 K, where spin reorientation is observed in the temperature region 150 – 250 K. For this higher temperature region, the process of spin reorientation region started below T_N .

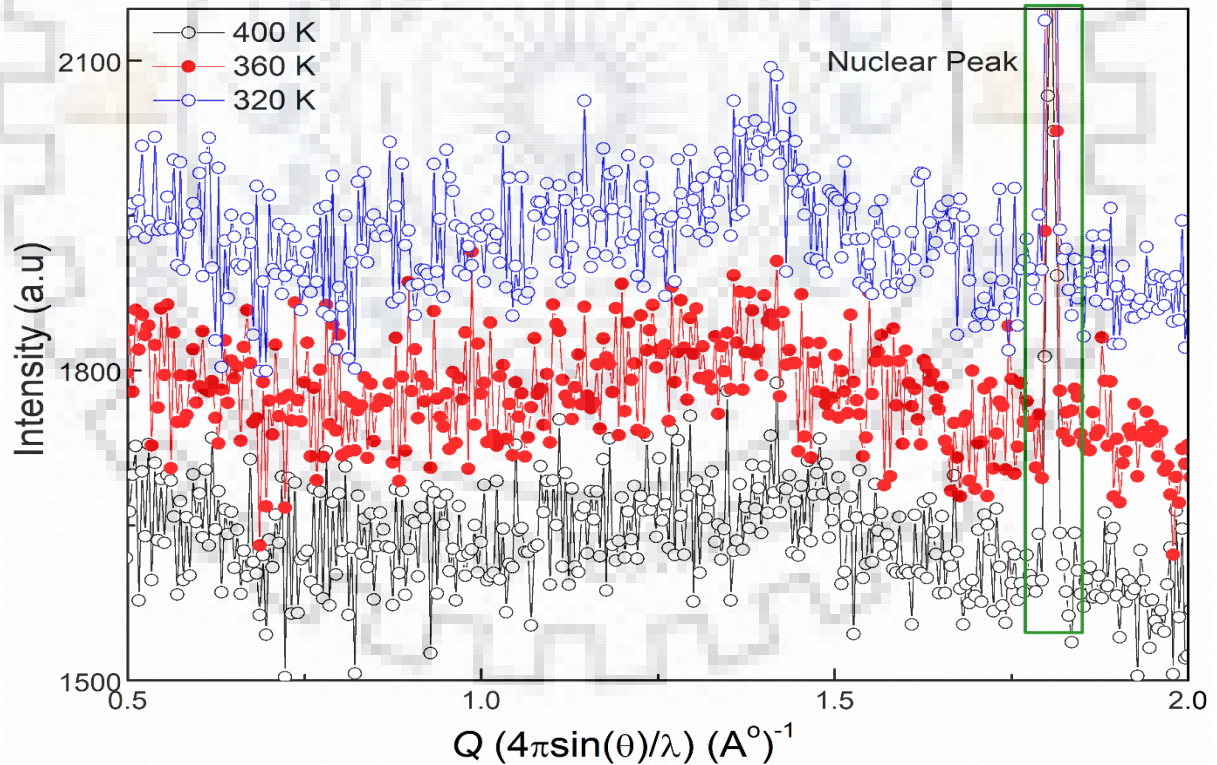


Figure.4.2. Neutron powder diffraction data from NFMO with a neutron wavelength of 2.414 \AA showing onset of short-ranged ordering centered around 1.4 \AA^{-1} . The box at 1.7 \AA^{-1} is from the (111) nuclear Bragg peak

III. **Low temperature (1.5 – 90 K) neutron diffraction measurements:** Finally, in the lower temperature region 1.5 – 90 K, 90, 50, 36, 15 and 1.5 K data is discussed in detail as it will cover entirely the reorientation transition region of that range. Since Mn and Fe occupy the same $4b$ site in NFMO, therefore Fe-Mn ordering is identical. On the other hand, Nd occupies $4c$ site and thus can order independently, however, in conjunction with the Fe-Mn ordering.

4.3.1.1 Short range diffused scattering

The neutron powder diffraction patterns, in the Q -range 0.5 - 2.0 \AA^{-1} , corresponding to the (011) and (101) magnetic Bragg peaks associated with G -type magnetic structure is shown in Figure 4.2. No trace of magnetic Bragg peak is observed in the 400-320 K temperature range. However even at 400 K, we observe diffused scattering centered at 1.4 \AA^{-1} . This clearly shows development of short ranged ordering at $1.6T_N$. From 400 to 320 K, the intensity of diffused peak increases, while the width decreases.

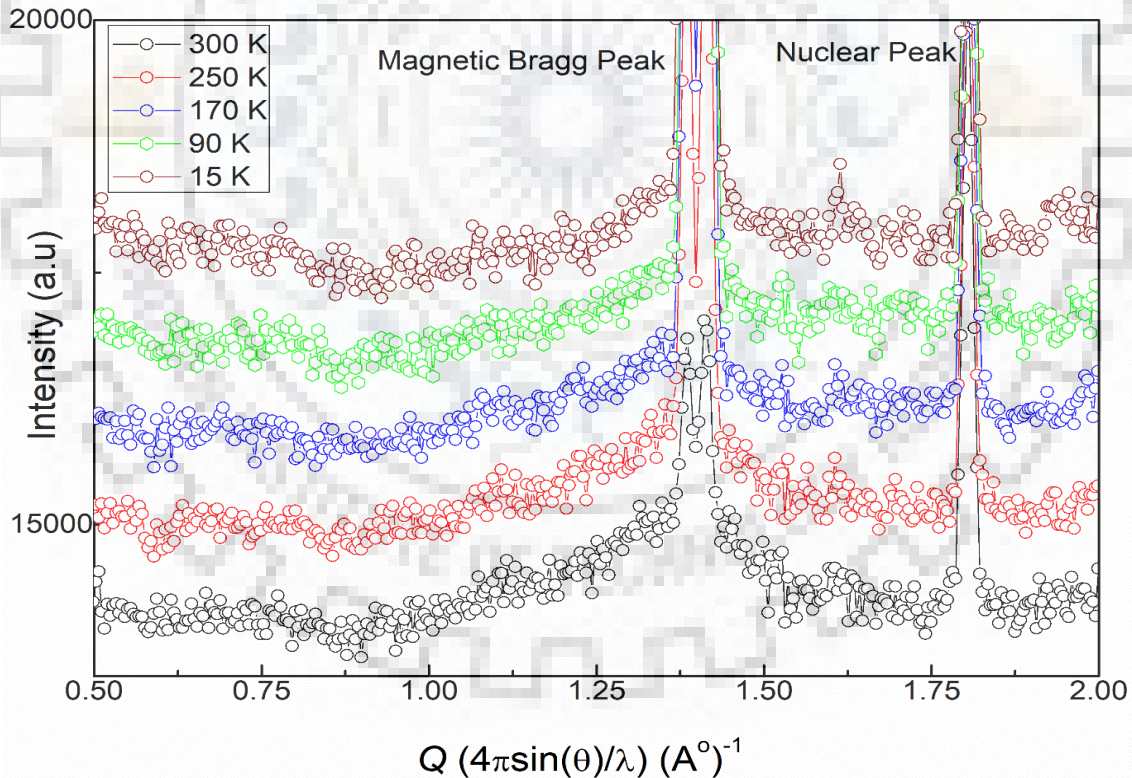


Figure 4.3. Neutron powder diffraction data from NFMO with a neutron wavelength of 2.52 \AA at D1B, ILL from $T = 300 \text{ K}$ to 15 K showing the prominent diffused scattering peak at 1.4 \AA^{-1} , on which the magnetic Bragg peak is superposed.

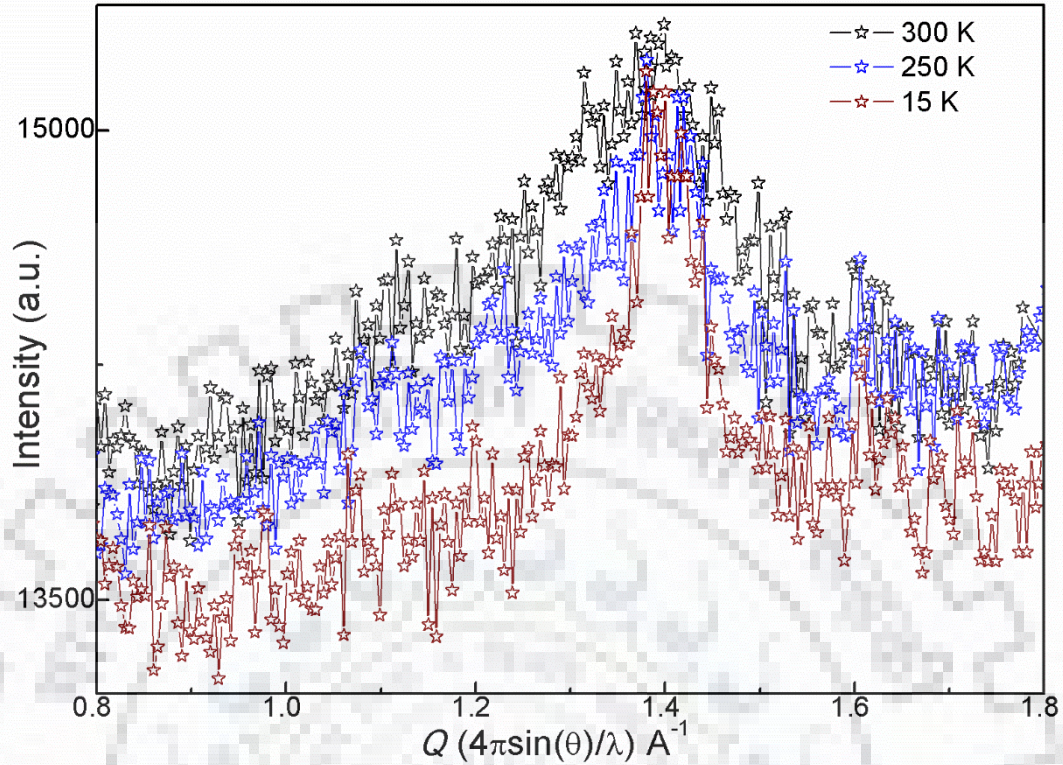


Figure 4.4 The diffused only magnetic peak obtained by removing the long ranged magnetic Bragg peaks.

In Figure 4.3, the enlarged neutron diffraction patterns corresponding to the same Q range as in Figure 4.2, obtained in temperature range of 300 to 15 K at D1B-ILL ($\lambda = 2.52 \text{ \AA}$) is shown. Interestingly, at 300 K itself, the diffraction pattern shows development of magnetic $\{(011), (101)\}$ Bragg peaks superposed over a large diffused scattering peak in the background. The width of Bragg peaks is resolution limited indicating the development of a long ranged G – type ordering at 300 K itself. For a qualitative understanding of the nature of diffused scattering, the diffused peak is shown in Figure 4.4 after removing the (101) and (011) magnetic Bragg peaks. The diffused scattering peak exists even at 15 K, though reduced in intensity and width. At 300 K, the diffused peak is a broad asymmetric peak, which tends to become more symmetric below 90 K. The origin of magnetic diffused scattering peak can be usually attributed either to a 2D long range ordering as observed in case of $\text{Ca}_{2.5}\text{Sr}_{0.5}\text{GaMn}_2\text{O}_8$ [198] or to a 2D short ranged correlation as observed in case of LaMnAsO [199]. In both the cases, the diffused peak can be described by Warren function, characterized by a gradual fall in intensity at higher Q , which is not seen in our system. On the contrary, our system shows a

gradual rise in intensity at low Q , and a more rapid fall towards large Q which indicates presence of short range ordering (SRO). Presence of correlations at higher wavelengths indicates the static nature of the SRO, in contrast with short-ranged dynamic correlations observed, for instance in IMnO_3 [200].

At 300 K, the line – shape is similar to the peak observed in pyrochlore $\text{Er}_2\text{Sn}_2\text{O}_7$ which shows absence of long ranged ordering even at 100mK [201]. Similar to the pyrochlore, the diffused scattering in our system can be attributed to 3D short range isotropic spin-spin correlations involving nearest (nn) and next nearest neighbors (nnn).

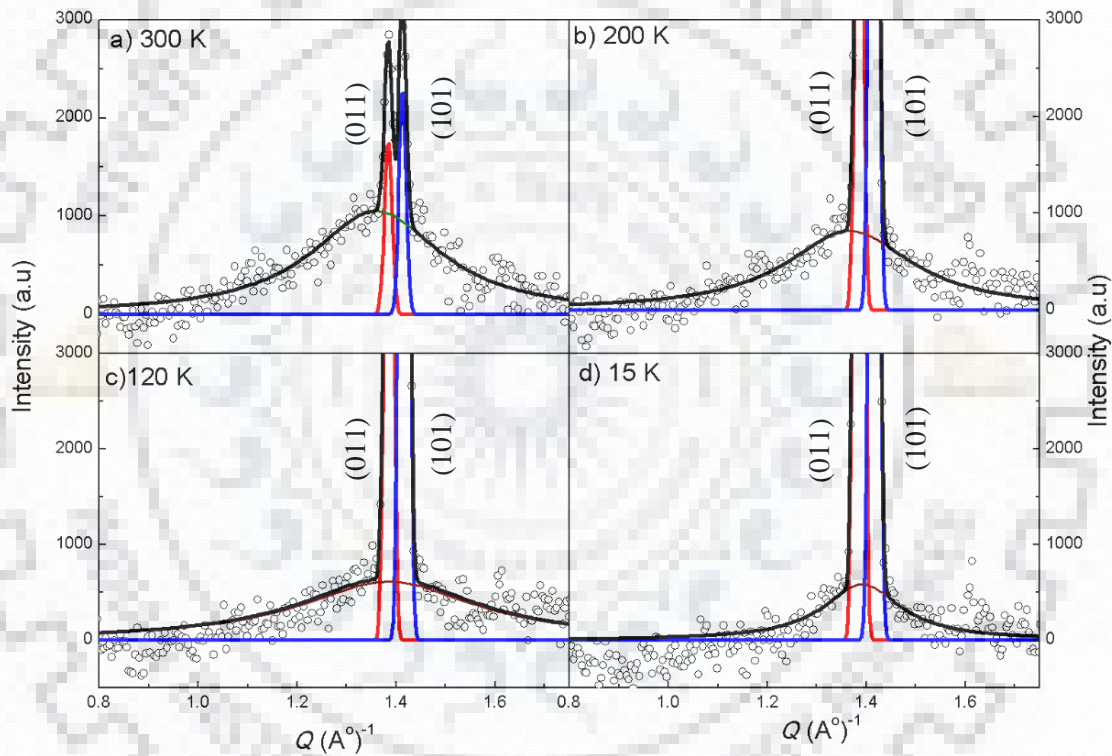


Figure 4.5 Neutron powder diffraction data of NFMO from (a) $T = 300$ K to (d) 15 K. the magnetic Bragg peaks are fitted to sum of two Gaussian functions, while diffused scattering is fitted to Lorentzian function peaks.

The nn interactions are antiferromagnetic, while the nnn interactions are ferromagnetic leading to the 3D SRO in our system. The peak – shape though asymmetric, can be approximated to a Lorentzian function, which is usually associated with 3D short ranged ordering [202]. To obtain reliable estimate of the parameters associated with the long range ordering (LRO) and SRO, the magnetic neutron scattering contribution was fitted to a sum of

two Gaussian functions (LRO) and Lorentzian function for SRO, as shown in Figure 4.5. The SRO peak has its center close to that of (011) Bragg peak at higher temperature (above 100 K). As shown in Figure 4.5 (d) clearly, the diffuse peak has asymmetry which is not captured by the Lorentzian function. It should also be mentioned that our magnetic Bragg peak cannot be fitted with two Lorentzian functions, suggesting that the origins of diffused scattering are not associated with smaller correlation lengths of the LRO near Néel temperature. In other words, the origin of the observed short range ordering is entirely different from the long range magnetic structure in our system (NFMO). With decreasing temperature (below 120 K), the quality of fitting reduces. As seen in Figure 4.5 (a-d), the area of the diffuse peak along with the FWHM decreases with temperature. The diffuse scattering around magnetic Bragg peaks

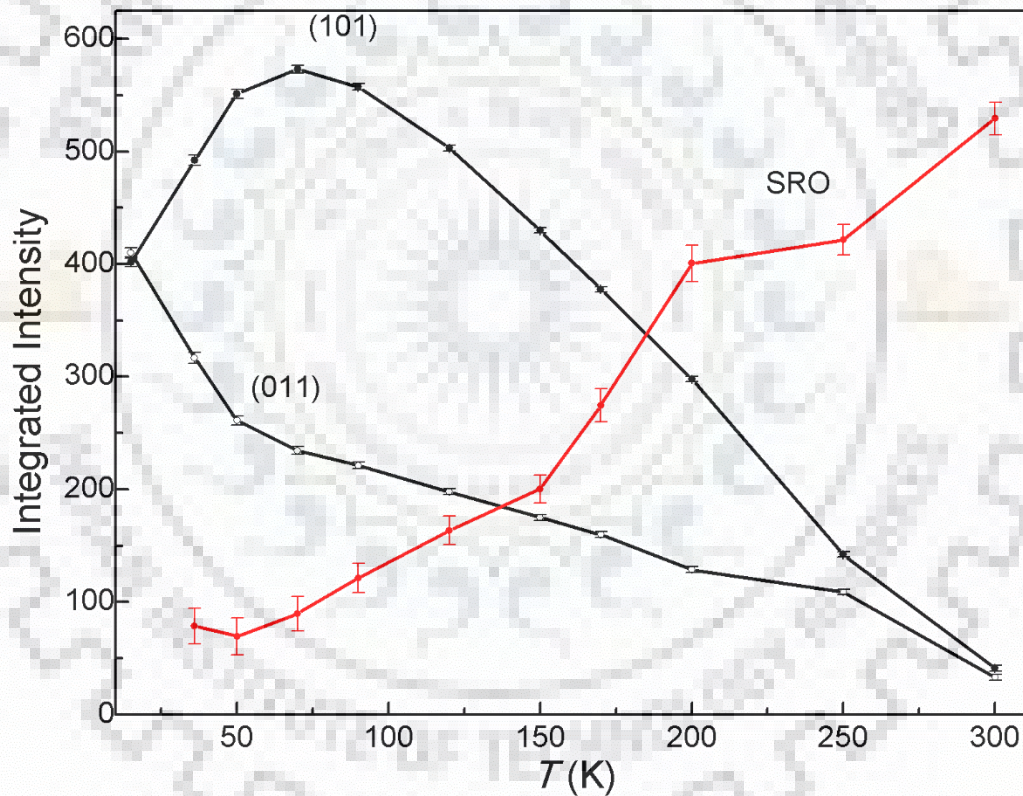


Figure 4.6 Temperature variation of intensity of the (011), (101) magnetic Bragg peaks, and the diffused peak

persists even down to 1.5 K (data is not shown here). The correlations length (ξ) of the SRO was obtained as $\xi = 2/\omega$; ω being the FWHM.

In Figure 4.6, the temperature variation of area of the SRO peak along with corresponding area of the (011) and (101) Bragg peaks is shown. The values of area above 300 K are not

shown since the data is obtained from a different instrument. At 300 K, the integrated intensity of the SRO peak is almost ten times greater than both the magnetic Bragg peaks. With decreasing temperature, there the area of the SRO peak decreases in comparison to the integrated area of (011) and (101) peaks.

In Figure 4.7, the temperature variations of diffuse peak's FWHM (ω) and the corresponding correlation length ξ are shown. At 400 K, the correlation length is nearly 4 Å, indicating the extremely short ranged nature of the ordering. However, between 360 and 340 K there is a sudden decrease in ω , indicating increase of the correlation length. The values of ω and correlation length do not vary from 300 till 200 K. However, ω continuously decreases from 200 K to 1.5 K, marking corresponding increase in correlation length. At $T = 1.5$ K, we obtain approximate correlation length of 50 Å.

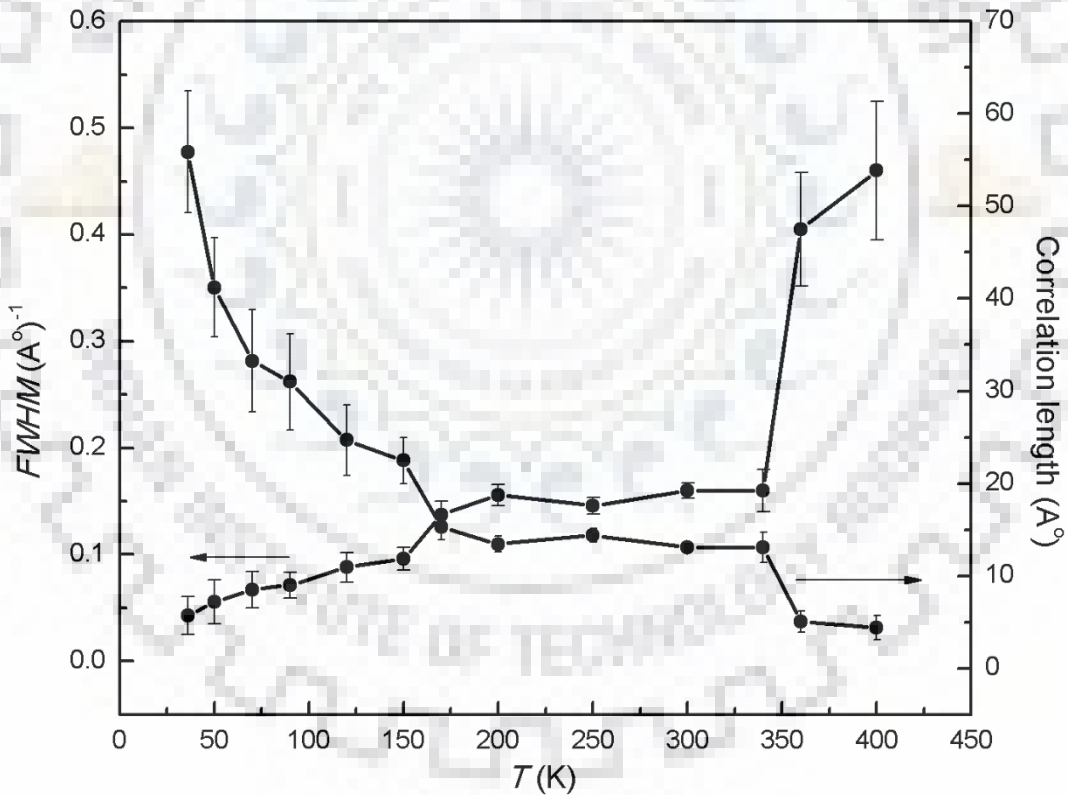


Figure 4.7 The temperature variation of FWHM and correlation length ξ

Thus, the above analyses indicate that the SRO in our system has an independent existence. Presence of SRO due to 3D short ranged correlations, that coexist with LRO has also been

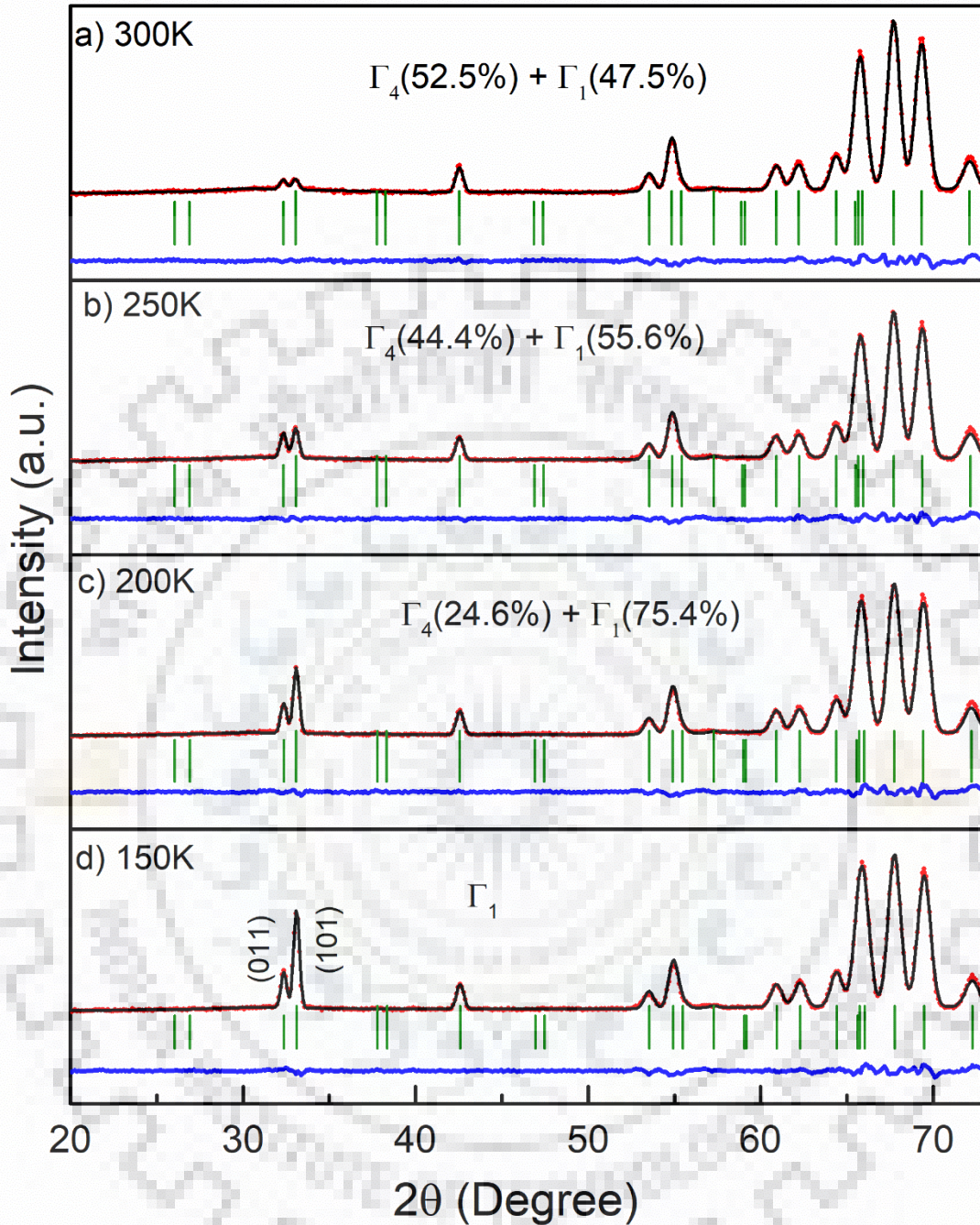


Figure 4.8. Experimental and refined powder neutron diffraction pattern for various temperature in the spin reorientation region measured at G4.1.

observed in MnO_2 [202]. However, in MnO_2 , the correlation length remains nearly constant with temperature, while in the case of NFM as shown in Figure 4.4 and 4.5, we observe that

there is a systematic increase in correlation length. Moreover, the position of Q_{centre} shows a shift towards the center of the LRO peaks just like in the case of MnO_2 [202].

The origins of the 3D SRO in NFMO can be attributed mainly to the difference in the nature of the isotropic exchange interactions arising from presence of two different transition metal ions. The random distribution of Fe and Mn leads to three different types of interactions, viz. Fe-Fe, Mn-Mn, Fe-Mn. The nn Fe-Fe interactions are isotropic with $J_{ab}(J_c) \sim -5.4$ meV. The Mn-Mn interactions are found to be $J_{ab} = 0.83$ meV and $J_c = -0.58$ meV, indicating an in-plane ferromagnetic and out-of-plane anti-ferromagnetic interaction. Interestingly it is found from Monte-Carlo simulations and first principles calculations, that the Mn-Fe interaction is highly anisotropic with $J_{ab} \sim 4.16$ meV and $J_c \sim 0.87$ meV [203]. Thus the variations in J can lead to a short ranged ordering of $\text{Fe}^{3+}/\text{Mn}^{3+}$ spins, that coexist with the predominant long ranged order.

4.3.1.2 High temperature (400 – 120 K) neutron diffraction measurements

High temperature (400 – 120 K) neutron diffraction measurements performed on G4.1, LLB have been studied in detail using FULLPROF suite of Rietveld refinement. Magnetic Bragg peak is not observed in the 400-320 K temperature range which indicate the absence of long range ordering of $\text{Fe}^{3+}/\text{Mn}^{3+}$ ions. However, we observe the signature of diffused scattering at 400 K with a broad peak near 32° as discussed in the previous section. This indicates the development of short range ordering above T_N .

In Figure. 4.8, we show the neutron diffraction patterns between 300 and 150 K covering the different magnetic structures. In Figure.4.8 (a), we observe the development of magnetic Bragg peaks superimposed on the diffused scattering peak. At 300 K, (Figure 4.8(a)) the intensity of magnetic Bragg peak is very low but the magnitude of (011) is little bit higher than (101), thus indicating the direction of easy axis towards x - axis which again confirms G - type ordering with majority of $\Gamma_4(G_x, F_z)$ magnetic structure. The pattern shown in Figure 4.8 (a) was refined with $\Gamma_4+\Gamma_1$ structure which resulted in small magnetic moments of 0.28(4) and 0.16(2) μ_B associated with Γ_4 and Γ_1 respectively. The quality of 300 K refinement data for pure Γ_4 magnetic structure or pure Γ_1 magnetic structure is not good resulting in the higher value of χ^2 . The presence of Γ_4 can be attributed to the presence of ordering arising due to Fe-

Fe interactions as seen in all parent orthoferrites [100] whereas the observation of Γ_1 (G_y) structure is attributed to altered Fe-Mn interaction due to the large single ion anisotropy of Mn^{3+} ions. This aspect is discussed further in next section.

The small value of the moment suggests that complete ordering is not achieved even though the FWHM is resolution limited. With decreasing temperature, the moments associated with Γ_4 and Γ_1 structures (M_x & M_y) (shown in Figure 4.9) increase in a gradual manner with a maximum near 250 K. From 250 K, the contribution from Γ_4 (G_x, F_z) starts to decrease, with an increase in the Γ_1 magnetic structure where the (101) peak start to increase as shown in Figure 4.8(b). Further on lowering of temperature, an increase in the ratio of $I(101)/I(011)$ is observed. At 200 K (Figure 4.8(c)), the magnetic structure is best refined by a mixture of Γ_1 and Γ_4 where the two phases exist in a ratio of 24.6:75.4, respectively. As the Γ_1 phase corresponds to G_y , the increase in Γ_1 volume fraction indicate the rotation of magnetic moments from x -axis towards y -axis on lowering the temperature. Finally, at 150 K (Figure 4.8 (d)) ratio of intensities of (011) and (101) becomes 1/3 indicating the existence of only one

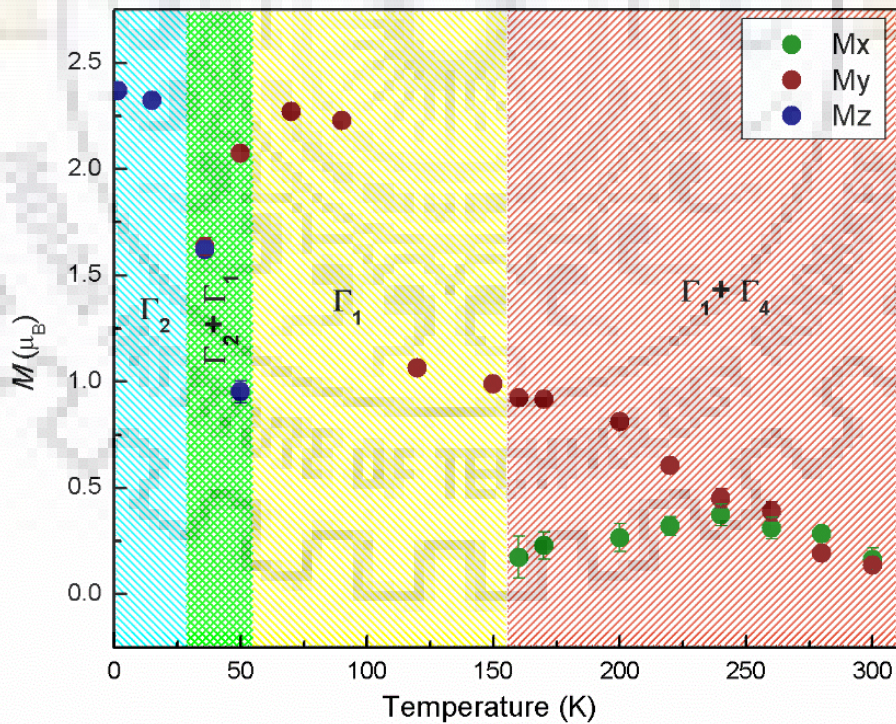


Figure 4.9 Temperature dependence of three components of ordered Fe^{3+} magnetic moment obtained from Rietveld refinement of powder neutron diffraction

magnetic phase, i.e. Γ_1 till 90 K. Interestingly, M_y shows a sudden increase in the range 100-120 K. From Figure 4.9, a gradual decrease in x component of magnetic moment is observed, while y component of magnetic moment increases.

4.3.1.3. Low temperature (1.5 – 90 K) neutron diffraction measurements

At 90 K (Figure 4.10 (a)), the best fit is obtained for Γ_1 representation, i.e., the G_y structure. The spins point in the y direction and the M atoms in the unit cell arrange as G -Type antiferromagnet as shown in Figure 4.11 (b). Also we do not observe any ferromagnetic component due to canting of the spins in accordance with Γ_1 representation. Thus in NFM, below T_N , the magnetic structure belongs to the Γ_1 representation with the y direction as easy axis, unlike the usual trend observed in orthoferrites (pure as well as substituted one at R or M sites) in which the first magnetic ordered structure belongs to Γ_2 (with moment along x direction) or Γ_4 (with moment along z direction) representations. Few orthoferrites, for instance, $\text{Dy}_{0.5}\text{Pr}_{0.5}\text{FeO}_3$, attain magnetic structure represented by the Γ_1 in the low-temperature phase after a spin reorientation transition from Γ_4 (high-temperature phase)[120]. In $\text{TbFe}_{0.5}\text{Mn}_{0.5}\text{O}_3$, the Γ_1 phase develops below spin reorientation transition from Γ_4 (high-temperature phase) as a co-existing phase with the high temperature Γ_4 phase as shown in Table 4.1[83]. Similarly, in DyFeO_3 , the Γ_1 phase is attained below 35 K [52]. Thus the Γ_1 phase can be attributed to the large single ion anisotropy of RE ions in Dy and Tb based orthoferrite compounds. However, in NFM, the Γ_1 phase seems to be the preferred magnetic ordering in the wide temperature range between two spin reorientations observed in the whole temperature range. Since the single ion anisotropy of Nd is much smaller and could be neglected in this high temperature region, the development of Γ_1 phase can be attributed to the single ion anisotropy of Mn ion. The Hamiltonian corresponding to single ion anisotropy term of Mn/Fe ions is given by $DS_z^2 - E(S_x^2 - S_y^2)$, where D and E are anisotropic constants. The necessary condition for stability of Γ_1 structure is $E > 0$ and $D > -E$ [48].

Though Fe and Mn ions are in the +3 oxidation state, the total wave function of Fe^{3+} ($S = 5/2$) has A_{1g} symmetry, which is like S -like and hence isotropic. On the other hand, in Mn^{3+} ($S = 2$), the total ground state wave function is E_g -type, which is highly anisotropic. From electron spin resonance studies of transition metal octahedral complexes, it is found that the values of D and E in Mn^{3+} complexes are almost two orders of magnitude larger than that in Fe^{3+}

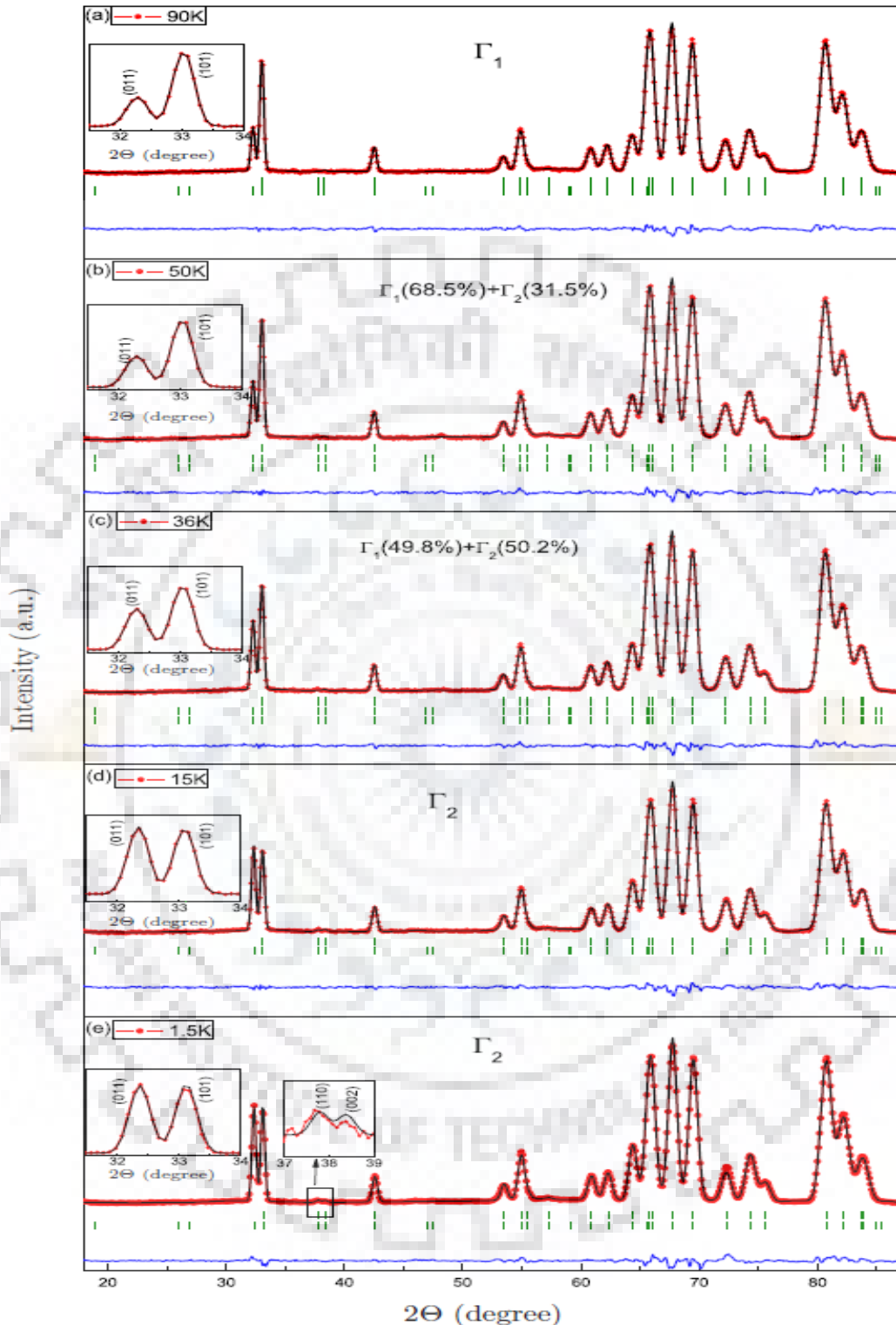
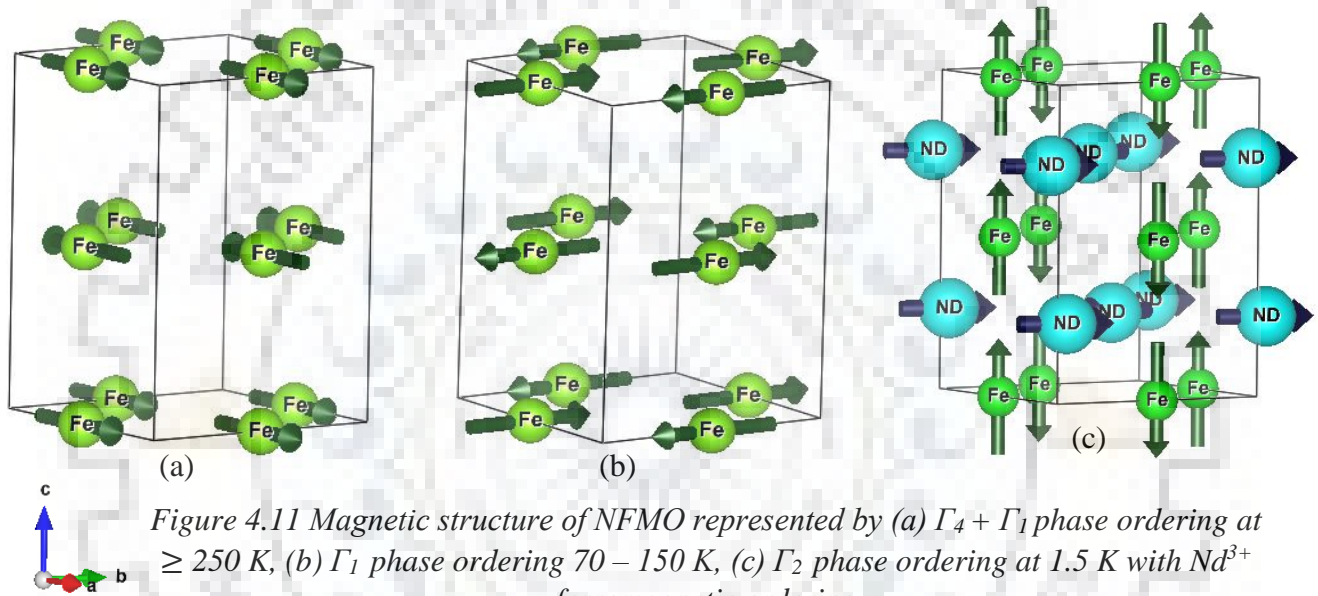


Figure 4.10 Experimental and refined neutron diffraction patterns of NFM0 for various temperatures from 1.5 to 90 K measured at DIB (CRG). Inset shows the changed in the magnetic Bragg peak as a function of temperature. Inset in (e) weak magnetic signal at 38° due to Nd magnetism (f_x)

complexes[204]. Thus the easy axis of magnetization of Fe/Mn sublattice is decided by the large single ion anisotropy of Mn^{3+} ion. To the best of our knowledge, this is first report of antiferromagnetic ordering with Γ_1 representation above spin reorientation transition temperature in orthoferrites.

At 50 K (Figure 4.10 (b)), an increase in the ratio of intensities of the (011)/(101) peaks is observed, indicating the process of ongoing reorientation. At this temperature, the magnetic structure is best refined by a mixture of Γ_1 and Γ_2 , wherein the two phase exist in a ratio of



68.5:31.5, respectively. The Γ_2 representation corresponding to $F_x G_z$ spin structure [as shown in Figure 4.10(c)], has the z direction as the easy axis for the major spin component. Similar to Γ_1 , the M sublattice spins also order as G -type in Γ_2 representation (M_z). At 36 K, the diffraction pattern is best fitted to combination of Γ_1 and Γ_2 occurring in the ratio 49.8:50.2 [Figure 4.10(c)]. From Figure 4.5, a gradual decrease in the y component of magnetic moment is observed, while there occurs a corresponding increase in the z component.

Finally, as shown in Figure 4.10 (d) and (e) for 15 and 1.5 K, respectively, intensities of both the magnetic peaks are comparable which suggests the existence of only one magnetic phase, i.e. Γ_2 at low temperatures. This also confirms the fact that the z component of spins is aligned as G type antiferromagnet. The refinements for 15 and 1.5 K as shown in Figure 4.10 (d) and (e) confirm that the magnetic structure entirely belongs to Γ_2 representation at these

Table 4.1 Magnetic structural details and transition temperatures of $\text{NdFe}_{0.5}\text{Mn}_{0.5}\text{O}_3$ from present studies and comparison with literature for end compounds NdFeO_3 , NdMnO_3 and related compounds. We list the three magnetic moment components along with rare earth moment M_R and the corresponding representations for various temperatures

Compound	T_N (K)	Spin reorientation		Magnetic Moment (μ_B)					T (K)	Ref.
		Range	IR	M_x	M_y	M_z	M_R	χ^2		
$\text{NdFe}_{0.5}\text{Mn}_{0.5}\text{O}_3$	250	300-150	$\Gamma_4 \rightarrow \Gamma_1$	0.277	0.250	-	-	4.36	300	This work
				0.415	0.519	-	-	4.35	250	“
				-	0.991	-	-	4.4	150	“
		60-30	$\Gamma_1 \rightarrow \Gamma_2$	-	2.22	-	-	3.83	90	“
				-	1.62	1.63	-	3.85	36	“
				-	-	2.42	0.13	6.86	1.5	“
NdFeO_3	690	160-70	$\Gamma_4 \rightarrow \Gamma_2$	3.84	-	0.46	-	1.58	290	[100]
				1.24	-	0.965	1.10 ^a	1.76	1.5	[100]
NdFeO_3 (Single Crystal)				-	-	-	0.9 ^b	-	0.5	[99]
NdMnO_3	78		Γ_5	2.80	-1.08	-	-	1.3	21	[189]
NdMnO_3	78		Γ_5	2.89	-1.44	-	-1.2	1.3	1.5	[189]
NdMnO_3	73	15	Γ_5	2.44	-1.66	-	-	-	1.5	[106]
							1.06			
$\text{TbFe}_{0.5}\text{Mn}_{0.5}\text{O}_3$	295	35-25	$\Gamma_4 \rightarrow \Gamma_1$ $\rightarrow \Gamma_4$	-	-	-	0.6	-	2	[83]
$\text{YFe}_{0.55}\text{Mn}_{0.45}\text{O}_3$	365	300	$\Gamma_4 \rightarrow \Gamma_1$	1.51	-	0.29	-	4.01	340	[41]
				-	3.4	0.16	-	5.46	2	[41]

temperatures. At 1.5 K, the maximum magnetic moment of 2.42 μ_B is obtained from the analysis, which is comparable to the value 2.2 μ_B estimated by Troyanchuka *et. al.*[110]

At 1.5 K, we observe the development of an additional weak magnetic signal at 38.2°, which is due to the ferromagnetic component of the Γ_2 representation. Hence the refinement was carried out assuming ordering of Nd spins in the Γ_2 representation corresponding to $F_x C_y$ arrangement, which yields a magnetic moment with a maximum limit to 0.13 μ_B . However, magnetic Bragg peak related C_y ordering of Nd spins is not observed, which should occur at 25°. Thus, the absence of antiferromagnetic ordering (C_y arrangement) suggests that the nature

of Nd ordering is ferromagnetic only. This is unlike the case of the NdFeO₃, which has antiferromagnetic ordering (C_y) with a moment value of $\sim 1 \mu_B$ as mentioned in Table 4.1. In NdMnO₃, the ferromagnetic component (without any antiferromagnetic ordering) of Nd develops in the z direction with a relatively high value of $1.2 \mu_B$ as in Table 4.1. The observed value of Nd magnetic moment ($0.13 \mu_B$) lies within the range of magnetic moments revealed from the DC magnetization data at low temperature. Though the ferromagnetic peak could arise due to canting of Fe/Mn spins, the observed value of $0.13 \mu_B$ is one order of magnitude higher compare to the moment arising due to DM interaction between canted spins of Fe/Mn ions. This value of magnetic moment, the large remanent magnetization, and coercivities from M - H loops indicate a role of the ferromagnetic polarization of Nd³⁺ sublattice in spin reorientation process of Fe/Mn spins which will be explained in detail in the next section. The variation of magnetic moments along all the three directions viz. M_x , M_y and M_z with the temperature is shown in Figure 4.9

4.3.1.4 Neutron depolarization

To establish the presence of ferromagnetic component further, the depolarization of incident polarized neutrons transmitted through the sample was checked. It may be noted that the incident neutron beam should not get depolarized for antiferromagnetic ordering. Figure 4.12 shows temperature dependence of the flipping ratio of polarized neutron spins. It remains constant down to ~ 75 K, below which it decreases slowly. The observed decrease in the flipping ratio confirms the presence of ferromagnetic correlations, as observed in the magnetization and neutron diffraction study. The slow decrease in the flipping ratio with temperature agrees well with neutron diffraction measurements where the volume fraction of the magnetic phase Γ_2 phase is directly correlated with the ferromagnetic component of the sample.

From the neutron diffraction, we can conclude that an antiferromagnetic G -type ordering exists in the mixture phase of Γ_4 and Γ_1 irreducible representation at 300 K and below 250 K (which is T_N according to magnetization data). Below 150 K, magnetic ordering is present in pure Γ_1 irreducible representation with the spins aligned along the b direction. The magnetic ordering in Γ_1 representation does not have any associated weak ferromagnetism due to canting of the spins. Spins start to reorient below 75 K and a new magnetic phase with Γ_2 representation

appears in combination with Γ_1 . An associated weak ferromagnetism also appears correlated to the Γ_2 phase. This is very clearly evident from the magnetization and depolarization measurements. The spin reorientation transition completes below 25 K and only one phase with Γ_2 (F_x , G_z) representation exists having G_z antiferromagnetic ordering and a weak ferromagnetic component due to Nd spins.

4.3.1.5 Phenomenological explanation of spin reorientation at low temperature

The process of reorientation, which is common to all orthoferrites, arises due to rotation of

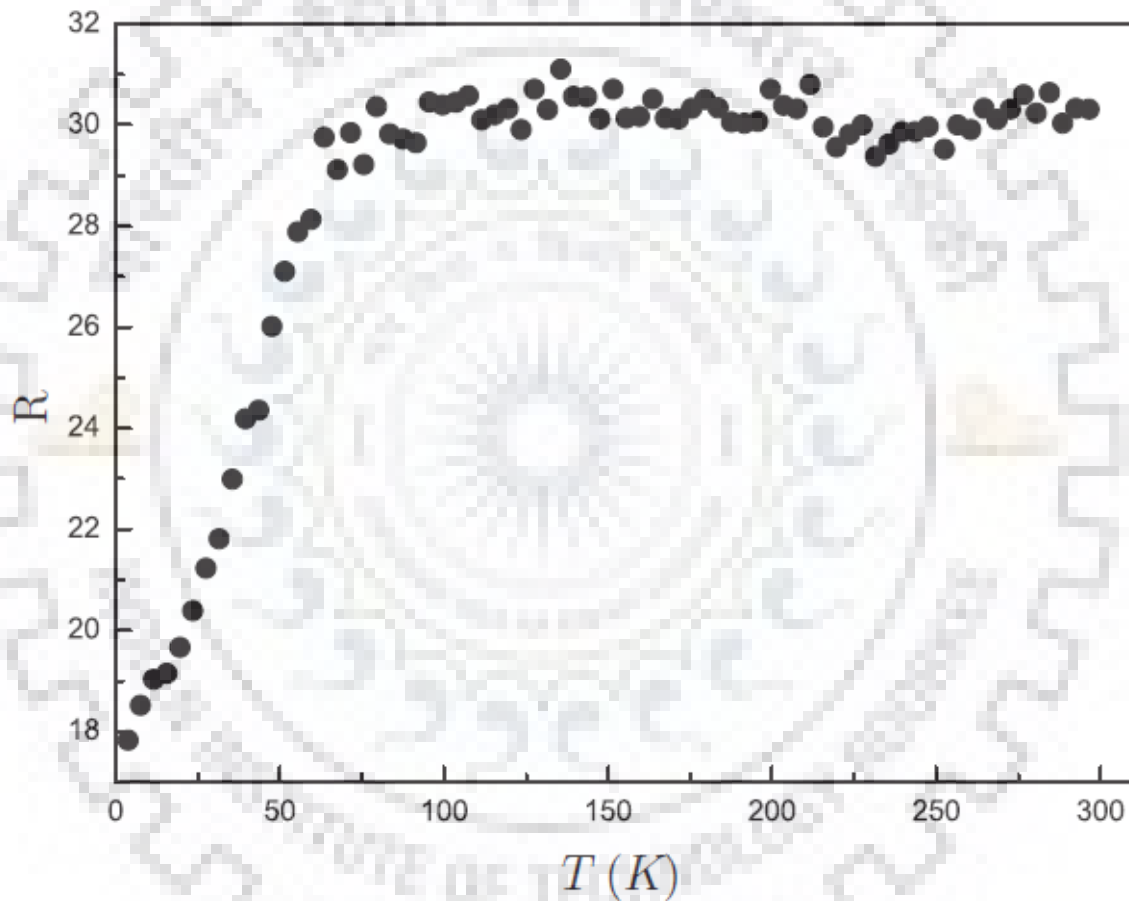


Figure 4.12 Temperature variation of flipping ratio (R) under an applied magnetic guide field of 50 Oe for NFM0. Polarized neutron spectrometer was used for measurement.

easy axis of magnetization with temperature or external magnetic field. Initially, it was believed that the temperature variation of anisotropic constants alone can be responsible for the spin reorientation. Horner *et. al.* [57] explained the reorientation process in terms of

variation of easy axis as a function of temperature by means of a simple Hamiltonian $H = K_1 \sin^2 \theta + K_2 \sin^4 \theta$, where K_1 and K_2 are the temperature-dependent anisotropic constants and θ is the angle of easy axis rotation. However, it was found later on that the antisymmetric and anisotropic symmetric exchange interaction between R and M spins are primarily responsible for the reorientation process [48]. In the parent compound NdFeO_3 , the spin reorientation occurs in the ac plane (i.e., the easy axis moves from a (x) to c (z) direction in a continuous manner between temperatures T_2 and T_1 below T_N). However, in NFMO, we observe the spin reorientation to happen in the bc plane resulting in the rotation of easy axis from b (y) to c (z) direction, between 75 and 25 K.

Below 150 K, spin configuration is $\Gamma_1 (A_x, G_y, C_z)$. In this configuration, there is no ferromagnetic component of magnetic ordering. At low temperatures the magnetic ordering is described as $\Gamma_2 (F_x, C_y, G_z : F_x^R, C_y^R)$, which has ferromagnetic components. Therefore, the reorientation region can be depicted as $\Gamma_{12} (G_x, C_y, F_z, A_x, G_y, C_z : F_x^R, C_y^R)$ in the region 70-20 K [48]. Thus in NFMO, the easy axis of the M spins rotates in the bc plane continuously in the spin reorientation region. We define a rotation angle θ , which describes the rotation of the easy axis. In the low temperature spin reorientation region, let θ correspond to the angle of

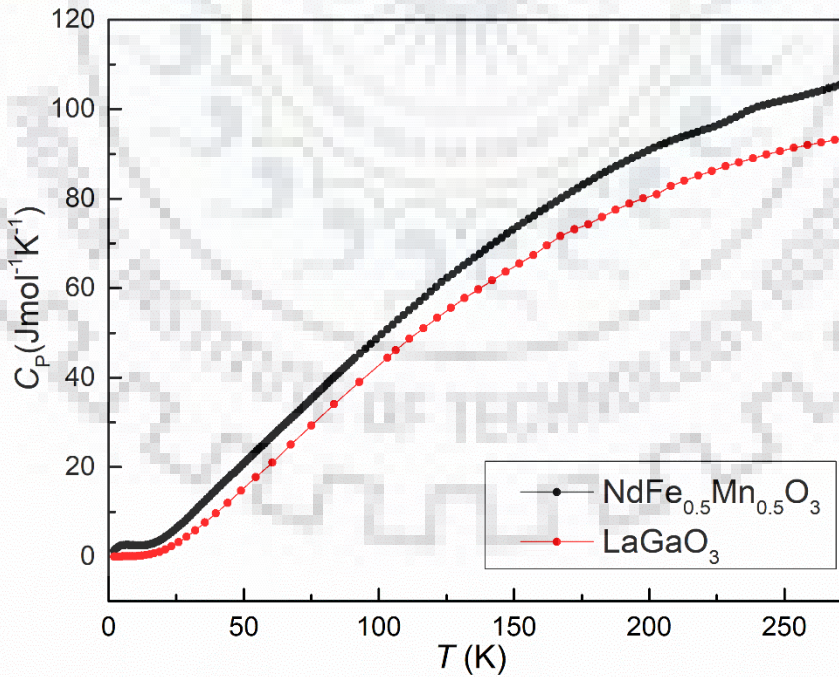


Figure 4.13 Specific heat of $\text{NdFe}_{0.5}\text{Mn}_{0.5}\text{O}_3$ and LaGaO_3

rotation of the easy axis in the bc plane, which varies between 0 and $\pi/2$ as the temperature is varied. Similar to the analysis given by Yamaguchi [48], one can understand the process of reorientation by means of effective fields acting on the M^{3+} spins generated by the anisotropic Nd- M interactions. The effective fields due to isotropic Nd- M interactions do not intend to change the magnetic symmetry. Below a certain temperature, θ starts increasing, and the terms proportional to $\text{Sin}\theta$ in free energy expression become nonzero. As a result, new anisotropic effective fields develop on M^{3+} spins, which are proportional to the antisymmetric Nd- M interactions. Due to these interactions, developed effective fields act along the z direction on the M^{3+} spins. Thus, the sublattice magnetization undergoes rotation in order to align parallel to the new effective field along z direction keeping the antiferromagnetic configuration.

4.3.2 Specific heat measurement

The heat capacity of NFMO for the temperature range 2-300 K is shown in Figure 4.13 along with the heat capacity for non-magnetic LaGaO₃. As shown in Figure 4.14, the magnetic contribution (ΔC_M), the specific heat of NFMO was subtracted from that of LaGaO₃ where the magnetic specific heat in the region corresponding to the PM-AFM transition is shown.

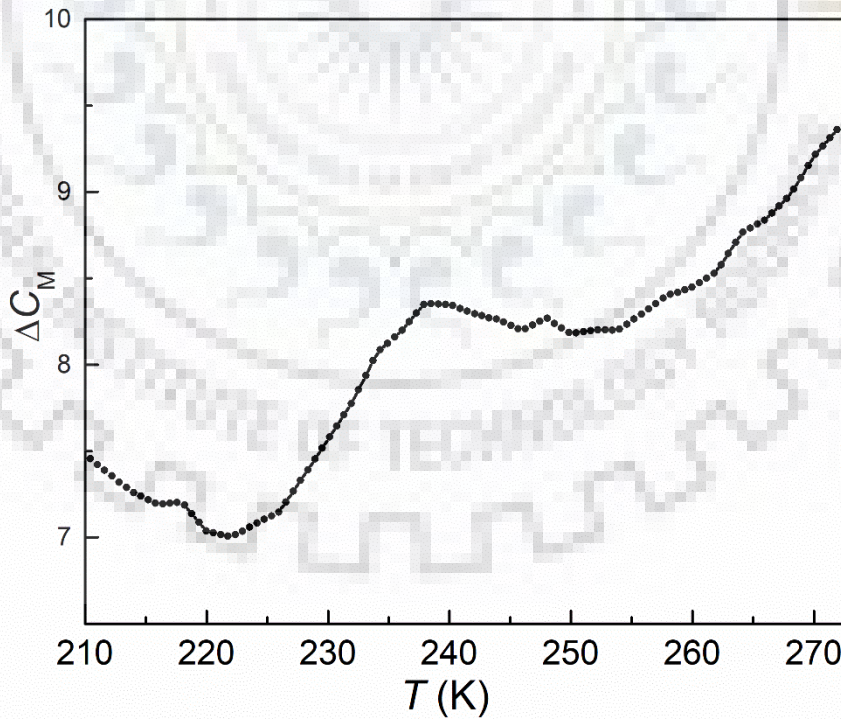


Figure 4.14 Magnetic contribution of specific heat of NFMO in the PM-AFM transition region

However a clear λ -shaped anomaly indicating a second order phase transition is not observed. This can be attributed to the presence of two different transition metal ions. Previous studies by Mihalik *et. al.* [109] show that with increase in Fe content the transition in $\text{NdMn}_{1-x}\text{Fe}_x\text{O}_3$ becomes broader. The integration of $\Delta C_M/T$, in the temperature range 220-280 K, yields a magnetic entropy value of 2.7 as $S_M = \int_0^T \Delta C_M/T$. The expected total magnetic entropy from Nd^{3+} and $\text{Fe}^{3+}/\text{Mn}^{3+}$ system is 4.09 (ground state multiplet of Nd^{3+} plus ground state multiplet of $\text{Fe}^{3+}/\text{Mn}^{3+}$)[59]. The reduction in experimental value can be attributed to the fact that the magnetic transition is not complete in the range 220 K even till 300 K. Evidences of short ranged correlations even above 300 K exist from neutron diffraction studies which can be attributed to randomness in the distribution of Fe and Mn atoms.

The specific heat measurements performed in the temperature range 2-30 K in the presence of 0, 3, and 5T applied field are shown in Figure 4.15. Near 5 K, Schottky anomaly is observed which is due to the crystal field splitting of the $4f$ states of Nd^{3+} ions similar to $\text{NdFe}_{0.3}\text{Mn}_{0.7}\text{O}_3$ [205]. We do not observe any second order phase transition associated with independent ordering of Nd^{3+} spins in the given temperature range unlike in NdFeO_3 [100] Application of field does not cause any appreciable change.

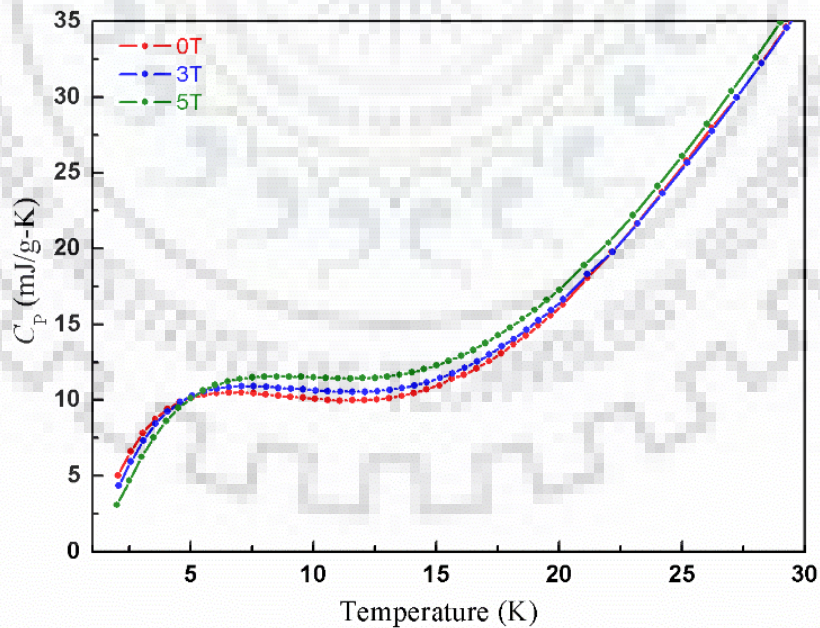


Figure 4.15. Specific heat of NFMO under zero magnetic field and applied field of 3 T and 5 T which shows the presence of Schottky anomaly at lower temperature region.

The total specific heat was fitted using a sum of lattice and Schottky terms as mentioned below.

$$C_p = C_{latt} + C_s \quad (4.2)$$

$$C_{latt} = B_3 T^3 + B_5 T^5 \quad (4.3)$$

$$C_s = \frac{1}{2} R \sum_{i=1}^2 w_i \frac{\left(\frac{\Delta_i}{k_B}\right)^2 \exp\left(\frac{\Delta_i}{k_B}\right)}{\left[1 + \exp\left(\frac{\Delta_i}{k_B}\right)\right]^2} \quad (4.4)$$

We have calculated the Debye temperature from the lattice part of the specific heat which is given as eq. 4.5

$$T_D = \left(\frac{12p\pi^4 R}{5B_3}\right)^{1/3} \quad (4.5)$$

where R is universal gas constant, p is the number of atoms in each unit cell. The Debye temperature obtained is around 420 K and is magnetic field independent. In the Schottky term, w_i is the weighted factor for different splitting Δ_i . In the lattice term, B_3 and B_5 are the coefficients [206].

The Schottky-like anomaly near 5 K, which is due to the splitting of lowest Kramer's doublet which is denoted as Δ/k_B in units of temperature. The crystal field effects cause splitting of $^4I_{9/2}$ state into five Kramers doublets[96]. The further splitting of Kramer's doublet is caused by the molecular field (H_{mf}) due to the Nd/Fe(Mn) interactions along with the Nd-Nd interactions. It is known that the magnetism in Kramers doublet ions is exchange driven rather than the bare crystal field splitting [207]. In the given temperature range (2 – 30 K), a satisfactory fit for specific heat was obtained for our system when we consider a sum of two Schottky terms with corresponding splittings Δ_1 and Δ_2 .

The values of Δ_1 for 0 and 5 Tesla are 6.70 and 8.33 K respectively. The values obtained are slightly higher than that of NdFeO₃ for which $\Delta \sim 5.6$ K [96]. The splitting in NdMnO₃ is much ($\Delta=21.6$ K) higher in comparison to NdFeO₃ due to Nd-Mn exchange interactions which is ferromagnetic in nature [103], [207]. The increase in values clearly can be attributed to the Nd³⁺-Mn³⁺ interactions which compete with pre-dominantly antiferromagnetic Nd³⁺-Fe³⁺ and Nd³⁺-Nd³⁺ interactions. Based on the values of the Schottky levels, we estimate values of molecular field and magnetic moment of Nd³⁺ ion. We have assumed that the molecular field

remains unchanged in spite the presence of external magnetic field. The splitting of Kramer`s doublet at 0 T and 5 T are given as $\Delta(0) = 2\mu H_{mf}$ and $\Delta(5) = 2\mu[H_{mf} + 5]$ respectively, where H_{mf} is molecular field acting on Nd^{3+} ion and μ is its magnetic moment[208]. Based on the above equations, the values obtained are $H_{mf} = 6.2$ T and $\mu = 0.8 \mu_B$ which however is greater than the value of Nd^{3+} moment from our neutron diffraction at 1.5 K. The values of molecular field interaction show that the interaction between Nd^{3+} - $\text{Mn}^{3+}/\text{Fe}^{3+}$ dominates in comparison to Nd^{3+} - Nd^{3+} interaction, thereby suppressing the independent ordering of Nd^{3+} moments.

4.4 Conclusion

Magnetic structure of polycrystalline $\text{NdFe}_{0.5}\text{Mn}_{0.5}\text{O}_3$ is studied using powder neutron diffraction in the temperature range 400 – 1.5 K. Diffused scattering is seen at 400 K, which is most prominent at 300 K and continues all the way till 1.5 K, the diffused scattering peak can be attributed to short ranged spin – spin correlation involving nearest and next nearest neighbor interactions. From 300 K till 1.5 K, the short ranged ordering coexists with the long ranged magnetic structure. With decreasing temperature, the correlation length of short range ordering increases while FWHM decreases.

At 300 K, the $\Gamma_4 (G_x, C_y, F_z)$ magnetic structure develops with $\Gamma_1 (A_x, G_y, C_z)$, coexisting with diffused scattering. At T_N , the $\text{Fe}^{3+}/\text{Mn}^{3+}$ develops Γ_1 magnetic structure superseding the Γ_4 structure. Unlike NdFeO_3 , the irreducible representation of magnetic symmetry in NFMO is Γ_1 below T_N with spins aligned along b direction in the G type magnetic structure. This is highly unusual, since this magnetic representation develops at lower temperature, below the spin reorientation transition, in most of the orthoferrites. The origin of this representation is attributed to the large single ion anisotropy of the Mn^{3+} ions, which is an order of magnitude larger than that of Fe^{3+} ion. However, a competing interaction starts to become prominent between the rare earth spins and transition metal ions, which results in a complete reorientation of Fe/Mn spins. The two-fold gradual spin reorientation occurs in NFMO, one between 150 and 300 K from Γ_4 to Γ_1 and other between 75 and 25 K from Γ_1 to Γ_2 . At the lowest temperature, the magnetic structure entirely belongs to Γ_2 representation with G type antiferromagnetic structure and spin is aligned along c axis. In addition, the ferromagnetic

component (F_x) due to Nd spins develops in Γ_2 phase with a value of $0.13 \mu_B$ obtained from our Rietveld analysis. I also found evidence of ferromagnetic correlations from neutron depolarization measurements. However, a ferromagnetic moment of $0.13 \mu_B$ is rather large in comparison to the expected value solely from the antisymmetric interactions between Mn and Fe. This confirms the definite role of Nd^{3+} spins in reorienting the Mn and Fe spins at lower temperatures.

From specific heat measurements performed at different applied fields in the temperature range 2 – 30 K, Schottky anomaly is observed around 5 K which has been fitted using 2 – level model. The values of Schottky splitting Δ , suggest that the Nd-Fe/Mn molecular field dominates at low temperatures.



Magnetic and thermal properties of Nd_{0.5}Dy_{0.5}FeO₃

5.1 Introduction

Rare – earth orthoferrites $R\text{FeO}_3$ ($R = \text{La, Nd, Dy...}$) have been extensively studied for their potential multiferroicity, magnetoelectric effects and other functional properties like ultrafast optical control of spins[206][207]. The orthoferrites belong to the family of perovskites and crystallize into the structure having the orthorhombic space group $Pbnm$ similar to manganites, cuprates, nickelates and cobaltates[211]. However, unlike the highly distorted MnO_6 octahedra of the manganites, the FeO_6 octahedra shows least distortion with nearly equal Fe – O bond lengths at room temperature[100]. Due to strong isotropic exchange interactions between the Fe^{3+} spins, the orthoferrites have a relatively high Néel temperature of $T_{\text{N1}} \sim 700$ K, below which the Fe^{3+} spins order in G - type antiferromagnetic configuration expressed with Γ_4 (G_x, A_y, F_z)[100]. Here, G_x represents G -type antiferromagnetic ordering with moment direction aligned primarily along crystallographic a direction and F_z corresponds to the weak ferromagnetic component arising from the canting of the Fe^{3+} spins due to Dzyloshinski – Moriya interactions [52]. Due to the isotropic and anisotropic exchange interactions between R^{3+} and Fe^{3+} , the easy axis of Fe^{3+} spins undergo spin – reorientation from a axis to either b axis or c axis of the crystal. This can be a gradual rotation as a function of temperature as in NdFeO_3 [90] or an abrupt one near 35 K as in DyFeO_3 [51].

The orthoferrite NdFeO_3 is a canted G -type antiferromagnet with Néel temperature (T_{N1}) of 690 K [100]. Below T_{N1} , the magnetic structure of Fe^{3+} sublattice is represented by Γ_4 (G_x, A_y, F_z) [90]. As the temperature decreases below 200 K, the Fe^{3+} spins continuously rotate in the ac plane between 200 K to 105 K resulting in Γ_2 (F_x, C_y, G_z) magnetic structure below 105 K. Below 20 K, additional magnetic Bragg peak in neutron diffraction indicate development of C_y^R ordering of the Nd^{3+} moments which belongs to Γ_2 representation. The ordering of Nd^{3+} and Fe^{3+} moments are compatible with each other from group theory. Due to centro-symmetric

nature of the magnetic space group $D_{2h} (m'm'm)$, the magnetoelectric tensor is expected to be zero. At $T_{N2} \sim 1.05$ K, the Nd^{3+} - Nd^{3+} interaction gives rise to a second magnetic ordering of Nd^{3+} moments which is an independent long range order of G -type in nature. [99].

Another orthoferrite which has drawn considerable attention for its intriguing properties is $DyFeO_3$. Though $DyFeO_3$ and $NdFeO_3$ are isostructural, the degree of structural distortion in $DyFeO_3$ is much larger. Like other orthoferrites, the Fe^{3+} magnetic moments of $DyFeO_3$ order with $\Gamma_4 (G_x, F_z)$ representation below $T_{N1} (\sim 650)$ [52]. Near 35 K, an abrupt spin reorientation occurs which results in change of magnetic structure from Γ_4 representation to $\Gamma_1 (G_y)$ which does not have any ferromagnetic component. This is also known as Morin transition. The magnetic structure of Fe^{3+} with $\Gamma_1 (G_y)$ representation persists till the lowest temperatures at zero field. The peculiarity of this magnetic structure is the absence of a net magnetic moment in any direction. Due to large single ion anisotropy, the Dy^{3+} spins are confined to the $a - b$ plane. Below $T_{N2} \sim 4$ K, the Dy^{3+} moments arrange in the $\Gamma_5 (G_x^R, A_y^R)$ configuration making an angle of 33° with the b axis. The studies on similar compounds viz. $DyAlO_3$ and $DyCrO_3$, have also revealed the role of strong Dy^{3+} single ion anisotropy. The Γ_5 structure is not symmetry compatible with Γ_1 . Recent reports have shown that the Fe^{3+} spins orient to a different magnetic structure [212]. The overall reduction in symmetry due to the Dy^{3+} ordering results in linear magneto-electric effect. A large ferroelectric polarization is observed due to the weak ferromagnetic ordering induced by magnetic field along the c axis of the crystal [46].

In view of the differences in nature of Fe and R-ordering in $NdFeO_3$ and $DyFeO_3$, it would be extremely interesting to look at the intermediate system $Nd_{0.5}Dy_{0.5}FeO_3$. In this situation, one would expect a very complex interplay of spin, lattice and orbital degrees of freedom between the Nd/Dy and Fe sublattices and hence a new set of magnetic structures. Substitution of Dy ions at the Nd site apparently tunes the super-exchange interactions, influences the magnetic symmetry and spin reorientation through the interaction of Nd^{3+} and Dy^{3+} among themselves and also with Fe^{3+} . Particularly it would be interesting to probe the rare-earth ordering in the system along with the possibility of a magneto-electric effect. In the present work, we have experimentally studied the bulk magnetization, heat capacity, dielectric effect under magnetic field. Neutron diffraction measurements were performed to establish the

complex magnetic structure of NDFO compound as well as to understand the underlying mechanism of spin reorientation and the nature of rare-earth ordering in this compound.

5.2 Experimental Method

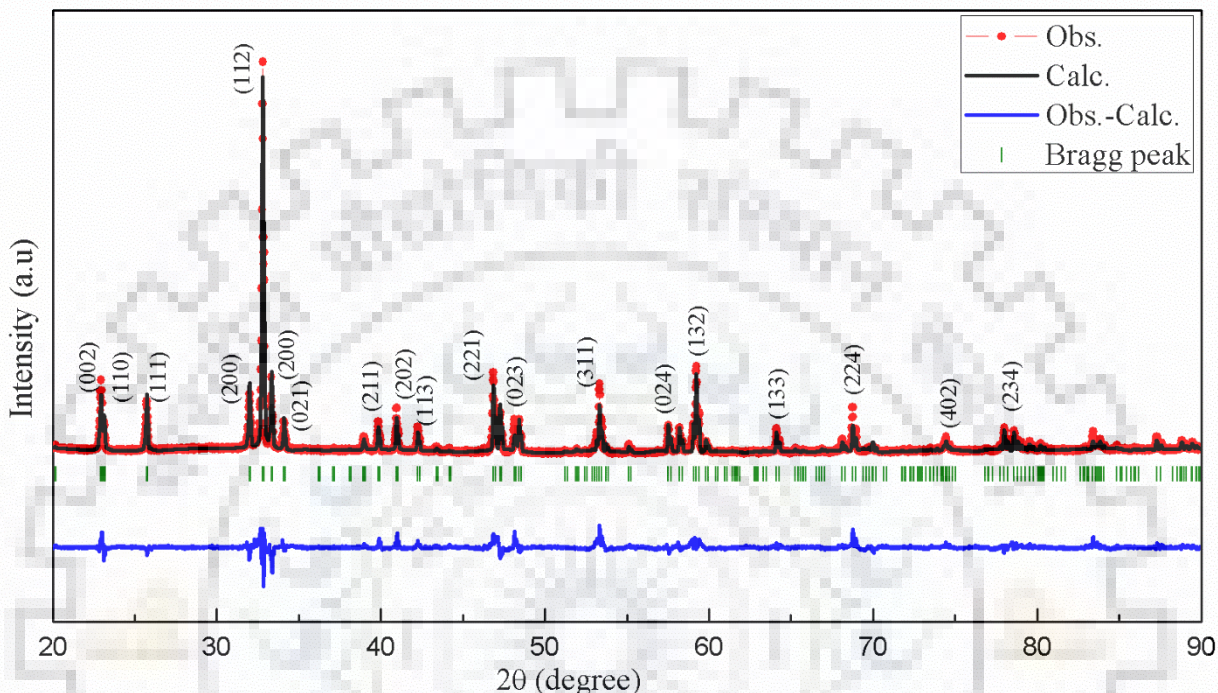


Figure 5.1 Observed X-ray diffraction pattern of NDFO at room temperature, refined using orthorhombic Pbnm space group

Powder sample of NDFO was synthesized using solid state reaction method. Nd_2O_3 , Dy_2O_3 and Fe_2O_3 were weighed according to appropriate stoichiometry and ground in an agate mortar for 12 hours. The heat treatment of the sample was carried out according to procedure explained in previous chapter. Structural phase of the sample was identified using a Bruker D8 two circle X-Ray diffractometer at $\text{CuK}\alpha$ wavelength. Bulk magnetization measurements were performed using vibrating sample magnetometer (VSM) module of the Quantum Design make Physical Property Measurement System (QD-PPMS). Zero field cooled (ZFC) and field (FC) measurements from 350 K to 5 K in 0.01 T field were carried out to identify the different magnetic transitions and their respective temperatures. Field variation of magnetization was carried out at various temperatures between 300 K and 5 K. Dielectric studies were carried out using an IM 3536 LCR meter between 2 to 300 K, at frequencies ranging from 1 KHz to 500 KHz in magnetic field values of 0, 0.1 and 1 Tesla. Heat capacity measurements in the

temperature range 2 – 200 K was carried out at zero field using a QD-PPMS. Additional heat capacity measurement in the milli-Kelvin range were carried out using the QD-PPMS with He³ option in fields of 0 and 5 T. Neutron diffraction studies at zero field were carried out at various temperature in the range of 1.5 – 300 K to identify the crystal as well as magnetic structure and their variations as a function of temperature. The studies were carried out a powder diffractometer G-41-I ($\lambda = 2.4206 \text{ \AA}$), at LLB, Saclay in France. The diffraction data were analyzed using FULLPROF suite of programs using the Rietveld method [169]. Magnetic structure was determined using irreducible representation from Basireps [213] and refined using FullProf.

5.3 Results and Discussion

5.3.1 Structural Characterization

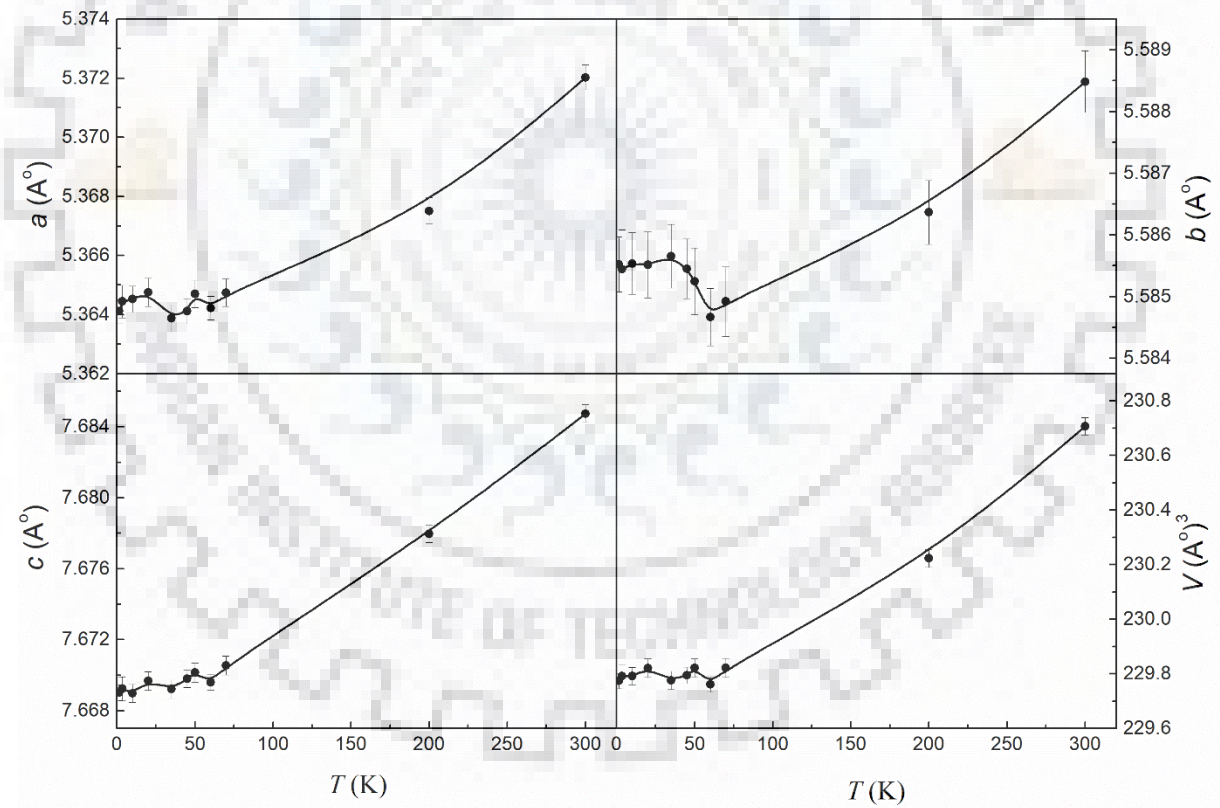


Figure 5.2 Temperature variation of lattice parameters and unit cell volume of NDFO

Figure 5.1 shows the room temperature powder X-Ray diffraction pattern of the NDFO along with refined pattern. The refinement confirmed that compound crystallizes in the

structure of orthorhombic $Pbnm$ space group. The refined structural parameters obtained from X-ray diffraction are listed in Table 5.1. The obtained a and c parameters of NDFO lie intermediate to that of $DyFeO_3$ and $NdFeO_3$ whereas the b parameter is closer to that of $DyFeO_3$. The obtained structural parameters from neutron and x-ray diffraction are comparable at room temperature.

Further, the neutron diffraction patterns were collected systematically at regular intervals between 1.5 K to 300 K. In table 5.1, the lattice constants along with Fe – O ($M = Fe$) and Nd (Dy) – O bond lengths of NDFO, obtained from the refinement of neutron diffraction data, are shown for 300, and 1.5 K along with the corresponding values obtained from room temperature X-ray diffraction data.

In Figure 5.2, shows the temperature variation of lattice parameters and unit cell volume of NDFO. We observe that all the three parameters show a continuous decrease till 50 K. From 50 K, b shows an increase till 30 K, below which it remains nearly constant. The trend in the lattice parameters are similar to that observed in $NdFeO_3$ [100]. The structural parameters refined from the neutron diffraction at 300 and 1.5 K are listed in Table 5.1. Three different Fe

Table 5.1 Structural parameters of $Nd_{0.5}Dy_{0.5}FeO_3$ obtained from neutron diffraction using Rietveld refinement for 300 K and 1.5 K

Parameters	300 K	1.5 K
a (Å)	5.3720 (5)	5.3643 (2)
b (Å)	5.5884 (6)	5.5860 (3)
c (Å)	7.6847 (9)	7.6686 (4)
Fe – O(1) (m) (Å)	2.0208 (8)	1.9661 (9)
Fe – O(2) (l) (Å)	2.0404 (19)	2.0176 (23)
Fe – O(2) (s) (Å)	2.0271 (20)	2.0373 (22)

– O bond lengths have been listed in Table 5.1 which correspond to the apical and in-plane bond lengths. Unlike the $RMnO_3$ manganites which have highly unequal bond lengths, the orthoferrites have nearly equal Fe – O bond lengths [101][105]. From Table 5.1 we can infer that there occurs a contraction in out-of plane bond lengths, while the in-plane bond lengths remain nearly constant with temperature. The changes in the lattice parameters close to 50 K coincides clearly with the spin – reorientation transition in NDFO observed from

magnetization and neutron diffraction measurements. This also indicates a strong possibility of magneto – elastic coupling within the spin reorientation region.

5.3.2 Magnetic Properties

As shown in Figure 5.3 and 5.4, zero field cooled (ZFC) and field cooled (FC) magnetization measurements were performed from 2 K to 300 K in presence of 100, 200, 500, 1000 and 5000 Oe external magnetic field values. Both parent compounds undergo transition from paramagnetic state to G - type antiferromagnetic state with magnetic structure $\Gamma_4 (G_x, F_z)$ near 700 K [100]. Thus, at 300 K, it has been expected NDFO is already in the antiferromagnetically ordered state with G – type structure and small ferromagnetic component (G_x, F_z) similar to DyFeO_3 and NdFeO_3 . As shown in Figure 5.3, a magnetic transition is observed in the ZFC-FC magnetization data below ≈ 75 K. In pure DyFeO_3 , an abrupt spin reorientation is observed at 50 K, which corresponds to $\Gamma_4 \rightarrow \Gamma_1$ transition[51]. The Γ_1 representation, which corresponds to antiferromagnetic G_y magnetic structure in Bertaut notation, does not contains any net effective ferromagnetic moment. Although our low field (100 Oe and 200 Oe) ZFC measurements show a drop in magnetization below 60 K, an increase in 100 and 200 Oe FC magnetization is observed contrary to the expected behavior from $\Gamma_1 (G_y)$ magnetic structure which belongs to low temperature phase of DyFeO_3 after abrupt spin reorientation. Such kind of peak in ZFC measurements can also be observed from a spin glass system, but ac susceptibility measurements (not shown) on NDFO rule out the possibility of a spin glass phase. As shown in Figure 5.4, the ZFC-FC measurements were also carried out at higher magnetic fields of 1000 and 5000 Oe. With increasing field, we see a gradual suppression of the downturn near 50 K, while at a field of 5000 Oe, the ZFC as well as FC magnetization show a continuous increase with field. As shown in inset of Figure 5.3, the magnetization also increases below 30 K during 100 and 200 Oe ZFC measurements.

As shown in Figure 5.5, M - H isotherm show qualitative as well as quantitative variation at different temperatures. At 300 K, the magnetization isotherm shows a slight non – linear behavior at high fields, along with a ribbon – like hysteresis loop at low fields as shown in the inset. The similar behavior is observed qualitatively for magnetization isotherms between 300 and 75 K. Below 75 K, M – H isotherm shows a nearly linear trend with a narrower hysteresis loop. The reduction in loop width coincides with the onset of magnetic transition in ZFC-FC

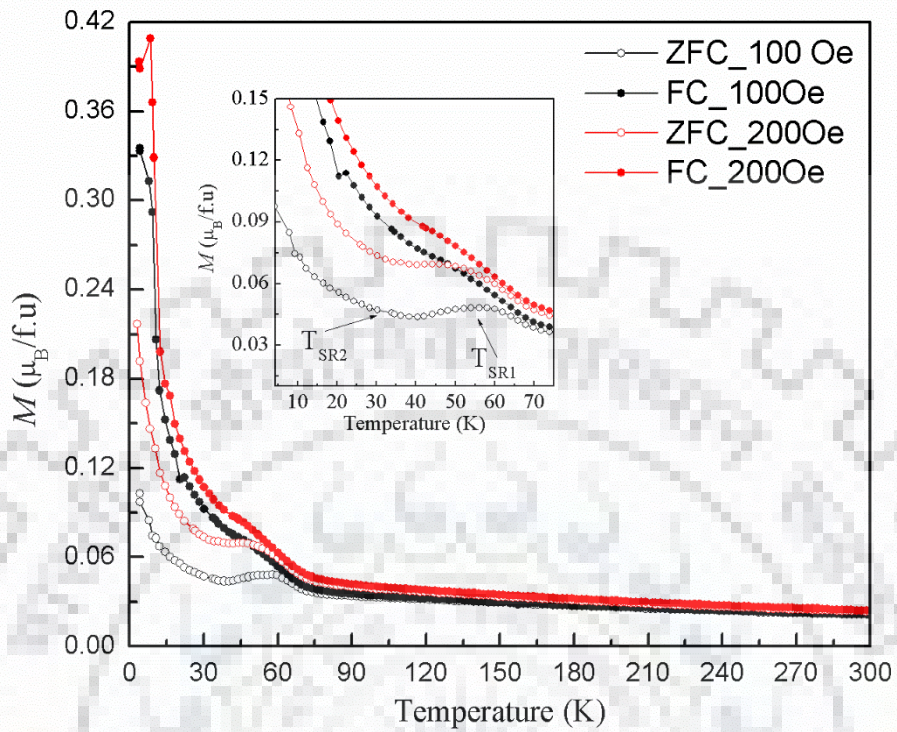


Figure 5.3 ZFC-FC plots of NDFO at 100 Oe and 200 Oe. In the inset transition due to spin reorientation is shown at $T_{SR1} = 60$ K and $T_{SR2} = 30$ K

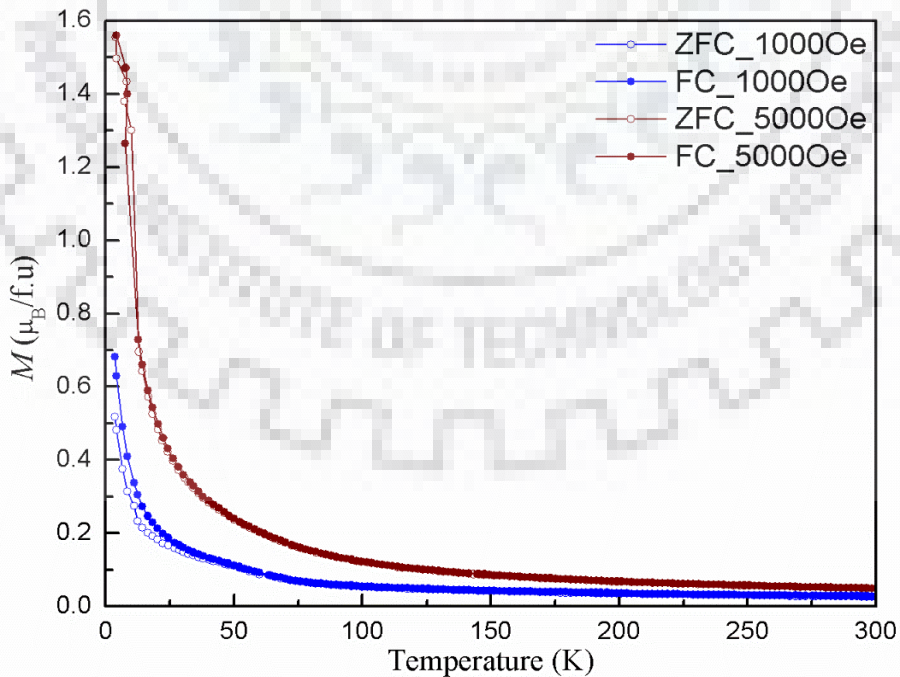


Figure 5.4 ZFC-FC plots of NDFO at 1000 Oe and 5000 Oe

measurements. Below 20 K, the magnetization in $M - H$ measurements show a non-linear behavior at high fields. At 5 K, the $M - H$ isotherm shows a completely different trend qualitatively as well as quantitatively. A large magnetization value of nearly $4 \mu_B/\text{f.u.}$ is

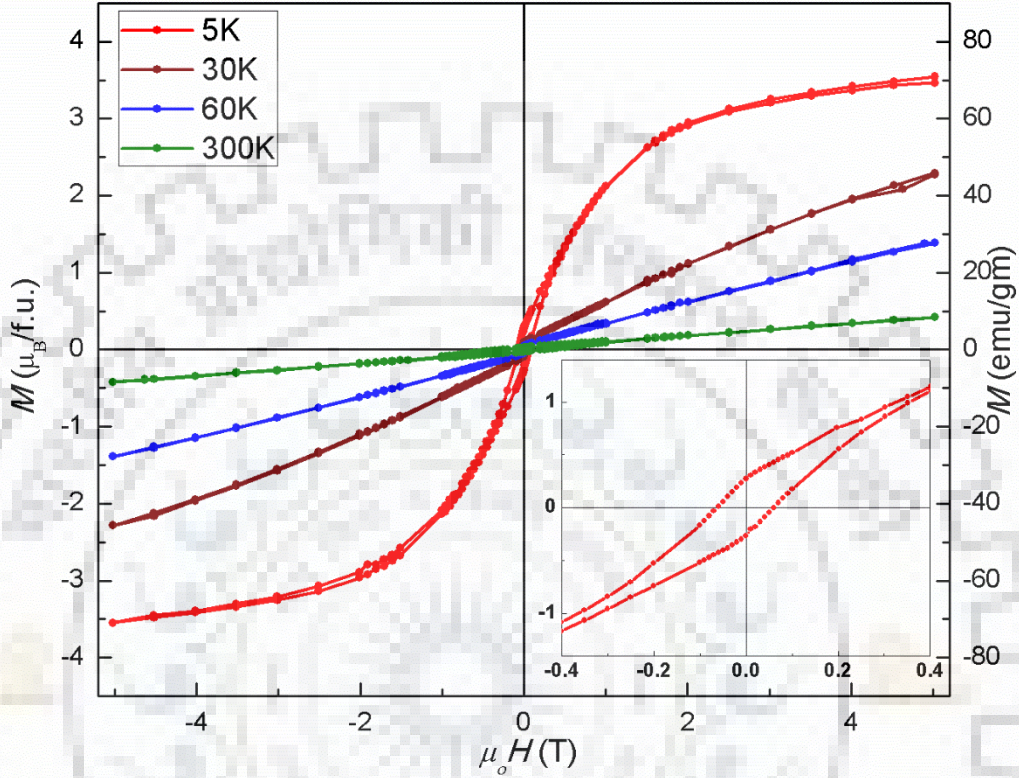


Figure 5.5 $M - H$ plots of NDFO at 5 K, 30 K, 60 K, 300 K, inset shows the $M - H$ at 5K in the field range $\pm 400\text{Oe}$.

attained at 5 T magnetic field. This can be attributed mainly to the large magnetic moment associated with the Dy^{3+} ($J = 15/2$) ion. Magnetization studies on single crystals of DyFeO_3 reveal that the magnetic moment of Dy^{3+} lies in the $a - b$ plane with an inclination of 33° with respect to the b axis. Thus in spite of 50% substitution by Nd atoms and polycrystalline nature of the sample, the values of magnetic moments are higher than the expected average value. The hysteresis loop parameters viz. coercivity and retentivity, even at 5 K suggest a possible ordering of the rare earth ions below 10 K. ZFC-FC and $M - H$ isotherms indicates the presence of a gradual spin reorientation below 75 K. The FC measurements also rule out the possibility of $G_y (\Gamma_1)$ magnetic structure without any ferromagnetic component which is usually observed as low temperature magnetic phase in DyFeO_3 . The ZFC and $M - H$ isotherms also infer a possibility of rare-earth ($\text{Dy}^{3+}/\text{Nd}^{3+}$) ordering at lower temperature (< 10 K). Magnetization

measurements cannot provide a conclusive evidence regarding the spin reorientation as well as rare earth ordering. Further, neutron diffraction measurements were carried out to understand the low temperature magnetic transition in NDFO.

5.3.3 Dielectric Properties

Since there is a prominent magneto-dielectric effect and field dependent ferroelectric polarization associated with Dy^{3+} ordering in DyFeO_3 , we have also performed dielectric studies in presence of applied field. The temperature variation of real (ϵ) and imaginary part (ϵ'') was measured at various frequencies between 5 KHz and 500 KHz at 0, 0.01 and 1 T. In Figure 5.6, plots of ϵ and loss factor $\tan(\delta)$ ($=\epsilon''/\epsilon'$) versus T are shown. At zero field, temperature variation of ϵ and $\tan(\delta)$ do not show any signature associated with spin reorientation below 100 K. Their rise above 200 K can be attributed to standard dielectric relaxor mechanisms. Moreover, we do not find any discernible changes in the magnitude of ϵ and $\tan(\delta)$ in presence of 1 T magnetic field. This clearly indicates absence of a

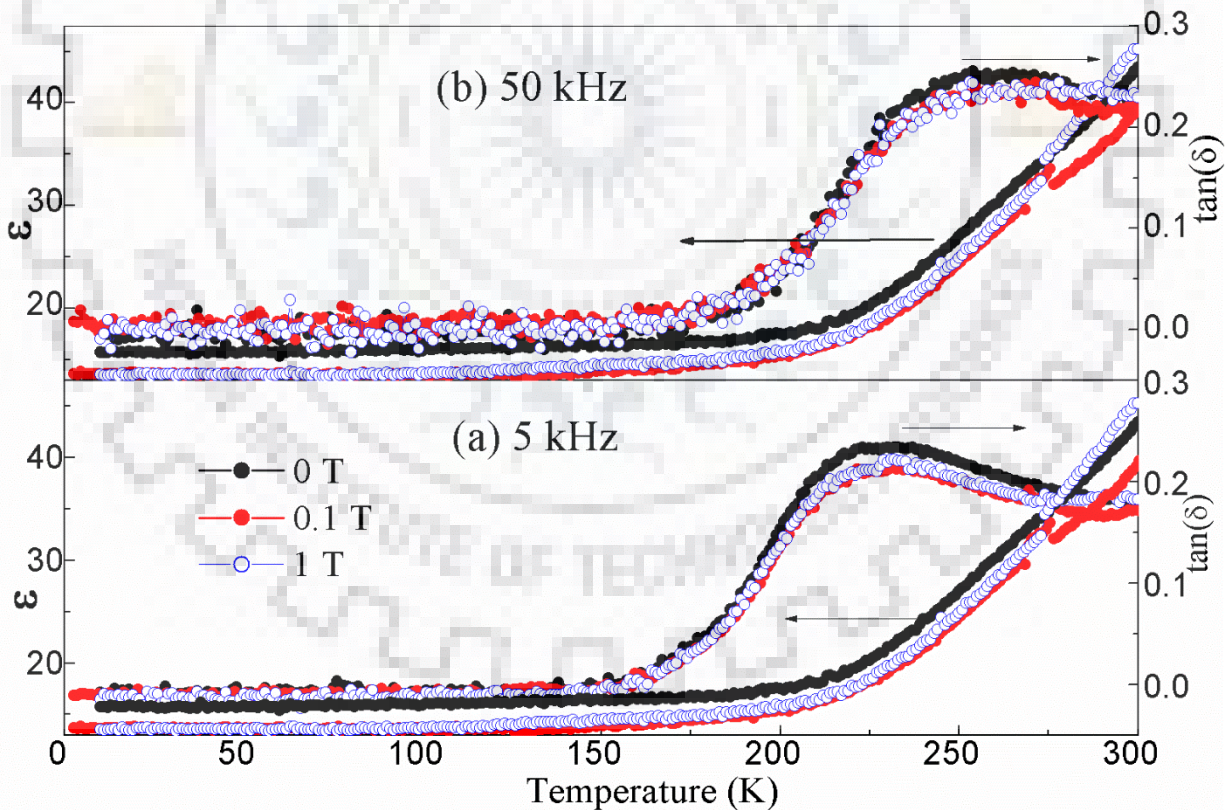


Figure 5.6 Temperature dependence of real part of dielectric constant (ϵ) and dielectric loss ($\tan(\delta)$) for a) 5 KHz and b) 50 KHz at various magnetic fields.

magnetodielectric effect, which is prominent in DyFeO_3 [46]. This suggests that the presence of Nd can significantly affect the ordering of Dy^{3+} moments.

5.3.4 Neutron Diffraction

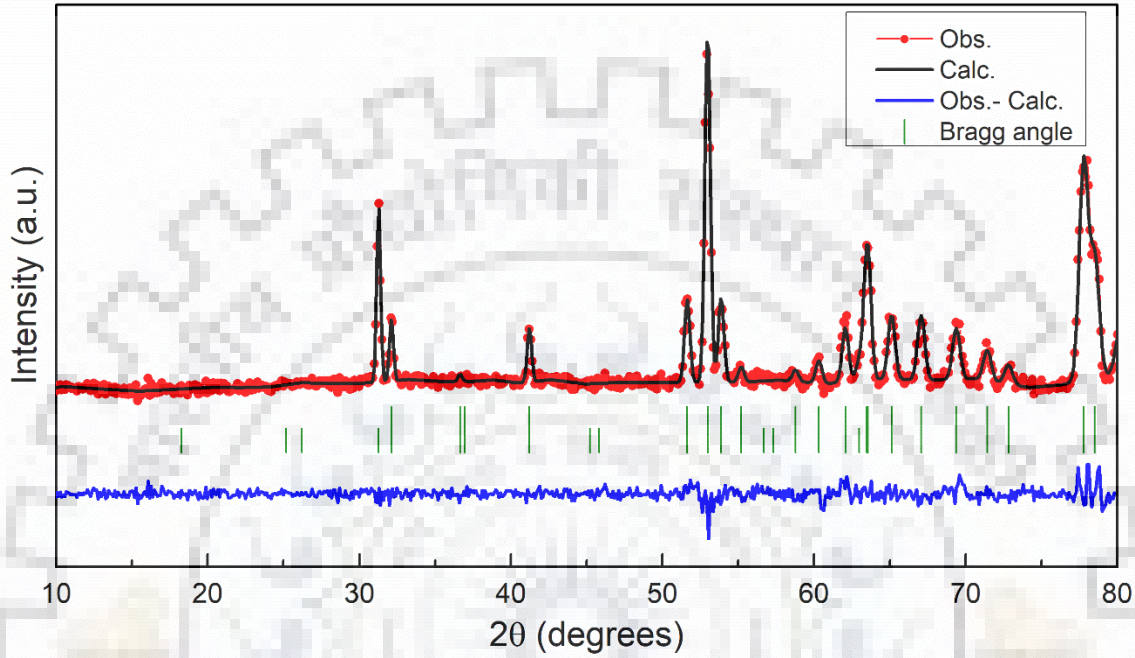


Figure 5.7 Powder neutron diffraction at 300 K with Γ_4 magnetic representation showing magnetic peak at 32°

In this section, a systematic evolution of the NDFO magnetic structure based on neutron diffraction data is discussed. Figure 5.7 shows neutron diffraction patterns between 75 and 1.5 K. At 300 K itself, the (101) and (011) magnetic peaks associated by G -type magnetic ordering of the Fe^{3+} spins near $2\theta = 32^\circ$ as shown in Figure 5.7. A ratio of 1/3 between the intensities of (101) and (011) magnetic peaks confirms that the magnetic structure belongs to the Γ_4 representation with a G_x ordering of the Fe^{3+} spins at 300 K. The ratio between the peaks remain nearly 1/3 down to 75 K which is shown in Figure 5.8. Below 75 K, a systematic increase in the intensity of (011) peak compared to the (101) peak is observed, which indicates the change in magnetic moment direction without modification of G -type magnetic structure i.e. spin reorientation. This change in the ratio of peaks intensities persists down to 20 K, wherein it was found that the intensities of both the peaks have become almost equal. The presence of magnetic ordering represented by Γ_2 irreducible representation (F_x , G_z) is evident by the equal intensities of the (011) and (101) peaks. Below 10 K the intensity of the (101)

peak again increases over the (011) peak which suggests a second reorientation/reoccurrence of a magnetic phase (Γ_4). At the lowest temperatures, viz. 3.5 K and 1.5 K, two prominent

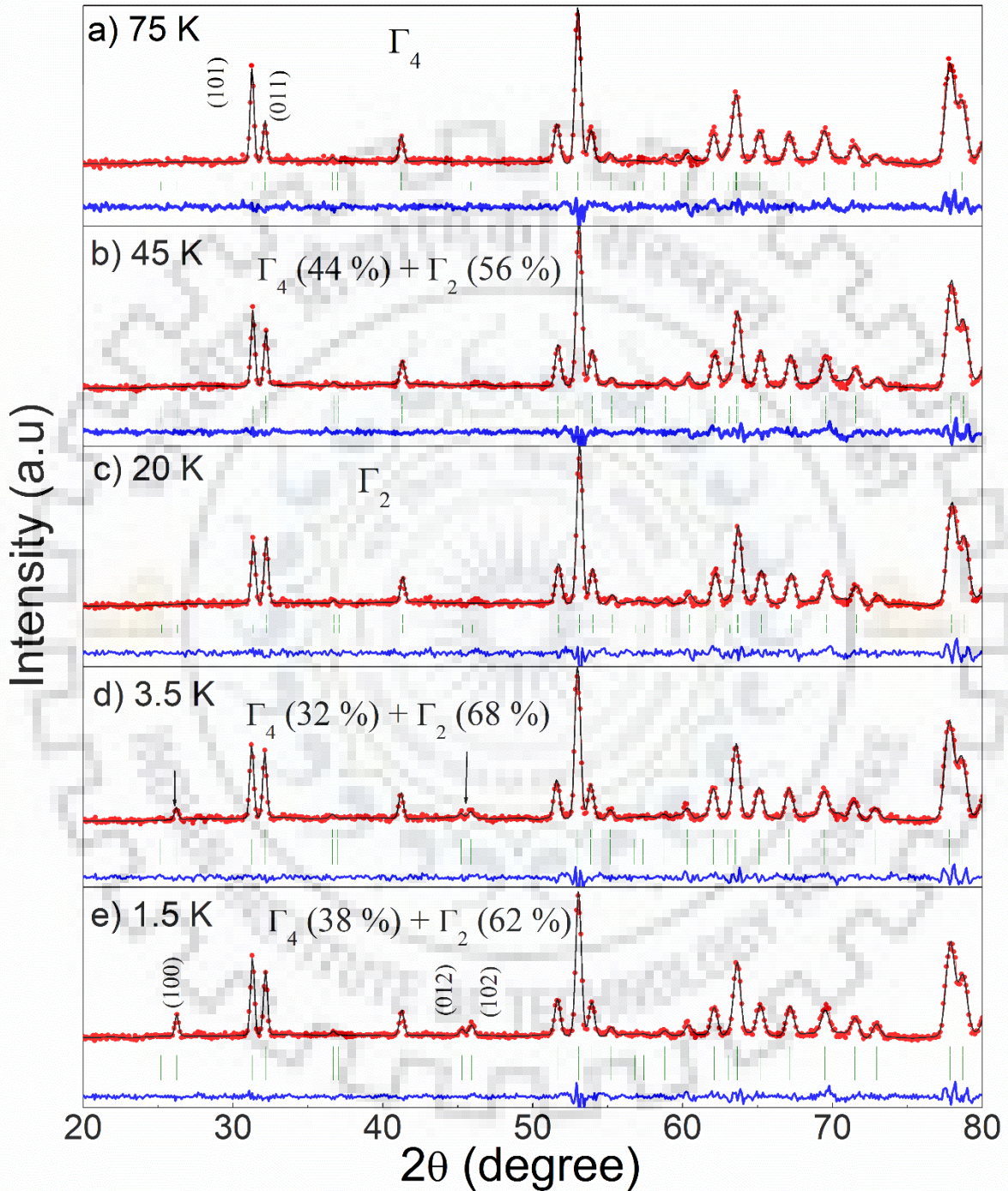


Figure 5.8 Evolution of magnetic peak in neutron diffraction data as a function of temperature

peaks are developing at 25 and 45°, which marks the ordering of the rare – earth ions as shown in Figure 5.8 (d) and (e).

To obtain the detailed spin configurations of the Fe^{3+} and $R^{3+}(\text{Nd}^{3+}/\text{Dy}^{3+})$ spins in the unit cell, the magnetic structure has been solved from the powder diffraction pattern for all temperatures between 300 and 1.5 K. The Fe atom occupies the $4b$ Wyckoff position, while the R atoms occupy the $4c$ sites. The magnetic ordering vector remains $k = (0,0,0)$, in the entire temperature range for both the Fe and R atoms. Following the symmetry analysis by Bertaut *et. al.*, there exists eight irreducible representations, Γ_1 to Γ_8 . Four out of these eight representations correspond to zero coefficients for the Fe site as discussed in detail in chapter 1 and chapter 4.

In NDFO from 300 K till 75 K (Figure 5.8 (a)) the magnetic structure belongs to Γ_4 representation, wherein the Fe spins are arranged as G_x type antiferromagnetic structure. From the diffraction pattern, I do not find any peak corresponding to the ferromagnetic F_z component especially (002) peak expected near 40°. A possible reason for this is the small values of canting angle leading to a ferromagnetic moment of less than $0.1 \mu_B$ which is not seen from

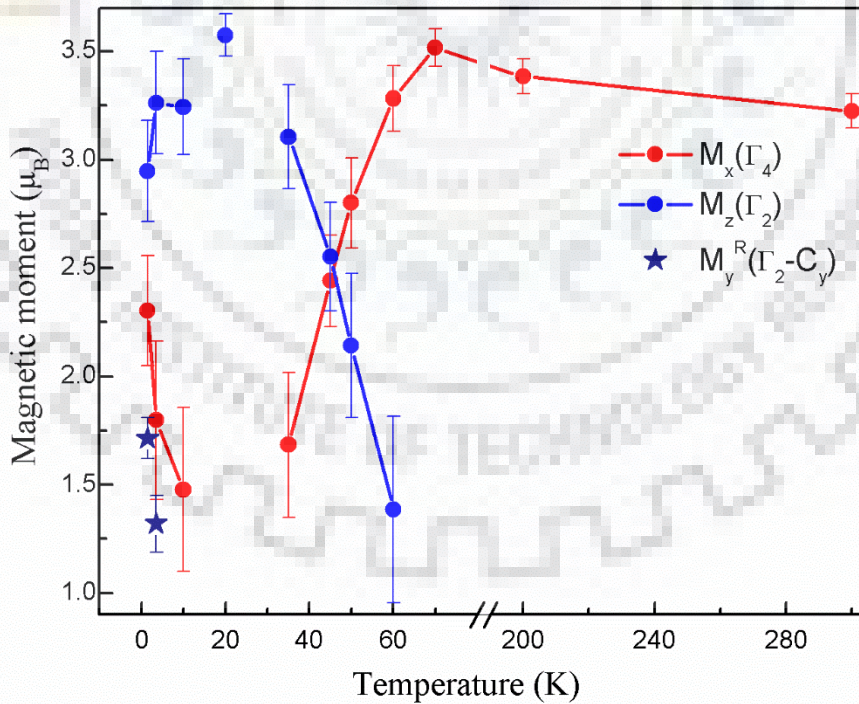


Figure 5.9 Temperature variation of Magnetic moment of Fe^{3+} and $\text{Nd}^{3+}/\text{Dy}^{3+}$ spins from 1.5 K to 300 K for the various representations

powder diffraction experiments. However, the spin arrangement is in agreement with the orthoferrites.

Below 60 K, the magnetic structure is best refined when the mixture of Γ_2 and Γ_4 representations is considered, indicating the ongoing process of spin reorientation. The refinements down to 20 K, clearly indicate that the gradual $\Gamma_4 \rightarrow \Gamma_2$ type spin reorientation takes place in NDFO, which is the usual second order reorientation observed in NdFeO₃. This is in contrast with the expected $\Gamma_4 \rightarrow \Gamma_1$ type abrupt spin reorientation/transition observed in DyFeO₃. As indicated by the equal ratio of (011) and (101) magnetic peaks at 20 K, our analysis confirmed that the magnetic structure belongs entirely to Γ_2 representation. Inclusion of Γ_4 leads to higher values of χ^2 . At 10 K and below, high temperature magnetic phase (Γ_4) again starts to reappear and the magnetic structure belongs to a mixture of $\Gamma_4 + \Gamma_2$ representations. The observed (100) magnetic peaks at 25° pertaining to rare earth R^{3+} ordering arises due to the C_y arrangement of R^{3+} (Nd³⁺/Dy³⁺) spins belonging to the Γ_2 representations.

Thus in our system the C - type ordering of (Nd³⁺/Dy³⁺) spins is unusual since (G_x^R, A_y^R) ordering is expected due to strong single ion anisotropy of Dy³⁺ spins as seen in Dy based orthoferrites and orthochromites. The temperature variation of the magnetic moments for the Fe³⁺ and R^{3+} spins for different representations as shown in Figure 5.9. From 300 K till 75 K a small increase in the magnetic moment associated with the Γ_4 representations of Fe³⁺ spins in G_x configuration is observed. Below 60 K, with the onset of spin reorientation, there is a systematic decrease in the magnetic moment along crystallographic a direction (M_x), while correspondingly the magnetic moment along c direction (M_z) shows an increase. Below 20 K,

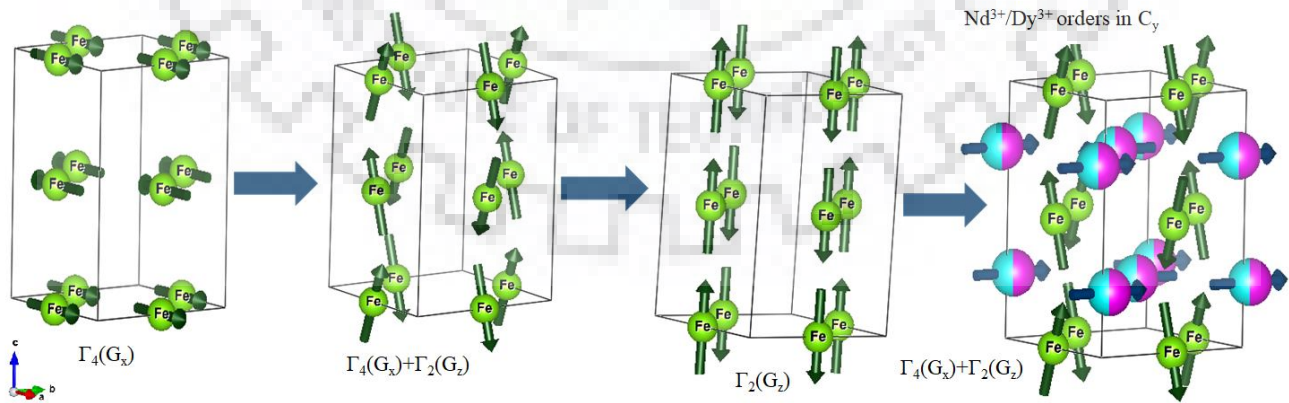


Figure 5.10 Variation of magnetic structure of NDFO from temperature 300 K to 1.5 K showing the gradual spin reorientation over the whole range

the M_z magnetic moment starts to decrease again, while the M_x again starts to increase. The values of total magnetic moment of Fe^{3+} is nearly $3.7 \mu_B$, which is lower than the theoretical value of $5 \mu_B$. The lowering of overall moment can be attributed to effects of covalency and also the polycrystalline nature of our samples. On the other hand, the magnetic moment of $\text{Nd}^{3+}/\text{Dy}^{3+}$ is nearly $1.8 \mu_B$, which is much lower than the expected ($6 - 7 \mu_B$) average moment of the $\text{Nd}^{3+}/\text{Dy}^{3+}$ sub-lattice. However, the value obtained in this study is twice the value of $0.9 \mu_B$, obtained in the single crystals of NdFeO_3 . This indicates the greater effect of the polarization of the rare – earth sub – lattice due to Fe^{3+} spins, which also causes the highly anisotropic Dy^{3+} moments to align in C - type ordering along with Nd^{3+} moments. The schematic representation of Fe^{3+} and rare-earth ($\text{Nd}^{3+}/\text{Dy}^{3+}$) magnetic structure along with temperature dependent successive spin reorientation is depicted in Figure 5.10.

In $R\text{FeO}_3$ (except for $R = \text{Dy}$), the symmetry of rare-earth just above (T_{N2}) is represented by, $\Gamma_2 (F_x^R, C_y^R)$ due to $R - \text{Fe}$ polarization effects. In DyFeO_3 , the large single anisotropy of the Dy^{3+} ion in the a - b plane, results in the $\Gamma_5 (G_x^R, A_y^R)$ magnetic ordering. Magnetic ordering represented by $\Gamma_5 (G_x^R, A_y^R)$ is also observed in DyAO_3 ($A = \text{Al}, \text{Sc}$) where A^{3+} is a non-magnetic ion. The Γ_5 representation belongs to the magnetic point group $m'm'm'$ which shows electric polarization on application of magnetic field, due to non- zero diagonal elements of the magnetoelectric tensor [49], [214]. Below 4.2 K, the combined magnetic ordering belongs to the $\Gamma_{15} (A_x, G_y, C_z; G_x^R, A_y^R)$ representation with magnetic point group $(D_2)222$, which possess a non – zero magnetoelectric tensor [49], [214]. A spontaneous ferroelectric polarization develops in DyFeO_3 when a magnetic field is applied along the c axis[51]. This is a result of $\Gamma_1 \rightarrow \Gamma_4$ rotation/transition of Fe^{3+} spins and the weak ferromagnetism in Γ_4 phase results in spontaneous ferroelectric polarization.

In NDFO, though clear signature of polarization of rare-earth magnetic moments is obtained at 3.5 K from neutron diffraction, the independent G - type ordering of the $\text{Nd}^{3+}/\text{Dy}^{3+}$ moment is not observed even down to 0.3 K which will be discussed in the next section in detail from specific heat data. At 1.5 K, while the R moments order in $\Gamma_2 (F_x^R, C_y^R)$ structure, the Fe^{3+} spins show a coexistence of Γ_2 and Γ_4 structure. The C_y ordering of R is not symmetry compatible with Γ_4 . However, we do not find any possible development of any ferromagnetic peak F_z^R which is expected from symmetry of Γ_4 representation. The magnetic point groups in

NDFO corresponding to Γ_2 and Γ_4 are $(C_{2h}) m'm'm$ and $(C_i) 2m'$ respectively. Both the point groups are non – polar and also do not possess any linear magnetoelectric coupling terms due to inversion symmetry. The absence of magnetoelectric effect in NDFO is also supported by absence of magneto-dielectric effect as shown in Figure 5.6. We can conclude that though NDFO behaves similar to NdFeO_3 and other orthoferrites, the greater polarization of the Dy^{3+} moment is unusual, which can be attributed predominantly to the $\text{Nd}^{3+} - \text{Dy}^{3+}$ interactions. The possible origins of the second spin reorientation can be understood by qualitatively by comparison with the magnetic behavior of DyFeO_3 . In DyFeO_3 , application of external magnetic field along the a axis results induces a $\Gamma_1 \rightarrow \Gamma_2$ ordering of Fe^{3+} moments, while simultaneous rotation of the Dy^{3+} moments from Γ_5 to Γ_3 structures occur. The magnetic field along b and c directions in DyFeO_3 results in $\Gamma_1 \rightarrow \Gamma_4$ spin screw and spin flop transitions respectively of the Fe^{3+} while the Dy^{3+} moments are unaffected. Thus in a similar manner, the effective molecular field acting on R^{3+} and Fe^{3+} moments may be present in NDFO due to large difference in magnetic moments of Nd^{3+} and Dy^{3+} moments and presence of the ferromagnetic field can cause the successive rotation of the Fe^{3+} spins from $\Gamma_2 \rightarrow \Gamma_4$. Thus even the small

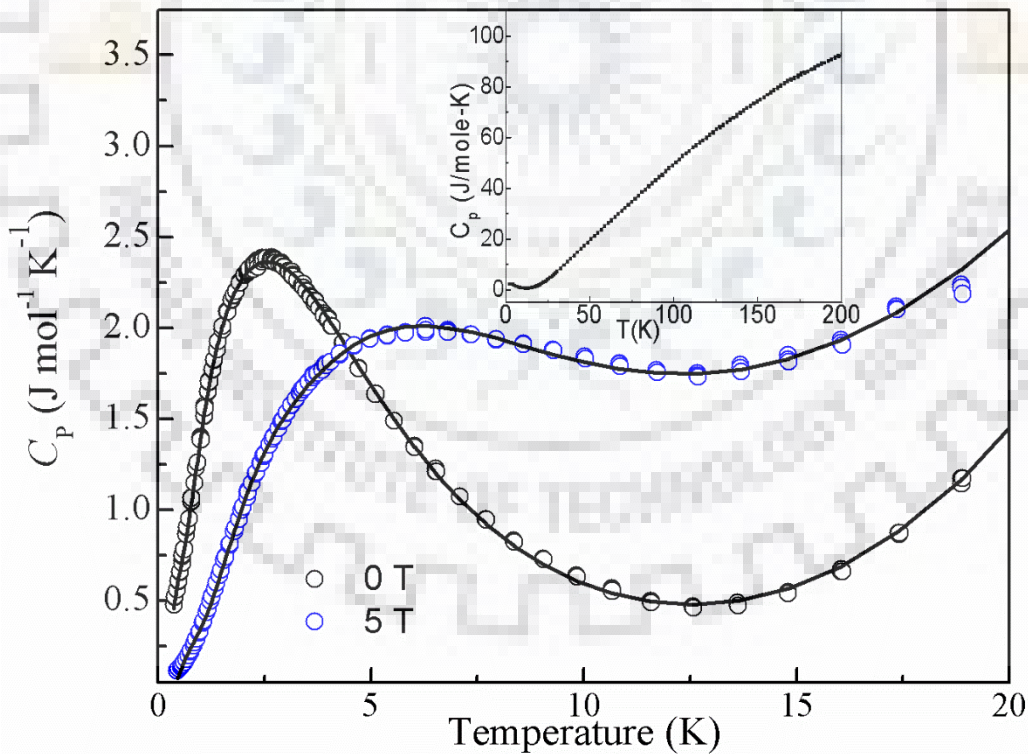


Figure 5.11 The specific heat of NDFO for various fields plotted along with the fitting results. The inset contains specific heat in full temperature range

effective fields can result in the re-emergence of the Γ_4 magnetic structure of the Fe^{3+} magnetic moments.

5.3.5 Specific Heat

The heat capacity C_p of NDFO for 0 and 5 T are shown in Figure 5.11 for temperature range 0.4-20 K. The inset of Figure 5.11 shows the specific heat values for 0 T, in the temperature range from 2 to 200 K. The heat capacity could not identify any distinct signature associated with the individual spin reorientations within the limit of measurement resolution. Below 10 K, a broad peak in specific heat is observed at 2.2 K which can be interpreted as the Schottky peak originating from crystal-field splitting of $4f$ electronic states in Nd^{3+} and Dy^{3+} ions. The λ -shaped anomaly associated with second order phase transition is absent in NDFO. This λ -shaped anomaly is seen prominently in DyFeO_3 at 4.2 K. On the other hand, NdFeO_3 shows a broad Schottky peak along with a less noticeable λ anomaly superposed on the Schottky peak at 1.05 K [215]. Thus a distinct discontinuity in C_p (second order transition) due to independent ordering of the rare-earth is completely absent in NDFO as per the heat capacity measurement. This is in agreement with our neutron diffraction results which confirmed the absence of independent ordering of rare-earth ($\text{Nd}^{3+}/\text{Dy}^{3+}$) ions. In a magnetic field of 5 T, there appears a considerable suppression of the Schottky peak. The zero field specific heat was fitted in the temperature range 0.4 – 20 K to sum of multiple Schottky terms and the T^3 term associated with the lattice specific heat.

$$C_p = \frac{1}{2}R \sum_{i=1}^n w_i \left(\frac{\Delta_i}{k_B T}\right)^2 \frac{\exp\left[-\frac{\Delta_i}{k_B T}\right]}{\left(1 + \exp\left[-\frac{\Delta_i}{k_B T}\right]\right)^2} + B_3 T^3 \quad (5.1)$$

In the above equation, Δ_i corresponds to the splitting of the i^{th} crystal field level. In the temperature range considered, satisfactory fitting result is obtained by only using sum of three ($n=3$) Schottky terms. The crystal field splittings Δ_i ($i = 1 - 3$) are 1.5, 4.5 and 9 K at 0 T. the value of Δ_1 (0.12 meV) obtained in the case of NDFO is smaller than the values reported for NdFeO_3 ($\Delta_1 \sim 5 \text{ K}$ (0.43 meV)). Similarly, in the case of Dy^{3+} systems like DyMnO_3 and $\text{Dy}_{0.5}(\text{Sr}/\text{Y})_{0.5}\text{MnO}_3$, the reported values of first energy splitting are also in the range between 5 to 8 K. In NDFO, presence of two Kramer's ions can cause additional complexity due to entirely different strengths of $\text{Nd}^{3+} - \text{Fe}^{3+}$ and $\text{Dy}^{3+} - \text{Fe}^{3+}$ molecular fields (interactions) which

can lift the degeneracy of the Kramer's doublet. In addition, there also exists the exchange fields between the rare-earth ions which can affect values of Δ_i in a more complex manner. Thus the ordering of rare-earth in NDFO is driven by the effects of molecular field due to Fe^{3+} spins, rather than independent rare-earth ordering.

5.4 Conclusion

NDFO polycrystalline samples were studied in detail to understand its complex magnetic and electric properties. The sample crystallizes in the space group $Pbnm$ with both Nd and Dy, occupying the same crystallographic position and thus being randomly distributed in the crystal. Though magnetic properties of NDFO are similar to that of NdFeO_3 , there are many interesting and significant differences between the two. Below T_N (~ 700 K), magnetic structure belongs to Γ_4 (G_x, A_y, F_z) representation, with the a axis being the easy axis of the Fe^{3+} magnetic moments. The large single anisotropy of Dy^{3+} which induces an abrupt $\Gamma_4 \rightarrow \Gamma_1$ reorientation is suppressed with 50% Nd substitution. Instead the gradual $\Gamma_4 \rightarrow \Gamma_2$ reorientation of the Fe^{3+} spins begin close to 75 K and results in magnetic structure represented by Γ_2 (F_x, G_z) at 20 K with the c axis as the easy axis. Interestingly, the magnetic structure given by Γ_4 re-emerges again below 10 K. This also coincides with the development of (010)-magnetic Bragg peak which corresponds to the C_y arrangement of the $\text{Nd}^{3+}/\text{Dy}^{3+}$ magnetic moments. This is unlike the independent (G_x, A_y) magnetic ordering associated usually with Dy^{3+} moments. The symmetry of the rare-earth ordering also does not support any magneto-electric coupling, which is also confirmed from our field dependent dielectric measurements.

At 1.5 K the rare-earth ordering results in magnetic moment of $1.8 \mu_B$, which is lower than the expected average magnetic moment of $\sim 5 \mu_B$ from $\text{Nd}^{3+}/\text{Dy}^{3+}$ magnetic ions, but the observed value ($1.8 \mu_B$) is much higher than the experimentally observed moments from Nd-ordering in NdFeO_3 . The complete absence of a λ -anomaly in heat capacity clearly indicates that the ordering of $\text{Nd}^{3+}/\text{Dy}^{3+}$ moments is induced by effective molecular field arising due to Fe^{3+} spins.

It can be concluded that due to the highly unequal magnetic moments of the rare-earth ions, a net magnetic moment field acts on the R as well as the Fe^{3+} moments. The net field can lead to additional second $\Gamma_2 \rightarrow \Gamma_4$ reorientation of the Fe^{3+} spins.

Magnetocaloric studies in $\text{Nd}_{0.5}\text{Dy}_{0.5}\text{FeO}_3$ and $\text{NdFe}_{0.5}\text{Mn}_{0.5}\text{O}_3$

6.1 Introduction

Magnetic refrigeration (MR), based on solid state materials, has attracted considerable attention due to its relatively higher cooling efficiency and eco-friendly nature in comparison to conventional refrigeration technologies [216]. Academic and commercial applications still rely mainly upon He (liquid and close cycle) to attain the temperature below 77 K. New alternatives, like MR, should be explored to achieve cryogenic temperatures below 77 K due to increasing scarcity of He gas [217]. Magnetocaloric effect (MCE), based on isothermal change in magnetic entropy, can be effective as an alternative of He to achieve cryogenic temperatures using MR. MCE from one single material is effective only for a small temperature window as significant change in the magnetic entropy is observed near ordering temperature e.g. Gd based compounds have been utilized extensively for cooling below 1 K since the discovery of adiabatic demagnetization in $\text{Gd}_2(\text{SO}_4) \cdot 8\text{H}_2\text{O}$ [218]. Diverse materials with large MCE and broad range of ordering temperatures, should be engineered to attain sub-Kelvin temperatures from 77 K for a sustainable and cost effective alternative of He based cooling [219].

Rare earth based intermetallics such as ErCr_2Si_2 , HoCuSi , PrSi , ErFeSi , ErMn_2Si_2 have shown significant entropy change upon switching on/off the magnetic field in low temperature range (< 77 K) [220]–[225]. In addition to rare earth intermetallics, rare earth orthoferrites ($R\text{FeO}_3$; R = rare earth element), orthochromites ($R\text{CrO}_3$), and manganites ($R\text{MnO}_3$) have been explored extensively for observation of significant MCE below 77 K [122], [124], [125], [131], [132], [226]–[235]. Significant entropy change ($> 10 \text{ JKg}^{-1}\text{K}^{-1}$) has been observed by directional variation of magnetic field with respect to the crystal axes in single crystals of TbFeO_3 [231], TmFeO_3 [231], ErFeO_3 [229], DyFeO_3 [236], TmMnO_3 [227], TbMnO_3 [227], HoMn_2O_5 [228] and by magnitude variation of magnetic field in powder samples like $\text{DyFe}_{0.5}\text{Cr}_{0.5}\text{O}_3$ [232], $\text{Dy}_{1-x}\text{Ho}_x\text{MnO}_3$ [125], $\text{SmCr}_{0.85}\text{Mn}_{0.15}\text{O}_3$ [226], DyCrO_3 [233], [234],

$\text{Dy}_{0.7}\text{R}_{0.3}\text{MnO}_3$ ($R = \text{Er, Ho, Y}$) [234], $\text{PrCr}_{0.85}\text{Mn}_{0.15}\text{O}_3$ [235], $\text{Tb}_{1-x}\text{Dy}_x\text{MnO}_3$ [131]. In single crystals, significant MCE is observed due to magneto-crystalline anisotropy and rare earth ordering. Order/disorder of rare-earth in presence/absence of magnetic field plays an important criterion in the observation of significant MCE. Above, mentioned examples of rare earth intermetallics, orthoferrites, orthochromites and manganite involve rare earth elements with large magnetic moment and low abundance (Tb, Tm, Dy, Er, Ho, Pr, Sm). Compounds, having rare-earth elements with relatively high abundance like La and Nd, show a small change in entropy and hence MCE in such compounds is not significant [216], [237]. Economic considerations require development of materials having high abundance rare-earth elements like La, Nd for cryogenics (<30 K) MR applications.

Table 6.1 Change in magnetic entropy for different rare earth Orthoferrites

Compound	T(K)	H (T)	$-\Delta S(\text{max})$ (JKg ⁻¹ K ⁻¹)	Ref.
TbFeO₃ (Single Crystal)	11	7	24.05	[123]
TmFeO₃ (Single Crystal)	17	7	11.93	[227]
DyFeO₃ (single crystal)	9	7	21.48	[124]
SmFe_{0.5}Mn_{0.5}O₃	18	7	5.6	[81]
GdFeO₃ (Single crystal)	2	9	52.5	[122]

In the present work, MCE has been studied in detail for powder form of:

- A. $\text{Nd}_{0.5}\text{Dy}_{0.5}\text{FeO}_3$ (NDFO)
- B. $\text{NdFe}_{0.5}\text{Mn}_{0.5}\text{O}_3$ (NFMO).

Parent compounds for NDFO are NdFeO_3 and DyFeO_3 as discussed in previous chapters. In NdFeO_3 and DyFeO_3 , Fe magnetic moments order in G – type canted antiferromagnetic configuration below 690 K and 645 K, respectively [51], [100], [121]. In NdFeO_3 gradual spin reorientation occurs below 200 K whereas in DyFeO_3 , abrupt spin reorientation occurs at 50 K. In both the cases, magnetic moment of Fe changes its direction while keeping G – type configuration [51], [100], [121]. Below 10 K, Nd and Dy moments order in C - type and G - type antiferromagnetic configurations in NdFeO_3 and DyFeO_3 respectively. In NdFeO_3 , low temperature Nd ordering is mainly driven by the magnetic structure of Fe magnetic moments [51], [100] whereas Dy ordering is independent of Fe magnetic structure in DyFeO_3 and is of

second order in nature[121]. It has been observed that the rare earth ordering is mainly responsible for observation of large MCE in the proximity of the ordering temperature.

For NFMO, one of the other parent compound is NdMnO₃. In NdMnO₃, Mn magnetic moments order as *A* – type antiferromagnetic structure below 75 K [130]. Nd moments order ferromagnetically along *c* axis below 13 K [189].

Rare earth ordering dictated by magnetic ordering of Fe moments is probably responsible for large ΔS_M values in rare earth orthoferrites. Although ordered Fe magnetic moments dictates the rare-earth ordering, but entropy change in proximity to rare earth ordering temperature is primarily contributed by order/disorder of rare earth moments. The ΔS_M value obtained for NDFO is quiet close to the ΔS_M values obtained from various rare earth (low abundance) orthoferrites, orthochromites and manganite powder samples e.g. 11.3 JKg⁻¹K⁻¹ at 5 K and $\Delta H = 4.5T$ for DyFe_{0.5}Cr_{0.5}O₃ [232], 6.3 Jkg⁻¹K⁻¹ at 10 K and $\Delta H = 5T$ for Dy_{0.6}Ca_{0.4}Fe_{0.5}Cr_{0.5}O₃ [238], 12 Jkg⁻¹K⁻¹ at 10 K and $\Delta H = 5T$ for Dy_{0.4}Er_{0.6}Fe_{0.5}Cr_{0.5}O₃ [239], 25 Jkg⁻¹K⁻¹ at 3.5 K and $\Delta H = 5T$ for Dy_{0.4}Gd_{0.6}Fe_{0.5}Cr_{0.5}O₃ [239], 5.019 JKg⁻¹K⁻¹ at 10 K and $\Delta H = 5T$ for SmCr_{0.85}Mn_{0.15}O₃ [226], 10.85 JKg⁻¹K⁻¹ at 5 K and $\Delta H = 4T$ for DyCrO₃ [234], and 12.5 JKg⁻¹K⁻¹ at 10.5 K and $\Delta H = 4T$ for HoMnO₃ [125]. Contrary to our case, low abundance rare-earth elements with high ionic magnetic moment values are used in all these previous reports.

In this detailed work on powder NFMO and NDFO, MCE in cryogenic temperature range has been calculated from magnetization. Maximum magnetic entropy change (ΔS_M) for NFMO is 2.69 JKg⁻¹K⁻¹ at 5.5 K by the application of 5T magnetic field (ΔH) while in the case of NDFO the value of ΔS_M is 10.38 JKg⁻¹K⁻¹ at 4 K by the application of 5T magnetic field. This value is quiet significant as considering the substitution of 50% Dy³⁺ with Nd³⁺. To the best of our knowledge, the value of ΔS_M is the largest for a compound having 50% substitution of Nd at cryogenic temperature

6.2 Experimental Technique

Polycrystalline NFMO and NDFO was prepared using standard solid state reaction method as explained in the previous chapters. Magnetization measurement were carried out using Superconducting Quantum Interference Device (SQUID) magnetometer of Quantum Design

magnetic measurement system-XL (MPMS-XL) and Physical property measurement system (PPMS) of Quantum Design. Zero Field Cooled (ZFC) and Field Cooled (FC) procedures were adopted to identify the magnetic phase and transition temperature between 5 K – 300 K at different applied magnetic fields. Detailed M - H isotherms were measured between 3 – 80 K and 0 – 5 T to estimate entropy change with the application of magnetic field.

6.3 Results and Discussion

6.3.1 $\text{Nd}_{0.5}\text{Dy}_{0.5}\text{FeO}_3$ (NDFO)

The refinement of X-Ray diffraction confirms the single phase of NDFO without any impurity. The compound crystallizes into orthorhombic structure with $Pbnm$ space group. X-

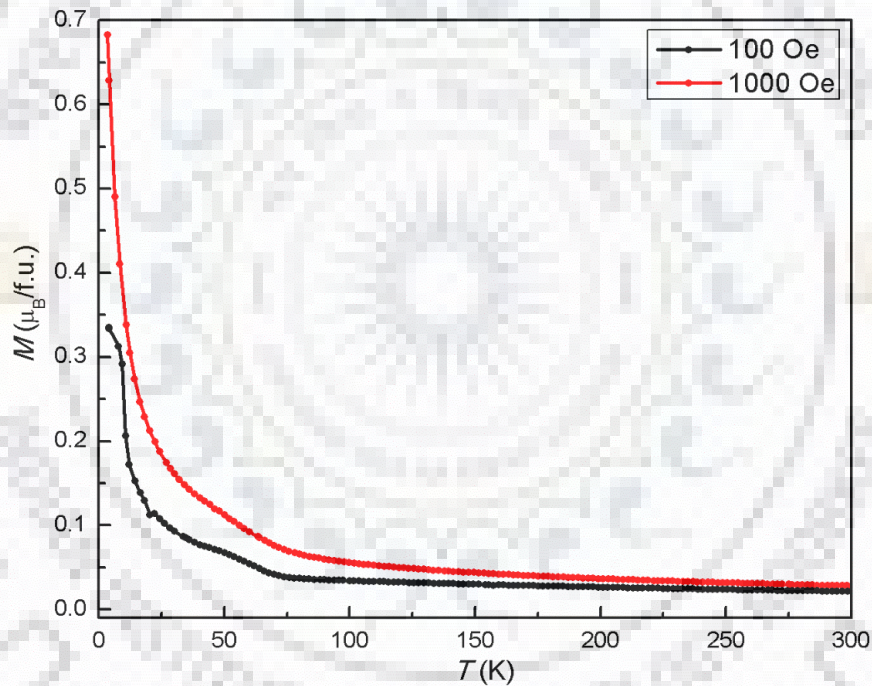


Figure 6.1 Field cooled curve of NDFO under 100 Oe and 1000 Oe applied field

ray diffraction and refined data along with obtained lattice parameters and bond lengths were provided in the previous chapter.

Figure 6.1 shows FC magnetization as a function of temperature in applied magnetic field of 100 and 1000 Oe of NDFO. As Néel temperature (T_N), determined by strong Fe-Fe exchange interaction, of NdFeO_3 and DyFeO_3 are 690 K and 645 K respectively [100], [121], NDFO is

expected to exhibit G – type canted antiferromagnetic order at room temperature. Room temperature magnetic order (G – type antiferromagnetic) of NDFO is confirmed from our neutron diffraction data discussed in previous chapter. At 300 K, M - H isotherm shows a linear magnetization having hysteresis and non-linearity close to zero field. Non-linearity and hysteresis occur most probably due to the ferromagnetic component generated by the canting of spins in the antiferromagnetic phase. As per the discussion in chapter 5, two magnetic transitions (75 and 35 K) were observed in magnetization data which is associated with complicated reorientation of already ordered Fe spins. Below 35 K, magnetization increases significantly, which is associated with the polarization of rare-earth spins (Nd/Dy) driven by Fe-Nd/Dy exchange interaction. As a result, Nd/Dy magnetic moments order into a C-type antiferromagnetic configuration below 10 K. This ordering is also confirmed by neutron diffraction.

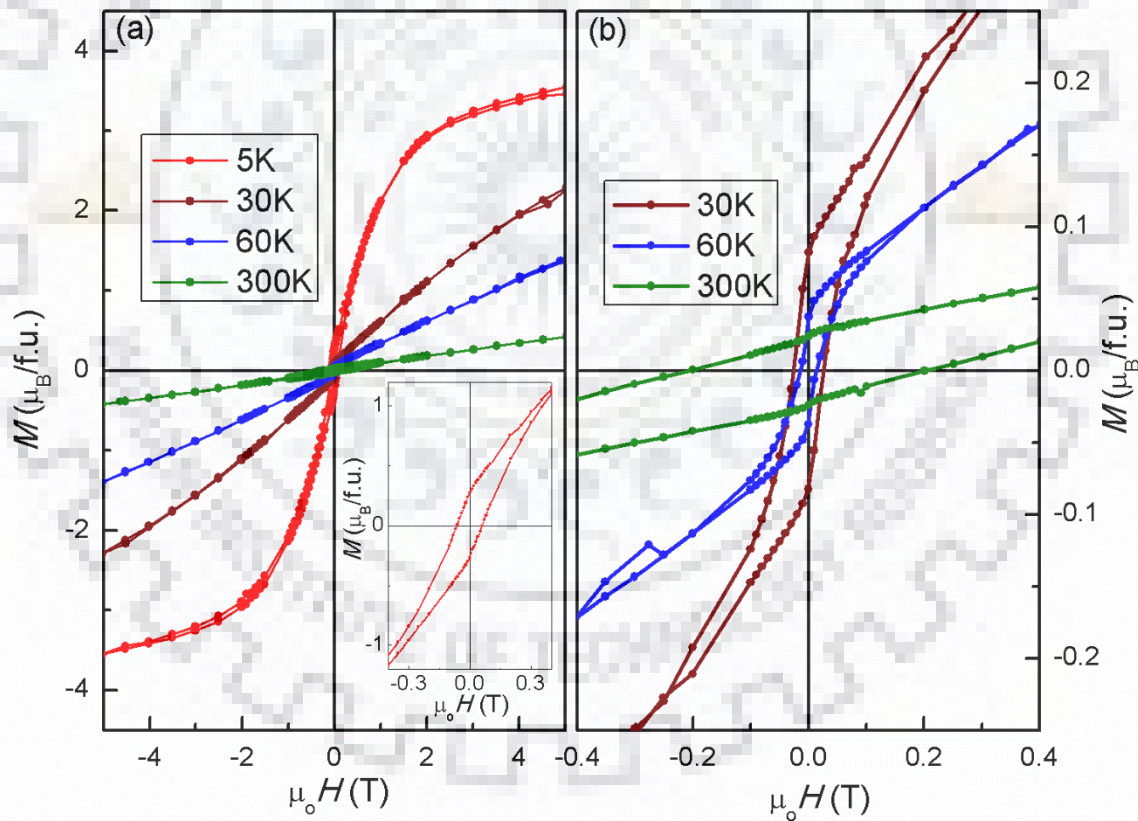


Figure 6.2 (a) M - H isotherm for NDFO at different temperatures. Inset shows the hysteresis with coercivity in M - H loop at 5 K. (b) 300, 60 and 30 K M - H isotherms data at low magnetic field values to show hysteresis with coercivity clearly.

In the Field cooled data, below 10 K, a large difference between magnetization is observed for two external magnetic field values. This difference is associated with rare earth magnetic moments and their ordering. This large difference in the magnetization, due to a change in external magnetic field, prompted us to probe the possibility of MCE in this temperature range.

Since entropy change ($S_M(T)$), which is an important parameter to measure MCE, can be calculated from $M-H$ isotherm [68], $M-H$ isotherm at different temperatures were measured to further explore the possibility of MCE in NDFO. Figure 6.2 shows magnetization as a function of external magnetic field (± 5 T) at four different temperatures, covering spin reorientation region and rare earth ordering. As shown in Figure 6.2 (a) $M-H$ loop at 300 K displays a linear behavior at high magnetic field and has non-linearity and hysteresis at low field (see Figure 6.2 (b)), which is expected from a canted antiferromagnet. Also as shown in Figure 6.2 (b), the coercivity starts to vary at 60 K which indicates the initiation of spin reorientation. Below 35 K, magnetization varies qualitatively as well as quantitatively as a function of magnetic field. Non-linearity and coercivity in magnetization data increases as temperature decreases. Below 10 K, magnetization data show signature of saturation at high magnetic field. The effect of saturation in magnetization becomes pronounced at 5 K. This behavior of

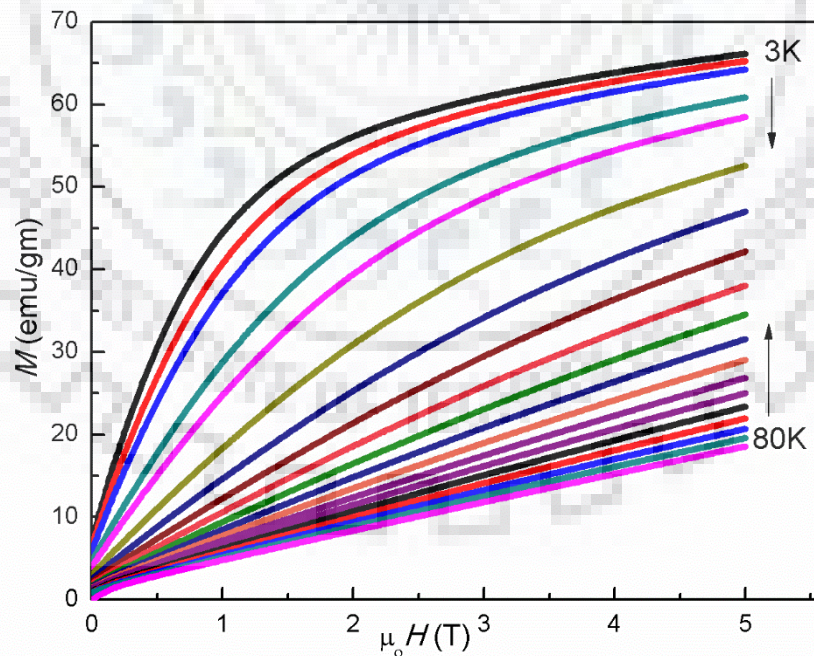


Figure 6.3 Field dependence of NDFO magnetization at different temperatures, measured to determine the adiabatic change in magnetic entropy

magnetization (saturation and non – linearity) can be attributed to the ordering of Nd/Dy spins. The saturation magnetic moment value of NDFO is $3.40 \mu_B/\text{f.u.}$ at 5 K and 4 T. Although paramagnetic (atomic) magnetic moments of Dy^{3+} and Nd^{3+} ions are 10.63 and $3.62 \mu_B$ respectively, crystal field environment and exchange interaction play important roles in determination of NDFO magnetic properties.

A comparison between isostructural orthoferrites like NdFeO_3 and DyFeO_3 is necessary to understand the observed magnetic properties and MCE of NDFO. Single crystal of DyFeO_3 has the magnetic moment of $7.56 \mu_B/\text{f.u.}$ along b -axis, $4.45 \mu_B/\text{f.u.}$ along a - axis and $0.84 \mu_B/\text{f.u.}$ along c - axis at 4.2 K and 4 T [52]. These large and anisotropic values are responsible for observed MCE of DyFeO_3 single crystal in rotating field [124]. DyFeO_3 powder sample should have an average value ($\approx 4.23 \mu_B/\text{f.u.}$ at 4.2 K and 4 T) of single crystal magnetization along different crystallographic axes [52]. On the other hand, low temperature magnetic moment of Nd ($0.9 \mu_B/\text{f.u.}$) was obtained from neutron diffraction studies on NdFeO_3 [99]. So an average value of $2.57 \mu_B/\text{f.u.}$ is expected from rare earth (50% Nd/50% Dy) magnetic moments in $\text{Nd}_{0.5}\text{Dy}_{0.5}\text{FeO}_3$. The observed value of $3.40 \mu_B/\text{f.u.}$ from magnetization data of NDFO is 32 % higher than expected value. The higher value can be attributed to a stronger

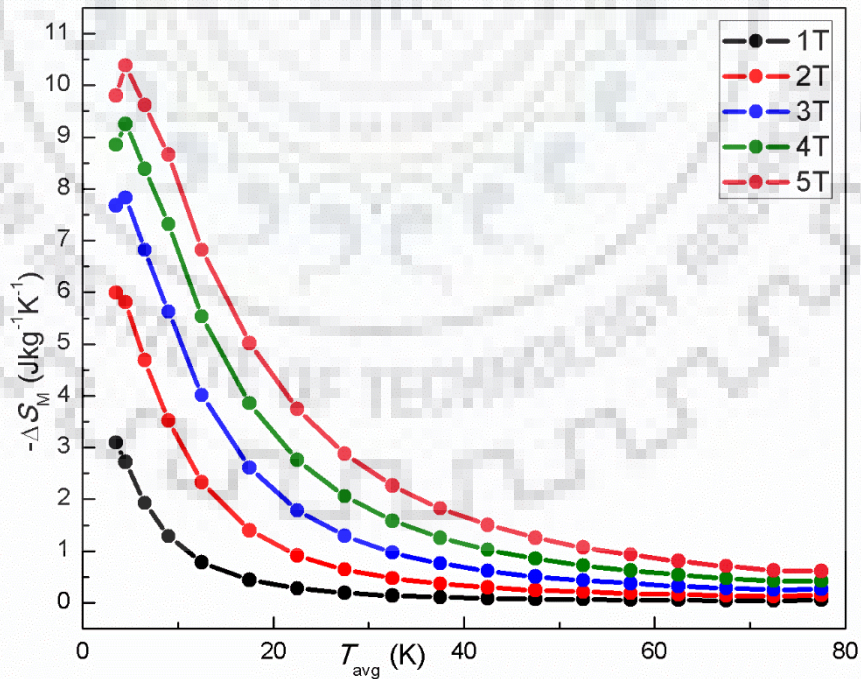


Figure 6.4 Calculated ΔS_M values for NDFO from experimental magnetization data are shown in the form of points for different values of ΔH

Dy³⁺-Nd³⁺ and Nd³⁺-Fe³⁺ interaction. Dy ordering in DyFeO₃ is *G* – type and is independent of the Fe magnetic structure due to weaker Dy³⁺-Fe³⁺ interaction, stronger anisotropic Dy³⁺-Dy³⁺ interaction and large single ion anisotropy value of Dy³⁺ [121]. On the other hand, Nd³⁺ ordering is *C* – type which is strongly influenced by magnetic structure of Fe³⁺ sublattice through stronger Nd³⁺-Fe³⁺ interaction [99]. In case of NDFO, rare-earth ordering (Nd³⁺/Dy³⁺) is *C* – type which is dictated by presence of a stronger Nd³⁺-Fe³⁺ exchange interaction. Nd³⁺-Dy³⁺ interaction is also very strong in NDFO which is comparable to Dy³⁺-Dy³⁺ in DyFeO₃. The modified magnetic structure of rare-earth in NDFO, stronger Nd³⁺-Dy³⁺ and Nd³⁺-Fe³⁺ interaction play crucial role in observation of high magnetic moment in NDFO than the expected value.

Below 30 K, change in magnetization with respect to temperature at different magnetic fields ($\delta M/\delta T|_H$) is large (evident from Fig. 6.2) which is indicative of large MCE below 30 K [68]. This confirms our motivation to investigate MCE in NDFO at cryogenic temperatures as initially suggested by FC magnetization data. The observation of substantial enhancement in magnetization below 30 K/25K, a basis for MCE, can be assigned to polarization and ordering of Nd/Dy magnetic moments. Also in NDFO, observed narrow hysteresis loops at low temperature are characteristics of desired MCE with good working efficiency.

Following magnetization results, a large entropy change in NDFO is expected due to rare-earth order-disorder transition. Magnetic entropy change in presence of magnetic field was calculated from isothermal magnetization measurements. Figure 6.3 shows the evolution of isothermal magnetization between 80 - 3 K with 0.01 T magnetic field step size. The magnetization data varies in a systematic way from linear behavior to non-linear at 60 K and saturates below 10 K. The change in magnetic entropy, responsible for MCE in NDFO, is calculated from the slope of temperature dependent magnetization data shown in Figure 6.3 using following equation derived from one of the Maxwell relations[68], [240].

$$\Delta S_M(T)_{\Delta H} = \int_{H_i}^{H_f} \left(\frac{\partial M(T,H)}{\partial T} \right)_H dH \quad (6.1)$$

Measured magnetization isotherms are discrete and require numerical integration of equation 6.1. Magnetic entropy change ($\Delta S_M(T_{avg})_{\Delta H}$) at $T_{avg} = \frac{T_1+T_2}{2}$ is calculated from two

magnetization isotherms measured at T_1 and T_2 using following equation obtained by numerical integration of equation 6.1[68].

$$\Delta S_M(T_{avg})_{\Delta H} = \frac{\delta H}{2\delta T} (\delta M_1 + 2 \sum_{i=2}^{n-1} \delta M_i + \delta M_n) \quad (6.2)$$

Where $T_{avg} = \frac{T_1+T_2}{2}$, $\delta T = T_2 - T_1 (T_2 > T_1)$, and δH is constant step size between H_i and H_f with n number of steps. In our case δH is 0.01 T, δM_1 , δM_n , δM_i represents the difference in magnetization values between T_1 and T_2 at 1st step of H (zero field), n^{th} step of H (H_f) and i^{th} step of H . From two isotherm magnetization measurements, ΔS_M is to be calculated at T_{avg} and also for other temperatures using the same procedure. Using different H_f (1,2,,4,5), ΔS_M is calculated for different ΔH whereas 0 T is taken as H_i in our case. The temperature dependent $-\Delta S_M$ is calculated from magnetization data as shown in Figure 6.3. using equation 6.2. The calculated values of $-\Delta S_M$, for various ΔH values, are shown Figure 6.4 and listed in Table 6.1. The maximum change in magnetic entropy for NDFO ($-\Delta S_M^{max}$ is $10.4 \text{ Jkg}^{-1}\text{K}^{-1}$) is observed close to 4 K and $\Delta H = 5 \text{ T}$. The low temperature rare-earth (Nd/Dy) ordering in NDFO is primarily responsible for the observed peak in $-\Delta S_M$ value. In the spin reorientation

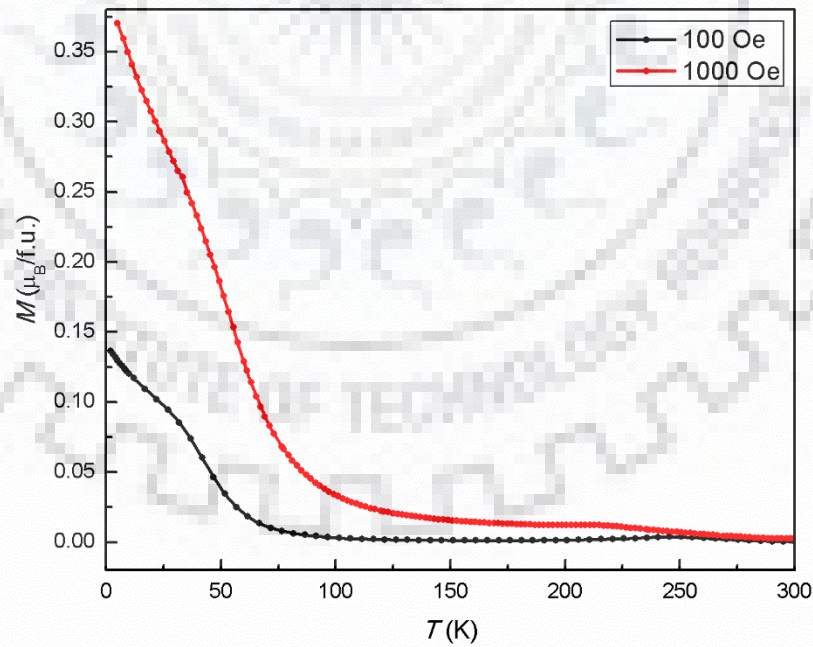


Figure 6.5 Field cooled magnetization for NFMO under an applied field 100 Oe and 1000 Oe showing the drastic difference in magnetization at lower temperature

region, there is no significant variation in $-\Delta S_M$ values which suggest that directional change of Fe^{3+} magnetic moments do not contribute in magnetic entropy change.

The measured value of $-\Delta S_M^{max}$ ($10.4 \text{ JKg}^{-1}\text{K}^{-1}$) in NDFO is quite close to the average of $-\Delta S_M^{max}$ values observed in DyFeO_3 single crystals along different crystallographic directions. Despite having 50% Nd, the observed $-\Delta S_M^{max}$ value in NDFO is either close to or higher than the values observed in other orthoferrites, orthochromites and manganites having 100% low abundance rare-earth elements like Dy, Ho, Tb, Sm as discussed in the introduction part. The value of $-\Delta S_M^{max}$ in NDFO is approximately 73% higher than the value observed in case of $\text{Dy}_{0.7}\text{Y}_{0.3}\text{CrO}_3$ where only 30% Dy ions are diluted.

6.3.2 $\text{NdFe}_{0.5}\text{Mn}_{0.5}\text{O}_3$ (NFMO)

As per discussion of chapter 3, X-ray diffraction confirms the orthorhombic structure of NFMO with $Pbnm$ space group. Magnetization measurement at 100 Oe shows paramagnetic-

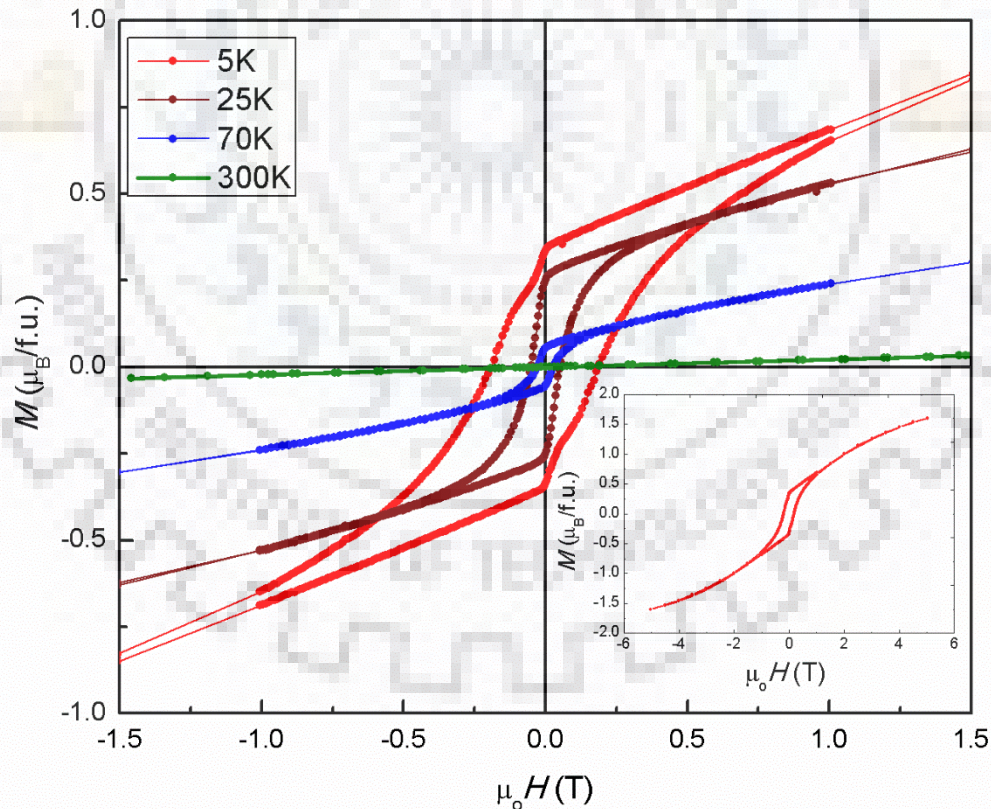


Figure 6.6 M - H isotherm of NFMO at different temperature showing clearly the hysteresis loop with coercivity at 5, 25 and 75 K while at 300 K paramagnetic behavior is shown. Inset shows the M - H isotherm at 5K under an applied field ($\pm 5 \text{ T}$)

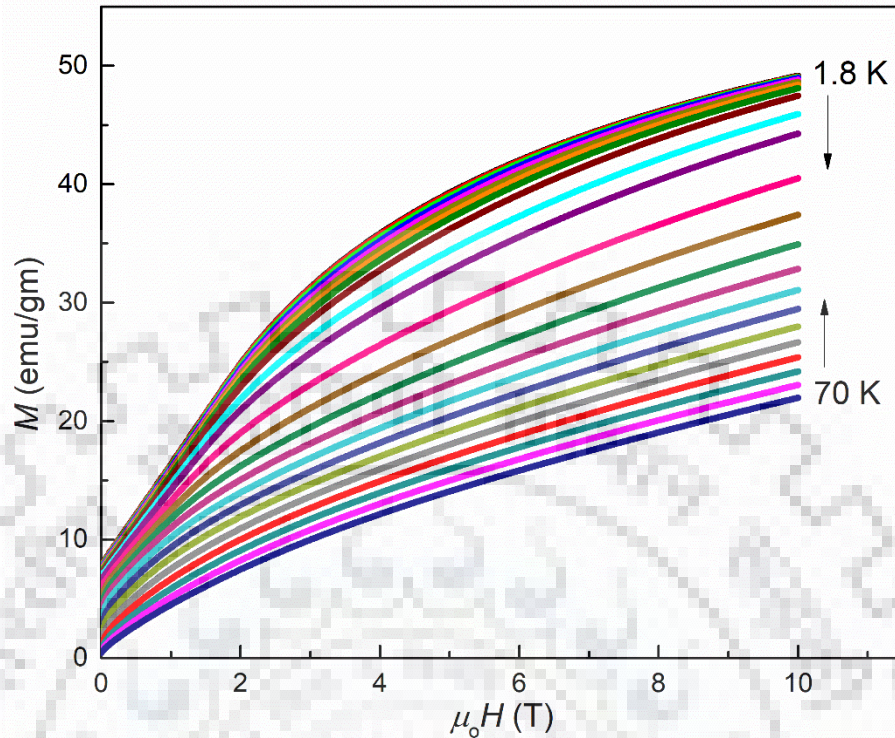


Figure 6.7 Field dependence of NFMO magnetization at different temperatures, measured to determine the adiabatic change in magnetic entropy

antiferromagnetic transition around 250 K which has been discussed in detail in chapter 3. In case of NFMO, though paramagnetic to antiferromagnetic transition occurs at 250 K, but there is another transition around 40 K, which is due to spin reorientation of $\text{Fe}^{3+}/\text{Mn}^{3+}$ ions which has already been discussed in detail in chapter 4. Difference in the behavior of magnetization under a higher applied field is quite evident in Figure 6.5. Below 80 K, a large difference in magnetization is observed which is associated due to $\text{Nd}^{3+} - \text{Fe}^{3+}/\text{Mn}^{3+}$ or $\text{Nd}^{3+} - \text{Nd}^{3+}$ interaction at lower temperature. In this compound, sublattice interaction and Jahn-Teller distortion of Mn^{3+} along with the presence of single ion anisotropy of Mn^{3+} contribute additional complexity due to the presence of Fe^{3+} and Mn^{3+} at the center of octahedra. When Fe^{3+} ion ($S=5/2$) is substituted by Mn^{3+} ($S=2$), then it weakens the $\text{Fe}^{3+} - \text{Fe}^{3+}$ interaction which resulted in the change in the effective anisotropy of the compound which further changes the spin reorientation temperature with the higher applied field. Below spin reorientation temperature, major contribution occurs due to the magnetization of rare earth orthoferrite which occurs at low temperature. In the case of NFMO, Nd^{3+} ordered into weak ferromagnetic along x direction below 4 K which is confirmed from powder neutron diffraction data. Due to the presence of

Nd^{3+} which is found in abundance in nature, possibility of the presence of MCE in this compound in the lower temperature range has been investigated.

The M - H plots are shown in Figure 6.6. At 300 K, the magnetization is linear indicating the paramagnetic nature of the sample. With decrease in temperature magnetization the M - H plots develop a narrow hysteresis loop with a linear behavior at high fields, indicating the anti-ferromagnetic nature of the samples. At 5 K, the M - H shows a wide hysteresis loop indicating presence of a large ferromagnetic component (as shown in inset of Figure 6.6). In a field of 5 T, the magnetization attains a value of nearly $1.6\mu_{\text{B}}/\text{f.u.}$ Comparing with the parent compounds, the magnetic moment of NdMnO_3 is nearly $2\mu_{\text{B}}/\text{f.u.}$ at 5 T [109] whereas, M - H studies on NdFeO_3 reveal a magnetic moment of $1\mu_{\text{B}}$ in a field of 5 T [100] at 5 K. The difference in the nature of rare-earth ordering and moment in both parent compounds further prompted us to explore the magnetocaloric behavior of NFMO.

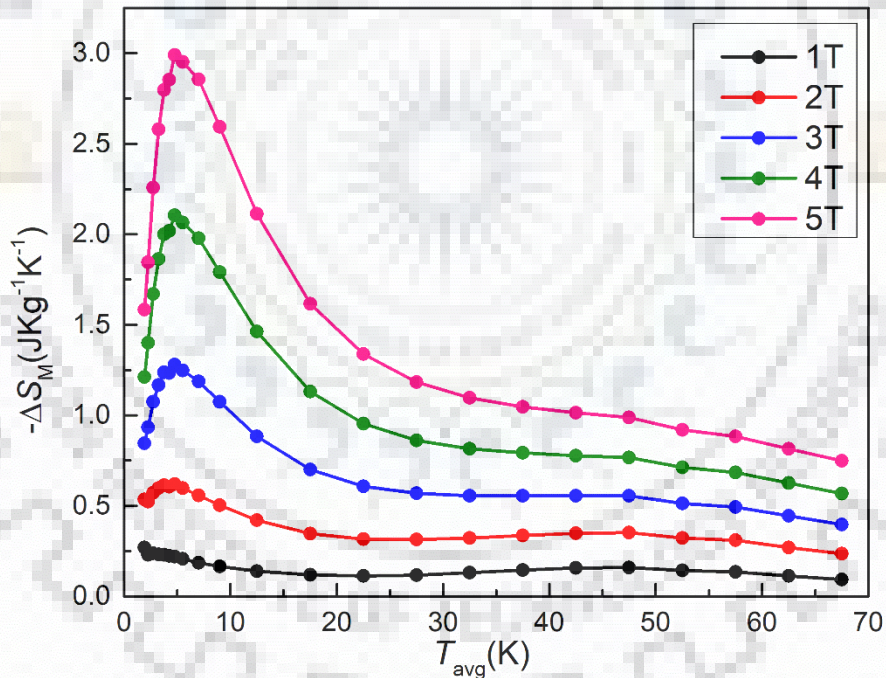


Figure 6.8 Calculated ΔS_M values for NFMO from experimental magnetization data are shown in the form of points for different values of ΔH

Magnetocaloric effect is defined as the change in entropy in the presence of applied magnetic field due to which a change in temperature occurs under adiabatic condition. To calculate the change in magnetic entropy magnetic moment as a function of applied field has

been measured in the temperature range 1.8 – 70 K using PPMS magnetometer of Quantum Design as shown in Figure 6.7.

The change in entropy has been calculated using from the slope of temperature dependent magnetization equation as discussed in the previous section

$$\Delta S_M(T)_{\Delta H} = \int_{H_i}^{H_f} \left(\frac{\partial M(T,H)}{\partial T} \right)_H dH \quad (6.3)$$

The variation of change in magnetic entropy with temperature at magnetic field in the range 1 T to 5 T is shown in Figure 6.8. The most significant changes in the maximum entropy change

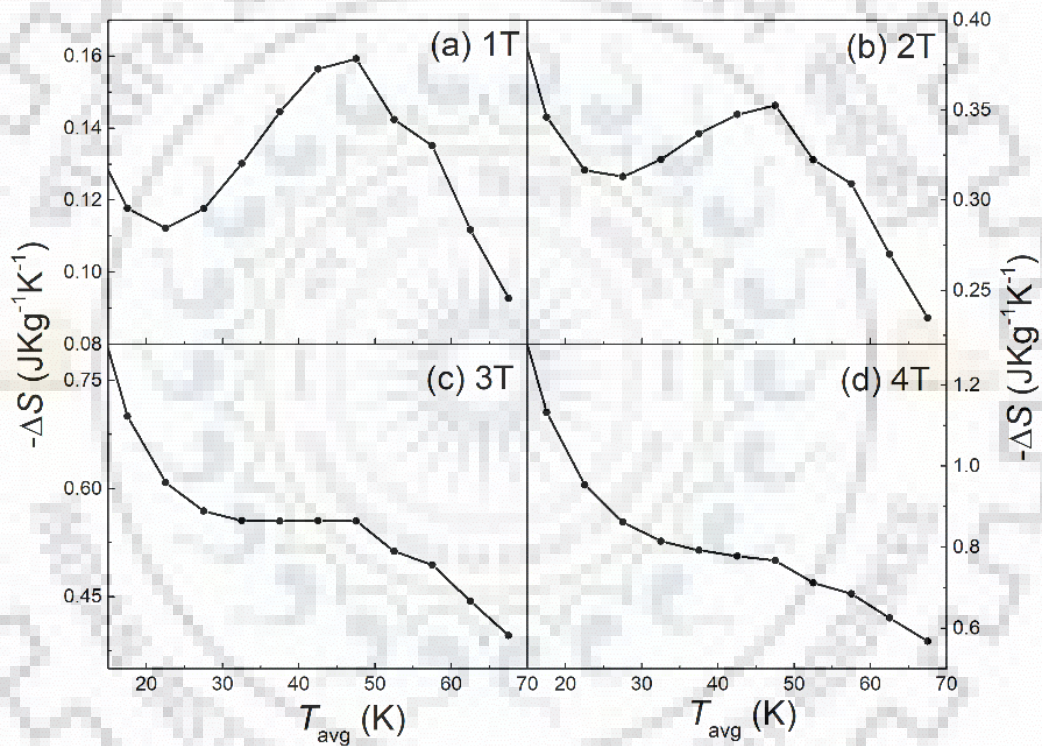


Figure 6.9 Variation of change in magnetic entropy under an applied magnetic field at spin reorientation region getting suppressed under a higher applied magnetic field.

occur in the field range 2-5 T. With increasing field, a maximum in ΔS_M shifts to a higher temperature, as shown in Table 6.1. In a field of 5 T, a change in entropy of nearly $2.98 \text{ Jkg}^{-1} \text{K}^{-1}$ is obtained. In the orthoferrites like DyFeO_3 and GdFeO_3 , the magnetic entropy change is an outcome of a second order phase transition associated with the ordering of the rare-earth. In NFMO, maximum change in entropy is $-\Delta S_M^{max} = 2.98 \text{ Jkg}^{-1} \text{K}^{-1}$ at 4.75 K for $\Delta H = 5 \text{ T}$. Due to the weaker Nd – Nd interaction very small change in entropy is observed. Though, despite

having Nd as rare earth, NdMnO₃ have $-\Delta S_M^{max} = 4.4 \text{ Jkg}^{-1}\text{K}^{-1}$, such a high value is obtained due to the fully magnetically ordered configuration as NdMnO₃ is A – type AFM which is ferromagnetic in plane and thus positive higher value of entropy change at 15 K leads to the stabilization of ferromagnetic like state in the compound [106]. In case of NFMO also, a weak ferromagnetic canting is observed at lower temperature due to Nd³⁺ ordering which will contribute in the magnetic entropy change and therefore the value of $-\Delta S_M^{max}$ is higher in NFMO as compared to other Nd based perovskites[234]. The change in entropy in NFMO can also be attributed to the development of the Nd³⁺ moments polarization due to the Nd/Fe-Mn interactions.

Interestingly, a discernable entropy change is also observed in the spin reorientation region. In a magnetic field variation between 0-1 T (Figure 6.9 (a)), a peak is observed near 45 K, indicating an excess entropy change of $\sim 0.06 \text{ JKg}^{-1}\text{K}^{-1}$. With an increase in the magnetic field, the peak gradually evolves as a “shoulder”-like feature. However, the slope change occurs even in a field of 3 T. This suggests that the magnetic field gradually suppresses the $\Gamma_1 \rightarrow \Gamma_2$ spin reorientation.

In table 6.1, comparison in the values of magnetic entropy change under an applied field for NDFO and NFMO is shown.

Table 6.2 Magnetic entropy change value for NDFO and NFMO for different applied field at 4 K and 6.5 K respectively

$\mu_0 H$ (T)	$-\Delta S_M^{max}$ (Jkg ⁻¹ K ⁻¹) (NDFO)	$-\Delta S_M^{max}$ (Jkg ⁻¹ K ⁻¹) (NFMO)
1	3.11	0.23
2	5.94	0.62
3	7.90	1.27
4	9.30	2.10
5	10.38	2.98

The relatively high values of $-\Delta S_M^{max}$ in polycrystalline NDFO as compare to NFMO samples make it a cost effective alternative in comparison to other rare-earth orthoferrites, orthochromites, and manganites for magnetic refrigeration at low temperatures and also prove

promising replacement of costlier and toxic gas refrigerant material in the lower temperature region.

6.4 Conclusion

A significantly large magnetocaloric is observed in polycrystalline $\text{Nd}_{0.5}\text{Dy}_{0.5}\text{FeO}_3$ in comparison to $\text{NdFe}_{0.5}\text{Mn}_{0.5}\text{O}_3$ samples at cryogenic temperatures. As expected, the magnetic ground state of NDFO and NFMO are canted antiferromagnetic having Néel temperature well above room temperature and around room temperature respectively. In case of NDFO, observed magnetic moment is $3.40 \mu_{\text{B}}/\text{f.u.}$ at 5 K in presence of 5 T magnetic field. This value is 32% higher than the expected average of observed values of NdFeO_3 and DyFeO_3 . Due to the observed high magnetization value and high rate of change of magnetization w.r.t. temperature, change in magnetic entropy was calculated from magnetization data. Maximum change in entropy is $10.38 \text{ Jkg}^{-1}\text{K}^{-1}$ at 4 K and 5 T for NDFO while for NFMO is $2.73 \text{ Jkg}^{-1}\text{K}^{-1}$ at 6.5 K and 5 T. Despite having 50% substitution of Dy with Nd atoms, the observed values of $-\Delta S_M^{\text{max}}$ is close to the average value of DyFeO_3 single crystals. This enhancement is quiet significant considering the fact that observed value of entropy change in case of Nd base compounds is usually not that significant. In case of $\text{NdFe}_{0.5}\text{Mn}_{0.5}\text{O}_3$ also, $-\Delta S_M^{\text{max}} = 2.73 \text{ Jkg}^{-1}\text{K}^{-1}$ is observed at 6.5K and 5T due to the presence of weak ferromagnetic component associated with rare-earth moments. Such a high value of entropy change in NFMO is surprising despite the absence of rare-earth antiferromagnetic ordering. Due to low cost and high abundance of Nd, it makes both NDFO and NFMO good alternative for magnetic refrigeration and could prove useful in many applications.

Growth and characterization of orthoferrite epitaxial thin film

7.1 Introduction

In the past years, lot of research has been done on orthoferrites due to their wide range of magnetic properties. Most of the studies that have been done are either on polycrystalline form or on single crystal. The ever increasing demand of miniaturization in magnetic recording media, with advances in the thin film growth techniques, has accelerated the investigation of orthoferrite thin films[241]. Epitaxial thin films of orthoferrites have not been explored in detail due to difficulty in preparation of these materials with good crystal quality and required stoichiometry[242] [243].

In case of transition metal oxides, striking contrast is usually observed between the physical properties of thin films and bulk. Further, it is easier as well as fruitful to utilize the properties of thin film in device application. Thin films have emerged as one of the most promising source to design various devices with significantly enhanced characteristics. From pulsed laser deposition, it has now become easier to deposit thin films of multi-element compounds[4][5].

In this work, orthoferrite thin films have been deposited of $\text{NdFe}_{0.5}\text{Mn}_{0.5}\text{O}_3$ using different PLD parameters that have been optimized according to the stoichiometry of the film. Schmool *et. al.* [245] has deposited the thin film of DyFeO_3 , GdFeO_3 , SmFeO_3 and YFeO_3 using PLD technique on quartz substrate at 450°C under high vacuum condition using Nd:YAG Laser. Under these condition very high Laser fluence 7 Jcm^{-2} have been used. During deposition partial oxygen pressure has been maintained between 0 to 80 mTorr. Deposited thin films have been studied using VSM and SQUID magnetometry. It has been observed that orthoferrite films have weak saturation magnetic moment and high coercive fields in the range 1.5 to 1.8 T. Further, it has been also observed that the magnetic moment of these orthoferrite films decreases with the increase in oxygen pressure [245]. Further, Berini *et. al.* deposited thin film

of SmFeO₃ on SiO₂ glass substrate using PLD technique by tuning the deposition parameter using KrF excimer laser of wavelength 248 nm [246]. In this case, deposition takes place at a very low fluence in the range 0.9 – 2.7 Jcm⁻² in contradiction to Schmool *et. al.* study where deposition of same orthoferrite film was performed at 7 Jcm⁻²[243], [245] . During the deposition of SmFeO₃, the substrate temperature is kept in the range 1023 K to 1098 K. The laser fluence was varied for different substrate temperatures [246]. Optical constants of the SmFeO₃ thin films were measured using ellipsometry.

Another study on doped orthoferrite thin film has been done by Mir *et. al.* on PrFe_{1-x}Ni_xO₃ (0 ≤ x ≤ 0.5) [247]. These thin films were deposited on LAO (001) substrate using KrF excimer laser (248 nm) with 1.8 Jcm⁻² fluence. In these films, the FWHM of these films decreases with the increase in Ni doping, and this is due to relaxation of substrate induced strain. During the deposition partial oxygen pressure was kept at 300 mTorr [247]. In another study by WenZhe *et. al.*, heterostructure of SmFeO₃ thin with SrRuO₃ electrode has been grown on STO (100) substrate [248]. For the deposition, laser fluence of 1.5 Jcm⁻² has been used with the repetition rate 3 Hz. It has been concluded that the heteroepitaxially grown film have large polarization and improper ferroelectricity due to lattice distortion [248].

Recently, Sultan *et. al.* deposited thin films for PrFe_{1-x}Mn_xO₃ (x = 0, 0.1, 0.3, 0.5) on Si substrate using PLD under fluence of 1.8 Jcm⁻² and 750°C substrate temperature [249]. During the deposition, partial oxygen pressure was kept at 330 mTorr. In these thin films, magnetization measurements are carried out using SQUID magnetometer. ZFC-FC were carried out in the temperature range 5 – 300 K under an applied field of 100 Oe. It has been observed that magnetization increases with decrease in temperature for all films except x = 0.1 where a peak is observed at 60 K. This anomaly in x = 0.1 is attributed to the spin reorientation effect [249]. Shang *et. al.* studied the magnetic property of YFeO₃ thin film deposited on SrRuO₃/SrTiO₃ (100) substrate using SQUID magnetometry [250]. A bifurcation between ZFC-FC data was observed in this study. Based on this bifurcation authors inferred that the YFeO₃ thin film shows spin canted weak antiferromagnetism below 260 K. It might be erroneous to draw such a conclusion based on a bifurcation in ZFC-FC magnetization which can be observed due to different kinds of magnetic order.

In this chapter, the deposition parameters of $\text{NdFe}_{0.5}\text{Mn}_{0.5}\text{O}_3$ (NFMO) thin film on STO substrates using pulsed laser deposition have been discussed. Film's structural and magnetic properties have been studied. NFMO thin film with controlled dimensions, crystallinity and homogeneity are required for potential device applications. Fabrication of high quality NFMO thin film will be helpful not only in device application but also in the development of heterostructures with other oxides that can result into the observation of unexpected phenomenon at the interface.

7.2 Experimental details

Epitaxial thin film sample of $\text{NdFe}_{0.5}\text{Mn}_{0.5}\text{O}_3$ (NFMO) has been deposited on [100] oriented STO substrate by PLD technique. Polycrystalline, stoichiometric, and monophasic NFMO target was synthesized using the solid state reaction route as discussed in chapter 3. The resulted powder for the compound was reground with PVA (PolyVinyl Alcohol) and pressed into pellet and then sintered at 1400°C for 24 hours.

The thickness of the film was controlled by the number of laser pulses used for deposition which is 5000 shots for the deposited film. The target was ablated using KrF excimer laser ($\lambda = 248\text{ nm}$) 5 Hz frequency and laser fluence of about 1.8 Jcm^{-2} has been used for the deposition

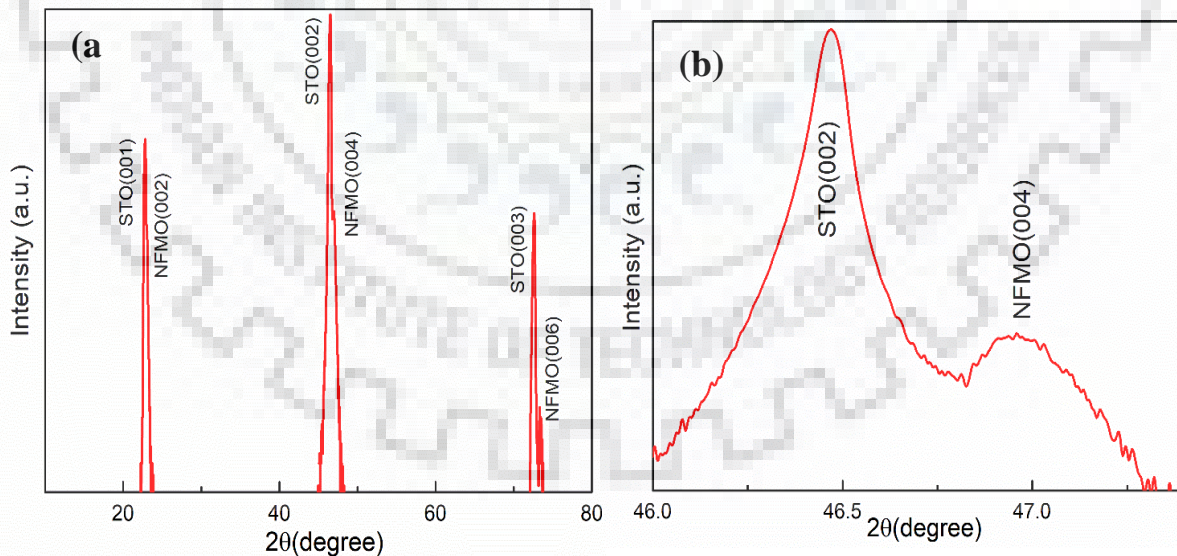


Figure 7.1 (a) $\theta/2\theta$ scan of NFMO thin film on STO substrate in the range 10° - 80°

(b) Narrow $\theta/2\theta$ scan of NFMO thin film on STO substrate in the range 46° - 47.8° to observe NFMO peak more clearly

for NFMO. The target to substrate distance was kept at 5 cm during deposition. Substrate temperature was kept at 750 °C. Partial oxygen pressure was maintained at 310 mTorr during deposition for NFMO. After deposition, the film was *in-situ* annealed for 1 hour under 500 Torr oxygen pressure in the deposition chamber and then slowly cooled down to room temperature.

Details regarding crystallinity and epitaxial quality of the films were obtained by using X-ray diffractometer (Rigaku “SmartLab” Diffractometer). Structural property of the films has been investigated using $\theta/2\theta$ scan mode of Rigaku diffractometer. Further, pole figure measurements were performed by choosing the diffraction angle with the help of bulk diffraction data, i.e. 2θ . Pole figure has been recorded for the tilt angle α (or $90^\circ - \chi$), varying from 0° to 90° and azimuthal angle, ϕ varying from 0° to 360° . The analysis of electronic structure of the thin film sample was carried out by X-ray photoelectron spectroscopy (XPS) on a PHI 5600 Versa Probe III Multi-technique system (Al K_α 1486.708 eV, step width = 0.05 eV, energy resolution = 0.5 eV, pass energy = 55 eV, base pressure of 10^{-7} mbar). The temperature dependent and field dependent magnetization were measured using SQUID

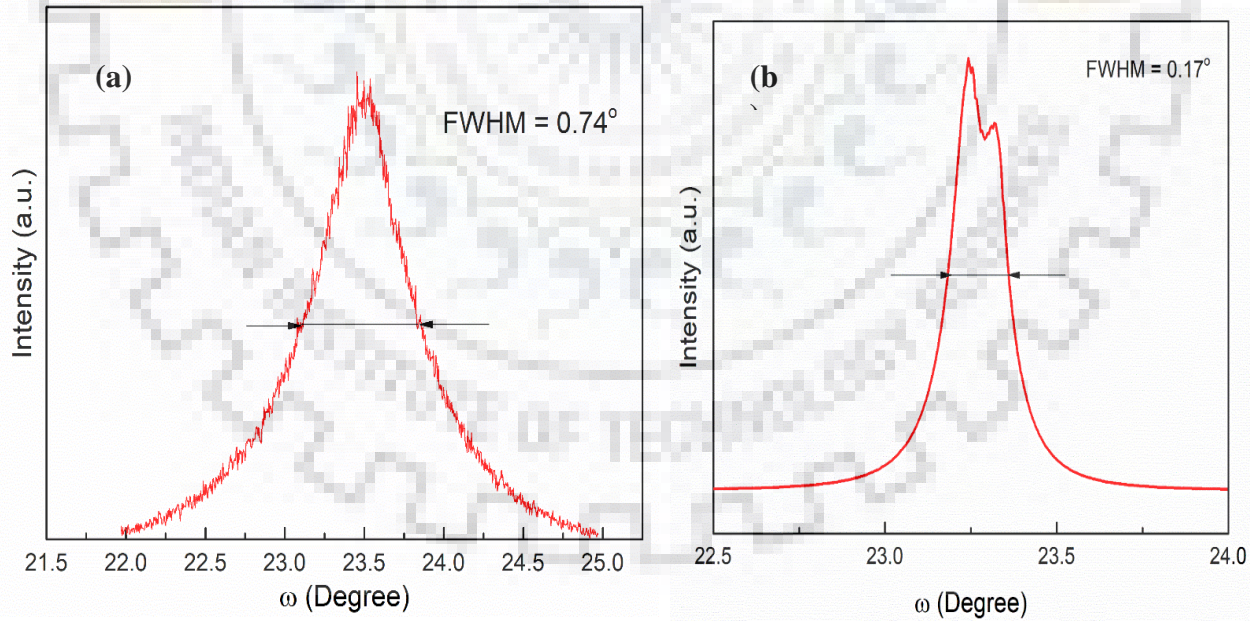


Figure 7.2 X-Ray Diffraction Rocking curve for the (a) NFMO (004) peak and (b) STO (002) peak

magnetometer (MPMS XL Evercool, Quantum Design) and Vibrating Sample Magnetometer of Quantum Design PPMS.

7.3 Results and Discussion

X-Ray diffraction for NFMO thin film on STO substrate is shown in Figure 7.1. The XRD patterns were recorded in 2θ range $10^\circ - 80^\circ$, with a step size of 0.02° and scan speed of 2 secs per step. The NFMO film preferentially grows with the $(00l)$ direction perpendicular to the STO substrate surface. The peaks shown in the Figure 7.1(a) are coming from the substrate while the film peaks are present in the form of shoulder on the right hand side of the substrate peak indicating lower inter-planer (out-of-plane) spacing for film in comparison to the substrate. As shown in Figure 7.1 (b), a detailed scan was performed around (002) substrate peak to study the (004) diffraction peak from the film. Peak related to the film's (004) planes is clearly observed at $\sim 47^\circ$. Further rocking (ω) scans were performed at (004) and (002) peaks of the film and substrate to obtain the information about the mosaicity. As shown in Figure 7.2

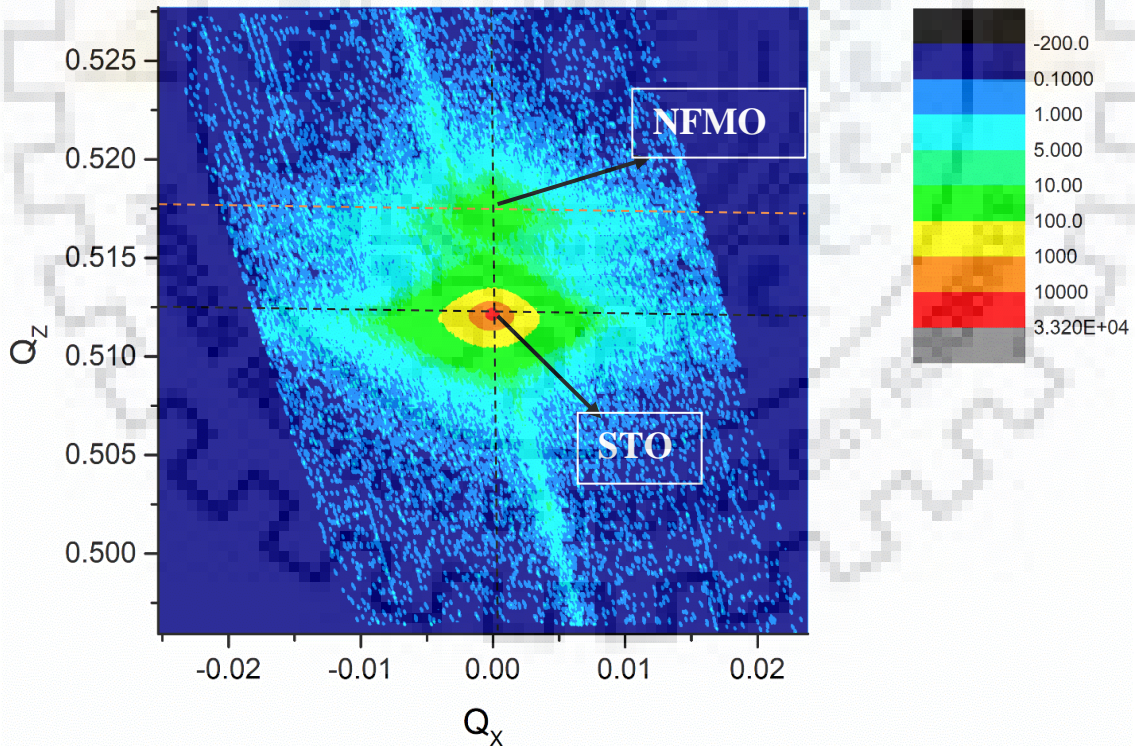


Figure 7.3 Logarithmic intensity mapping along symmetric (002) peak in reciprocal space for NFMO thin film on STO substrate

(a), the full width half maxima (FWHM) of the film peak is 0.74° which is higher than the value observed for the substrate. But substrate clearly shows presence of two facets at 0.07° to each other as shown in Figure 7.2 (b). Presence of such misaligned facets (crystallites) in substrate limits the crystal quality (mosaicity) of the thin film. We can conclude from θ - 2θ measurements that the film has grown with reasonable mosaicity and out-of-plane alignment of the crystallites. The out-of-plane c lattice parameter, calculated from (004) film peak, is 7.77 \AA while the c lattice parameter of the bulk NFMO is 7.70 \AA . This variation in c -axis parameter might be related either due to the strain in the film or due to the change in oxygen stoichiometry.

In Figure 7.3, reciprocal space mapping of (004) symmetric peak of NFMO thin film on STO substrate is shown. The measured intensity is plotted with logarithmic scale in contour form as a function of reciprocal space vector components, Q_x and Q_z . The vertical line drawn i.e. parallel to Q_z axis through the maximum intensity for NFMO as well as STO crosses near $Q_x = 0$ [251].

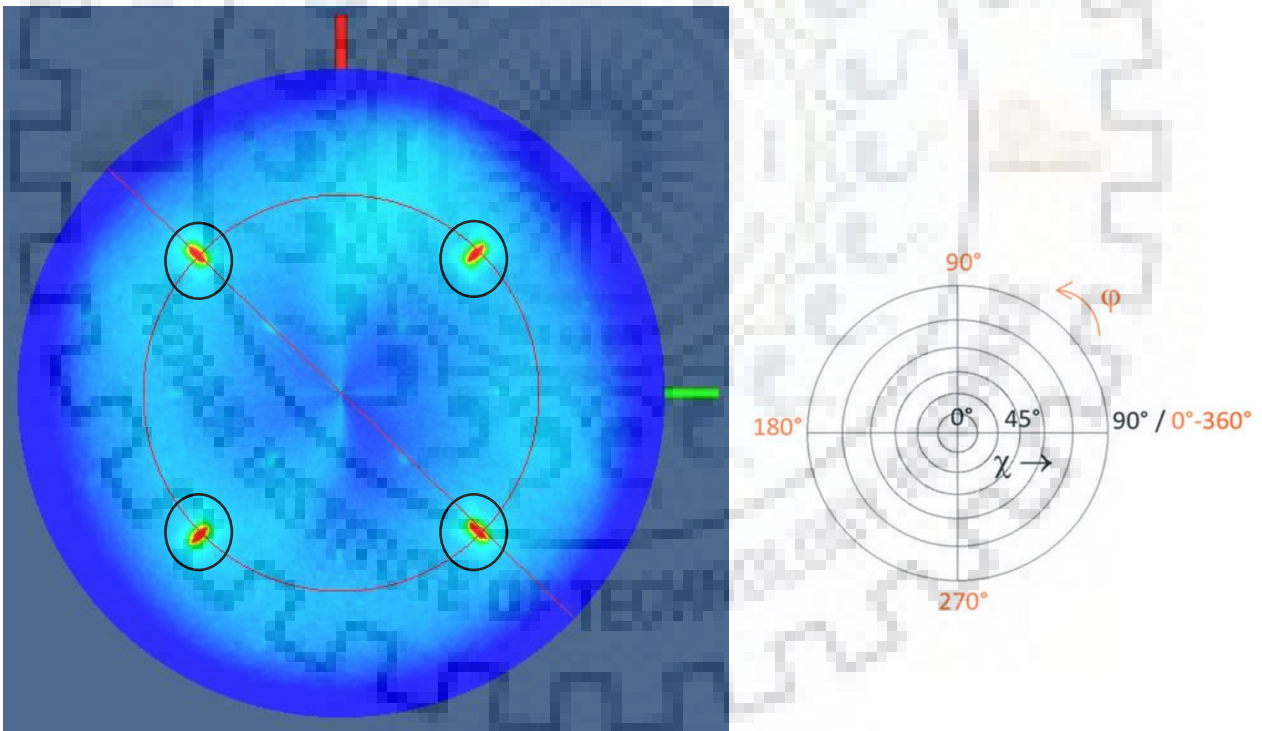


Figure 7.4 Pole figure measurement on the logarithmic scale at (022) peak and black color circled data points indicate the (022) peak planes. Picture showing the angles related to pole figure is adapted from ref [249]

The texture of NFMO thin film on STO substrate has further been investigated by performing pole figure measurements. The measurements were performed on (022) diffraction

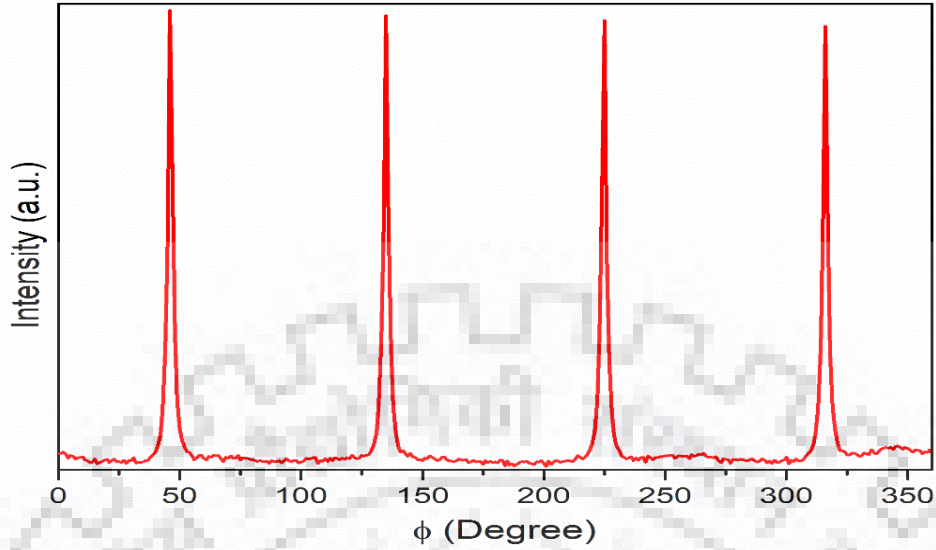


Figure 7.5 ϕ scan of in-plane (022) peak of NFMO thin film on STO substrate

peak at $2\theta = 39.84^\circ$. In the pole figure measurement, reflections from the film shows four streaks as measured from the azimuthal and sample tilting angular scans. As shown in Figure 7.4, four sharp peaks are observed at $\alpha (90^\circ - \chi) = 35^\circ$ or $\chi = 55^\circ$. These four sharp peaks are shown with black outlined circle in Figure 7.4. Another set of weak peaks are also present at $\alpha = 65^\circ$ or $\chi = 25^\circ$. These peaks correspond to (103) Bragg peak that is present at $2\theta = 38.72^\circ$ in

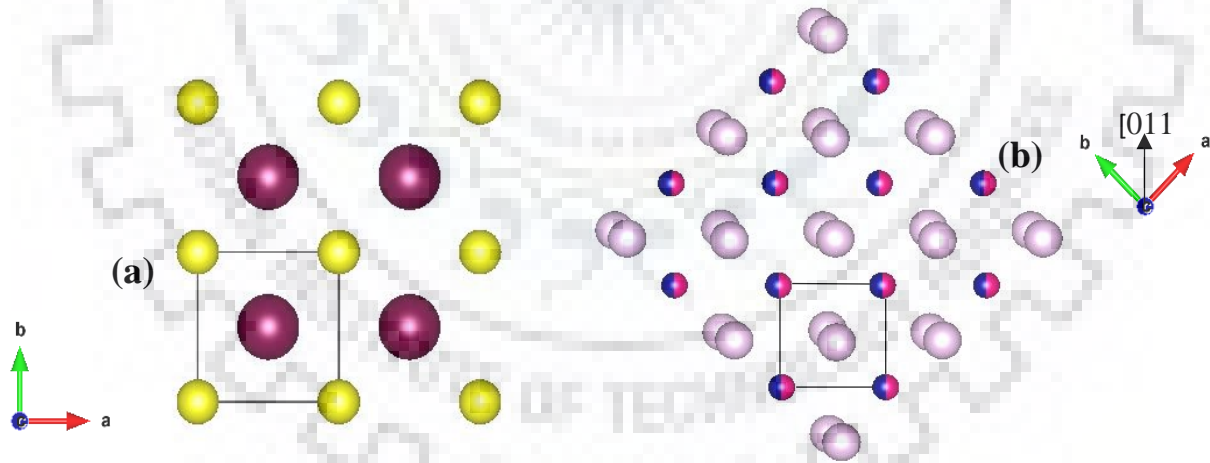


Figure 7.6 Atomic arrangement of (a) STO (100) with (b) NFMO (022) thin film. Ti and Sr atoms are shown with yellow and mauve color respectively in (a). Fe and Mn atoms occupy the same position in (b) shown with pink and blue color respectively, while Nd atom is shown by purple color

the bulk diffraction data. The (022) diffraction peaks are present at $\alpha (90^\circ - \chi) = 35^\circ$. The presence of the (022) plane at $\alpha (90^\circ - \chi) = 35^\circ$ means that (002) plane is oriented at 55° from

the surface normal of the film and substrate. This confirms that the film is epitaxially grown on the substrate with (00*l*) orientation i.e. the (00*l*) planes are oriented along the surface normal of the substrate (00*l*).

Φ scan for $\chi = 55^\circ$ at $2\theta = 39.84^\circ$ is shown in Figure 7.5. The Φ scan confirmed the epitaxial nature of the thin film along the (022) direction. In the Figure 7.5, four distinct peaks are present separated by 90° shows the four-fold pseudo cubic symmetry for the deposited thin film [252].

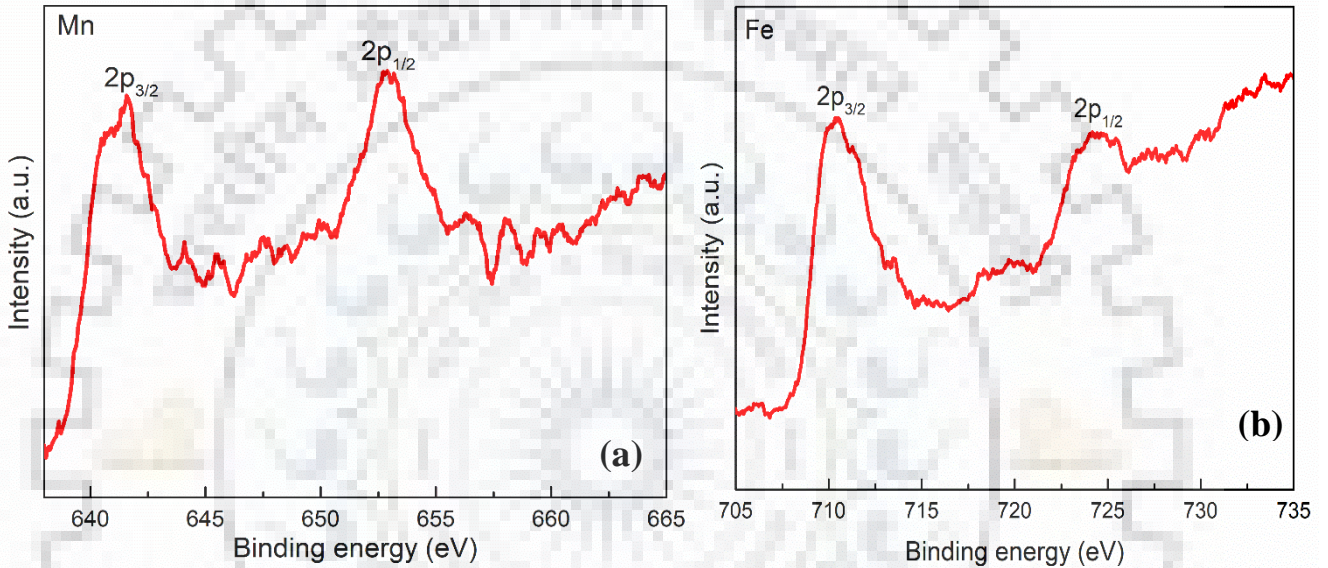


Figure 7.7 (a) XPS spectra for Mn2p and (b) XPS spectra for Fe2p in NFMO thin film

Figure 7.6 shows the sketches for NFMO thin film deposited on STO substrate. This Figure has been created using the VESTA software. The Figure 7.6 (a) shows the schematic of STO crystal structure with *c*-axis as out-of-plane direction. In-plane lattice constant of STO is 3.905 Å which is shown by the edge of the marked square. Figure 7.6 (b) shows the crystal structure of NFMO having *c*-axis as out-of-plane direction. If [110] direction of NFMO crystal structure is oriented along the [100] or [010] direction of the STO, in-plane pseudo-cubic lattice constant of NFMO is 3.904 Å which is almost same as the STO lattice constant. So NFMO grows on STO with [00*l*] out of plane orientation and with a 45° in-plane rotation. This is also confirmed by the observation of peaks around 45° , 135° , 225° , and 315° in Φ scan shown in Figure 7.5.

Further, XPS analysis was carried out to know the electronic structure of elements present on the surface of NFMO thin film. Figure 7.7 (a) and (b) shows the HR-XPS doublet for Mn2p

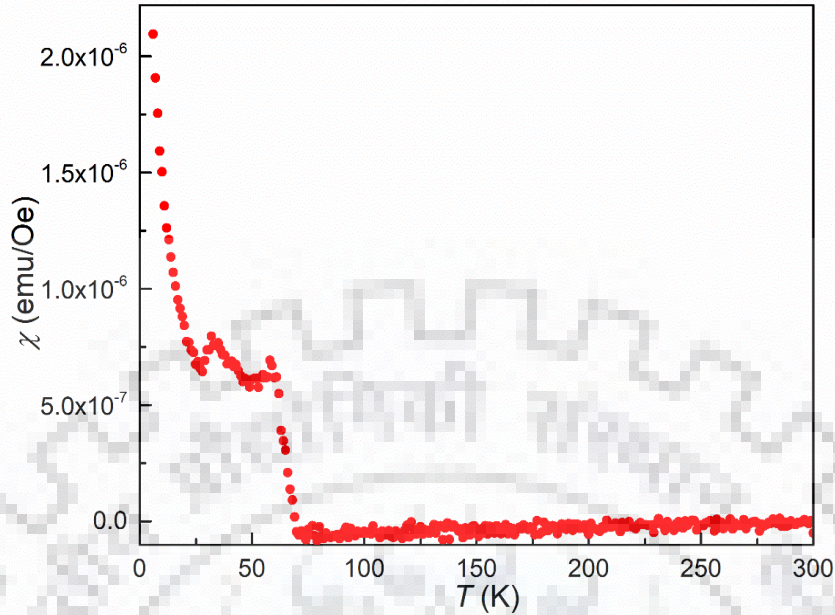


Figure 7.8 AC susceptibility of NFMO thin film on STO substrate in presence of zero DC field

and Fe2p respectively. In Figure 7.7 (a) shows the Mn 2p core-level spectrum of the representative sample. The spectrum exhibits the spin-orbit split $2p_{1/2}$ and $2p_{3/2}$ peaks located at 653.42 and 641.80 eV, respectively. The spin-orbit splitting of Mn2p exhibited an energy separation of $\Delta E = 23$ eV. The dominant peak of Mn $2p_{3/2}$ at 641.80 eV is attributed to the bonding between the Mn and O atoms on the sample surface. These values are very close to that of Mn $2p_{1/2}$ (653.40 eV) and Mn $2p_{3/2}$ (641.70 eV) in Mn₂O₃, indicating that the valence state of Mn in the NFMO thin film is +3 [253]. In addition, the HR-XPS spectra of Fe2p core levels of the prepared sample was recorded and presented in Figure 7.7 (b). As shown in Figure 7.7(b), the Fe2p spectra is also revealed a doublet at peak position 710.45 and 724.31 eV due to spin orbit interaction. The spin orbit splitting of Fe2p exhibited an energy separation of $\Delta E = 14$ eV[254]. On comparison with the literature of Fe₂O₃, it has been concluded that the Fe exist in +3 oxidation state on the surface of NFMO thin film [254]

To study the magnetic property of NFMO thin film, ac-susceptibility measurement in presence of zero applied DC field has been performed in SQUID magnetometer. Temperature dependent magnetization measurements were carried out in the temperature range 2 - 300 K and data was recorded during the cooling process as shown in Figure 7.8. AC susceptibility

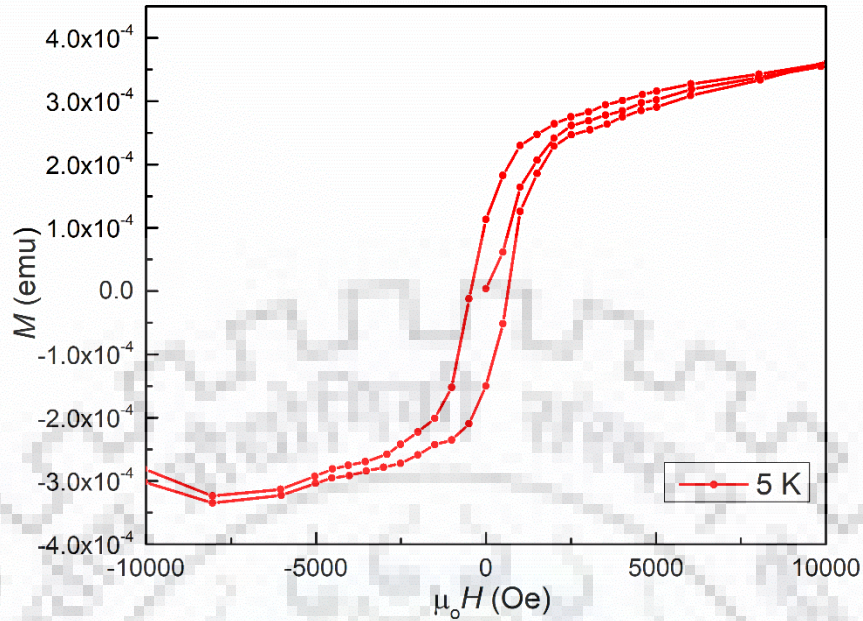


Figure 7.9 *M-H isotherm of NFMO thin film on STO substrate at 5 K*

measurement at 999 Hz was performed in 3.08 Oe AC field. As shown in the Figure 7.8, a magnetic transition occurs below 77 K. Increase in magnetization below 26 K marks the onset of the another magnetic transition.

On comparison with the bulk magnetization data as per discussion in Chapter 3, first magnetic transition at 77K might be related to the spin reorientation of $\text{Fe}^{3+}/\text{Mn}^{3+}$ ions in the film. In the bulk NFMO, spin reorientation occurs in the same temperature range. PM-AFM transition of bulk NFMO could not be observed in the susceptibility data of thin film limited by the instrument sensitivity. Magnetic transition below 26 K could be related to the rare-earth polarization.

Further, measurements of magnetization (M) versus applied field (H) were performed at 5 K within the range of -1 T to +1 T applied magnetic field as shown in Figure 7.9 after subtracting the substrate $M-H$ isotherm at 5 K in the same applied field range. $M-H$ isotherm of substrate is also non-linear with a saturation magnetization of the order of 5×10^{-5} e.m.u. Such a nonlinear magnetization is probably due to presence of magnetic impurities in substrate. As shown in the Figure 7.9, saturation magnetization is approximately 3×10^{-4} which is one order of magnitude larger than the substrate value.

. The presence of coercivity and relatively large saturation magnetization at 5 K indicate the presence of magnetic ordering in NFMO thin film.

7.4 Conclusion

The epitaxial thin film of NFMO and NDFO has been deposited on STO substrate using PLD excimer laser. XRD analysis suggests that the deposited thin film is epitaxial and growth of the film occurs along c axis with good mosaicity and out-of-plane alignment of the crystallites. From pole figure analysis of the film, it has been concluded that the deposition of the film was out-of-plane with 45° in-plane rotation with almost same pseudo cubic lattice constant as of the STO substrate.

From XPS analysis of NFMO thin film, it has been observed that both Fe and Mn exist in +3 oxidation state and no trace of impurity has been found out. Further, magnetic transition has been observed in the temperature range 5 – 70 K from AC susceptibility measurement of NFMO thin film. These transitions are attributed due to the possible spin reorientation of $\text{Fe}^{3+}/\text{Mn}^{3+}$ ions and rare-earth (Nd) moments. M - H isotherm at 5 K also confirms the magnetic ordering of the thin film. Further resonant X-ray measurements are required to probe the nature of magnetic ordering in the NFMO thin film.

Conclusion and future scope

8.1 General Conclusions

In this thesis, Orthoferrite NdFeO_3 has been studied in detail with 50 % doping of Mn on Fe site in one case while 50 % doping of Dy on Nd site in the other case. These compounds are studied through structural, magnetic and thermal properties. Each chapter in the thesis ends with a section where the conclusions pertaining to that chapter are collated. This chapter briefs the conclusions along with the scope for future work of this thesis.

Polycrystalline $\text{NdFe}_{0.5}\text{Mn}_{0.5}\text{O}_3$ was prepared using conventional solid – state reaction route. From structural analysis of the compound, it has been confirmed that the compound synthesizes into orthorhombic structure, where Fe and Mn occupy the same atomic position (disordered arrangement) rather than rock salt (ordered) arrangement. From Rietveld refinement of X-ray diffraction, it is not possible to establish clearly, regarding the structure as orthorhombic (disordered/Perovskite) or monoclinic (ordered/double Perovskite). From powder neutron diffraction at room temperature, it has been confirmed that the structure of the compound is orthorhombic rather than monoclinic where $\text{Fe}^{3+}/\text{Mn}^{3+}$ ions are in disordered state. Further, variation of lattice parameter obtained from powder neutron diffraction over a range of temperature 1.5 – 400 K has been studied in detail, where anomaly is observed in b lattice parameter at 150 K which can be attributed to magneto-elastic effect. From magnetic measurements, two magnetic transitions have been observed in the compound, first transition occurs approximately at 250 K which is the transition temperature from paramagnetic behavior to antiferromagnetic ordering while other transition is observed below 70 K which is due to spin reorientation of $\text{Fe}^{3+}/\text{Mn}^{3+}$ spins. Further, Mössbauer study shows that there is sextet present over the range of temperature 100 – 5 K due to Fe^{3+} ordering. On fitting the data, sextet has been deconvoluted into two sextets namely A and B. The ratio and relative area of these two sextets changes, confirming the spin reorientation of Fe^{3+} spins. It has been observed that,

relative area of one sextet decreases with the temperature while the area of other sextet increases with nearly equal value at 36 K.

Detailed powder neutron diffraction of NFMO is performed in the temperature range 400 – 1.5 K to study the magnetic structure of the compound. In NFMO, diffused scattering is observed at 400 K itself, which becomes most prominent at 300 K and continues all the way down to 1.5 K. The diffused scattering peak can be attributed to short ranged spin-spin correlation involving nearest and next nearest neighbor interactions. From 300 K till 1.5 K, 3D SRO, though independent, but still, coexists with the long ranged magnetic structure. With decreasing temperature, the correlation length of SRO increases. This is first report related to the presence of independent 3D SRO coexisting with LRO over the whole range of temperature in Orthoferrites. Further, at 300 K, mixture of $\Gamma_4 (G_x, C_y, F_z)$ and $\Gamma_1 (A_x, G_y, C_z)$ magnetic structure develops, coexisting with diffused scattering. Below T_N (250 K) obtained from the SQUID magnetometer, there is an increase in the volume fraction of Γ_1 magnetic structure superseding the fraction of Γ_4 structure. At 150 K, there is a sharp jump in the moment value, due to Γ_1 magnetic structure, similar to sharp jump in b lattice parameter of NFMO. Below 150 K, magnetic structure of NFMO is mainly given by the irreducible representation of Γ_1 . The presence of Γ_1 below T_N is not observed in any other Orthoferrite. This unusual magnetic structure in NFMO occur primarily due to the presence of large single ion anisotropy of Mn^{3+} which is an order of magnitude larger than Fe^{3+} . In most of the Orthoferrites, spin reorientation occurs due to the presence of weak ferromagnetism associated with the canting of antiferromagnetically ordered spins in the G -type configuration. Thus spin reorientation occurs either from $\Gamma_4 (G_x, F_z)$ to $\Gamma_1 (G_y)$ (in the case of $DyFeO_3$) or from $\Gamma_4 (G_x, F_z)$ to $\Gamma_2 (F_x, G_z)$ (in the case of $NdFeO_3$). But in the case of NFMO, inspite of the presence of pure Γ_1 magnetic structure without the presence of any weak ferromagnetic canting, spin reorientation of Fe^{3+}/Mn^{3+} spins has been observed. Below 75 K, Fe^{3+}/Mn^{3+} spins again undergoes the process of gradual spin reorientation from Γ_1 magnetic symmetry to $\Gamma_2 (F_x, C_y, G_z)$ changing the direction gradually from b to c axis. At 1.5 K, Nd^{3+} spins also order ferromagnetically along a direction along with Γ_2 magnetic symmetry of Fe^{3+}/Mn^{3+} . Thus in NFMO, we observe a possible two-fold spin reorientation of the type $\Gamma_4/\Gamma_1 \rightarrow \Gamma_1$ in the temperature range 300-150 K and $\Gamma_1 \rightarrow \Gamma_2$ in the lower temperature region (70-20 K). Finally, from specific heat

measurement, Schottky anomaly is observed at lower temperature suggesting the domination of Nd-Fe/Mn molecular field.

In present thesis, I also studied $\text{Nd}_{0.5}\text{Dy}_{0.5}\text{FeO}_3$, where 50% of Nd^{3+} site is substituted by Dy^{3+} ions. The polycrystalline $\text{Nd}_{0.5}\text{Dy}_{0.5}\text{FeO}_3$ was prepared using conventional solid – state reaction route. Similar to parent compounds i.e. NdFeO_3 and DyFeO_3 , crystal structure of the compound is orthorhombic with $Pbnm$ space group. In this compound, change in lattice parameter, obtained from powder neutron diffraction, coincides with the transition in magnetic measurement indicating spin reorientation of Fe^{3+} ions. From magnetic measurements, M - T shows two transitions at 60 K and 30 K, possible reason might be spin reorientation of Fe^{3+} spins. This has been further confirmed from the M - H measurements over the same range of temperature. In NDFO, the magneto-dielectric effect is not observed which has been observed very prominently in DyFeO_3 . Absence of magneto-dielectric effect confirms the effect of Nd^{3+} moments on the ordering of Dy^{3+} moments. To study the magnetic structure of the compound in detail, powder neutron diffraction has been performed in the temperature range 1.5 – 300 K. Rietveld refinement of the data shows gradual spin reorientation of Fe^{3+} ions in the temperature range 75 to 20 K from Γ_4 to Γ_2 , which is usual in Orthoferrite but in contrast to abrupt $\Gamma_4 \rightarrow \Gamma_1$, as seen in DyFeO_3 . Below 10 K, a second spin reorientation $\Gamma_2 \rightarrow \Gamma_4$ is initiated where Fe^{3+} spins start rotating gradually from c direction to a direction coinciding with the C - type antiferromagnetic rare earth ordering along b direction. The rare earth ordering (C -type) in NDFO is similar to Nd^{3+} ordering in NdFeO_3 which is also C - type at 1.5 K but completely different from Dy^{3+} ordering in DyFeO_3 which is G - type. The rare earth ordering in NDFO is not independent to Fe^{3+} magnetic ordering due to low anisotropy and there is competing behavior between R^{3+} - R^{3+} and R^{3+} - Fe^{3+} magnetic interaction ($R = \text{Nd, Dy}$). In heat capacity measurement, there is complete absence of second order λ -anomaly indicating that the ordering of $\text{Nd}^{3+}/\text{Dy}^{3+}$ moments is induced by effective molecular field arising due to Fe^{3+} spins.

In the next chapter, comparative study of the magnetocaloric effect of NFMO and NDFO has been studied. Due to large difference between magnetization curves under different externally applied magnetic field in NDFO as well as in NFMO leads to the study of magnetocaloric effect in both the compounds. Detailed M - H isotherm of NDFO shows relatively higher value of saturated magnetic moment at 5 K under an applied field of 4 T. This

indicates that the crystal field environment and exchange interaction play important role in the determination of magnetic properties. In the case of NDFO, maximum entropy change is calculated as $10.38 \text{ JKg}^{-1}\text{K}^{-1}$ at 4K under an applied field of 5 T whereas, in the case of NFMO, maximum change in entropy is $2.73 \text{ JKg}^{-1}\text{K}^{-1}$ at 6.5 K under 5 T applied field. In the case of NDFO, low temperature rare earth ($\text{Nd}^{3+}/\text{Dy}^{3+}$) ordering is responsible. Large value of magnetic entropy change at lower temperature is due to the influence of $R^{3+}\text{-Fe}^{3+}$ interaction on order-disorder transition of rare earth ion. In the case of NFMO, though smaller value of entropy change is observed in comparison to NDFO, but the observed value is larger in comparison to most of the Nd based transition metal oxides. In NFMO, maximum entropy change is observed in the two temperature regions: (i) below 10 K, the maximum value is $2.73 \text{ JKg}^{-1}\text{K}^{-1}$ under an applied field of 5 T, (ii) in the spin reorientation region (75-20 K), a significant entropy change is observed which decreases with an increase in applied field. In NFMO, change in entropy below 10 K is due to the possible development of Nd^{3+} moment polarization because of Nd/Fe-Mn interactions and may be beneficial for application based on magnetic refrigeration. Another entropy change observed in the spin reorientation region could be useful for the devices based on low field application.

In the next chapter of the thesis, thin film of NFMO has been deposited on STO substrate using pulsed laser deposition. Deposited thin films are epitaxial having good mosaicity with an out-of-plane alignment along *c*-axis. The growth of NFMO on STO substrate have in-plane 45° rotation of (100) and (010) plane with the corresponding planes of STO substrate. Further, XPS is performed to confirm the oxidation state of Fe and Mn ion on the surface of thin film. Valence state of Fe and Mn found to be in +3 state on the surface. To study the magnetic properties of the NFMO thin films, *ac* susceptibility measurements were performed, where low temperature transition due to spin reorientation of $\text{Fe}^{3+}/\text{Mn}^{3+}$ ions is observed.

8.2 Future Scope

The work done in the present thesis is mainly focused on the study of magnetic properties of two polycrystalline Orthoferrite compounds: (i) $\text{NdFe}_{0.5}\text{Mn}_{0.5}\text{O}_3$, (ii) $\text{Nd}_{0.5}\text{Dy}_{0.5}\text{FeO}_3$. Thin films of $\text{NdFe}_{0.5}\text{Mn}_{0.5}\text{O}_3$, are also deposited by pulsed laser deposition. The work on the present topic can be further extended in the polycrystalline as well in the thin film form.

In the polycrystalline form, magnetic structure of Orthoferrites can be studied in detail where 50% Fe^{3+} site will be doped by Cr^{3+} ions. Both Cr^{3+} as well as Fe^{3+} ions are known for their unique property of undergoing spin reorientation with the lowering of temperature. Thus, with the presence of both ions on the same, it would be very interesting to study the behavior of $\text{Fe}^{3+}/\text{Cr}^{3+}$ ions as well as the rare earth ordering in such compound. It has been known widely that $\text{Fe}^{3+}\text{-O-Fe}^{3+}$ and $\text{Cr}^{3+}\text{-O-Cr}^{3+}$ interactions are antiferromagnetic in nature while $\text{Fe}^{3+}\text{-O-Cr}^{3+}$ favors weak ferromagnetic ordering. In case of Chromites, magnetic structure depends on the rare earth ions, for instance in the case of rare earth ions with even electron i.e. Ho, Tm, Cr^{3+} ions are found in Γ_2 magnetic structure below Néel temperature. For rare earth ions with odd electron i.e. Nd, Gd, Dy, Cr^{3+} ions undergo abruptly either from $\Gamma_4 \rightarrow \Gamma_1$ for ErCrO_3 or abrupt transition from $\Gamma_2 \rightarrow \Gamma_1$ for NdCrO_3 . In the case of Orthoferrites, magnetic structure below Néel temperature is independent of rare earth ions and $R^{3+}\text{-Fe}^{3+}$ exchange interaction contributes to the spin reorientation of Fe^{3+} ions. Thus, it would be interesting to study the compound with 50% doping of Cr^{3+} ion on Fe^{3+} site for different rare earth ions. Chromites are also well known to show the multiferroicity behavior which is not seen in Orthoferrites usually except controversial case of DyFeO_3 . Thus with the doping of Cr^{3+} ions in Orthoferrite makes it efficient for applications based on multiferroicity as well as spin reorientation.

In the form of thin film, Orthoferrites can be deposited on different substrates to study the structural property of film in detail. Due to deposition of film on different substrate, the strain in the films can be controlled. Physical properties of the film can be controlled by depositing the film in the presence of different oxygen pressure. Effect of oxygen stoichiometry will also resulted as change in the structural as well as magnetic property due to possible change in the oxidation state of transition metal ions. As Orthoferrites are antiferromagnetic in nature, thus it is not possible to study their magnetic properties using magnetometers. Therefore, for detailed magnetic analysis of these thin films, resonant X-ray or XMLD would be preferred. After the detailed analysis of structure and magnetic properties of the deposited film, thin films can be utilized in the memory devices using ultrafast spin dynamics.



BIBLIOGRAPHY

- [1] M. K. Kinyanjui, Y. Lu, N. Gauquelin, M. Wu, A. Frano, P. Wochner, M. Reehuis, G. Christiani, G. Logvenov, H.-U. Habermeier, G. A. Botton, U. Kaiser, B. Keimer, and E. Benckiser, "Lattice distortions and octahedral rotations in epitaxially strained $\text{LaNiO}_3/\text{LaAlO}_3$ superlattices," *Appl. Phys. Lett.*, vol. 104, no. 22, pp. 3–7, 2014.
- [2] Kenta Shimamoto, Saumya Mukherjee, Sebastian Manz, Jonathan S. White, Morgan Trassin, Michel Kenzelmann, Laurent Chapon, Thomas Lippert, Manfred Fiebig, Christof W. Schneider & Christof Niedermayer, "Tuning the multiferroic mechanisms of TbMnO_3 by epitaxial strain," *Nat. Publ. Gr.*, pp. 1–9, 2017.
- [3] P. Umek, A. Zorko, and D. Arcon, "Magnetic Properties of Transition-Metal Oxides: from Bulk to Nano", *ChemInform Abstract* vol. 42, no. 42. 2011.
- [4] C. Rao, "Transition Metal Oxides," *Annu. Rev. Phys. Chem.*, vol. 40, no. 1, pp. 291–326, 2002.
- [5] Da Woon Jeong, Woo Seok Choi, Satoshi Okamoto, Jae-Young Kim, Kyung Wan Kim, Soon Jae Moon, Deok-Yong Cho, Ho Nyung Lee & Tae Won Noh, "Dimensionality control of d -orbital occupation in oxide superlattices," *Sci. Rep.*, vol. 4, pp. 1–5, 2014.
- [6] M. Rössle, C. N. Wang, P. Marsik, M. Yazdi-Rizi, K. W. Kim, A. Dubroka, I. Marozau, C. W. Schneider, J. Humlíček, D. Baeriswyl, and C. Bernhard "Optical probe of ferroelectric order in bulk and thin-film perovskite titanates," *Phys. Rev. B - Condens. Matter Mater. Phys.*, vol. 88, no. 10, pp. 1–7, 2013.
- [7] D. Khomskii, *Transition metal compounds*, vol. 1. 2014.
- [8] C. N. R. Rao and G. V. Subba Rao, "Electrical conduction in metal oxides," *Phys. Status Solidi*, vol. 1, no. 4, pp. 597–652, 1970.
- [9] A. Munoz-Paez, "Transition Metal Oxides: Geometric and Electronic Structures: Introducing Solid State Topics in Inorganic Chemistry Courses," *J. Chem. Educ.*, vol. 71, no. 5, pp. 381, 2009.

- [10] M. Bluschke, A. Frano, E. Schierle, M. Minola, M. Hepting, G. Christiani, G. Logvenov, E. Weschke, E. Benckiser and B. Keimer “Transfer of Magnetic Order and Anisotropy through Epitaxial Integration of 3d and 4f Spin Systems,” *Phys. Rev. Lett.*, vol. 118, no. 20, pp. 1–5, 2017..
- [11] Masatoshi Imada, Atsushi Fujimori and Yoshinori Tokura “Metal-insulator transitions”, *Rev. Mod. Phys.*, vol. 70, no. 4, 1998.
- [12] M. B. Salamon and M. Jaime, “The physics of manganites: Structure and transport,” *Rev. Mod. Phys.*, vol. 73, no. 3, pp. 583–628, 2001.
- [13] Y. S. Lee, J.S.Lee, K.W.Kim, T.W.Noh, JaejunYu, E. J. Choi, G.Cao and J. E. Crow, “Pseudogap formation in 4d transition metal oxide BaRuO₃,” *Europhys. Lett.*, vol. 55, no. 2, pp. 280–286, 2001.
- [14] C. Moure and O. Peña, “Recent advances in perovskites: Processing and properties,” *Prog. Solid State Chem.*, vol. 43, no. 4, pp. 123–148, 2015.
- [15] B. Kumari, P. R. Mandal, and T. K. Nath, “Magnetic, magnetocapacitance and dielectric properties of BiFeO₃ nanoceramics,” *Adv. Mater. Lett.*, vol. 5, no. 2, pp. 84–88, 2014.
- [16] S. Geller, “Crystal Structure of Gadolinium orthoferrite, GdFeO₃,” *The Journal of Chemical Physics*, vol. 24, no. 6, pp-1236-1239, 1956.
- [17] A.S. Bhalla, Ruyan Guo, Rustum Roy, “The perovskite structure – a review of its role in ceramic science and technology”, *Mat Res Innovat*, Vol. 4, pp. 3–26, 2000.
- [18] K. S. Aleksandrov, “The sequences of structural phase transitions in perovskites,” *Ferroelectrics*, vol. 14, no. 1, pp. 801–805, 1976.
- [19] A. Urushibara, Y. Moritomo, T. Arima, A. Asamitsu, G. Kido, and Y. Tokura, “Insulator-metal transition and giant magnetoresistance in La_{1-x}Sr_xMnO₃,” *Phys. Rev. B*, vol. 51, no. 20, pp. 14103–14109, 1995.
- [20] J.-S. Zhou, J. B. Goodenough, J. M. Gallardo-Amores, E. Morán, M. A. Alario-Franco, and R. Caudillo “Hexagonal versus perovskite phase of manganite RMnO₃ (R = Y, Ho

- , Er , Tm , Yb , Lu)" *Phys. Rev. B.*, Vol. 74, pp. 014422 1–7, 2006.
- [21] J. H. Van Santen and G. H. Jonker, "Ferromagnetic compounds of manganese with perovskite structure," *Physica*, vol. 16, no. 3, pp. 337–349, 1950.
- [22] C. Zener, "Interaction Between the d Shells in the Transition Metals," *Phys. Rev.*, vol. 81, no. 1939, pp. 440, 1951.
- [23] Christof W. Schneider, Saumya Mukherjee, Kenta Shimamoto, Saikat Das, Hubertus Luetkens, Jonathan S. White, Matthias Bator, Yi Hu, Jochen Stahn, Thomas Prokscha, Andreas Suter, Zaher Salman, Michel Kenzelmann, Thomas Lippert, and Christof Niedermayer "Coexisting multiple order parameters in single-layer LuMnO_3 films," *Phys. rev. B*, vol. 94, pp. 054423, 2016.
- [24] R. von Helmolt, J. Wecker, B. Holzapfel, L. Schultz, and K. Samwer 'Siemens, "Giant Negative Magnetoresistance in Perovskitelike $\text{La}_{2/3}\text{Ba}_{1/3}\text{MnO}_x$ Ferromagnetic Films", *Phys. Rev. Lett.*, vol. 71, no. 14, pp. 2331–2333, 1993.
- [25] J. G. Bednorz and K. A. Müller, "Possible High T_c Superconductivity in the Ba-La-Cu-O system", *Z. Phys. B. Condensed Matter*, vol. 193, pp. 189–193, 1986.
- [26] Thomas Lottermoser, Thomas Lonkai, Uwe Amann, Dietmar Hohlwein, Jörg Ihringer & Manfred Fiebig, "Magnetic phase control by an electric field" *Nature*, vol. 430, no. 6999, pp. 541–543, 2004.
- [27] Sang-Wook Cheong, and Maxim Mostovoy "Multiferroics: a magnetic twist for ferroelectricity," *Nature.*, vol. 3, no. 3, pp. 533–565, 1962.
- [28] T. H. Lin, C. C. Hsieh, C. W. Luo, J.-Y. Lin, C. P. Sun, H. D. Yang, C.-H. Hsu, Y. H. Chu, K. H. Wu, T. M. Uen, and J. Y. Juang "Magnetism-induced ferroelectric polarization in the c -axis-oriented orthorhombic HoMnO_3 thin films," *J. Appl. Phys.*, vol. 106, no. 10, 2009.
- [29] Kenta Shimamoto, Saumya Mukherjee, Nicholas S. Bingham, Anna K. Suszka, Thomas Lippert, Christof Niedermayer, and Christof W. Schneider "Single-axis-dependent structural and multiferroic properties of orthorhombic RMnO_3 ($R = \text{Gd} - \text{Lu}$)," *Phys. Rev. B.*, vol. 184105, pp. 1–9, 2017.

- [30] A. H. Bobeck, "Properties and Device Applications of Magnetic Domains in Orthoferrites," *Bell Syst. Tech. J.*, vol. 46, no. 8, pp. 1901–1925, 1967.
- [31] Andrew H. Bobeck, Robert F. Fischer, Anthony .J. Perkeski, J. P. Remeika, and L. G. Van Uitert "Application of Orthoferrites to Domain-Wall Devices," *IEEE Trans. Magn.*, vol. 5, no. 3, pp. 544–553, 1969, pp. 544–553, 1969.
- [32] S. O. Demokritov, A. I. Kirilyuk, N. M. Kreines, V. I. Kudinov, V. B. Smirnov, and M. V. Chetkin, "Interaction of the moving domain wall with phonons," *J. Magn. Mater.*, vol. 102, no. 3, pp. 339–353, 1991.
- [33] Y. S. Didosyan, V. Y. Barash, N. A. Bovarin, H. Hauser, and P. Fulmek, "Magnetic field sensor by orthoferrites," *Sensors Actuators, A Phys.*, vol. 59, no. 1–3, pp. 56–60, 1997.
- [34] Y. S. Didosyan, H. Hauser, G. A. Reider, R. Glatz, and H. Wolfmayr, "Magnetization reversal and aftereffect in orthoferrites," *J. Appl. Phys.*, vol. 93, no. 10, pp. 8755–8757, 2003.
- [35] R. M. Bozorth, V. Kramer, and J. P. Remeika, "Magnetization in single crystals of some rare-earth orthoferrites," *Phys. Rev. Lett.*, vol. 1, no. 1, pp. 3–4, 1958.
- [36] B. T. Laboratories and M. Pill, "Magnetic Properties of Some Orthoferrites," *Readings*, vol. 337, no. 1950, 1956.
- [37] D. Treves, "Magnetic studies of some orthoferrites", *Phys. Rev. Lett.*, vol. 125, no. 6, pp. 1843-1853, 1962.
- [38] Ya. B. Bazaliy, L. T. Tsymbal, G. N. Kakazei, A. I. Izotov, and P. E. Wigen "Spin-reorientation in ErFeO_3 : Zero-field transitions, three-dimensional phase diagram, and anisotropy of erbium magnetism," *Phys. Rev. B - Condens. Matter Mater. Phys.*, vol. 69, no. 104429, pp. 1–10, 2004.
- [39] M. Eibschütz, S. Shtrikman, and D. Treves, "Mössbauer Studies of Fe^{57} in Orthoferrites," *Phys. Rev.*, vol. 156, no. 2, pp. 562–577, 1967.
- [40] Hui Shen, Zhenxiang Cheng, Fang Hong, Jiayue Xu, Shujuan Yuan, Shixun Cao and

- Xiaolin Wang, "Magnetic field induced discontinuous spin reorientation in ErFeO₃ single crystal," *Appl. Phys. Lett.*, vol. 103, no. 192404, pp. 1-5, 2013.
- [41] P. Mandal, C.R. Serrao, E. Suard, V. Caignaert, B. Raveau, A. Sundaresan, C.N.R. Rao, "Spin reorientation and magnetization reversal in the perovskite oxides, YFe_{1-x}Mn_xO₃ (0≤x≤0.45): A neutron diffraction study," *J. Solid State Chem.*, vol. 197, pp. 408–413, 2013.
- [42] I. Dzyaloshinsky, "A Thermodynamic Theory of "weak ferromagnetism of antiferromagnetics," *Journal of Phys. Chem. Solids*, vol. 4, pp. 241–255, 1958.
- [43] Toru Moriya, "Anisotropic Superexchange Interaction and Weak Ferromagnetism", *Phys. Rev. Lett.*, vol. 120, no. 1, 1960.
- [44] D. Treves, "Studies on orthoferrites at the Weizmann Institute of Science," *J. Appl. Phys.*, vol. 36, no. 3, pp. 1033–1039, 1965.
- [45] R. L. White, "Review of recent work on the magnetic and spectroscopic properties of the rare-earth orthoferrites," *J. Appl. Phys.*, vol. 40, no. 3, pp. 1061–1069, 1969.
- [46] Y. Tokunaga, S. Iguchi, T. Arima, and Y. Tokura, "Magnetic-field-induced ferroelectric state in DyFeO₃," *Phys. Rev. Lett.*, vol. 101, no. 9, pp. 3–6, 2008.
- [47] J. Marwchal, "Etude structure par diffraction magnetique," vol. 28, pp. 2143–2154, 1967.
- [48] T. Yamaguchi, "Theory of spin reorientation in rare-earth orthochromites and orthoferrites," *J. Phys. Chem. Solids*, vol. 35, no. 4, pp. 479–500, 1974.
- [49] T. Yamaguchi and K. Tsushima, "Magnetic symmetry of rare-earth orthochromites and orthoferrites," *Phys. Rev. B*, vol. 8, no. 11, pp. 5187–5198, 1973.
- [50] Smita Chaturvedi, Priyank Shyam, Rabindranath Bag, Mandar M. Shirolkar, Jitender Kumar, Harleen Kaur, Surjeet Singh, A. M. Awasthi, and Sulabha Kulkarn, "Nanosize effect: Enhanced compensation temperature and existence of magnetodielectric coupling in SmFeO₃," *Phys. Rev. B*, vol. 96, no. 2, pp. 1–13, 2017.
- [51] L. Prelorendjo, C. Johnson, M. Thomas, and B. Wanklyn, "Spin reorientation transitions

- in DyFeO₃ induced by magnetic fields,” *J. Phys. C Solid State Phys.*, vol. 13, pp. 2567–2578, 1980.
- [52] G. Gorodetsky, B. Sharon, and S. Shtrikman, “Magnetic properties of an antiferromagnetic orthoferrite,” *J. Appl. Phys.*, vol. 39, no. 2, pp. 1371–1372, 1968.
- [53] V. V. Eremenko, S. L. Gnatchenko, N. F. Kharchenko, P. P. Lebedev, K. Piotrowski, H. szymczak and R. Szymczak, “New magnetic phase transitions in DyFeO₃,” *Europhys. Lett.*, vol. 11, p. 1327, 1987.
- [54] R. Bag and S. Singh, “Magnetic phase transitions in HoFeO₃ single crystals grown using the optical floating-zone method,” *AIP Conf. Proc.*, vol. 1832, pp. 1–4, 2017.
- [55] T. Chatterji, A. Stunault, and P. J. Brown, “Single crystal polarized neutron diffraction study of the magnetic structure of HoFeO₃,” *J. Phys. Condens. Matter*, vol. 29, no. 38, 2017.
- [56] T. Chatterji, M. Meven, and P. J. Brown, “Temperature evolution of magnetic structure of HoFeO₃ by single crystal neutron diffraction,” *AIP Adv.*, vol. 7, no. 045106, pp. 1–11, 2017.
- [57] H. Horner and C. M. Varma, “Nature of spin-reorientation transitions,” *Phys. Rev. Lett.*, vol. 20, no. 16, pp. 845–846, 1968.
- [58] Quantum Design, “Heat Capacity Option User’s Manual,” *Test*, no. 1085–150, H-1, pp. 43, 1999.
- [59] F. Bartolomé, J. Bartolomé, M. Castro, and J. J. Melero, “Specific heat and magnetic interactions in NdCrO₃,” *Phys. Rev. B - Condens. Matter Mater. Phys.*, vol. 62, no. 2, pp. 1058–1066, 2000.
- [60] N. Ghosh, “Effect of magnetic field on Nd_{0.7}Pb_{0.3}MnO₃ single crystal,” *J. Magn. Mater.*, vol. 323, no. 5, pp. 405–409, 2011.
- [61] A. K. Raychaudhuri, A. Guha, I. Das, R. Rawat, and C. N. R. Rao, “Specific heat of single-crystalline Pr_{0.63}Ca_{0.37}MnO₃ in the presence of a magnetic field,” *Phys. Rev. B - Condens. Matter Mater. Phys.*, vol. 64, no. 16, pp. 1–9, 2001.

- [62] A. Podlesnyak, S. Rosenkranz, F. Fauth, W. Marti, H. J. Scheel, and A. Furrer, “Crystal-field levels in the distorted perovskite PrGaO_3 ,” *J. Phys. Condens. Matter*, vol. 6, no. 22, pp. 4099–4106, 1994.
- [63] C. P. Reshmi, S. Savitha Pillai, K. G. Suresh, and M. R. Varma, “Near room temperature magnetocaloric properties of Fe substituted $\text{La}_{0.67}\text{Sr}_{0.33}\text{MnO}_3$,” *Mater. Res. Bull.*, vol. 48, no. 2, pp. 889–894, 2013.
- [64] A. Tishin, Y. Spichkin, T. M. Effect, A. Tishin, and Y. Spichkin, “The Magnetocaloric Effect and Its Applications (Chapter 1),” *New York*, vol. 6, no. 11, pp. 1–28, 2003.
- [65] N. A. de Oliveira and P. J. von Ranke, “Theoretical aspects of the magnetocaloric effect,” *Phys. Rep.*, vol. 489, no. 4–5, pp. 89–159, 2010.
- [66] V. Basso, “Basics of the magnetocaloric effect,” arXiv: 1702.08347v1, 2017.
- [67] E. V. Sampathkumaran, I. Das, R. Rawat, and S. Majumdar, “Magnetocaloric effect in Gd_2PdSi_3 ,” *Appl. Phys. Lett.*, vol. 77, no. 3, pp. 418–420, 2000.
- [68] V. K. Pecharsky and K. A. Gschneidner, “Magnetocaloric effect from indirect measurements: Magnetization and heat capacity,” *J. Appl. Phys.*, vol. 86, no. 1, pp. 565–575, 1999.
- [69] M. H. Phan, S. B. Tian, D. Q. Hoang, S. C. Yu, C. Nguyen, and A. N. Ulyanov, “Large magnetic-entropy change above 300 K in CMR materials,” *J. Magn. Magn. Mater.*, vol. 258–259, pp. 309–311, 2003.
- [70] T. Chakraborty, H. Nhalil, R. Yadav, A. A. Wagh, and S. Elizabeth, “Magnetocaloric properties of R_2NiMnO_6 (R=Pr, Nd, Tb, Ho and Y) double perovskite family,” *J. Magn. Magn. Mater.*, vol. 428, pp. 59–63, 2017.
- [71] V. K. Pecharsky and K. A. Gschneidner, “Some common misconceptions concerning magnetic refrigerant materials,” *J. Appl. Phys.*, vol. 90, no. 9, pp. 4614–4622, 2001.
- [72] O. Tegus, E. Brück, K. H. J. Buschow, and F. R. de Boer, “Transition-Metal-Based Magnetic Refrigerants for Room-Temperature Applications,” *Letters to nature*, vol. 415, pp. 150-152, 2002.

- [73] P. M. Woodward, "Octahedral Tilting in Perovskites. I. Geometrical Considerations," *Acta Crystallogr. Sect. B Struct. Sci.*, vol. 53, no. 1, pp. 32–43, 1997.
- [74] P. M. Woodward, "Octahedral Tilting in Perovskites. II. Structure Stabilizing Forces," *Acta Crystallogr. Sect. B Struct. Sci.*, vol. 53, no. 1, pp. 44–66, 1997.
- [75] J. Geck, P. Wochner, S. Kiele, R. Klingeler, A. Revcolevschi, M. v. Zimmermann, B. Büchner and P. Reutler, "Orbital order induced ferromagnetic insulating properties," *New J. Phys.*, vol. 6, pp. 1–27, 2004.
- [76] J. Kanamori, "Crystal distortion in magnetic compounds," *J. Appl. Phys.*, vol. 14, no. 5, 1960.
- [77] Y. Murakami, J. P. Hill, D. Gibbs, M. Blume, I. Koyama, M. Tanaka, H. Kawata, T. Arima, Y. Tokura, K. Hirota, and Y. Endoh "Resonant X-Ray Scattering from Orbital Ordering in LaMnO_3 " *Phys. Rev. Lett.*, vol. 81, no. 3, pp. 582–585, 1998.
- [78] W. Tong, B. Zhang, S. Tan, and Y. Zhang, "Probability of double exchange between Mn and Fe in $\text{LaMn}_{1-x}\text{Fe}_x\text{O}_3$," *Phys. Rev. B - Condens. Matter Mater. Phys.*, vol. 70, no. 014422, pp. 1–6, 2004.
- [79] O. F. de Lima, J. A. H. Coaquira, R. L. de Almeida, L. B. de Carvalho, and S. K. Malik, "Magnetic phase evolution in the $\text{LaMn}_{1-x}\text{Fe}_x\text{O}_{3+y}$ system," *J. Appl. Phys.*, vol. 105, no. 1, pp. 013907, 2009.
- [80] M. Mihalik jr., Z. Jagličić, M. Fitta, V. Kavečanský, K. Csach, A. Budziak, J. Briančin, M. Zentkova, M. Mihalik, "Structural and magnetic study of $\text{PrMn}_{1-x}\text{Fe}_x\text{O}_3$ compounds," *Journal of Alloys and Compounds*, vol. 685, pp. 652-661, 2016.
- [81] M. C. Silva-Santana, C. A. Dasilva, P. Barrozo, E. J. R. Plaza, L. De Los Santos Valladares, and N. O. Moreno, "Magnetocaloric and magnetic properties of $\text{SmFe}_{0.5}\text{Mn}_{0.5}\text{O}_3$ complex perovskite," *J. Magn. Magn. Mater.*, vol. 401, pp. 612–617, 2016..
- [82] K. Bouziane, A. Yousif, I. A. Abdel-Latif, K. Hricovini, and C. Richter, "Electronic and magnetic properties of $\text{SmFe}_{1-x}\text{Mn}_x\text{O}_3$ orthoferrites ($x=0.1, 0.2, \text{ and } 0.3$)," *J. Appl. Phys.*, vol. 97, no. 10, pp. 5–8, 2005.

- [83] Harikrishnan S. Nair, Tapan Chatterji, C. M. N. Kumar, Thomas Hansen, Hariharan Nhalil, Suja Elizabeth, and André M. Strydom “Magnetic structures and magnetic phase transitions in the Mn-doped orthoferrite TbFeO_3 studied by neutron powder diffraction,” *J. Appl. Phys.*, vol. 119, no. 5, pp. 053901, 2016.
- [84] Yifei Fang, Ya Yang, Xinzhi Liu, Jian Kang, Lijie Hao, Xiping Chen, Lei Xie, Guangai Sun, Venkatesh Chandragiri, Chin-Wei Wang, Yiming Cao, Fei Chen, Yuntao Liu, Dongfeng Chen, Shixun Cao, Chengtian Lin, Wei Ren & Jincang Zhang “Observation of re-entrant spin reorientation in $\text{TbFe}_{1-x}\text{Mn}_x\text{O}_3$,” *Sci. Rep.*, vol. 6, no. August, pp. 33448, 2016.
- [85] M. Wang, T. Wang, S. Song, and M. Tan, “Structure-controllable synthesis of multiferroic YFeO_3 nanopowders and their optical and magnetic properties,” *Materials (Basel)*, vol. 10, no. 626, pp. 1-6, 2017.
- [86] C. J. Howard, B. J. Campbell, H. T. Stokes, M. A. Carpenter, and R. I. Thomson, “Crystal and magnetic structures of hexagonal YMnO_3 ,” *Acta Crystallogr. Sect. B Struct. Sci. Cryst. Eng. Mater section B.*, vol. 69, no. 6, pp. 534–540, 2013.
- [87] N. Sharma, A. Das, S. K. Mishra, C. L. Prajapat, M. R. Singh, and S. S. Meena, “Magnetic and dielectric behavior in $\text{YMn}_{1-x}\text{Fe}_x\text{O}_3$ ($x \leq 0.5$),” *J. Appl. Phys.*, vol. 115, no. 21, pp. 213911, 2014.
- [88] W. C. Koehler, E. O. Wollan and M. K. Wilkinson, “Neutron diffraction study of the Magnetic Properties of Rare-Earth-Iron perovskites,” *Phys. Rev.*, vol. 118, no. 1, pp. 58-70, 1960.
- [89] L. Chen, T. Li, S. Cao, S. Yuan, F. Hong, and J. Zhang, “The role of 4f-electron on spin reorientation transition of NdFeO_3 : A first principle study,” *J. Appl. Phys.*, vol. 111, no. 10, 2012.
- [90] S. J. Yuan, W. Ren, F. Hong, Y. B. Wang, J. C. Zhang, L. Bellaiche, S. X. Cao and G. Cao “Spin switching and magnetization reversal in single-crystal NdFeO_3 ,” *Phys. Rev. B - Condens. Matter Mater. Phys.*, vol. 87, no. 18, pp. 1–6, 2013.
- [91] S. Chanda, S. Saha, A. Dutta, and T. P. Sinha, “Raman spectroscopy and dielectric

- properties of nanoceramic NdFeO₃,” *Mater. Res. Bull.*, vol. 48, no. 4, pp. 1688–1693, 2013.
- [92] Junjie Jiang, Gaibei Song, Dongyang Wang, Zuanming Jin, Zhen Tian, Xian Lin, Jiaguang Han, Guohong Ma, Shixun Cao and Zhenxiang Cheng, “Magnetic-field dependence of strongly anisotropic spin reorientation transition in NdFeO₃: A terahertz study,” *J. Phys. Condens. Matter*, vol. 28, no. 11, pp. 0–6, 2016.
- [93] H. Pinto and H. Shaked, “Long wavelength neutron diffraction study of the magnetic structures of PrFeO₃ and NdFeO₃” vol. 10, pp. 663–665, 1972.
- [94] I. Sosnowska and E. Steichele, “Magnetic structure of NdFeO₃ and PrFeO₃ investigated with a high resolution neutron time-of-flight diffractometer,” *AIP Conf. Proc.*, vol. 89, pp. 309–311, 1982.
- [95] I. Sosnowska, E. Steichele and A. Hewat, “Reorientation phase transition in NdFeO₃” *Physica B*, vol. 136, pp. 394–396, 1986.
- [96] R. Przenioslo, I. Sosnowska, M. Loewenhaupt, and A. Taylor, “Crystal field excitations of NdFeO₃,” *J. Magn. Magn. Mater.*, vol. 140144, pp. 2151–2152, 1995.
- [97] R. Przenioslo, I. Sosnowska, P. Fischer, “Magnetic moment ordering of Nd³⁺ ions in NdFeO₃,” *J. Magn. Magn. Mater.*, vol. 140, no. 140144, pp. 2153–2154, 1995.
- [98] R. Przenioslo, I. Sosnowska, P. Fischer, W. Marti, F. Bartolomé, J. Bartolomé, E. Palacios, R. Sonntag, “Magnetic moment ordering of Nd³⁺ ions in NdFeO₃ at low temperature,” *J. Magn. Magn. Mater.*, vol. 160, no. 140144, pp. 370-371, 1996.
- [99] J. Bartolomé, E. Palacios, M. D. Kuźmin, F. Bartolomé, I. Sosnowska, R. Przeniosło, R. Sonntag and M. M. Lukina “Single-crystal neutron diffraction study of Nd magnetic ordering in NdFeO₃ at low temperature,” *Phys. Rev. B*, vol. 55, no. 17, pp. 11432–11441, 1997.
- [100] W. Sławiński, R. Przeniosło, I. Sosnowska, and E. Suard, “Spin reorientation and structural changes in NdFeO₃,” *J. Phys. Condens. Matter*, vol. 17, no. 29, pp. 4605–4614, 2005.

- [101] S. Y. Wu, C. M. Kuo, H. Y. Wang, W.-H. Li, K. C. Lee, J. W. Lynn and R. S. Liu
“Magnetic structure and spin reorientation of the Mn ions in NdMnO₃,” *J. Appl. Phys.*,
vol. 87, no. 9, p. 5822, 2000.
- [102] R. Rasera and G. Catchen, “Mn-site hyperfine fields in LaMnO₃ and NdMnO₃ measured
using perturbed-angular-correlation spectroscopy,” *Phys. Rev. B*, vol. 58, no. 6, pp.
3218–3222, 1998.
- [103] S. Jandl, V. Nekvasil, M. Diviš, A. A. Mukhin, J. Hölsä, and M. L. Sadowski,
“Infrared study of the crystal-field excitations in NdMnO₃ in high magnetic fields,”
Phys. Rev. B - Condens. Matter Mater. Phys., vol. 71, no. 2, pp. 1–6, 2005.
- [104] T. Chatterji, B. Ouladdiaf, and D. Bhattacharya, “Neutron diffraction investigation of
the magnetic structure and magnetoelastic effects in NdMnO₃,” *J. Phys. Condens.
Matter*, vol. 21, no. 30, 2009.
- [105] T. Chatterji, G. J. Schneider, L. van Eijck, B. Frick, and D. Bhattacharya, “ Direct
evidence for the Nd magnetic ordering in NdMnO₃ from the hyperfine field splitting of
Nd nuclear levels ,” *J. Phys. Condens. Matter*, vol. 21, no. 12, p. 126003, 2009.
- [106] A. Kumar, S. M. Yusuf, and C. Ritter, “Nd-ordering-driven Mn spin reorientation and
magnetization reversal in the magnetostructurally coupled compound NdMnO₃,” *Phys.
Rev. B*, vol. 96, no. 1, pp. 1–10, 2017.
- [107] T. Chakraborty, R. Yadav, S. Elizabeth, and H. L. Bhat, “Evolution of Jahn–Teller
distortion, transport and dielectric properties with doping in perovskite NdFe_{1-x}Mn_xO₃
(0 ≤ x ≤ 1) compounds,” *Phys. Chem. Chem. Phys.*, vol. 18, no. 7, pp. 5316–5323, 2016.
- [108] J Lazurova, M Mihalik, M Mihalik jr., M Vavra, M Zentkova, J Briancin, M Perovic,
V Kusigerski, O Schneeweiss, P Roupцова, K V Kamenev, M Misek, Z Jaglicic,
“Magnetic Properties and Mössbauer spectroscopy of NdFe_{1-x}Mn_xO₃,” *J. Phys. Conf.
Ser.*, vol. 592, p. 012117, 2015.
- [109] M. Mihalik jr., M. Mihalik, J. Lazúrová, M. Fitta, M. Vavra, “Magnetic properties of
NdMn_{1-x}Fe_xO_{3+δ} (0 ≤ x ≤ 0.3) system,” *J. Magn. Magn. Mater.*, vol. 345, pp. 125–133,
2013.

- [110] I. O. Troyanchuk, M. V. Bushinsky, H. Szymczak, M. Baran, and K. Bärner, “Magnetic structure of the manganites heavily doped by Fe and Cr ions,” *J. Magn. Mater. Mater.*, vol. 312, no. 2, pp. 470–475, 2007.
- [111] J. T. Zhang, X. M. Lu, J. Zhou, J. Su, K. L. Min, F. Z. Huang, and J. S. Zhu, “First-principles study of structural, electronic, and magnetic properties of double perovskite $\text{Ho}_2\text{MnFeO}_6$,” *Phys. Rev. B*, vol. 82, no. 22, pp. 224413, 2010.
- [112] R. C. Sherwood, L.G. Van Uitert, R. Wolfe and R. C. Lecraw, “Variation of the reorientation temperature and magnetic crystal anisotropy of the rare-earth orthoferrites” *Phys. Letts.*, vol. 25, no. 4, pp. 297–298, 1967.
- [113] L. G. Marshall, J. G. Cheng, J. S. Zhou, J. B. Goodenough, J. Q. Yan, and D. G. Mandrus, “Magnetic coupling between Sm^{3+} and the canted spin in an antiferromagnetic SmFeO_3 single crystal,” *Phys. Rev. B - Condens. Matter Mater. Phys.*, vol. 86, no. 6, pp. 3–7, 2012.
- [114] X. Zhao, K. Zhang, X. Liu, B. Wang, K. Xu, and S. Cao, “Spin reorientation transition in,” vol. 015201, no. October 2015, pp. 0–6, 2016.
- [115] K. Xu *et al.*, “Hetero-seed and hetero-feed single crystal growth of $\text{Sm}_x\text{Dy}_{1-x}\text{FeO}_3$ perovskites based on optical floating zone method,” *J. Cryst. Growth*, vol. 467, pp. 111–115, 2017.
- [116] M. Eibschütz, “Lattice constants of orthoferrites,” *Acta Crystallogr.*, vol. 19, no. 3, pp. 337–339, 1965.
- [117] K. P. Belov, A. M. Kadomtseva, B. Krynetskii, T. L. Ovchinnikova, and V. A. Timofeeva, “Transitions due to spin reorientation in a $\text{Ho}_{0.5}\text{Dy}_{0.5}\text{FeO}_3$ single crystal,” *Sov. Phys. JETP*, vol. 36, no. 6, pp. 1136–1137, 1973.
- [118] A. Bhattacharjee, K. Saito, and M. Sorai, “Heat capacity and magnetic phase transitions of rare-earth orthoferrite HoFeO_3 ,” *J. Phys. Chem. Solids*, vol. 63, no. 4, pp. 569–574, 2002.
- [119] Guohua Wang, Weiyao Zhao, Yiming Cao, Baojuan Kang, Jincang Zhang, Wei Ren and Shixun Cao, “Temperature-induced spin reorientation and magnetization jump of

- rare-earth orthoferrite $\text{Ho}_{0.5}\text{Pr}_{0.5}\text{FeO}_3$ single crystal” *J. Alloys Compd.*, vol. 674, pp. 300–304, 2016.
- [120] Hailong Wu, Shixun Cao, Ming Liu, Yiming Cao, Baojuan Kang, Jincang Zhang and Wei Ren, “Twofold spin reorientation and field-induced incomplete phase transition in single-crystal $\text{Dy}_{0.5}\text{Pr}_{0.5}\text{FeO}_3$,” *Phys. Rev. B - Condens. Matter Mater. Phys.*, vol. 90, no. 144415, pp. 1–5, 2014.
- [121] Jinchun Wang, Juanjuan Liu, Jieming Sheng, Wei Luo, Feng Ye, Zhiying Zhao, Xuefeng Sun, Sergey A. Danilkin, Guochu Deng, and Wei Bao, “Simultaneous occurrence of multiferroism and short-range magnetic order in DyFeO_3 ,” *Phys. Rev. B*, vol. 93, no. 140403, pp. 6–10, 2016.
- [122] M. Das, S. Roy, and P. Mandal, “Giant reversible magnetocaloric effect in a multiferroic GdFeO_3 single crystal,” *Phys. Rev. B*, vol. 96, no. 174405, pp. 1–8, 2017.
- [123] Yiming Cao, Maolin Xiang, Weiyao Zhao, Guohua Wang, Zhenjie Feng, Baojuan Kang, Alessandro Stroppa, Jincang Zhang, Wei Ren, and Shixun Cao, “Magnetic phase transition and giant anisotropic magnetic entropy change in TbFeO_3 single crystal,” *J. Appl. Phys.*, vol. 119, no. 063904, pp. 1–7, 2016.
- [124] Ke Ya-Jiao, Zhang Xiang-Qun, Ge Heng, Ma Yue, and Cheng Zhao-Hua “Low field induced giant anisotropic magnetocaloric effect in DyFeO_3 single crystal,” *Chinese Phys. B*, vol. 24, no. 3, p. 037501, 2015.
- [125] Mingjie Shao, Shixun Cao, Shujuan Yuan, Jin Shang, Baojuan Kang, Bo Lu, and Jincang Zhang, “Large magnetocaloric effect induced by intrinsic structural transition in $\text{Dy}_{1-x}\text{HoxMnO}_3$,” *Appl. Phys. Lett.*, vol. 100, no. 222404, pp. 1–5, 2012.
- [126] A. Venimadhav, F. Sher, J. P. Attfield, and M. G. Blamire, “Oxygen assisted deposition of $\text{Sr}_2\text{FeMoO}_6$ thin films on $\text{SrTiO}_3(100)$,” *J. Magn. Magn. Mater.*, vol. 269, no. 1, pp. 101–105, 2004.
- [127] H. Kawanaka, I. Hase, S. Toyama, and Y. Nishihara, “Iron spin state of double perovskite oxide Sr_2FeWO_6 ,” *Phys. B Condens. Matter*, vol. 281, pp. 518–520, 2000.
- [128] H. Labrim, A. jabar, A. Belhaj, S. Ziti, L. Bahmad, L. Laânab, and a. Benyoussef,

- “Magnetic proprieties of $\text{La}_2\text{FeCoO}_6$ double perovskite: Monte Carlo study,” *J. Alloys Compd.*, vol. 641, pp. 37–42, 2015.
- [129] S. Vasala and M. Karppinen, “ $\text{A}_2\text{B}'\text{B}''\text{O}_6$ perovskites: A review,” *Prog. Solid State Chem.*, vol. 43, no. 1–2, pp. 1–36, 2015.
- [130] S. Y. Wu, C. M. Kuo, H. Y. Wang, W. H. Li, K.C. Lee, J. W. Lynn, and R.S. Liu, “Magnetic structure and spin reorientation of the Mn ions in NdMnO_3 ,” *J. Appl. Phys.*, vol. 87, no. 9, pp. 5822–5824, 2002.
- [131] N. Pavan Kumar and P. Venugopal Reddy, “Investigation of magnetocaloric effect in Dy doped TbMnO_3 ,” *Mater. Lett.*, vol. 132, pp. 82–85, 2014.
- [132] J. L. Jin, X. Q. Zhang, G. K. Li, Z. H. Cheng, L. Zheng, and Y. Lu, “Giant anisotropy of magnetocaloric effect in TbMnO_3 single crystals,” *Phys. Rev. B - Condens. Matter Mater. Phys.*, vol. 83, no. 18, pp. 1–5, 2011.
- [133] D. Debnath, C. Kim, S. H. Kim, and K. E. Geckeier, “Solid-state synthesis of silver nanoparticles at room temperature: Poly (vinyl pyrrolidone) as a tool,” *Macromol. Rapid Commun.*, vol. 31, no. 6, pp. 549–553, 2010.
- [134] A. Ceylan, S. Ozcan, C. Ni, and S. Ismat Shah, “Solid state reaction synthesis of NiFe_2O_4 nanoparticles,” *J. Magn. Magn. Mater.*, vol. 320, no. 6, pp. 857–863, 2008.
- [135] A. R. West, *Solid State Chemistry and its Applications*. 1984.
- [136] A. Venimadhav, A. Soukiassian, D. A. Tenne, Qi Li, X. X. Xi, D. G. Schlom, R. Arroyave, Z. K. Liu, H. P. Sun, Xiaoqing Pan, Minhyea Lee and N. P. Ong “Structural and transport properties of epitaxial Na_xCoO_2 thin films,” *Appl. Phys. Lett.*, vol. 87, no. 17, pp. 1–3, 2005.
- [137] A. Yadav and S. Chaudhary, “Effect of growth temperature on the electronic transport and anomalous Hall effect response in co-sputtered Co_2FeSi thin films,” *J. Appl. Phys.*, vol. 118, no. 19, 2015.
- [138] A. Yadav and S. Chaudhary, “Effect of growth temperature on structural, magnetic, and transport properties of $\text{Co}_2\text{Cr}_{0.6}\text{Fe}_{0.4}\text{Al}$ Heusler alloy sputtered thin films,” *J. Appl.*

Phys., vol. 117, no. 8, pp. 0–8, 2015.

- [139] K. Bajaj, J. Jesudasan, V. Bagwe, D. C. Kothari, and P. Raychaudhuri, “Correlation between effects of electric current and magnetic field on transport properties of electron-doped manganite $\text{La}_{0.7}\text{Ce}_{0.3}\text{MnO}_3$ thin films,” *J. Phys. Condens. Matter*, vol. 19, no. 38, p. 382202, 2007.
- [140] S. Husain, A. Kumar, S. Akansel, P. Svedlindh, and S. Chaudhary, “Anomalous Hall effect in ion-beam sputtered Co_2FeAl full Heusler alloy thin films,” *J. Magn. Magn. Mater.*, vol. 442, pp. 288–294, 2017.
- [141] A. M. Kamerbeek, E. K. De Vries, A. Dankert, S. P. Dash, B. J. Van Wees, and T. Banerjee, “Electric field effects on spin accumulation in Nb-doped SrTiO_3 using tunable spin injection contacts at room temperature,” *Appl. Phys. Lett.*, vol. 104, no. 21, 2014.
- [142] Naresh Kumar, N.G. Kim, Y.A. Park, N. Hur, J.H. Jung, K.J. Han, K.J. Yee, “Epitaxial growth of terbium iron garnet thin films with out-of-plane axis of magnetization,” *Thin Solid Films*, vol. 516, no. 21, pp. 7753–7757, 2008.
- [143] Tony Low, A. S. Rodin, A. Carvalho, Yongjin Jiang, Han Wang, Fengnian Xia, and A. H. Castro Neto, “Tunable optical properties of multilayer black phosphorus thin films,” *Phys. Rev. B - Condens. Matter Mater. Phys.*, vol. 90, no. 7, pp. 3–7, 2014.
- [144] M. Raju, S. Chaudhary, and D. K. Pandya, “Multi-jump magnetic switching in ion-beam sputtered amorphous $\text{Co}_{20}\text{Fe}_{60}\text{B}_{20}$ thin films,” *J. Appl. Phys.*, vol. 114, no. 5, 2013.
- [145] M. Ohring, *The Materials Science of Thin Films*. 2013.
- [146] M. Hepting, M. Minola, A. Frano, G. Cristiani, G. Logvenov, E. Schierle, M. Wu, M. Bluschke, E. Weschke, H.-U. Habermeier, E. Benckiser, M. Le Tacon, and B. Keimer, “Tunable charge and spin order in PrNiO_3 thin films and superlattices,” *Phys. Rev. Lett.*, vol. 113, no. 22, pp. 1–5, 2014.
- [147] J. A. Greer, “History and current status of commercial pulsed laser deposition equipment,” *J. Phys. D. Appl. Phys.*, vol. 47, no. 3, 2014.

- [148] Hans-Ulrich Krebs, Martin Weisheit, Jörg Faupel, Erik Súske, Thorsten Scharf, Christian Fuhse, Michael Störmer, Kai Sturm, Michael Seibt, Harald Kijewski, Dorit Nelke, Elena Panchenko, and Michael Buback, "Pulsed Laser Deposition (PLD) - a Versatile Thin Film Technique" pp. 1–14, 2001.
- [149] Douglas H. Lowndes, D. B. Geohegan, A. A. Puretzky, D.P. Norton and C. M. Rouleau, "Synthesis of Novel Thin - Film materials by pulsed laser deposition", vol. 3, 1981.
- [150] L. Alff, P. Komissinskiy, A. Radetinac, T. Sirman, and M. Vafae, "The role of cationic and anionic point defects in pulsed laser deposition of perovskites," *J. Phys. D. Appl. Phys.*, vol. 47, no. 3, p. 034012, 2014.
- [151] Kai Wang, "Laser based fabrication of Graphene" *Intech*, capter 4, pp. 77-95, 2016.
- [152] H. Krebs *et al.*, "Pulsed Laser Deposition (PLD) - a Versatile Thin Film Technique UHV-chamber," *Adv. Solid State Phys. SE - 36*, pp. 505–518, 2003.
- [153] P. R. Willmott and J. R. Huber, "Pulsed laser vaporization and deposition," *Rev. Mod. Phys.*, vol. 72, no. 1, pp. 315–328, 2000.
- [154] B.D. Cullity and S.R. Stock, *Elements of X-RAY DIFFRACTION Second Edition*. 1978.
- [155] Bruker, "D8 X-ray Diffractometer Vol. I-Instrument Manual," vol. I, 2016.
- [156] *Thin Film Characterization with Rigaku "SmartLab" XRD system*, Application Laboratories Rigaku Corp., Japan.
- [157] Y. Krockenberger, M. Reehuis, M. Tovar, K. Mogare, M. Jansen, and L. Alff, "A neutron scattering study of the crystal and magnetic structure of $\text{Sr}_2\text{CrOsO}_6$," *J. Magn. Magn. Mater.*, vol. 310, no. 2 suppl. part 2, pp. 1854–1856, 2007.
- [158] M. Reehuis, C. Ulrich, A. Maljuk, Ch. Niedermayer, B. Ouladdiaf, A. Hoser, T. Hofmann, and B. Keimer., "Neutron diffraction study of spin and charge ordering in $\text{SrFeO}_{3-\delta}$," *Phys. Rev. B - Condens. Matter Mater. Phys.*, vol. 85, no. 18, pp. 1–15, 2012.
- [159] J. Rossat-Mignod, "Magnetic Structures," chapter 19, vol. 23, pp. 69–157, 1987.
- [160] Tapan Chatterji, "Neutron Scattering from Magnetic Materials" Elsevier, 2006.

- [161] Jill Trehwella, “Scattering of neutrons: Basics”.
- [162] “Neutron Scattering,” ppt.
- [163] Jason T. Haraldsen, “Introduction to neutron scattering,” ppt.
- [164] J. Rodríguez-Carvajal, “Recent advances in magnetic structure determination by neutron powder diffraction,” *Phys. B Phys. Condens. Matter*, vol. 192, no. 1–2, pp. 55–69, 1993.
- [165] “D1B Diffractometer” , ILL, pp. 1–2, 2019.
- [166] “G4-1 Cold neutron two-axis diffractometer PYRRHIAS,” 2015.
- [167] K. R. Rao, “National facility for neutron beam research,” *Pramana - J. Phys.*, vol. 63, no. 1, pp. 5–14, 2004.
- [168] L. B. McCusker, R. B. Von Dreele, D. E. Cox, D. Louër, and P. Scardi, “Rietveld refinement guidelines,” *J. Appl. Crystallogr.*, vol. 32, no. 1, pp. 36–50, 1999.
- [169] “Rietveld analysis_ppt.” .
- [170] R. L. Fagaly, “Superconducting quantum interference device instruments and applications,” *Rev. Sci. Instrum.*, vol. 77, no. 10, 2006.
- [171] Cort Johnson, Natalie L. Adolphi, Kimberly L. Butler, Debbie M. Lovato, Richard Larson, Peter D.D. Schwindt, Edward R. Flynn “Magnetic relaxometry with an atomic magnetometer and SQUID sensors on targeted cancer cells,” *J. Magn. Magn. Mater.*, vol. 324, no. 17, pp. 2613–2619, 2012.
- [166] S. Tanaka, Y. Kitamura, Y. Hatsukade, T. Ohtani, and S. Suzuki, “Metallic contaminant detection system using multi-channel high T_c SQUIDs,” *J. Magn. Magn. Mater.*, vol. 324, no. 21, pp. 3487–3490, 2012.
- [167] K. Gramm, L. Lundgren, and O. Lundgren, “SQUID magnetometer for magnetization measurements,” *Phys. Scr.*, vol. 13, no. 2, pp. 93–95, 1976.
- [168] G. A. Prinz, “Spin-Polarized Transport,” *Phys. Today*, vol. 48, no. 4, pp. 58–63, 1995.
- [169] G. A. Prinz, “Magnetoelectronics applications,” *J. Magn. Magn. Mater.*, vol. 200, no.

- 1–3, pp. 57–68, 1999.
- [176] A. E. Berkowitz and K. Takano, “Exchange anisotropy - a review” *J. Magn. Magn. Mater.*, vol. 200, pp. 552–570, 1999.
- [177] C. H. Back and H. C. Siegmann, “Ultrashort magnetic field pulses and the elementary process of magnetization reversal,” *J. Magn. Magn. Mater.*, vol. 200, no. 1–3, pp. 774–785, 1999.
- [178] A. K. Zvezdin and A. A. Mukhin, “Magnetolectric interactions and phase transitions in a new class of multiferroics with improper electric polarization,” *JETP Lett.*, vol. 88, no. 8, pp. 505–510, 2008.
- [179] I. Fina, L. Fbrega, X. Martí, F. Sánchez, and J. Fontcuberta, “Magnetic switch of polarization in epitaxial orthorhombic YMnO₃ thin films,” *Appl. Phys. Lett.*, vol. 97, no. 23, pp. 95–98, 2010.
- [180] A. V. Kimel, A. Kirilyuk, A. Tsvetkov, R. V. Pisarev, and T. Rasing, “Laser-induced ultrafast spin reorientation in the antiferromagnet TmFeO₃,” *Nature*, vol. 429, no. 6994, pp. 850–853, 2004.
- [181] J. A. De Jong, A. V. Kimel, R. V. Pisarev, A. Kirilyuk, and T. Rasing, “Laser-induced ultrafast spin dynamics in ErFeO₃,” *Phys. Rev. B - Condens. Matter Mater. Phys.*, vol. 84, no. 10, pp. 1–8, 2011.
- [182] L. T. Tsymbal, Ya. B. Bazaliy, V. N. Derkachenko, V. I. Kamenev, G. N. Kakazei, F. J. Palomares, and P. E. Wigen, “Magnetic and structural properties of spin-reorientation transitions in orthoferrites,” *J. Appl. Phys.*, vol. 101, no. 12, pp. 0–7, 2007.
- [183] Ravi Kumar, R. J. Choudhary, M. Wasi Khan, J. P. Srivastava, C. W. Bao, H. M. Tsai, J. W. Chiou, K. Asokan, and W. F. Pong “Structural, electrical transport and x-ray absorption spectroscopy studies of LaFe_{1-x}Ni_xO₃ (x≤0.6),” *J. Appl. Phys.*, vol. 97, no. 9, 2005.
- [184] Ravi Kumar, R. J. Choudhary, M. Ikram, D. K. Shukla, S. Mollah, P. Thakur, K. H. Chae, Basavaraj Angadi and W. K. Choi “Structural, electrical, magnetic, and

- electronic structure studies of $\text{PrFe}_{1-x}\text{Ni}_x\text{O}_3$ ($x \leq 0.5$),” *J. Appl. Phys.*, vol. 102, no. 7, 2007.
- [185] Abida Bashir, M Ikram, Ravi Kumar, P Thakur, K H Chae, W K Choi and V R Reddy, “Structural, magnetic and electronic structure studies of $\text{NdFe}_{1-x}\text{Ni}_x\text{O}_3$ ($0 \leq x \leq 0.3$).,” *J. Phys. Condens. Matter*, vol. 21, no. 32, p. 325501, 2009.
- [186] T. Bora and S. Ravi, “Sign reversal of magnetization and tunable exchange bias field in $\text{NdCr}_{1-x}\text{Fe}_x\text{O}_3$ ($x = 0.05-0.2$),” *J. Magn. Magn. Mater.*, vol. 386, no. 3, pp. 85–91, 2015.
- [187] Ankita Singh, A. Jain, Avijeet Ray, Padmanabhan B., Ruchika Yadav, Vivian Nassif, Sajid Husain, S. M. Yusuf, T. Maitra, and V. K. Malik. “Spin reorientation in $\text{NdFe}_{0.5}\text{Mn}_{0.5}\text{O}_3$: Neutron scattering and ab initio study”, *Phys. Rev. B*, vol. 96, no. 14, p. 144420, 2017.
- [188] Matúš Mihalik, Marián Mihalik, Andreas Hoser, Daniel M. Pajerowski, Dominik Kriegner, Dominik Legut, Kristof M. Lebecki, Martin Vavra, Magdalena Fitta, and Mark W. Meisel., “Magnetic structure of the mixed antiferromagnet $\text{NdMn}_{0.8}\text{Fe}_{0.2}\text{O}_3$,” *Phys. Rev. B*, 2017.
- [189] A. Muñoz, J. A. Alonso, M. J. Martínez-Lope, J. L. García-Muñoz, and M. T. Fernández-Díaz, “Magnetic structure evolution of NdMnO_3 derived from neutron diffraction data,” *J. Phys. Condens. Matter*, vol. 12, no. 7, pp. 1361–1376, 2000.
- [190] J. A. Alonso, M. J. Martínez-Lope, M. T. Casais, and M. T. Fernández-Díaz, “Evolution of the Jahn-Teller distortion of MnO_6 octahedra in RMnO_3 perovskites (R = Pr, Nd, Dy, Tb, Ho, Er, Y): A neutron diffraction study,” *Inorg. Chem.*, vol. 39, no. 5, pp. 917–923, 2000.
- [191] R. Yadav and S. Elizabeth, “Magnetic frustration and dielectric relaxation in insulating $\text{Nd}_2\text{NiMnO}_6$ double perovskites,” *J. Appl. Phys.*, vol. 117, no. 5, 2015.
- [192] A. Anshul, R. K. Kotnala, R. P. Aloysius, A. Gupta, and G. A. Basheed, “Magnetodielectric coupling in epitaxial $\text{Nd}_2\text{CoMnO}_6$ thin films with double perovskite structure,” *J. Appl. Phys.*, vol. 115, no. 8, 2014.

- [193] I. Dass, J. Q. Yan, and B. Goodenough, "Oxygen stoichiometry, ferromagnetism, and transport properties of $\text{La}_{2-x}\text{NiMnO}_{6+\delta}$," *Phys. Rev. B - Condens. Matter Mater. Phys.*, vol. 68, no. 6, pp. 1–12, 2003.
- [194] F. Hong, Z. Cheng, H. Zhao, H. Kimura, and X. Wang, "Continuously tunable magnetic phase transitions in the $\text{DyMn}_{1-x}\text{Fe}_x\text{O}_3$ system," *Appl. Phys. Lett.*, vol. 99, no. 9, pp. 3–6, 2011.
- [195] F. Hong, Z. Cheng, S. Zhang, and X. Wang, "Dielectric relaxation in the $\text{DyMn}_{1-x}\text{Fe}_x\text{O}_3$ system," *J. Appl. Phys.*, vol. 111, no. 3, p. 034104, 2012.
- [196] S. Blundell, "Magnetism in Condensed Matter - Stephen Blundell," 2001.
- [197] H. Nhalil, H. S. Nair, S. R., A. M. Strydom, and S. Elizabeth, "Spin-reorientation and weak ferromagnetism in antiferromagnetic TbMnO_3 ," *J. Appl. Phys.*, vol. 117, no. 17, pp. 0–5, 2015.
- [198] S. M. Yusuf, A. K. Bera, N. S. Kini, I. Mirebeau, and S. Peti "Two- and three-dimensional magnetic ordering in the bilayer manganite $\text{Ca}_{2.5}\text{Sr}_{0.5}\text{GaMn}_2\text{O}_8$," *Phys. Rev. B - Condens. Matter Mater. Phys.*, vol. 74, no. 18, pp. 8–12, 2006.
- [199] M. A. McGuire and V. O. Garlea, "Short- and long-range magnetic order in LaMnAsO ," *Phys. Rev. B*, vol. 93, no. 5, pp. 1–9, 2016.
- [200] X. Fabrèges, I. Mirebeau, S. Petit, P. Bonville, and A. A. Belik, "Frustration-driven magnetic order in hexagonal InMnO_3 ," *Phys. Rev. B - Condens. Matter Mater. Phys.*, vol. 84, no. 5, 2011.
- [201] P M Sarte, H J Silverstein, B T K Van Wyk, J S Gardner, Y Qiu, H D Zhou and C R Wiebe, "Absence of long-range magnetic ordering in the pyrochlore compound $\text{Er}_2\text{Sn}_2\text{O}_7$," *J. Phys. Condens. Matter*, vol. 23, no. 38, 2011.
- [202] M. Reguluski, R. Przeniosło, I. Sosnowska, and J. U. Hoffmann, "Short and long range magnetic ordering in $\beta\text{-MnO}_2$: A temperature study," *J. Phys. Soc. Japan*, vol. 73, no. 12, pp. 3444–3447, 2004.
- [203] D. M. Pajerowski, "Mixing A -type and G -type B -site antiferromagnetism in AMn_{1-}

- $x\text{Fe}_x\text{O}_3$ (A=La,Nd),” *Phys. Rev. B*, vol. 98, no. 13, pp. 1–12, 2018.
- [204] R. Gerber and G. Elbinger, “Contribution of Fe^{2+} , Mn^{3+} and Fe^{3+} ions to the magnetic anisotropy of $\text{Mg}_x\text{Mn}_{0.6}\text{Fe}_{2.4-x}\text{O}_4$,” *J. Phys. C Solid State Phys.*, vol. 3, no. 6, pp. 1363–1375, 1970.
- [205] J. E. Gordon, R. A. Fisher, Y. X. Jia, N. E. Phillips., S. F. Reklis, D. A. Wright and A. Zettl “Specific heat of $\text{Nd}_{0.67}\text{Sr}_{0.33}\text{MnO}_3$,” *Phys. Rev. B.*, vol. 59, no. 1, pp. 127–130, 1999.
- [206] S Harikrishnan, C M Naveen Kumar, H L Bhat, Suja Elizabeth, U K Rößler ,K Dörr, S Rößler and S Wirth “Investigations on the spin-glass state in $\text{Dy}_{0.5}\text{Sr}_{0.5}\text{MnO}_3$ single crystals through structural, magnetic and thermal properties,” *J. Phys. Condens. Matter*, vol. 20, no. 27, p. 275234, 2008.
- [207] J. Hemberger, M. Brando, R. Wehn, V. Yu. Ivanov, A. A. Mukhin, A. M. Balbashov, and A. Loid, “Magnetic properties and specific heat of RMnO_3 (R=Pr, Nd)” *Phys. Rev. B*, vol. 69, no. 6, p. 064418, 2004.
- [208] J. López, O. F. de Lima, P. N. Lisboa-Filho, and F. M. Araujo-Moreira, “Specific heat at low temperatures and magnetic measurements in $\text{Nd}_{0.5}\text{Sr}_{0.5}\text{MnO}_3$ and $\text{R}_{0.5}\text{Ca}_{0.5}\text{MnO}_3$ (R =Nd, Sm, Dy, and Ho) samples,” *Phys. Rev. B*, vol. 66, no. 21, p. 214402, 2002.
- [209] Guochu Deng, Peiyin Guo, Wei Ren, Shixun Cao, Helen E. Maynard-Casely, Maxim Avdeev, and Garry J. McIntyre, “The magnetic structures and transitions of a potential multiferroic orthoferrite ErFeO_3 ,” *J. Appl. Phys.*, vol. 117, no. 16, 2015.
- [210] Y. Du, Z. X. Cheng, X. L. Wang, and S. X. Dou, “Lanthanum doped multiferroic DyFeO_3 : Structural and magnetic properties,” *J. Appl. Phys.*, vol. 107, no. 9, p. 317, 2010.
- [211] F.-K. Chiang, M.-W. Chu, F. C. Chou, H. T. Jeng, H. S. Sheu, F. R. Chen, and C. H. Chen “Effect of Jahn-Teller distortion on magnetic ordering in $\text{Dy}(\text{Fe},\text{Mn})\text{O}_3$ perovskites,” *Phys. Rev. B - Condens. Matter Mater. Phys.*, vol. 83, no. 24, pp. 10–13, 2011.
- [212] Z. Y. Zhao, X. Zhao, H. D. Zhou, F. B. Zhang, Q. J. Li, C. Fan, X. F. Sun, and X. G. Li,

- “Ground state and magnetic phase transitions of orthoferrite DyFeO_3 ,” *Phys. Rev. B - Condens. Matter Mater. Phys.*, vol. 89, no. 22, pp. 1–8, 2014.
- [213] E. Hovestreydt, M. Aroyo, S. Sattler, and H. Wondratschek, “KAREP - a program for calculating irreducible space-group representations,” *J. Appl. Crystallogr.*, vol. 25, no. 4, pp. 544–544, 1992.
- [214] A. K. Zvezdin and A. A. Mukhin, “On the effect of inhomogeneous magnetoelectric (flexomagnetoelectric) interaction on the spectrum and properties of magnons in multiferroics,” *JETP Lett.*, vol. 89, no. 7, pp. 328–332, 2009.
- [215] F. Bartolomé, M. D. Kuzmin, J. Bartolome, J. Blasco, J. Garcia, and F. Sapina, “Low-Temperature Specific-Heat of NdMO_3 (M=Co, Fe, Cr, Ni) - Magnetic-Ordering of Nd,” *Solid State Commun.*, vol. 91, no. 3, pp. 177–182, 1994.
- [216] M. H. Phan and S. C. Yu, “Review of the magnetocaloric effect in manganite materials,” *J. Magn. Magn. Mater.*, vol. 308, no. 2, pp. 325–340, 2007.
- [217] D. Kramer, “NASA sees a future with nuclear power,” *Phys. Today*, vol. 70, no. 12, pp. 26–29, 2017.
- [218] W. F. Giauque and D. P. MacDougall, “Attainment of Temperatures Below 1° K by Demagnetization of $\text{Gd}_2(\text{SO}_4)\cdot 8\text{H}_2\text{O}$ ” *Phys. Rev.*, no. 43, p. 768, 1933.
- [219] A. Gschneidner, V. K. Pecharsky, and A. O. Tsokol, “Recent developments in magnetocaloric materials,” *Reports Prog. Phys.*, vol. 68, no. 6, pp. 1479–1539, 2005.
- [220] L. Li, W. D. Hutchison, D. Huo, T. Namiki, Z. Qian, and K. Nishimura, “Low-field giant reversible magnetocaloric effect in intermetallic compound ErCr_2Si_2 ,” *Scr. Mater.*, vol. 67, no. 3, pp. 237–240, 2012.
- [221] J. Chen, B. G. Shen, Q. Y. Dong, F. X. Hu, and J. R. Sun, “Giant reversible magnetocaloric effect in metamagnetic HoCuSi compound,” *Appl. Phys. Lett.*, vol. 96, no. 15, 2010.
- [222] J. L. Snyman and A. M. Strydom, “Anomalous magnetic ground state in PrSi evidenced by the magnetocaloric effect,” *J. Appl. Phys.*, vol. 111, no. 7, 2012.

- [223] P. K. Das, A. Bhattacharyya, R. Kulkarni, S. K. Dhar, and A. Thamizhavel, “Anisotropic magnetic properties and giant magnetocaloric effect of single-crystal PrSi,” *Phys. Rev. B - Condens. Matter Mater. Phys.*, vol. 89, no. 13, pp. 1–9, 2014.
- [224] H. Zhang, B. G. Shen, Z. Y. Xu, J. Shen, F. X. Hu, J. R. Sun, and Y. Long “Large reversible magnetocaloric effects in ErFeSi compound under low magnetic field change around liquid hydrogen temperature,” *Appl. Phys. Lett.*, vol. 102, no. 9, 2013
- [225] L. Li, K. Nishimura, W. D. Hutchison, Z. Qian, D. Huo, and T. Namiki, “Giant reversible magnetocaloric effect in ErMn₂Si₂ compound with a second order magnetic phase transition,” *Appl. Phys. Lett.*, vol. 100, no. 15, pp. 2–6, 2012.
- [226] S. Kumar, I. Coondoo, M. Vasundhara, A. K. Patra, A. L. Kholkin, and N. Panwar, “Magnetization reversal behavior and magnetocaloric effect in SmCr_{0.85}Mn_{0.15}O₃ chromites,” *J. Appl. Phys.*, vol. 121, no. 4, pp. 0–7, 2017.
- [227] J. L. Jin, X. Q. Zhang, H. Ge, and Z. H. Cheng, “Rotating field entropy change in hexagonal TmMnO₃ single crystal with anisotropic paramagnetic response,” *Phys. Rev. B - Condens. Matter Mater. Phys.*, vol. 85, no. 21, pp. 1–5, 2012.
- [228] M. Balli, S. Jandl, P. Fournier, and M. M. Gospodinov, “Anisotropy-enhanced giant reversible rotating magnetocaloric effect in HoMn₂O₅ single crystals,” *Appl. Phys. Lett.*, vol. 104, no. 23, pp. 1–6, 2014.
- [229] R. Huang, S. Cao, W. Ren, S. Zhan, B. Kang, and J. Zhang, “Large rotating field entropy change in ErFeO₃ single crystal with angular distribution contribution,” *Appl. Phys. Lett.*, vol. 103, no. 16, 2013.
- [230] W. Zhong, C.-T. Au, and Y.-W. Du, “Review of magnetocaloric effect in perovskite-type oxides,” *Chinese Phys. B*, vol. 22, no. 5, p. 057501, 2013.
- [231] Y.-J. Ke, X.-Q. Zhang, Y. Ma, and Z.-H. Cheng, “Anisotropic magnetic entropy change in RFeO₃ single crystals(R = Tb, Tm, or Y),” *Sci. Rep.*, vol. 6, no. June 2015, p. 19775, 2016.
- [232] L. H. Yin, J. Yang, R. R. Zhang, J. M. Dai, W. H. Song, and Y. P. Sun, “Multiferroicity and magnetoelectric coupling enhanced large magnetocaloric effect in

- DyFe_{0.5}Cr_{0.5}O₃,” *Appl. Phys. Lett.*, vol. 104, no. 3, pp. 1–6, 2014.
- [233] A. McDannald, L. Kuna, and M. Jain, “Magnetic and magnetocaloric properties of bulk dysprosium chromite,” *J. Appl. Phys.*, vol. 114, no. 11, 2013.
- [234] A. McDannald and M. Jain, “Magnetocaloric properties of rare-earth substituted DyCrO₃,” *J. Appl. Phys.*, vol. 118, no. 4, pp. 0–5, 2015.
- [235] S. Kumar, I. Coondoo, M. Vasundhara, S. Kumar, A. L. Kholkin, and N. Panwar, “Structural, magnetic, magnetocaloric and specific heat investigations on Mn doped PrCrO₃ orthochromites,” *J. Phys. Condens. Matter*, vol. 29, no. 19, 2017.
- [236] Y. J. Ke, X. Q. Zhang, H. Ge, Y. Ma, and Z. H. Cheng, “Low field induced giant anisotropic magnetocaloric effect in DyFeO₃ single crystal,” *Chinese Phys. B*, vol. 24, no. 3, 2015.
- [237] L. H. Yin, J. Yang, P. Tong, X. Luo, W. H. Song, J. M. Dai, X. B. Zhu, and Y. P. Sun., “Magnetocaloric effect and influence of Fe/Cr disorder on the magnetization reversal and dielectric relaxation in RFe_{0.5}Cr_{0.5}O₃ systems,” *Appl. Phys. Lett.*, vol. 110, no. 19, p. 192904, 2017.
- [238] M. K. Sharma, T. Basu, K. Mukherjee, and E. V. Sampathkumaran, “Enhancement of magnetic ordering temperature and magnetodielectric coupling by hole doping in a multiferroic DyFe_{0.5}Cr_{0.5}O₃,” *J. Phys. Condens. Matter*, vol. 29, no. 8, pp. 0–4, 2017.
- [239] M. K. Sharma, T. Basu, K. Mukherjee, and E. V. Sampathkumaran, “Effect of rare-earth (Er and Gd) substitution on the magnetic and multiferroic properties of DyFe_{0.5}Cr_{0.5}O₃,” *J. Phys. Condens. Matter*, vol. 28, no. 42, 2016.
- [240] M. Foldeaki, W. Schnelle, E. Gmelin, P. Benard, B. Koszegi, A. Giguere, R. Chahine, and T. K. Bose “Comparison of magnetocaloric properties from magnetic and thermal measurements Comparison of magnetocaloric properties from magnetic and thermal measurements,” vol. 309, no. 1997, 2017.
- [241] Jing Ma, Jiamian Hu, Zheng. Li, and Ce-Wen Nan, “Recent Progress in Multiferroic Magnetoelectric Composites : from Bulk to Thin Films,” *Advanced Materials*, vol. 23, pp. 1062–1087, 2011.

- [242] H. U. Habermeier, "Thin films of perovskite-type complex oxides," *Mater. Today*, vol. 10, no. 10, pp. 34–43, 2007.
- [243] D. S. Schmool, N. Keller, M. Guyot, R. Krishnan, and M. Tessier, "Magnetic and magneto-optic properties of orthoferrite thin films grown by pulsed-laser deposition," *J. Appl. Phys.*, vol. 86, no. 10, pp. 5712–5717, 1999.
- [244] J. Röder, T. Liese, and H. Krebs, "Pulsed Laser Deposition," *ANDOR*, vol. 10, no. 20, pp. 2–3, 2011.
- [245] D. S. Schmool, N. Keller, M. Guyot, R. Krishnan, and M. Tessier, "Evidence of very high coercive fields in orthoferrite phases of PLD grown thin " *Journ. of Magnetism and magnetic Materials*, vol. 195, pp. 291–298, 1999.
- [246] Y. Dumont *et al.*, "Pulsed laser deposition and optical characterizations of the magnetic samarium orthoferrite," *Thin Solid Films*, vol. 520, no. 6, pp. 1890–1894, 2011.
- [247] Bruno Berini, Jan Mistrik, Yves Dumont, Elena Popova, Arnaud Fouchet, Joseph Scola, Niels Keller, "Pulsed laser deposition and optical characterizations of the magnetic samarium orthoferrite," *Thin Solid Films*, vol. 520, no. 6, pp. 1890–1894, 2011.
- [248] W. Si, K. Huang, X. Wu, and S. Feng, "Epitaxial thin film of SmFeO_3 ferroelectric heterostructures," *Sci. China Chem.*, vol. 57, no. 6, pp. 803–806, 2014.
- [249] K. Sultan, M. Ikram, S. Gautam, H.-K. Lee, K. H. Chae, and K. Asokan, "Structural, magnetic and electronic structure studies of $\text{PrFe}_{1-x}\text{Mn}_x\text{O}_3$ ($x = 0, 0.1, 0.3, 0.5$) thin films grown on Si (100)," *J. Alloys Compd.*, vol. 628, pp. 151–157, 2015.
- [250] M. Shang, C. Wang, Y. Chen, F. Sun, and H. Yuan, "The multiferroic epitaxial thin film YFeO_3 ," vol. 175, pp. 23–26, 2016.
- [251] D. Roy, S. Sakshath, G. Singh, R. Joshi, and S. V Bhat, "Investigation on two magnon scattering processes in pulsed laser deposited epitaxial nickel zinc ferrite thin film," *J. Phys. D. Appl. Phys.*, vol. 125004, p. 125004.

- [252] Gauthier Lefevre, Sébastien Saitzek, Florent Blanchard, Anthony Ferri, Pascal Roussel, Rachel Desfeux and Adlane Sayede, “Microstructure and oxidation resistance of relaxed epitaxial nickel thin films grown on (100)- and (110)-SrTiO₃ substrates by pulsed laser deposition,” *CrystEngComm*, vol. 20, pp. 5061–5073, 2018.
- [253] M. A. Stranick, “Mn₂O₃ by XPS”, *Surface Science Spectra*, vol. 6, no. 39, 1999.
- [254] M. M. Rahman and A. M. Asiri, “Development of ionic-sensor based on sono-chemically prepared low-dimensional β-Fe₂O₃ nanoparticles onto flat-gold electrodes by an electrochemical approach”, *Sensing and Bio-Sensing Research*, 2015.

